2-24-2020 3:30 PM

Early Meteoritic Records of Asteroidal Melt and Impact Environments

Brendt Hyde
The University of Western Ontario

Graduate Program in Geology
A thesis submitted in partial fulfillment of the requirements for the degree in Doctor of Philosophy

Supervisor
Moser, Desmond
The University of Western Ontario Co-Supervisor
Tait, Kimberly
Royal Ontario Museum

Abstract

The characterization of meteorites formed in early melt and impact environments helps deepen our understanding of the processes involved in the formation and modification of terrestrial bodies in the solar system. The main objective of this thesis is to interpret and describe a range of igneous and metamorphic environments on asteroidal bodies, through the chemical, microstructural and isotopic analysis of meteorites, and to place these in the context of evolving rocky bodies in the early protoplanetary disk. Study of the meteorite Northwest Africa (NWA) 869 has led to the novel discovery of a eucrite impactor clast in chondritic regolith material. Secondary heating from additional impact(s) formed a basaltic melt, in a rim surrounding the clast, which has bulk characteristics similar to some planetary achondrites. This finding reveals an alternate pathway to achondrite formation and illustrates the mixing of chemical reservoirs in the solar system. Phosphate thermochronology measurements carried out *in situ* on NWA 7680 and 6962 revealed that they have remained below 350-550 °C since the time of the early protoplanetary disk (4578 ± 17 Myr ago for NWA 7680). Both meteorites have compositions and textures consistent with formation through short-lived differentiation processes on a primitive CR chondrite-like parent body, preserve evidence of some of the earliest known asteroidal melts, and contain Cr and O isotopic evidence for rapid (within several million years) establishment of chemical reservoirs within the protoplanetary disk. Finally, a textural analysis of graphite and diamond disposition in the ureilites NWA 11950 and 11951 was conducted to test recent planetary models invoking diamond as a relic of static metamorphism within an early planet-sized body. The results of the textural study are instead consistent with a paragenesis by shock waves passing from lower (carbon) to higher (silicates) shock impedance materials. This thesis has established the nature and timescale of some of the earliest formation and modification processes on rocky bodies in our solar system, providing physical evidence with which to improve our models of planetary evolution.

Keywords

meteorites, L chondrite, eucrite, ureilite, carbonaceous achondrite, NWA 869, NWA 7680, NWA 6962, NWA 11950, NWA 11951, impact, shock, impact breccia, impact melt, differentiation, early solar system, diamonds, geochronology, thermochronology, Raman spectroscopy, cathodoluminescence, electron backscatter diffraction, oxygen isotopes.

Summary for Lay Audience

Meteorites provide snapshots of our solar system's formation and evolution through time. Key processes in the transition from the presolar disk to planets include melting and collision. These processes are important because they ultimately led to the formation of the Earth and other planets and the outgassing of volatiles to their surfaces. The main objective of this thesis is to describe some of the earliest melting processes which initiated on asteroids, as represented in meteorites, to obtain a better understanding of how and for what duration rocky bodies experienced melting and differentiation. The results of this research include evidence of rocks that have gone through the differentiation process impacting and mixing with more primitive rocks on the surface of an asteroid. Information about the melt mixing occurring during impact processes is vital to our understanding about how distinct objects accrete, grow and evolve over time. The study of a second set of meteorites has revealed new insights into the diversity and timing of melt processes; including evidence of previously unknown early (> 4.5 billion years ago) melt environments on a primitive asteroid in the outer solar system. Additional work carried out on a third set of meteorites has found evidence of high pressure impact shock-related diamonds in meteorites from a partially differentiated parent body. The shock formation of diamonds in these meteorites challenges the views of early melt processes, as some studies suggest the requirement of a large planet to form the diamonds at depth. The knowledge gained through this thesis stems from customized methodologies and integrating analytical techniques, enabling a deepening of our understanding of early formation and modification processes on rocky bodies in our solar system.

Co-Authorship Statement

Chapter 2: Brendt Hyde carried out all electron imaging, EDS mapping, SEM-based quantitative EDS/WDS analyses and EBSD mapping. Training of SEM-based techniques was provided by Ivan Barker. Brian Joy carried out EPMA with spot selection and data refinement and interpretation being carried out by Brendt Hyde. Oxygen isotope analyses were carried out by Douglas Rumble and Michelle Thompson. Interpretation of the oxygen isotope data included Brendt Hyde. Kimberly Tait and Desmond Moser provided supervision and helped with the interpretation and writing of this study.

This chapter has been accepted for publication:

Hyde B. C., Tait K. T., Moser D. E., Rumble D., Thompson M. S. (2020) Accretionary mixing of a eucrite impactor and the regolith of the L chondrite parent body. *Meteoritics & Planetary Science* 55:20-35

Chapter 3: Brendt Hyde carried out all electron imaging, EDS mapping and CL imaging. Raman spectroscopy work was carried out by Brendt Hyde. Trace element analyses and U-Pb isotope ratio analyses were carried out by James Darling, Hugo Moreira and Brendt Hyde. Brian Joy carried out EPMA with spot selection and data refinement and interpretation being carried out by Brendt Hyde. Oxygen isotope analyses were carried out by Neil Banerjee, Arshad Ali and Iffat Jabeen. Interpretation of the oxygen isotope data included Brendt Hyde. Qing-Zhu Yin and Matthew Sanborn carried out Cr-isotope analyses on the samples. These analyses are not included in this chapter; however, the data aided in the interpretation of results presented here. Desmond Moser and Kimberly Tait provided supervision and helped with the interpretation and writing of this study.

Chapter 4: Brendt Hyde carried out all electron imaging, EDS mapping, SEM-based quantitative EDS/WDS analyses and CL imaging. Raman spectroscopy work was carried out by Brendt Hyde. Oxygen isotope analyses were carried out by Karen Ziegler, but interpretation was done by Brendt Hyde. Kimberly Tait and Desmond Moser provided supervision and helped with the interpretation and writing of this study.

Appendix 1: Brendt Hyde carried out all SEM-based quantitative EDS spot analyses and quantitative EDS mapping. The initial set-up for these analyses was aided by training from Ivan Barker. Brian Joy provided EPMA data and helped with standard selection. Desmond Moser and Kimberly Tait provided supervision and helped with the writing of this study.

This appendix was a part of a topical conference:

Hyde B. C., Moser D. E., Tait K. T., Barker I. R. and Joy B. R. 2016. Development of Quantitative Energy Dispersive Spectrometry with a Field Emission Gun Scanning Electron Microscope for Use in Meteorite Studies (Abstract). Electron Probe Microanalysis Topical Conference (EPMA 2016).

Appendix 5: Brendt Hyde carried out all electron imaging, CL imaging, EBSD mapping and Raman spectroscopy. Desmond Moser and Kimberly Tait provided supervision and helped with the interpretation and writing of this study.

Acknowledgments

I would like to thank my supervisors Kimberly Tait and Desmond Moser for their help, support and encouragement. This thesis would not be a reality without their continued guidance. Kim was the first to introduce me to the world of meteorites and Des introduced me to geochronology. I am extremely lucky to be able to play a part in both of these worlds.

I would also like to extend a special thanks to David Gregory. David donated many of the meteorites used in this thesis work and has provided continuous support for my work and the work of countless students over the years.

This thesis would also not have been possible without the help of the ZAPLab team and my friends and colleagues at the Royal Ontario Museum. Thank you to Ivan Barker, Giancarlo Jones, Gabriel Arcuri, Lisa Cupelli, Connor Davis, Lee White, Tanya Kizovski, Ian Nicklin, Veronica DiCecco, Katherine Dunnell, Tony Steede, Malcolm Back, Steve Korchinos, Sean Yokoyama, Keane Tirona, Ana Černok and Matt Duffy.

Thank you to the administrative staff in Earth Science at Western and at the Royal Ontario Museum. Thank you to Barry Price for continuous technical support over the years.

A special thank you to my coauthors that allowed me to work with them and learn through experience: James Darling, Brian Joy, Douglas Rumble, Michelle Thompson, Qing-Zhu Yin, Matthew Sanborn, Neil Banerjee, Arshad Ali, Iffat Jabeen and Hugo Moreira. Instrument support was also appreciated from Karen Ziegler.

Roberta Flemming, Elizabeth Webb, Sean Shieh and Phil McCausland are thanked for teaching and academic advice.

Matt Izawa and James Rolfe are thanked for their words of encouragement.

I wish to acknowledge financial support from NSERC, OGS, the University of Western Ontario and the Mineralogical Association of Canada. The support was much appreciated.

I would also like to thank my family Edward, Joan, Derek and Michael Hyde and my animal family Ruby, Gobo, Cinnabun and Wembly.

Table of Contents

List of Tables

List of Figures

List of Appendices

Chapter 1

Introduction

1.1 Opening Statement

The compositions and textures of primitive meteorites record events that took place before the Earth was fully-formed, providing a snapshot of the otherwise hidden pathways to planet formation in our solar system. Melt processes occurring in the primitive solar system were important steps in the building of planets, moons and asteroids. These processes were the result of surface impacts and internal heating by radioactive decay and differentiation, all of which played a significant role in planetesimal formation (e.g., Weiss and Elkins-Tanton 2013). On Earth, evidence of these early melt environments has been erased by continued planetary differentiation, plate tectonics, surface weathering and large-scale impacts. The main objective of this thesis is to interpret and describe some of the early processes initiating on asteroidal bodies, as represented in meteorites, to obtain a better understanding of how and for what duration rocky bodies experienced the growth and melting processes that ultimately led to the formation of the Earth and other planetary bodies.

1.2 Meteorites by Definition

1.2.1 Background

The solar system's formation began 4.567 billion years ago (Connelly et al. 2012). Some of the first solids to form in this early solar nebula were chondrules and calcium- and aluminum-rich inclusions (CAIs) (Connelly et al. 2012). Chondrules represent dust aggregates that were quickly melted and cooled at temperatures <1000 K (Connelly et al. 2012 and references therein). Since chondrules crystallized from a molten silicate droplet, they generally retain a spheroidal shape and contain silicate minerals including olivine and pyroxene. The CAIs contain calcium and aluminum-rich minerals. Their shapes are more irregular than chondrules and they are often white in colour. The majority of CAIs crystallized as fine-grained condensates from a gas at high temperatures (>1300 K), with some experiencing later re-melting (Connelly et al. 2012 and references therein). Two

main types of models have been proposed to account for the heating events that caused CAI and chondrule formation: shock-wave models and the x-wind model (Krot et al. 2009 and references therein). Shock-wave models suggest that transient heating events occurred as a result of shock-waves passing through the early solar system. The source of these shockwaves are unknown, but many possibilities have been proposed, including fast moving planetesimals, collisions, disk instabilities and stellar phenomena (Krot et al. 2009 and references therein). The x-wind model suggests that materials were heated close to the early sun by flares and then transported further out into the solar system by the magnetocentrifugally-driven x-wind (Krot et al. 2009 and references therein).

These early solids coalesced to become the first rocky bodies in our solar system. The objects that survived the multitude of impacts occurring in the forming solar system went on to become the asteroids, planets and moons that we know today. Some of these rocky bodies generated enough heat to melt and differentiate (large asteroids, planets and moons), while others retained the compositions and textures associated with the solar system's birth. This long history has been investigated largely through the examination of meteorites. Meteorites are objects originating from space that survive the transit and impact into a terrestrial surface. For the Earth this means surviving transit through the atmosphere (NASA). Meteorites can potentially come from planets or moons, but they largely originate from asteroids. Asteroids are solid bodies containing rocky (mainly silicate and oxide) material as well as Fe-metal and in some cases ice. These objects did not become large enough to reach planet-status. The majority of these bodies are currently found in the main asteroid belt between Mars and Jupiter.

Some of the first solids forming in the early solar nebula are seen today in primitive meteorites in the form of chondrules and CAIs. Meteorites containing these objects are referred to as *chondrites* (Fig. 1.1). Meteorites from parent bodies that grew large enough to melt and differentiate have lost these primitive textures and compositions and are thus called *achondrites* (Fig. 1.1). As one might imagine, there are objects that fall within a transitional stage between these two groups. These are referred to as *primitive achondrites*. These meteorites generally do not contain chondrules, but do retain mineralogical and/or geochemical properties associated with a primitive source

environment. There is debate amongst researchers regarding the exact definitional boundaries between these three types of meteorites. Most notably the group of meteorites referred to as ureilites are thought to be achondrites by some, but primitive achondrites by others (e.g., Bischoff et al. 2001; Weisberg et al. 2006). Ureilites are a unique type of meteorite with heterogeneous geochemical compositions (e.g., Rumble et al. 2010) suggesting a primitive source environment; however, they otherwise appear to be from a more evolved parent body. There are many meteorite classification schemes available for use and most share similar methods for defining a meteorite's class. For the purposes of this thesis we will use the scheme provided in Weisberg et al. (2006) (Fig. 1.2).

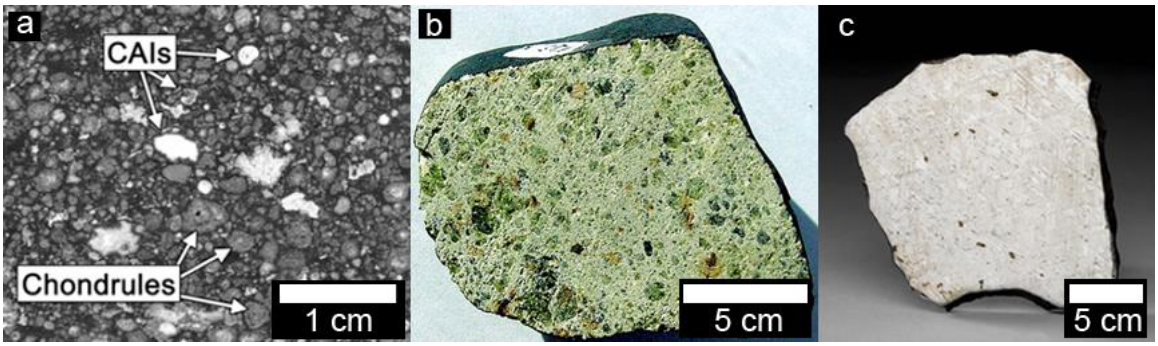

Figure 1.1. Cut sections of meteorites. a) a carbonaceous chondrite (e.g., Allende) composed of primitive chondrules (round) and CAIs (white and irregular). b) a diogenite (e.g., Johnstown) meteorite originating from the mantle of a differentiated parent body. c) an iron meteorite (e.g., Gibeon) originating from the core of a differentiated parent body. The images originated from MacPherson and Boss (2011), Northern Arizona University and the Royal Ontario Museum, respectively.

1.2.2 Source of Meteorites for this Thesis Project

The meteorites examined in this thesis came from the extensive meteorite collection at the Royal Ontario Museum, which hosts a wide selection of rare meteorites. These meteorites are named for the location where they struck the Earth. In this case they all came from the deserts of Northwest Africa (NWA). The meteorite materials examined in this thesis include a primitive chondrite (L chondrite, NWA 869) containing a more evolved achondrite clast (eucrite). Additionally, this thesis includes meteorites

representing primitive melts (NWA 7680 and 6962) and ureilites (NWA 11950 and 11951).

1.3 Characterizing Meteorites Geochemically

1.3.1 Classifying Meteorites

Determining where an unknown meteorite should be placed within a classification scheme (Fig. 1.2) can be a challenging task. Many meteorites have similar textures and compositions; however, geochemical trends have been determined to help distinguish between the various meteorite groups and to help define new groups. Major and minor element geochemistry of component minerals in meteorites can be used to help determine a meteorite's classification. A list of minerals analyzed and mentioned in this thesis can be found in Table 1.1. The composition of pyroxene has been used for classification and to determine parent body sources for meteorites (e.g., Fig. 1.3; Karner et al. 2006; Papike et al. 2003). The compositional trends observed are most likely attributed to the volatility of Mn versus Fe. This would explain the increase in Mn/Fe with increasing distance from the Sun; with the exception of the Moon, which would have lost Mn through its impact origin (Karner et al. 2006). The minor element composition of olivine has also been used to differentiate between meteorite groups. This is particularly useful for the primitive achondrites (Fig. 1.4; Goodrich et al. 2011). Perhaps the most utilized technique for classifying meteorites is oxygen isotope analysis (e.g., Clayton and Mayeda 1996; Clayton and Mayeda 1999). This technique has been used to distinguish between different meteorite groups and suggest relations between previously separated groups (Fig. 1.5; Franchi et al. 2001). Recent work has used chromium isotope analyses in combination with oxygen isotope analyses to further refine the meteorite groups and associations between these groups (Fig. 1.6; Sanborn et al. 2018; see section 3.2 for further discussion). These geochemical classification tools are used throughout the main chapters of this thesis.

Table 1.1. List of minerals analyzed and mentioned in this thesis.

Name	Ideal Formula	Short Form (if applicable)
pyroxenes		***Py***
diopside	$MgCaSi_2O_6$	Di
hedenbergite	$FeCaSi_2O_6$	Hd
augite	$Ca(Mg,Fe)Si_2O_6$	
pigeonite	$(Ca,Mg,Fe)(Mg,Fe)Si_2O_6$	
enstatite	$MgSiO_3$	En
ferrosilite	$FeSiO_3$	Fs
olivines		***Ol***
forsterite	Mg_2SiO_4	Fo
fayalite	Fe_2SiO_4	Fa
feldspars		
anorthite	$CaAl_2Si_2O_8$	An
albite	$NaAlSi_3O_8$	Ab
orthoclase	$KAlSi_3O_8$	Or
additional minerals		
quartz	SiO_2	
tridymite	SiO_2	
nepheline	$(Na,K)AlSiO_4$	Ne
diamond	C	
graphite	C	
lonsdaleite	C	
pyrrhotite	$Fe_{(1-x)}S$	S
chromite	$FeCr_2O_4$	Chr
ilmenite	$FeTiO_3$	
merrillite	$Ca_9NaMg(PO_4)_7$	Mer
apatite	$Ca_5(PO_4)_3(OH,F,Cl)$	
fluorapatite	$Ca_5(PO_4)_3F$	Ap
zircon	$ZrSiO_4$	
baddeleyite	ZrO_2	

Note: minerals in solid solution are often denoted in the text by a short form notation. For instance a mineral of Fa_{30} describes the Fe-content of a given olivine. In this case, the composition is equivalent to 30% fayalite and 70% forsterite.

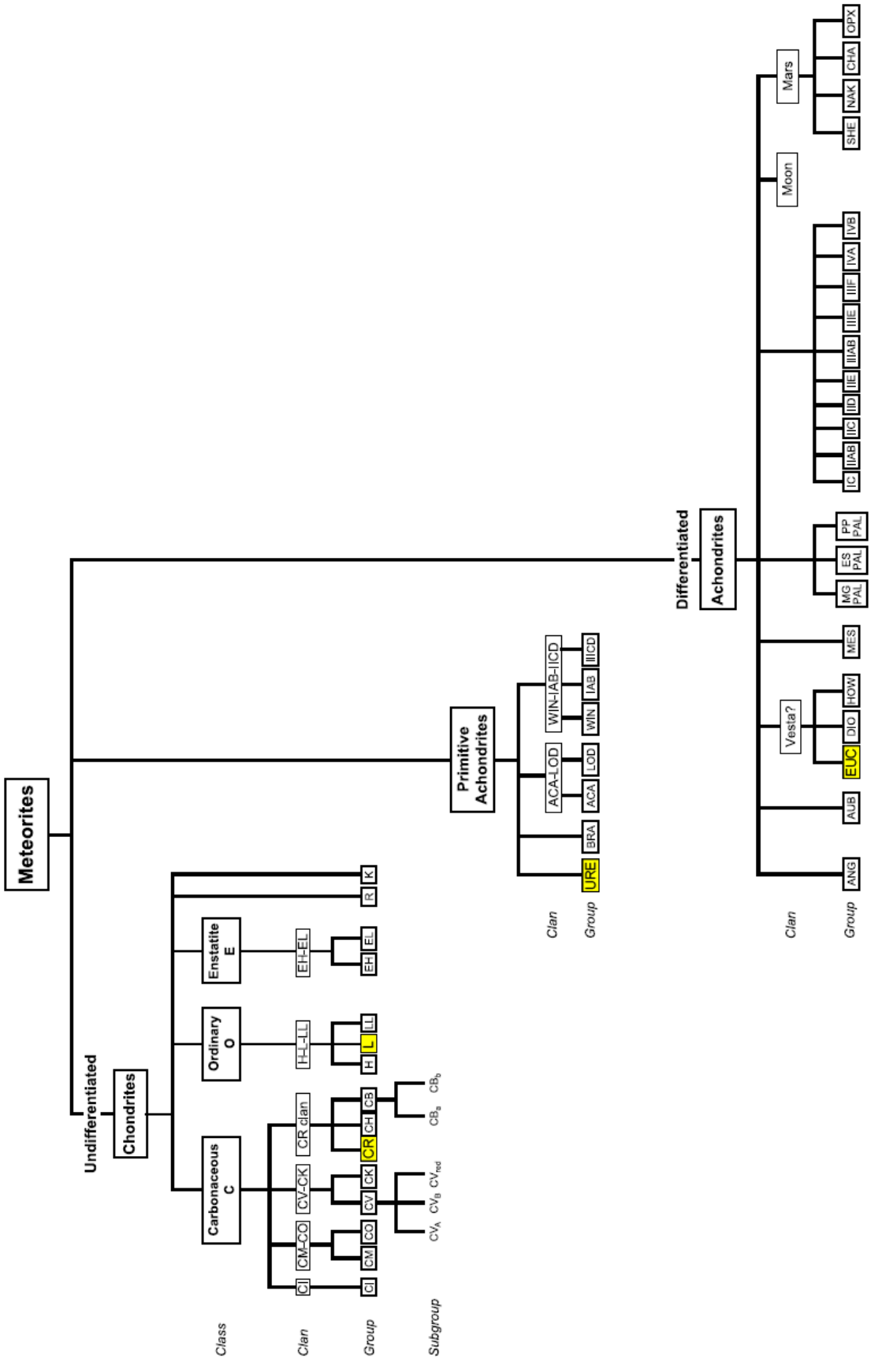
Meteorites
Undifferentiated
Chondrites
Carbonaceous C
Ordinary O
Enstatite E
R
K
CI
CM–CO
CV–CK
CR clan
CH
CB
EH–EL
H–L–LL
EH
EL
H
L
LL
CM
CO
CV
CK
CR
CH
CB
CV_A CV_B CV_red
CB_a CB_b
Class
Clan
Group
Subgroup
Primitive Achondrites
ACA–LOD
WIN–IAB–IICD
URE
BRA
ACA
LOD
WIN
IAB
IIICD
Clan
Group
Differentiated Achondrites
Vesta?
Moon
Mars
ANG
AUB
EUC
DIO
HOW
MES
MG PAL
ES PAL
PP PAL
IC
IIAB
IIC
IID
IIE
IIIAB
IIIE
IIIF
IVA
IVB
SHE
NAK
CHA
OPX
Clan
Group

Figure 1.2. (previous page) Diagram expressing the systematics of meteorite classification and showing the major meteorite divisions, classes, clans, and groups and relationships among meteorite groups. URE - ureilite, ACA - acapulcoite, LOD - lodranite, ANG - angrite, AUB - aubrite, BRA - brachinite, WIN - winonaite, HED - howardite-eucrite-diogenite, MES - mesosiderite, MG PAL - main-group pallasite, ES PAL - Eagle Station pallasite, PP PAL - pyroxene pallasite, SHE - shergottite, NAK - nakhlite, CHA - chassignite, OPX - orthopyroxenite (figure and description modified from Weisberg et al. 2006). Note: Meteorite groups highlighted in yellow are the main groups studied in this thesis.

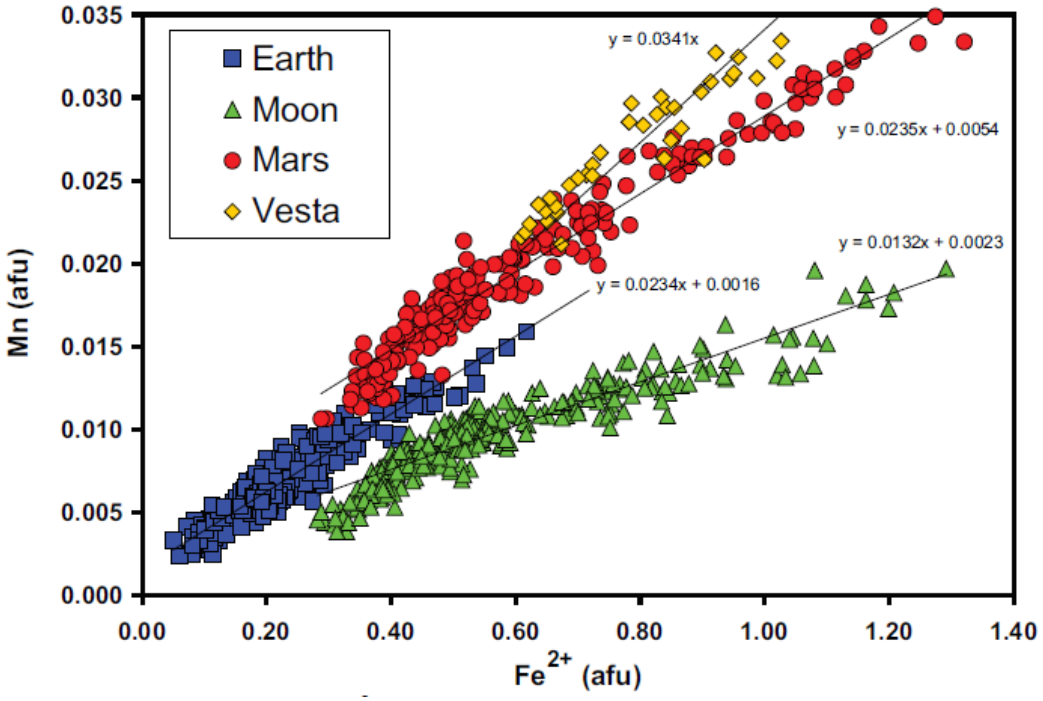

Figure 1.3. Mn vs. Fe^{2+} in atoms per 6-oxygen formula unit (afu) for pyroxene analyses from the Earth, Moon, Mars and Vesta. Best-fit trendlines are indicated and their equations are given (figure and description taken directly from Karner et al. 2006).

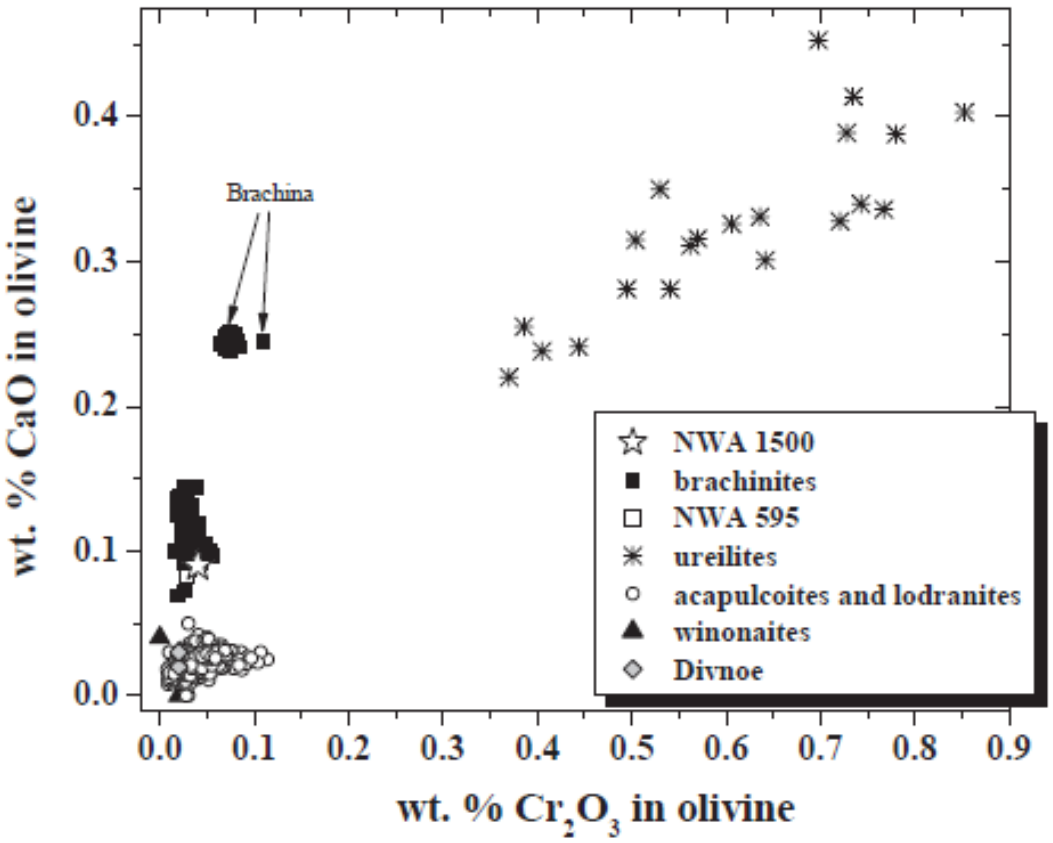

Figure 1.4. CaO and Cr_2O_3 contents of olivine in various primitive achondrites (figure and description taken directly from Goodrich et al. 2011. See reference for data sources).

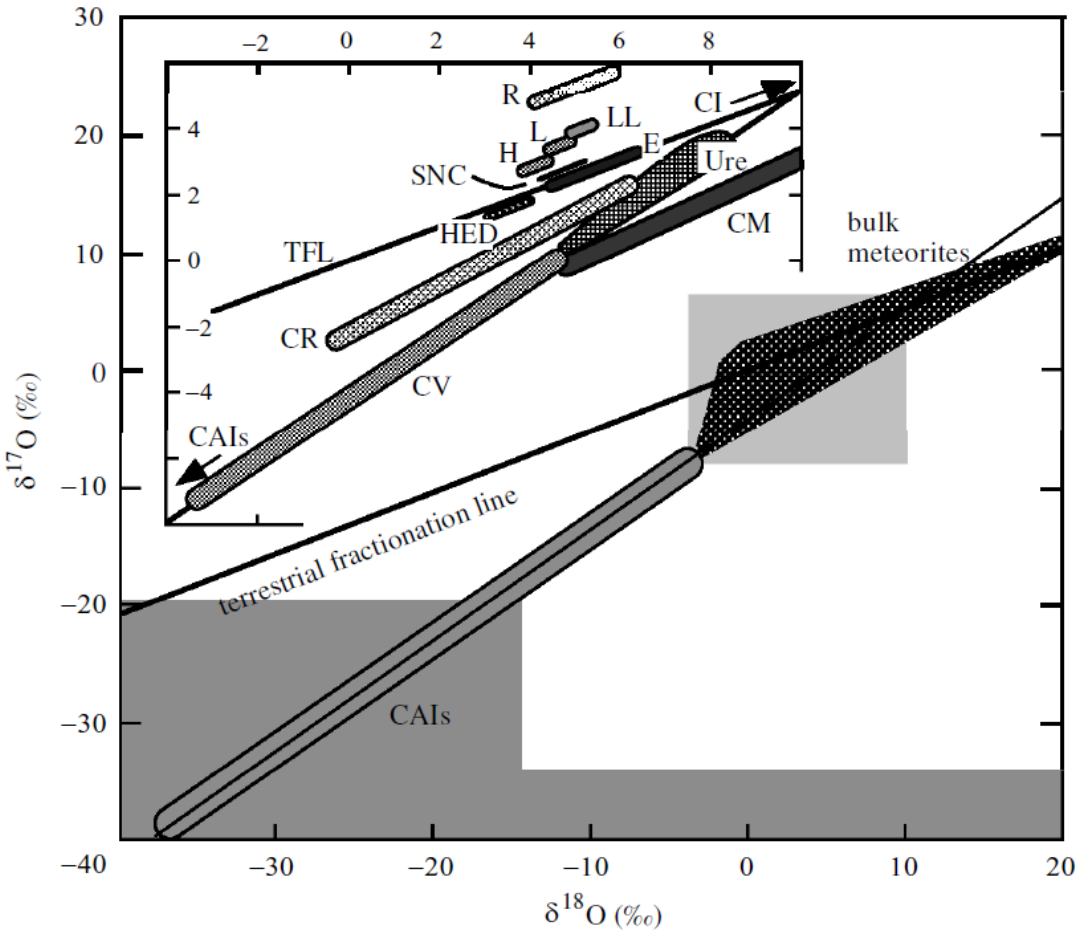

Figure 1.5. Oxygen-isotopic composition of bulk meteoritic materials. Inset covers area of the light grey box. The main groups of chondritic and achondritic meteorites, covering the range of values displayed by these types, are shown. TFL - terrestrial fractionation line, which is shown for reference; H, L and LL are all types of ordinary chondrites; R - R chondrites; CR, CV and CM are carbonaceous chondrites; E - enstatite chondrites and aubrites; SNC - shergottites, nakhlites and Chassigny; HED - howardites, eucrites and diogenites; Ure - ureilites; CAIs -calcium-aluminium-rich inclusions Note: see section 1.4.4 for definitions of δ-notation on the axes. (figure and description taken directly from Franchi et al. 2001. See reference for data sources).

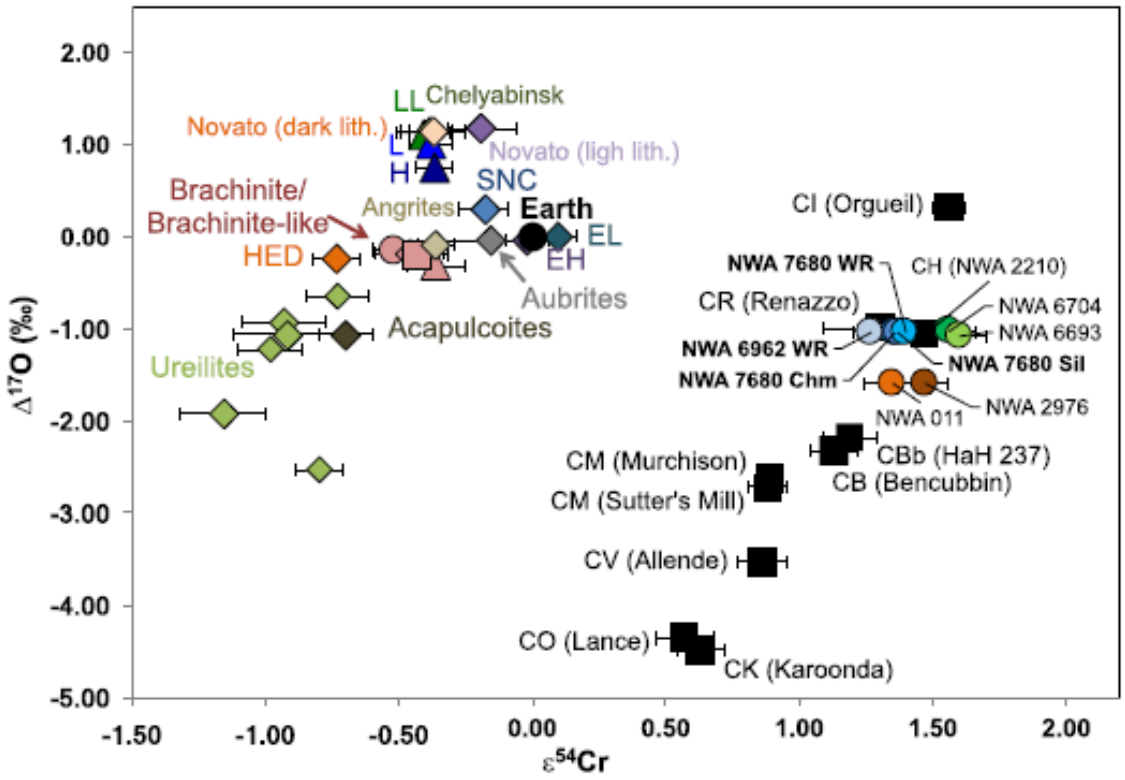

Figure 1.6. $\varepsilon^{54}Cr$ vs. $\Delta^{17}O$ diagram showing NWA 7680/6962 in comparison to other achondrite and chondrite meteorites (figure and description taken directly from Sanborn et al. 2018. See reference for data sources). The meteorites cluster into two groupings: the non-carbonaceous (left) and carbonaceous (right) (See section 3.2 for further discussion). Note: See section 1.4.4 for definitions of Δ-notation on the axis. $\varepsilon^{54}Cr$ is the deviation of $^{54}Cr/^{52}Cr$ from the terrestrial ratio ($x10^{-4}$).

1.3.2 *In Situ* U-Pb Isotope Ratio Geochronology and Thermochronology

Precise measurements of U-Pb isotope ratios can allow researchers to determine dates for crystallization and modification events occurring on a given parent body. These determinations utilize the known decay rates of U isotopes to their corresponding stable Pb isotopes. An advantage of the U-Pb dating system over other isotopic dating systems is the fact that two isotope decay chains occur at rates that are applicable to geologic and cosmic phenomena, allowing an internal check on determined age information. The half-life of ^{238}U (which decays to ^{206}Pb) is 4.468 billion years and the half-life ^{235}U (which

decays to ^{207}Pb) is 704 million years (e.g., Davis et al. 2003). Minerals that incorporate U into their structure during formation, but reject Pb, provide useful geologic clocks for study and *in situ* analysis of these minerals can provide dating information with very little damage to a given sample (see section 1.4.3). A mineral often used for geochronology studies is zircon, which incorporates U during crystallization and has a high closure temperature to loss of radiogenic Pb (Fig. 1.7), meaning diffusion rates of elements in the structure quickly slow down as the rock cools. In some cases, age determinations from these mineral grains result in crystallization ages; however, ages of metamorphic significance, including impact phenomena can also be determined (e.g., Moser et al. 2011). Phosphate minerals can provide an additional source of age information. Apatite is the most common phosphate mineral in the Earth's crust and is ubiquitous, being found in essentially all rock types (Hughes and Rakovan 2015). Uranium substitutes into the apatite structure through many different coupled substitutions with the simplest being $U^{4+} + [\ ] = 2Ca^{2+}$ (Luo et al. 2009). These properties have led to apatite being used for U-Pb dating. The U-Pb closure temperature for apatite is much lower than that of zircon, occurring at 350 – 550 °C depending on grain size and cooling rate (Cherniak et al. 1991; Chew and Spikings 2015; Harrison et al. 2002; Fig. 1.7). This property allows scientists to carry out thermochronology studies, using apatite to probe thermal events in the rock record, even those of relatively low geologic temperatures. The sensitivity of apatite (and related phosphates) to thermal resetting and the fact that it is found in most rock types makes it an ideal candidate for thermochronology studies of meteorites (see Chapter 3).

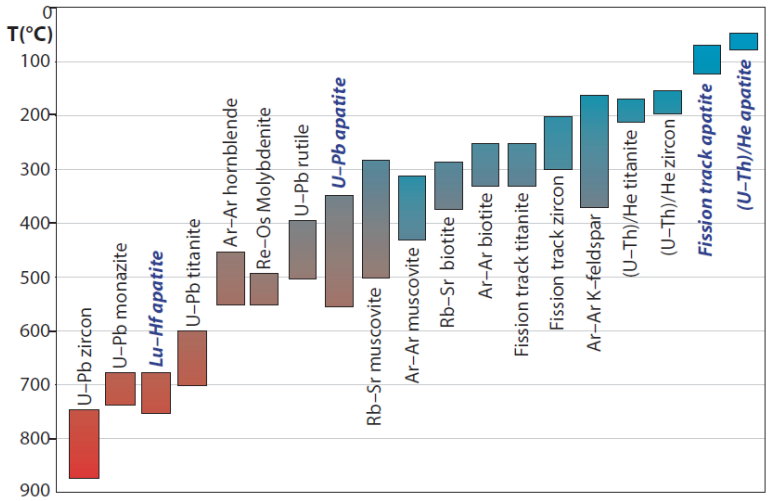

Fig. 1.7 Closure temperatures for minerals commonly used for geochronology and thermochronology (Chew and Spikings 2015).

1.4 Instrumentation

The analyses carried out for this thesis made use of numerous instruments. The specific analytical set-ups can be found in the methods sections in Chapters 2, 3 and 4. The basic underlying principles of these analytical methods and their purpose are described below.

1.4.1 Electron Beam Techniques

The Hitachi SU6600 Field Emission Scanning Electron Microscope (FE-SEM), at the University of Western Ontario Zircon and Accessory Phase Laboratory, used for this thesis provided multiple analytical options for characterizing meteorites. When an electron beam strikes a sample's surface the emitted and scattered components can be measured to obtain information about the sample's chemical composition and orientation microstructure (Fig. 1.8). The analytical techniques utilized with this system are described below:

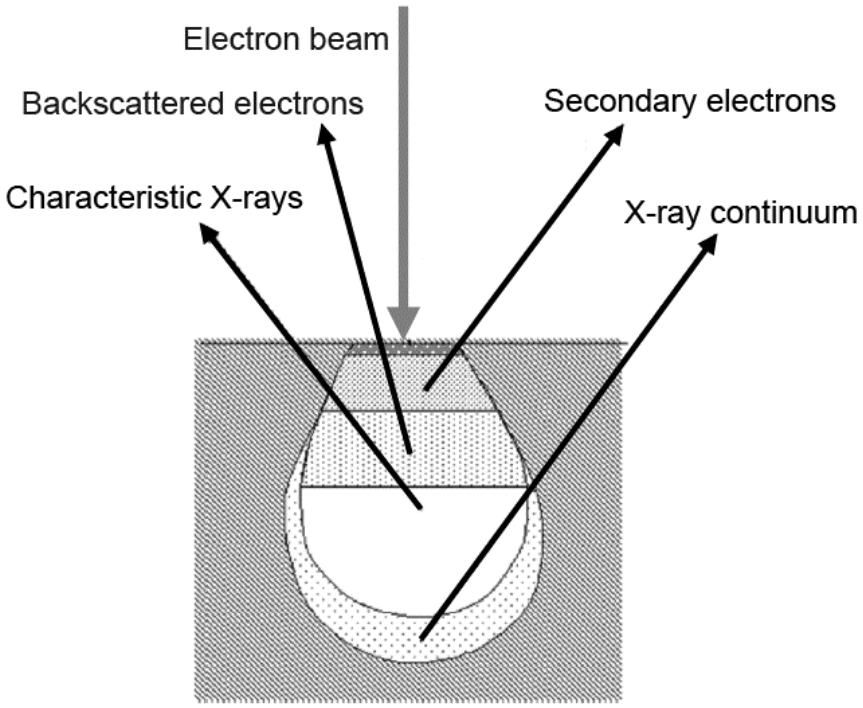

Figure 1.8. A representative image showing an electron beam striking a sample's surface and the resulting scattered and emitted components that can be measured along with the relative interaction volumes. Modified from Zhou et al. (2006).

1.4.1.1 Electron Imaging

Both backscattered electron (BSE) imaging and secondary electron (SE) imaging were used to image the polished sections in this thesis. Backscattering of electrons is an elastic scattering process whereby the incident electrons are scattered back towards a detector (Fig. 1.9). The BSE images provide a first glimpse of the phases with high density phases appearing high intensity (e.g. metal) and low density phases appearing dark (e.g. graphite) (e.g., Chapter 4, Fig. 4.2). Secondary electrons are produced through inelastic scattering due to the interaction of the primary electron beam and the sample's electrons (Fig. 1.9). The SE images provide information about sample topography. This is particularly useful information in samples showing differential polishing hardness properties leading to peaks (e.g. diamond) and valleys (e.g. graphite) (e.g., Chapter 4, Fig. 4.8).

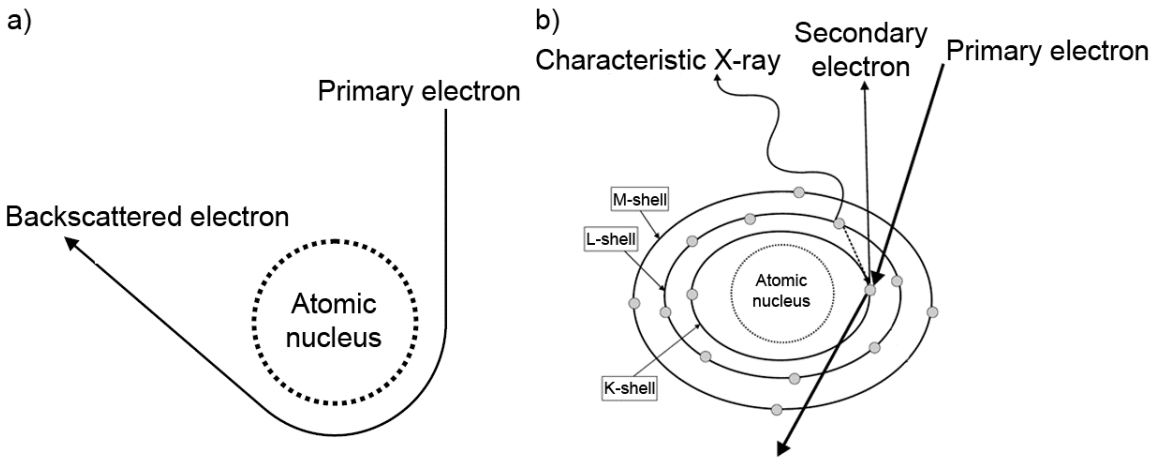

Figure 1.9. a) The generation of backscattered electrons from a primary electron beam interacting with a sample atom. b) Secondary electrons production and removal of a lower energy shell electron. This position is then filled by a higher energy shell electron, which releases energy, in the form of a characteristic X-ray, as it moves to the lower shell. Modified from Michler (2008).

1.4.1.2 Energy Dispersive and Wavelength Dispersive X-ray Spectrometry

When an electron beam strikes a sample's surface it produces characteristic X-ray emissions which depend on the elemental make-up of the sample (Fig. 1.9). The incident electron beam removes a lower energy shell electron of a given element. This position is in turn filled by a higher energy shell electron, which releases energy as it moves to the lower shell. This energy release is equivalent to the energy difference between the shells and is unique to the element in question. When the energy and intensity of these X-rays are measured this is referred to as energy dispersive X-ray spectrometry (EDS) (e.g. Appendix 1). When quantitative measurements are required, the energies are measured relative to a characteristic energy of a calibration standard (e.g. pure silicon). These EDS spectra are measured using a detector, such as a silicon drift detector (SDD). These detectors measure the energy of the X-rays by determining the amount of ionization that is produced in the detector material. This ionization produces a charge, which is what the detector electronics actually measure. Elemental concentrations determined by EDS can even be mapped across a polished section (e.g., Chapter 2, Fig. 2.2). Through the use of diffracting crystals wavelength dispersive X-ray spectrometry (WDS) can be carried out. Multiple crystals can be used to optimize the diffraction from specific characteristic X-rays and to allow for the collection of data from multiple elements simultaneously. The advantage of WDS is its spectral resolution, which provides the ability to measure elements that may overlap in an EDS analysis. This also allows for better quantification for minor and trace elements. Measurements for this thesis that utilized WDS include analyses on the FE-SEM (e.g., Chapter 4, Table 4.1) and from an electron microprobe (e.g., Chapter 2, Table 2.1).

1.4.1.3 Cathodoluminescence

Electron beam irradiation can cause the emission of visible light through a process known as cathodoluminescence (CL) (Fig. 1.10). This energy emission is the result of 1) band-band electron transitions, 2) electron-defect assisted transitions and 3) impurity induced transitions within band gaps. The resulting luminescence can be imaged and may highlight the chemical microstructure of the phase in question. This can reveal

information about the formation and modification environments for minerals that are CL active (e.g., Chapter 3, Fig. 3.12).

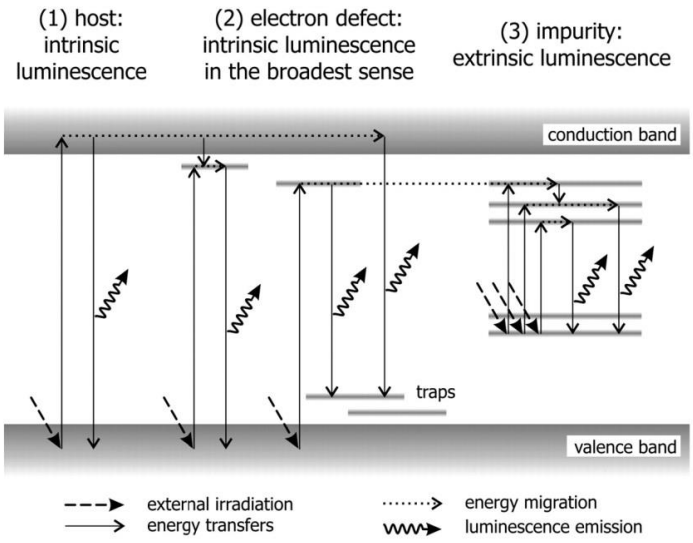

Figure 1.10. Energy diagram showing three types of CL generated during electron beam irradiation (Nasdala et al. 2003).

1.4.1.4 Electron Backscatter Diffraction

Highly polished samples can also be tilted at a high angle in the FE-SEM allowing electrons to diffract through the surface layers of the sample, forming diffraction patterns call Kikuchi bands on a detector. This type of analysis is called electron backscatter diffraction (EBSD) (Fig. 1.11). The Kikuchi bands observed can be transformed back into crystal lattice space. This allows minerals to be structurally identified and it allows their structural orientation to be examined and even mapped (e.g., Chapter 2, Fig. 2.4).

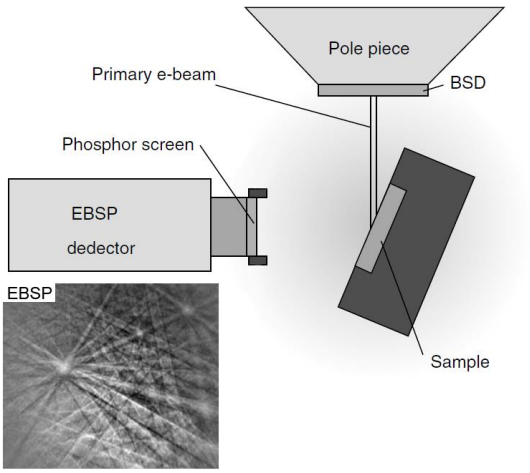

Figure 1.11. The EBSD set-up shows a sample tilted at a high angle, so that the incoming primary electron beam only interacts with a small volume of the material at the surface. The diffracted beam is then imaged on a phosphor screen. An example electron backscatter diffraction pattern (EBSP) is shown with diagnostic Kikuchi bands. Also shown is the backscattered electron detector (BSD). Modified from Maitland and Sitzman (2006).

1.4.2 Micro-Raman Spectroscopy

This project used a Horiba LabRAM ARAMIS micro-Raman spectrometer. Raman spectroscopy is a type of molecular spectroscopy that utilizes the principles of Raman scattering (Fig. 1.12). The energy changes, or Raman shifts, are measured relative to an incident laser beam energy. These shifts can be used to identify minerals and make observations of crystallinity. Raman spectroscopy is generally non-destructive and requires little sample preparation, making it ideal for meteorite studies. This technique also provides the ability to discriminate between phases with identical chemical composition (e.g., Chapter 4, Fig. 4.6).

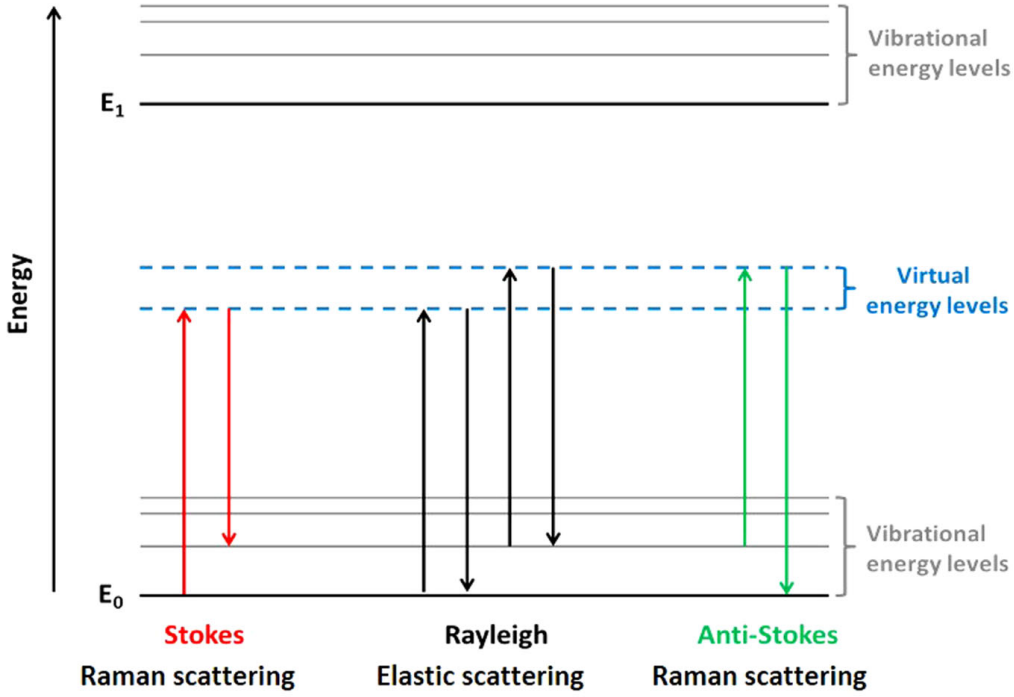

Figure 1.12. Energy level diagram showing the effects of Raman scattering. When laser light interacts with a molecule it is excited to a virtual state. When the laser light is scattered elastically this is referred to as Rayleigh scattering (left). When Raman scattering occurs the scattered light either receives (anti-Stokes) or loses (Stokes) energy from interacting with the molecules of the sample (Ember et al. 2017).

1.4.3 Laser Ablation Inductively Coupled Plasma Mass Spectrometry

Trace element analysis was carried out using laser ablation inductively coupled plasma mass spectrometry (LA-ICP-MS). This instrument uses a laser to ablate material from the sample (Fig. 1.13) which is then transported to a mass spectrometer where the isotope abundances of a given element are measured. This thesis made use of Agilent 7500cs (quadrupole) ICP-MS system with a New-Wave UP213 (213 nm) solid-state Nd:YAG laser and an Analytic Jena Plasma Quant MS Elite ICP-MS with an ASI RESOlution SE 193 nm excimer laser. Both systems utilize a quadrupole mass spectrometer, which consists of four parallel cylindrical rods. In this type of spectrometer the sample's ablated ions are separated based on their trajectories in oscillating electric fields applied to the rods (Fig. 1.14). The ion selection is based on their mass-to-charge ratio. Isotope abundances can be measured relative to standard materials providing absolute abundances. Ratio measurements can also be measured, as is the case for U-Pb isotope ratio geochronology studies (e.g., Chapter 3).

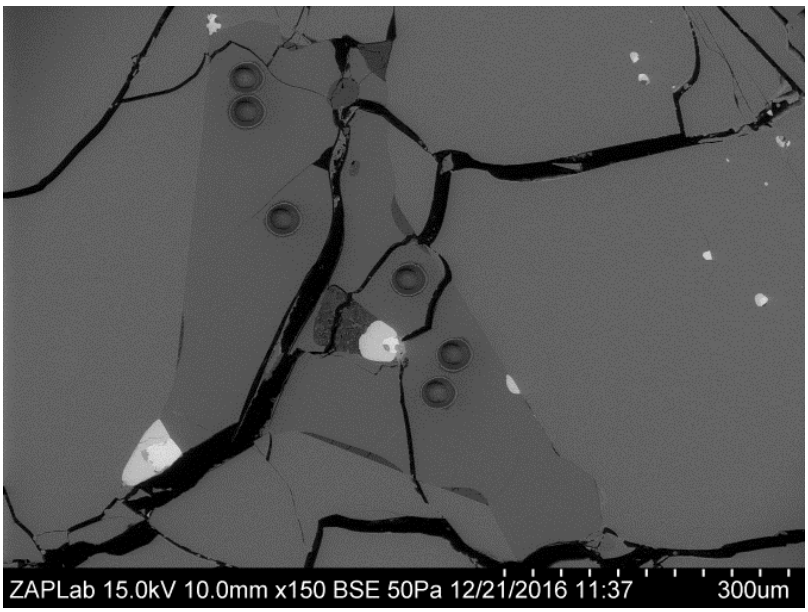

Figure 1.13. Backscattered electron image of a merrillite grain from the meteorite NWA 7680 (Chapter 3). Six round laser ablation pits are seen in the figure. This ablated material was used to determine trace element concentrations and U-Pb isotope ratio information for the sample.

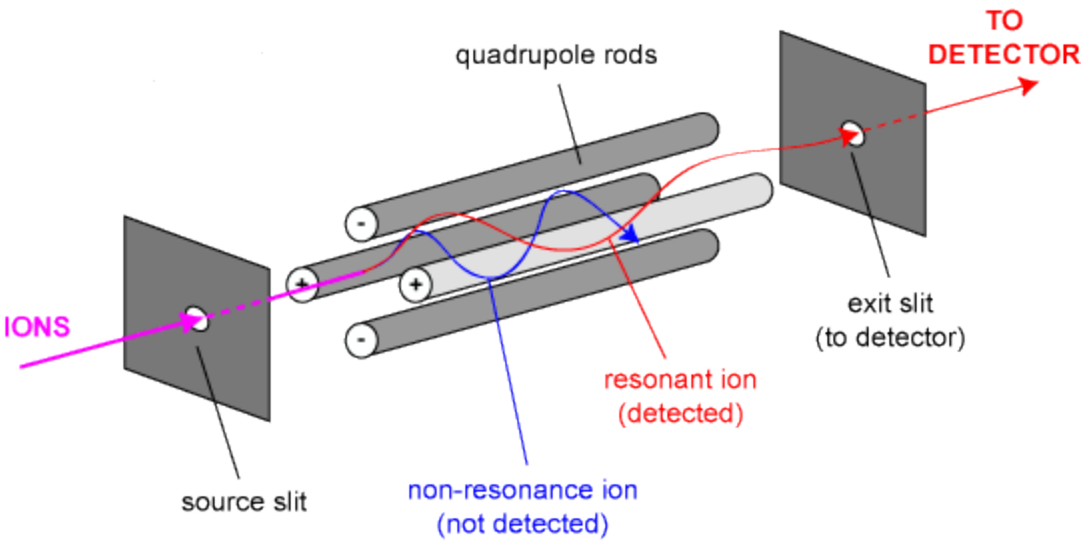

Figure 1.14. Schematic of a quadrupole mass spectrometer. The figure shows a detected ion that has made its way through the electric fields generated by the rods. An undetected ion is also shown, which did not have the mass to charge ratio selected by the mass spectrometer (University of Bristol).

1.4.4 Triple Oxygen Isotope Analyses

There are three naturally occurring stable isotopes of oxygen ^{16}O, ^{17}O and ^{18}O. The ratios of these isotopes can be measured by a mass spectrometer and measurements are usually recorded in δ notation. This notation is the ratio of ^{17}O or ^{18}O to ^{16}O relative to a standard (eq. 1.1). The standard usually used is Vienna Standard Mean Ocean Water (VSMOW). Measurements can also be recorded in Δ notation, which allows data from meteorites to be plotted relative to terrestrial values (eq. 1.2). In order to use this notation knowledge of the slope of the Terrestrial Fractionation Line (TFL) is required. Here 0.52 is used, but values can vary depending on the lab being used (e.g. Sections 2.3.6 and 4.3.4). The TFL is the product of fractionation processes in earth materials that depend on the mass of the isotopes involved (e.g. ^{17}O versus ^{18}O).

$$\delta^x O = \frac{\frac{^xO}{^{16}O}sample - \frac{^xO}{^{16}O}Standard}{\frac{^xO}{^{16}O}Standard} \times 1000‰ \; (eq.\,1.1)$$

$$\Delta^{17}O = \delta^{17}O - 0.52\delta^{18}O \ (eq. 1.2)$$

Triple oxygen isotope analysis is utilized in meteorite research in large part due to the prevalence of non-mass dependant fractionation effects that help to separate meteorite groups from one another (Fig. 1.5). These non-mass dependant fractionation characteristics are indicative of the environment in which the meteorites formed within the early solar nebula. The processes responsible for such fractionations are in debate, but they could be the result of a process referred to as self-shielding (e.g., Young et al. 2008). This thesis work utilized laser fluorination techniques at the University of Western Ontario, the Carnegie Institute of Washington and the University of New Mexico. The separate analytical set-ups are best described in the methods sections of the subsequent chapters; however, all of the systems used a laser-based fluorination (BrF_5) system for extracting oxygen from predominantly silicate minerals.

1.5 Thesis Structure

The interplay between heat derived from surface impacts and internal heating is complex and ultimately both heat sources led to the growth and differentiation of the rocky bodies in our solar system. This thesis has been broken into three main chapters that look at meteorites from asteroids that bear evidence of: 1. Accretionary impact melting, 2. Heating of a primitive asteroid, and 3. Impact effects on a partially differentiated parent body.

1.5.1 Accretionary Impact Melting (Chapter 2)

Near-surface rocks from asteroids contain impact melt products generated as the asteroids accreted material during impacts with other bodies. These impact processes are recorded on a number of terrestrial bodies and are represented in meteorite collections in regolith breccias. Chapter 2 will describe the first identification of a eucrite impactor clast found in an L chondrite regolith breccia. Eucrites come from a differentiated parent body, likely the asteroid Vesta (Mittlefehldt 2015), while the L chondrite parent is much more primitive. A rim around the eucrite clast is a mixture of breccia and igneous phases, which are ultimately the result of impact processes. The textures and chemical mixing

observed provide evidence for an unconsolidated L chondrite target material, suggesting multiple impacts were required to finally consolidate the rock.

1.5.2 Thermal History of a Primitive Asteroid (Chapter 3)

In the early solar system, some asteroids grew large enough to begin the process of differentiation, but did not generate enough internal heat to complete the process; thus crystallizing the first stages of internal melting and differentiation in their rock record. Chapter 3 introduces the meteorites NWA 7680 and NWA 6962 from one of these primitive melt environments. Both meteorites are plagioclase-rich and NWA 7680 is also Fe-metal-rich, signifying that they both formed through short-lived differentiation processes that resulted in the pooling of melt products. Geochemically, both meteorites could have formed through fractionation processes on a CR chondrite-like parent body. This is consistent with chromium isotope work carried out on these two meteorites (Sanborn et al. 2018). CR chondrites are a primitive meteorite group containing components from the early solar system (e.g. chondrules). Finding evolved melts from such a primitive parent body provides an unparalleled view of the first stages of melting and differentiation. These findings have led to the use of the term "carbonaceous achondrites" to describe these intriguing rocks that mark the early stages of differentiation processes. Dating work carried out on these meteorites shows that they have not been heated above 350-550 °C since the first several million years of the solar system's history. This suggests that the textures and compositions they exhibit are truly representative of primitive melt environments.

1.5.3 Diamond Formation on a Partially Differentiated Parent Body (Chapter 4)

Evidence of early melt environments can be complicated by later impact events producing shock features. Chapter 4 explores diamond formation in ureilite meteorites. Ureilites are thought to represent partial-melt residues from the mantle of their parent body (e.g., Scott et al. 1993; Warren et al. 2006) and are carbon-rich (e.g., Grady et al. 1985; Smith et al. 2001). Recent work on this meteorite group has suggested that diamonds found in these meteorites are produced at depth within a large parent body the

size of Mercury or Mars (Nabiei et al. 2018). In chapter 4 we show carbon textures (diamond and graphite) that suggest the diamonds in two ureilites (NWA 11950 and NWA 11951) have instead formed through high pressure impact events. This negates the need for a planet-sized parent body for these two meteorites.

1.6 Thesis Impact

The meteorites presented in these three chapters provide a wide ranging view of the types of melt environments found in the early solar system. These chapters add to our depth of knowledge regarding early melt environments and in turn give us a better view of formation mechanisms at play during the formation of planets, moons and asteroids.

1.7 References

Bischoff A. 2001. Meteorite classification and the definition of new chondrite classes as a result of successful meteorite search in hot and cold deserts. *Planetary and Space Science* 49(8):769-776.

Cherniak D. J., Lanford W. A. and Ryerson F. J. 1991. Lead diffusion in apatite and zircon using ion implantation and Rutherford backscattering techniques. *Geochimica et Cosmochimica Acta* 55(6):1663-1673.

Chew D. M. and Spikings R. A. 2015. Geochronology and thermochronology using apatite: time and temperature, lower crust to surface. *Elements* 11(3):189-194.

Clayton R. N. and Mayeda T. K. 1996. Oxygen isotope studies of achondrites. *Geochimica et Cosmochimica Acta* 60(11):1999-2017.

Clayton R. N. and Mayeda T. K. 1999. Oxygen isotope studies of carbonaceous chondrites. *Geochimica et Cosmochimica Acta* 63(13-14):2089-2104.

Connelly J. N., Bizzarro M., Krot A. N., Nordlund Å., Wielandt D. and Ivanova M. A. 2012. The absolute chronology and thermal processing of solids in the solar protoplanetary disk. *Science* 338(6107):651-655.

Davis D. W., Williams I. S. and Krogh T. E. 2003. Historical development of zircon geochronology. *In Zircon, Reviews in mineralogy and geochemistry*, 53(1), edited by Hanchar J. M. and Hoskin P. W. O. Washington: Mineralogical Society of America. pp.145-181.

Ember K. J., Hoeve M. A., McAughtrie S. L., Bergholt M. S., Dwyer B. J., Stevens M. M., Faulds K., Forbes S. J. and Campbell C. J. 2017. Raman spectroscopy and regenerative medicine: a review. *NPJ Regenerative medicine* 2(1):1-10.

Franchi I. A., Baker L., Bridges J. C., Wright I. P. and Pillinger C. T. 2001. Oxygen isotopes and the early Solar System. *Philosophical Transactions of the Royal Society of London. Series A: Mathematical, Physical and Engineering Sciences* 359(1787):2019-2035.

Goodrich C. A., Kita N. T., Spicuzza M. J., Valley J. W., Zipfel J., Mikouchi T. and Miyamoto M. 2011. The Northwest Africa 1500 meteorite: Not a ureilite, maybe a brachinite. *Meteoritics & Planetary Science* 45(12):1906-1928.

Grady M. M., Wright I. P., Swart P. K. and Pillinger C. T. 1985. The carbon and nitrogen isotopic composition of ureilites: implications for their genesis. *Geochimica et Cosmochimica Acta* 49(4):903-915.

Harrison T. M., Catlos E. J. and Montel J. M. 2002. U-Th-Pb dating of phosphate minerals. *In Phosphates: Geochemical, Geobiological and Materials Importance, Reviews in Mineralogy and Geochemistry*, 48(1), edited by Kohn M. J., Rakovan J. and Hughes J. M. Washington: Mineralogical Society of America. pp.524-558.

Hughes J. M. and Rakovan J. F. 2015. Structurally robust, chemically diverse: apatite and apatite supergroup minerals. *Elements* 11(3):165-170.

Karner J., Papike J. J., and Shearer C. K. 2006. Comparative planetary mineralogy: Pyroxene major-and minor-element chemistry and partitioning of vanadium between pyroxene and melt in planetary basalts. *American Mineralogist* 91(10):1574-1582.

Krot A. N., Amelin Y., Bland P., Ciesla F. J., Connelly J., Davis A. M., Huss G. R., Hutcheon I. D., Makide K., Nagashima K. and Nyquist L. E. 2009. Origin and chronology of chondritic components: A review. *Geochimica et Cosmochimica Acta*, 73(17):4963-4997.

Luo Y., Hughes J. M., Rakovan J. and Pan Y. 2009. Site preference of U and Th in Cl, F, and Sr apatites. *American Mineralogist* 94(2-3):345-351.

MacPherson G. J. and Boss A. 2011. Cosmochemical evidence for astrophysical processes during the formation of our solar system. *Proceedings of the National Academy of Sciences* 108(48):19152-19158.

Maitland T. and Sitzman S. 2006. Electron backscatter diffraction (EBSD) technique and materials characterization examples. In Scanning Microscopy for Nanotechnology, edited by Zhou W., and Wang Z. L. New York: Springer. pp. 41–75.

Michler G. H. 2008. Scanning Electron Microscopy (SEM). In Electron Microscopy of Polymers, Berlin: Springer. pp. 87–120.

Mittlefehldt D. W. 2015. Asteroid (4) Vesta: I. The howardite-eucrite-diogenite (HED) clan of meteorites. *Chemie der Erde-Geochemistry* 75(2):155-183.

Moser D. E., Cupelli C. L., Barker I. R., Flowers R. M., Bowman J. R., Wooden J. and Hart J. R. 2011. New zircon shock phenomena and their use for dating and reconstruction of large impact structures revealed by electron nanobeam (EBSD, CL, EDS) and isotopic U–Pb and (U–Th)/He analysis of the Vredefort dome. *Canadian Journal of Earth Sciences* 48(2):117-139.

Nabiei F., Badro J., Dennenwaldt T., Oveisi E., Cantoni M., Hébert C., El Goresy A., Barrat J. A. and Gillet P. 2018. A large planetary body inferred from diamond inclusions in a ureilite meteorite. *Nature communications* 9(1):1327.

NASA, Solarsystem.nasa.gov/asteroids-comets-and-meteors/meteors-and-meteorites/overview/, accessed Nov. 19, 2019.

Nasdala L., Zhang M., Kempe U., Panczer G., Gaft M., Andrut M. and Plötze M. 2003. Spectroscopic methods applied to zircon. *In Zircon, Reviews in Mineralogy and Geochemistry*, 53(1), edited by Hanchar J. M. and Hoskin P. W. O. Washington: Mineralogical Society of America. pp.427-467.

Northern Arizona University, https://www.cefns.nau.edu/geology/naml/Meteorite/Diogenite.html, accessed Dec. 17, 2019.

Papike J. J., Karner J. M., and Shearer C. K. 2003. Determination of planetary basalt parentage: a simple technique using the electron microprobe. *American Mineralogist* 88: 469–472.

Royal Ontario Museum, https://collections.rom.on.ca/objects/1867727/gibeon?ctx=9966b343-90ab-41f2-b3d1-73059e28b93c&idx=32, accessed Dec. 17, 2019.

Rumble D. III, Zolensky M. E., Friedrich J. M., Jenniskens P. and Shaddad M. H. 2010. The oxygen isotope composition of Almahata Sitta. *Meteoritics & Planetary Science* 45(10-11):1765-1770.

Sanborn M. E., Yin Q. Z., Hyde B. C., Tait K. T. and Moser D. E. 2018. Early differentiation in the carbonaceous chondrite forming region of the solar nebula: New insight from the achondrites Northwest Africa 7680/6962 (abstract #2296). 49th Lunar and Planetary Science Conference.

Scott E. R., Taylor G. J. and Keil, K. 1993. Origin of ureilite meteorites and implications for planetary accretion. *Geophysical Research Letters* 20(6):415-418.

Smith C., Franchi I., Wright I., Grady M. and Pillinger C. 2001. New data on carbon isotopic compositions of some ureilites (abstract #1878). 32nd Lunar and Planetary Science Conference.

University of Bristol, http://www.bris.ac.uk/nerclsmsf/techniques/gcms.html, accessed Dec. 17, 2019.

Warren P. H., Ulff-Møller F., Huber, H. and Kallemeyn G. W. 2006. Siderophile geochemistry of ureilites: a record of early stages of planetesimal core formation. *Geochimica et Cosmochimica Acta* 70(8):2104-2126.

Weisberg M. K., McCoy T. J. and Krot A. N. 2006. Systematics and evaluation of meteorite classification. *Meteorites and the early solar system II*.

Weiss B. P. and Elkins-Tanton L. T. 2013. Differentiated planetesimals and the parent bodies of chondrites. *Annual Review of Earth and Planetary Sciences* 41:529-560.

Young E. D., Kuramoto K., Marcus R. A., Yurimoto H. and Jacobsen S.B. 2008. Mass-independent oxygen isotope variation in the solar nebula. *Reviews in Mineralogy and Geochemistry*, *68*(1), edited by MacPherson G. J., Mittlefehldt D. W., Jones J. H. and Simon S. B. Virginia: Mineralogical Society of America. pp.187-218.

Zhou W., Apkarian R. P., Wang Z. L., and Joy D. 2006. Fundamentals of scanning electron microscopy. In Scanning Microscopy for Nanotechnology, edited by Zhou W., and Wang Z. L. New York: Springer. pp. 1–40.

Chapter 2

Accretionary mixing of a eucrite impactor and the regolith of the L chondrite parent body

2.1 Abstract

Northwest Africa (NWA) 869 is the largest sample of chondritic regolith breccia, making it an ideal source for research on accretionary processes and primordial chemical mixing. One such process can be seen in detail through the first identification of a eucrite impactor clast in an L chondrite breccia. The ~7 mm diameter clast has oxygen isotope compositions ($\Delta^{17}O$ = -0.24, -0.26‰) and pigeonite and augite elemental compositions typical for eucrites, but with high areal abundance of silica (9.5 %) and ilmenite (1.5 %). The rim around the clast is a mixture of breccia and igneous phases, the latter due to either impactor-triggered melting or later metamorphism. The rim has an oxygen isotope composition falling on a mixing line between known eucrite and L chondrite compositions ($\Delta^{17}O$ = 0.33‰) and, coincidentally, on the Mars fractionation line. Pyroxene grains from the melt component in the rim have elemental compositions that fall on a mixing line between the average eucrite pyroxene composition and equilibrated L chondrite composition. The margins of chondritic olivine crystal clasts in the rim are enriched in Fe as a result of diffusion from the Fe-rich melt and suggest cooling on the scale of hours. The textures and chemical mixing observed provide evidence for an unconsolidated L chondrite target material, differing from the current lithified state of NWA 869 material. The heterogeneity of oxygen isotope and chemical signatures at this small length scale serve as a cautionary note when extrapolating from small volumes of materials to deduce planetesimal source characteristics.

2.2 Introduction

The accretion of rocky bodies encompasses a wide range of impact related phenomena. These range from the initial slow (<~1 mm/s) agglomeration of dust (e.g., Blum 2018) to gravity and collision driven accretion (Weidenschilling 2000) and finally to late accretion (Bottke et al. 2010; Brasser et al. 2016; Day et al. 2012; Tait and Day 2018). Some

aspects of this final late accretion can be observed in the regolith of modern planets, moons and asteroids. Regolith breccia meteorites provide a rare look at this near-surface process (e.g., Bischoff et al. 2006); however, systematic and thorough studies of these diverse regolith rocks are often hindered by sample size. Northwest Africa 869 is the largest sample of chondritic regolith breccia; comprised of thousands of stones weighing an estimated seven tonnes (Metzler et al. 2011). This amount of material provides researchers with the opportunity to examine whole collections of stones to look for evidence of processes such as shock melting, impact accretion and reservoir mixing. A systematic investigation of 257 kg of NWA 869 material in the collection of the Royal Ontario Museum (ROM) has already revealed several intriguing impact related textures and clasts (this study; Hyde et al. 2015; McCausland et al. 2017; Thompson et al. 2011) demonstrating the importance of a continued study of this breccia.

Northwest Africa 869 is classified as a L3-6 chondritic regolith breccia (Matsuda et al. 2006; Osawa and Nagao 2006; Metzler et al. 2011; Welten et al. 2011); a rarity among the L chondrites, which contain only 3% regolith breccia by number (Bischoff and Schultz 2004; Bischoff et al. 2018). The L chondrite parent body's impact history has been the subject of substantial study. A catastrophic impact disrupted the parent body ~470 Myr ago (e.g., Korochantseva et al. 2007) leading to an increase in L chondrite impacts here on Earth (e.g., Greenwood et al. 2007). There is evidence that this event subsequently led to the mid-Ordovician ice age (Schmitz et al. 2019).

Additionally, evidence of xenolithic clasts in L chondrite meteorites has added to our knowledge of impact accretion and intermixing of chemically and texturally distinct lithologies. Igneous clasts have been previously reported in NWA 869, including a 1.7 cm igneous clast and a 4.9 cm impact melt clast thought to be unrelated to the L chondrite host (Metzler et al. 2011), but their origins have not been related to any known meteorite group. The majority of igneous clasts in ordinary chondrites do not originate from other differentiated parent bodies. Such clasts are generally the result of melt processes involving broadly chondritic materials (e.g., Ruzicka et al. 2019). These clasts can be related to nebular processes occurring prior to the formation of planetesimals, or impact melt processes and this classification scheme has been applied to additional clasts found

in NWA 869 (Ruzicka et al. 2019). Xenolithic clasts from external sources are the only intact textural and mineralogical record of late-stage impact accretion processes. Breccia meteorites provide an opportunity to investigate the origin of dynamic mixing in the asteroid population, the components involved in late stage geochemical mixing and allow us to describe the processes responsible for this mixing in detail.

Examining textures and determining chemical and mineralogical compositions resulting from impacts between known meteorite types provides a needed test for geochemical mixing models. When mixing is seen on the thin section-scale, however, the source materials are often anomalous/ungrouped, or primary textures and compositions have been modified by subsequent processes (e.g., Bischoff et al. 2013; Dyl et al. 2012). Here we report a detailed investigation of a xenolithic clast, its interaction rim with the host breccia, and propose a link to a known meteorite group using mineralogy, geochemistry, texture, and oxygen isotope composition. Particular attention is paid to mafic mineral compositions and oxygen isotope compositions; two properties often used for meteorite typing. We suggest that the results from this small-scale interaction are instructive for accurately interpreting broader chemical trends from the solar system's terrestrial bodies.

2.3 Samples and Analytical Methods

2.3.1 NWA 869 Material Used in this Study

The type specimen of NWA 869 (Connolly et al. 2006) was acquired alongside 257 kg of associated material collected at the same time. All of this associated material was donated to the ROM. The donated stones generally have a dark wind ablated surface. When cut, the stones reveal brecciated matrix material and primarily chondritic clasts. This study involves a 31.5 g stone from the ROM's collection (M56004). After initial study of the sample, a representative thin section was made and used for micro-analyses (Fig. 2.1).

2.3.2 Electron Probe Microanalysis

Electron probe microanalysis (EPMA) was carried out on the xenolithic clast components using a JEOL JXA-8230 instrument equipped with five wavelength dispersive spectrometers at Queen's University. All analyses used a 15 kV accelerating voltage.

Pyroxene, plagioclase and sulfide analyses used a 20 nA beam current, while ilmenite and silica used a 30 nA and 10 nA beam current, respectively. All analyses were carried out with a 0.5-1 µm spot size except for silica, which used a 2 µm defocused beam. Standards used for microprobe analyses are given in the supplementary material (Appendix 2 - A2.1). All analyses had a 3σ detection limit of < 0.1 wt. % oxide, except for SiO_2 in silica (0.11 wt. %).

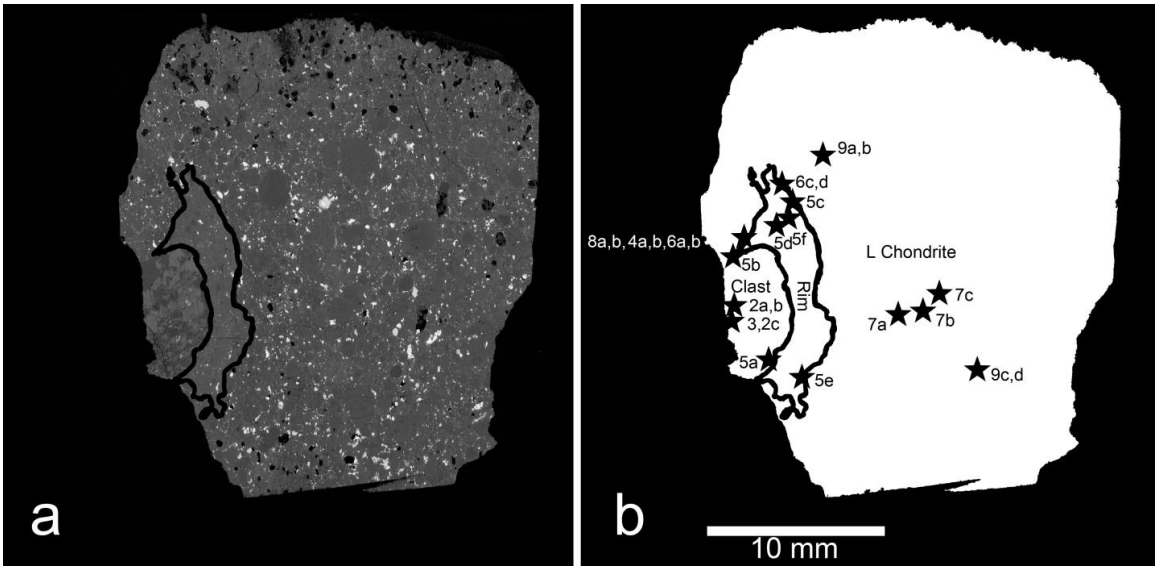

Figure 2.1. a) Backscatter electron image of thin section with the rim outlined in black. b) Map showing locations of all figures. Note: Figures are 2.#, # values shown above.

2.3.3 Backscatter Electron Imaging, X-Ray Mapping and Modal Analysis

Backscatter electron (BSE) imaging and chemical mapping (Fig. 2.2) were carried out using a Hitachi SU6600 Field Emission Scanning Electron Microscope (FE-SEM) at the University of Western Ontario. An Oxford XMax silicon drift detector (80 mm^2) was used for energy dispersive X-ray spectrometry (EDS) measurements (INCA software). Locations of BSE images in the thin section are shown in Figure 2.1. Modal analysis used the BSE threshold method (e.g., Day et al. 2006) and the ImageJ software package (Schneider et al. 2012).

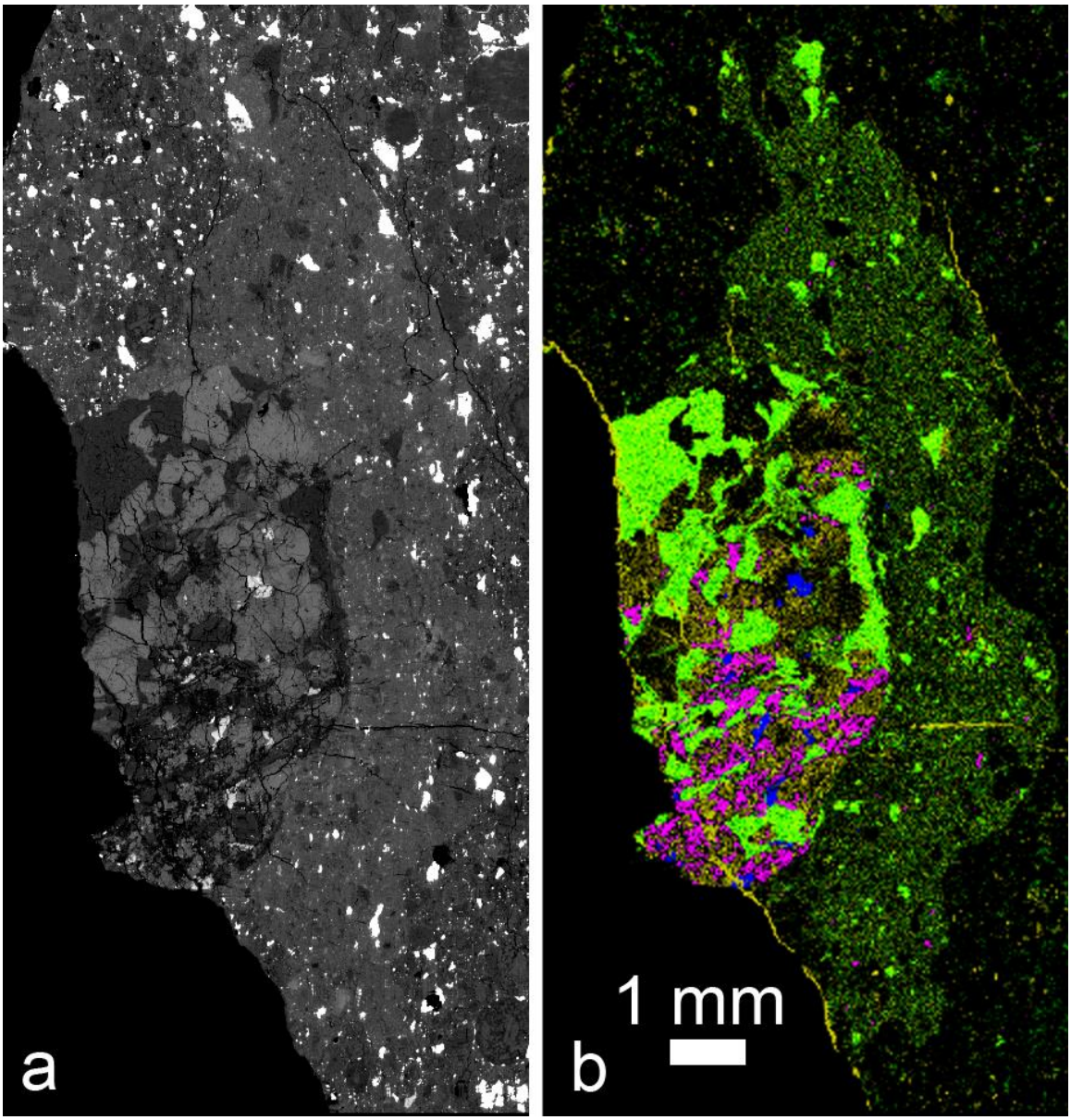

Figure 2.2. a) Backscatter electron image showing the xenolithic clast (left and centre) embedded in the L chondrite breccia. b) Element map of (a) showing Si (purple), Ti (blue), Al (green) and Ca (yellow). The Ca in the fractures is hosted in calcite from terrestrial weathering. Contrast and brightness values for each element were adjusted to highlight the silica-ilmenite-rich nature of the clast and the compositional transitions from the clast to the chondritic breccia.

2.3.4 Quantitative Energy Dispersive Spectrometry and Wavelength Dispersive Spectrometry

Quantitative standards-based EDS analyses were performed on the chondrite and rim components using the FE-SEM previously discussed. A conductive Si standard (commercial wafer) was used to verify and adjust peak positions and monitor beam current stability. Standards used for analysis can be found in the supplementary material along with analytical conditions (Appendix 2 - A2.2). For analysis of small features (e.g., impact rim material), grains showing compositional zoning (e.g., unequilibrated pyroxene) and equilibrated chondritic material, a high-resolution aperture set-up was used. Dead time was kept low (~10%) to minimize coincidence peaks. This set-up allows for quantification of major and minor elements, in many cases with sub-wt. % precision (Hyde et al. 2016; Appendix 1); however, determination of detection limits and quantification at low concentrations can be hindered by peak overlaps with undetermined minor/trace elements. In materials with low Fe content (e.g., some unequilibrated chondrules), wavelength dispersive spectrometry (WDS) measurements were required to verify Fe concentrations, which provided a 3σ detection limit of 0.02 wt. % Fe.

2.3.5 Electron Backscatter Diffraction

Electron backscatter diffraction (EBSD) was used to help confirm mineral identifications and to observe grain orientation. This analysis used the FE-SEM system described previously and an Oxford Instruments Nordlys EBSD detector. The sample was polished using 0.05 µm alumina powder (Buehler) in oil (Beta Diamond Products). During analysis the sample mount was tilted to 70° and raised to a working distance of 19 mm. A 20 kV accelerating voltage was used to generate Kikuchi bands and Oxford HKL Channel 5 software was used for indexing. A range of 5 to 7 detected bands were required for identification, which were detected using band edges.

2.3.6 Oxygen Isotope Analysis

Triple-oxygen isotope data were collected to compare the xenolithic clast to known meteorite groups and to confirm the L chondrite origin of the host rock. Samples were drilled from an exposed cut surface using procedures from van Drongelen et al. (2016).

These samples included clast, rim and the host L chondrite breccia material. Drilling was done away from weathered veins and surfaces. Powder samples (2.5-4.0 mg) were compacted into sample holders with a stainless-steel rod and oven-dried for two days. The dried samples were then loaded into a reaction chamber which was heated and evacuated for several hours. The chamber was then repeatedly fluorinated (25 torr of BrF_5) and evacuated, and then fluorinated overnight. Evacuation and fluorination were repeated the following morning until measured room-temperature fluorination products, non-condensable in liquid nitrogen, were reduced to a negligible blank. For analysis, the samples were fluorinated by heating with a 30 W SYNRAD CO_2 laser in an atmosphere of 30 torr BrF_5.

Two aliquots of a reference standard, Gore Mountain garnet (USNM 107144, obtained through J. Post, Smithsonian Institution), were analyzed for every four unknowns. The reference garnet gives a $\delta^{18}O_{VSMOW}$ value of 6.0 ‰ in comparison to UWG-2 (Rumble et al. 1997; Valley et al. 1995). The two sigma standard deviations of eight Gore Mountain garnet analyses measured were: $\Delta^{17}O$±0.02, $\delta^{17}O$±0.06, and $\delta^{18}O$±0.13 ‰. The value used for the slope of the terrestrial fractionation line (TFL) in this study is 0.526 (± 0.001) (Rumble et al. 2007).

2.4 Results

2.4.1 Petrography and Microstructure

Initial inspection of the sample and a representative thin section (Figs. 2.1 and 2.2) reveals three distinct lithologies. The majority of the sample is composed of a chondrule-rich breccia typical of NWA 869 material (Lithology 1). A xenolithic clast is distinguished based on an absence of obvious chondrules (Lithology 2). This is surrounded by a rim of material (Lithology 3) that is brecciated and often fine-grained (grains that are sub-micrometre to tens of micrometres in diameter) or seemingly amorphous as it appears isotropic in cross-polarized light (Appendix 2 - A2.3). Each lithology is discussed in detail below:

2.4.1.1 Lithology 1: L Chondrite Breccia

Clasts are poorly defined in the L chondrite breccia and are generally small, on the order of a few millimetres maximum, with most observable clasts being single chondrules or "chondrule-clasts". This texture indicates that the brecciation process has mechanically broken up materials down to the level of single chondrules. Primary chondrule textures are common, such as barred olivine chondrules (Appendix 2 - A2.4a). However, surrounding primary grains, there is often crystallized mesostasis composed of plagioclase and sometimes pyroxene (Appendix 2 - A2.4b). Some chondrules contain unequilibrated, zoned pyroxene grains (Appendix 2 - A2.5a). The pyroxene grains always contain Mg-rich cores and transition to more Fe-rich edges near grain boundaries and cracks (Appendix 2 - A2.5b). Further unequilibrated chondrite textures are seen in the form of an armored chondrule (Appendix 2 - A2.5c) with an igneous rim (Appendix 2 - A2.5d) and a Mg-rich chondrule (Appendix 2 - A2.6a and A2.6b). The Mg-rich chondrule contains abundant veins of Fe-metal, and the mesostasis regions show evidence of crystallization (Appendix 2 - A2.6c). Within the breccia we focus on a clast that is distinct in terms of texture and higher silica content such that it is clearly xenolithic.

2.4.1.2 Lithology 2: Xenolithic Clast

The clast measures ~7 mm (longest dimension) in the thin section (Figs. 2.1 and 2.2) and contains 52% pyroxene (pigeonite and augite), 37% plagioclase, 9.5% silica and 1.5% ilmenite (by area). The upper portion of the clast in Figure 2.2 shows a remnant coarser-grained intergrowth texture. This region includes pigeonite and anorthite areas as large as ~1 mm. The remnant pigeonite often contains lamellae of augite. Regions where pyroxene grains have been sheared occur in the section with the most obvious example shown in Figures 2.3a and 2.3b. This particular deformation zone extends through the majority of the clast, but does not extend into the rim or host L chondrite breccia. Electron backscatter diffraction orientation mapping shows that the remnant pyroxene grains are now granular in texture. Where pervasive, this results in an aggregate microtexture of domains with maximum diameter of a few micrometres each (Fig. 2.4). Phase identifications by EBSD agree with EDS element maps (Figs. 2.4b and 2.4c). The

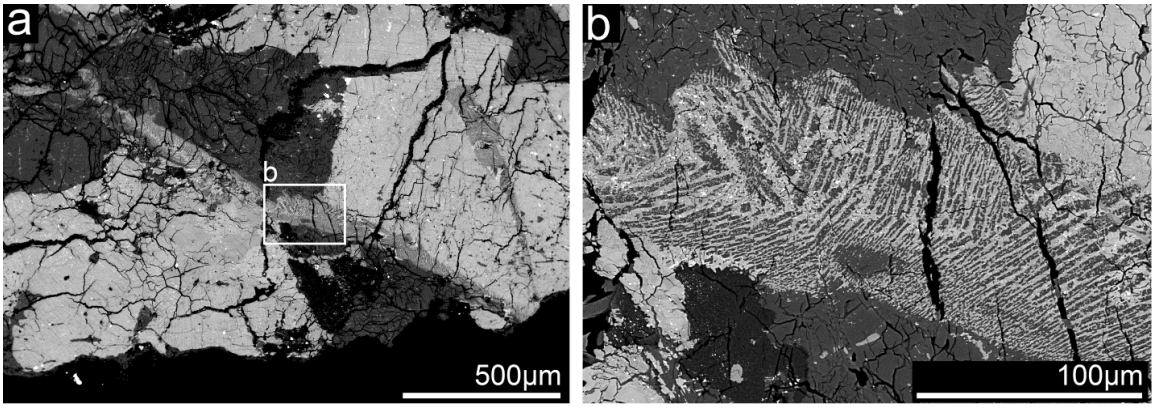

Figure 2.3. Backscatter electron images of the xenolithic clast showing relict coarse-grained texture. a) A large sheared pyroxene grain surrounded by primarily anorthite. b) A higher magnification image of the sheared region.

variations in orientation (Euler angles relative to plane of section) are mapped for both pyroxene and anorthite (Fig. 2.4d). Some regions of anorthite do not diffract suggesting these regions are amorphous, poorly crystalline, or crystalline at a length scale not resolvable by conventional EBSD (< 100 nm). This is consistent with crossed polarized light imaging, which often shows the anorthite to be dark with patches of crystalline material (Appendix 2 - A2.3). In some cases, the crystalline material is pyroxene suggesting some minor melt mixing between the two phases. The reverse also occurs, with anorthite appearing within remnant pyroxene regions (Figs. 2.4a, 2.4b and 2.4c). The lower portion seen in Figure 2.2 is more silica-rich (purple) and shows a greater degree of melting and brecciation. Fine-grained material is seen throughout the silica-rich domains (Fig. 2.5a) and remnant grain shapes are less well-defined than in the coarser-grained region. Electron backscatter diffraction measurements indicate that some of the silica is quartz (Fig. 2.4b), whereas other areas show weak or no diffraction, similar to the anorthite. No high temperature or high pressure silica minerals were detected in the regions examined in this study. The pyroxene in the silica-rich area is predominantly augite. Ilmenite is found throughout the clast; however, it is more abundant in silica-rich areas. Minor phases in the clast include Fe-sulfide (pyrrhotite-group), zircon, titanite and a rare earth element-rich Ca-phosphate.

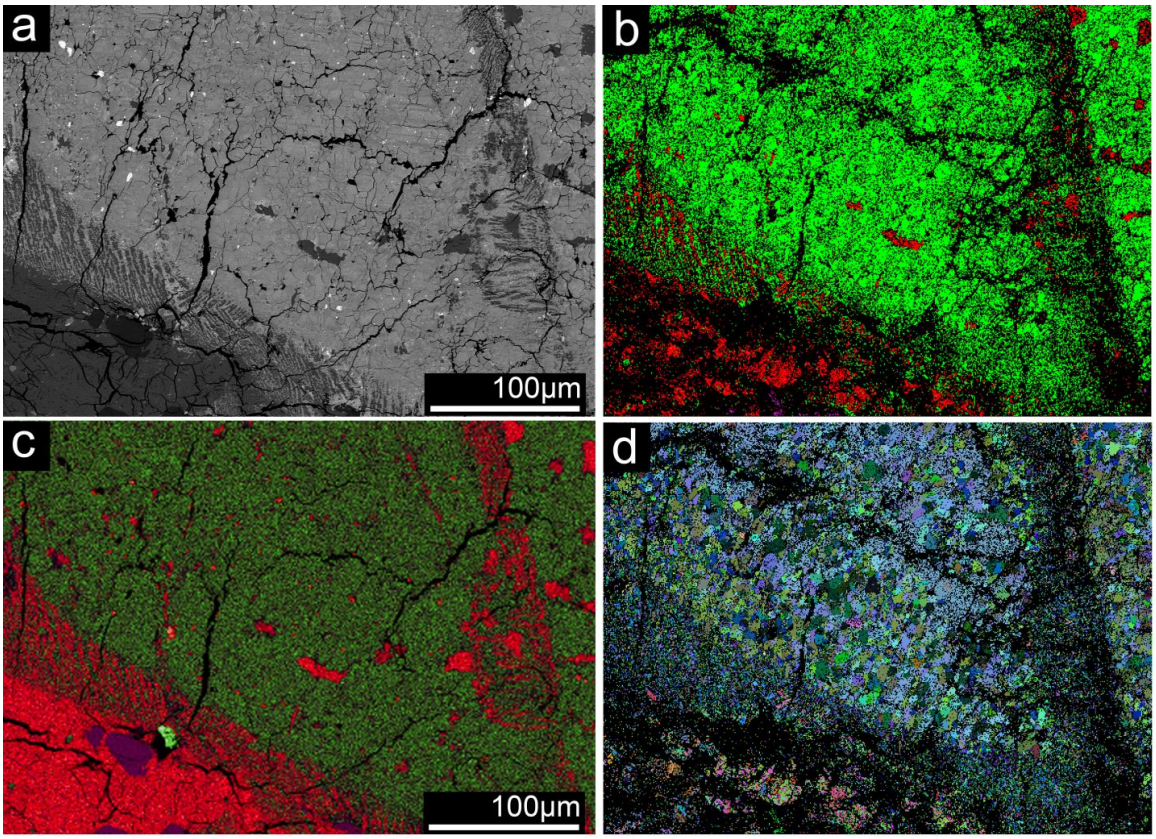

Figure 2.4. Micro-texture of pyroxene, anorthite and quartz in the relict coarse texture region of the xenolithic clast. a) A BSE image of a region predominantly composed of pigeonite (right) and anorthite (bottom left). b) Same region with phases identified by EBSD. Green is pyroxene, red is anorthite and purple is quartz. c) An element map of the same region showing Mg in green, Al in red and Si in purple. d) An Euler angle map showing that there is variability in orientation of granules a few micrometres across or smaller.

2.4.1.3 Lithology 3: Rim Surrounding the Xenolithic Clast

The xenolithic clast is rimmed by a mixture of fine-grained breccia, melt-derived phases and coarser pieces from the xenolithic clast and L chondrite host. The rim is generally 1-3 mm in width, but in one region is non-existent (Figs. 2.1 and 2.2 top). It exhibits internal variation in grain size and composition. Close to the xenolithic clast, the rim is predominantly a fine-grained (micrometre to submicrometre scale) assemblage of

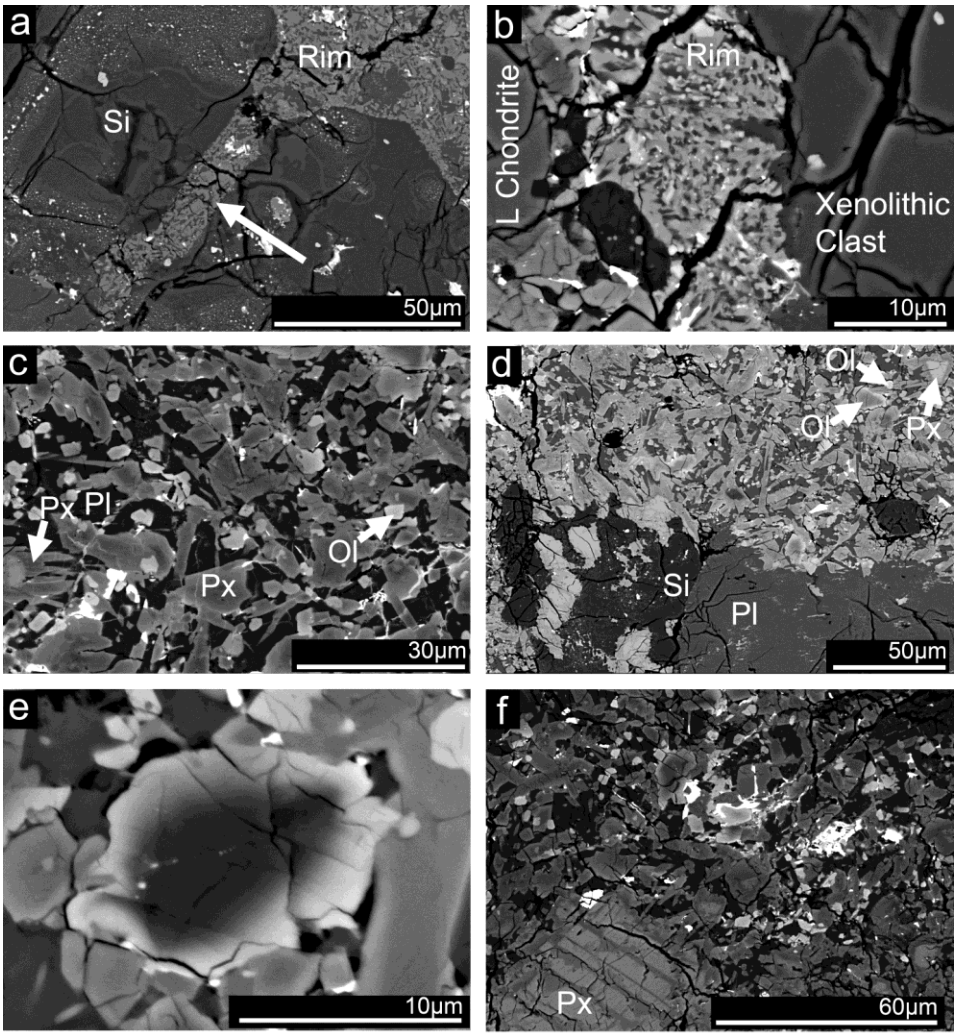

Figure 2.5. a) Backscatter electron image of the silica-rich region of the xenolithic clast. The silica contains abundant, often sub-micron inclusions with a range of compositions. Rim material is intruding into the xenolithic clast (arrow). b) Fine-grained pyroxene, olivine and plagioclase from the rim situated between the xenolithic clast (right) and L chondrite breccia (left). c) A typical texture from the rim showing coarser pyroxene, olivine and plagioclase. The olivine and pyroxene often show core to edge variations in brightness and thus chemistry. d) A region of the rim containing large silica-plagioclase-rich domains. e) Olivine in the rim showing transition from high Mg-olivine (core) to a more Fe-rich composition. f) A large pyroxene grain in the rim originating from the xenolithic clast showing lamellae. This and other pyroxene grains in the image show growth of new pyroxene composition around their edges. Note the following short forms: Silica (Si), pyroxene (Px), plagioclase (Pl) and olivine (Ol).

pyroxene, olivine and plagioclase (Fig. 2.5b) and this material locally intrudes the xenolithic clast (Fig. 2.5a). The rim material typically becomes coarser (to grain sizes of 10s of micrometres) further away from the xenolithic clast (Figs. 2.5c and 2.5d). There are regions containing silica and/or plagioclase originating from the precursor materials and contributing to the melt-derived plagioclase surrounding the pyroxene and olivine in the rim (Fig. 2.5d). Olivine grains originating from the L chondrite breccia (Fig. 2.5e) are identifiable because of a narrow zone of Fe-enrichment parallel to the grain margin (Figs. 2.5d and 2.5e). Grains that are sub-micrometre to a few micrometres in diameter show similar Fe contents and are presumed to have been L chondrite grains pervasively enriched, due to their smaller size (Fig. 2.5c). Pyroxene grains from the L-chondrite breccia and xenolithic clast are also apparent in the rim and show Fe-enrichment and Mg-enrichment (Fig. 2.5d) respectively. This elemental enrichment is also seen as anhedral forms along original grain/clast boundaries (Fig. 2.5c). Anhedral pyroxene grains with more homogeneous compositions are also found and these grains do not show textures or compositions directly associated with the xenolithic clast or L chondrite (Figs. 2.5b and 2.5c). The contact relationship between the outer rim boundary and the L chondrite varies from region to region. In some areas the rim material intrudes the L chondrite breccia and some regions of L chondrite material show a reduction in grain size adjacent to the rim (Figs. 2.6a and 2.6b). A thin region of fine-grained material can be seen in some areas along the rim-L chondrite boundary (Figs. 2.6c and 2.6d). The modal mineralogy of the rim varies from one location to another; however, fine-grained regions (Fig. 2.5b) are the most homogenized and are most representative of the true bulk mineralogy. The fine-grained material is 61% pyroxene, 9.5% olivine, <1% metal and 28.5% is a mixture of plagioclase, silica, and/or glass (by area %). This composition is broadly that of an olivine basalt.

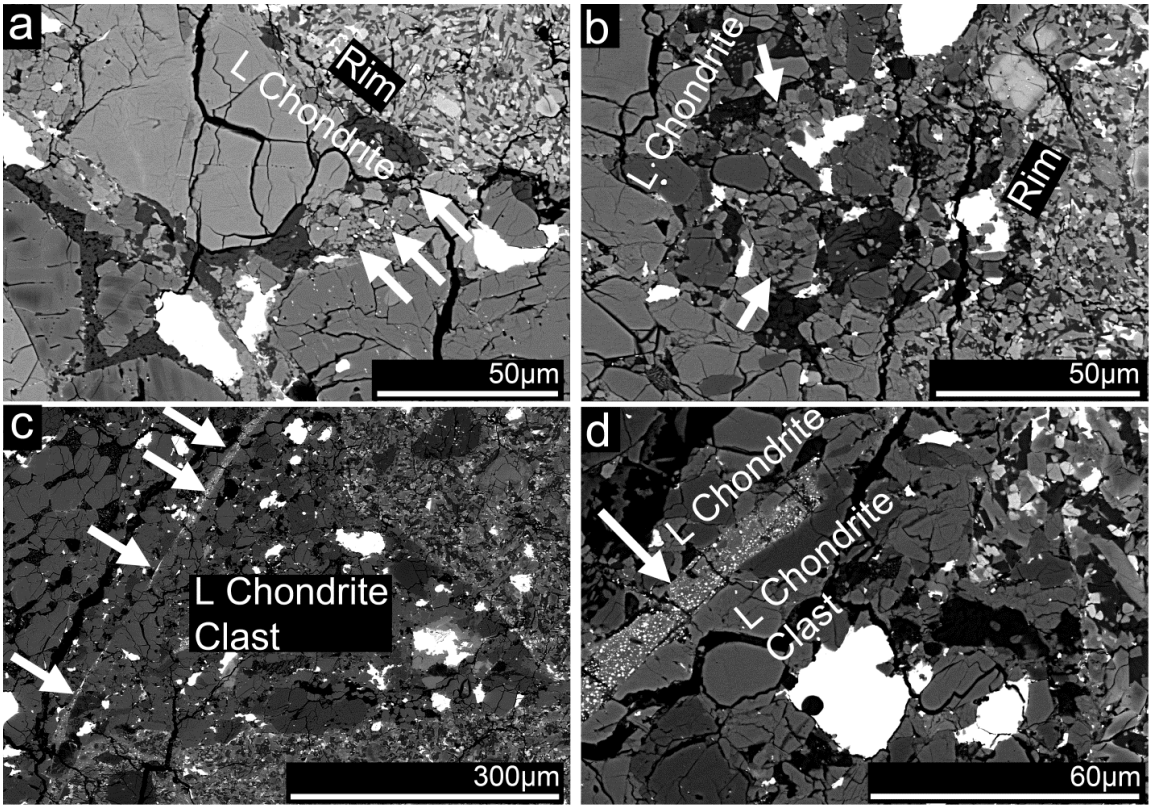

Figure 2.6. Backscatter electron images of rim edges showing: a) rim melt material intruding into and modifying chondritic breccia (arrows). b) Heat from the rim formation extensively modifying adjacent breccia reducing grain size (arrows). c) A large chondritic clast enclosed by rim material. A thin region of fine-grained melt, or reaction rim is seen along the left edge (arrows). This is seen more clearly in higher magnification d) (arrow).

2.4.2 Phase Chemistry

2.4.2.1 L Chondrite Breccia

The compositions of chondrule olivine and pyroxene grains were measured by quantitative EDS/WDS. An armored chondrule and high-Mg chondrule both contained unequilibrated olivine compositions, whereas other chondrules contained zoned unequilibrated pyroxene (Appendix 2 - A2.7 and A2.8). Analyses from equilibrated chondritic material are shown in Appendix 2 (A2.8) and are consistent with an L chondrite origin. Measurements of unequilibrated material were grouped by single chondrules only.

2.4.2.2 Xenolithic Clast

Silicate, ilmenite and sulfide compositions were all measured by EPMA and are presented in Table 2.1. The pyroxene compositions were consistent with pigeonite and augite (Fig. 2.7). Analyses of pigeonite grains also sampled augite lamellae and mixtures of the two, resulting in the mixing line observed. The concentration of Mn in the pyroxene increases with increasing Fe content (Fig. 2.8). Anorthite measurements with EPMA resulted in element totals of between 99.1 wt. % and 101.3 wt. % and an average composition of $An_{86}Or_1$. This average composition undoubtedly contains material with a range of structural variability; however, the high totals and stated variability in composition (Table 2.1) suggest that these structural changes have not had a substantial effect on major element chemistry. Silica in the clast is composed predominantly of SiO_2 with variable contribution from minor elements such as Al and Fe. The ilmenite contains a small amount of Fe^{3+} in its structure and the Fe-sulfides present belong to a pyrrhotite-group mineral(s).

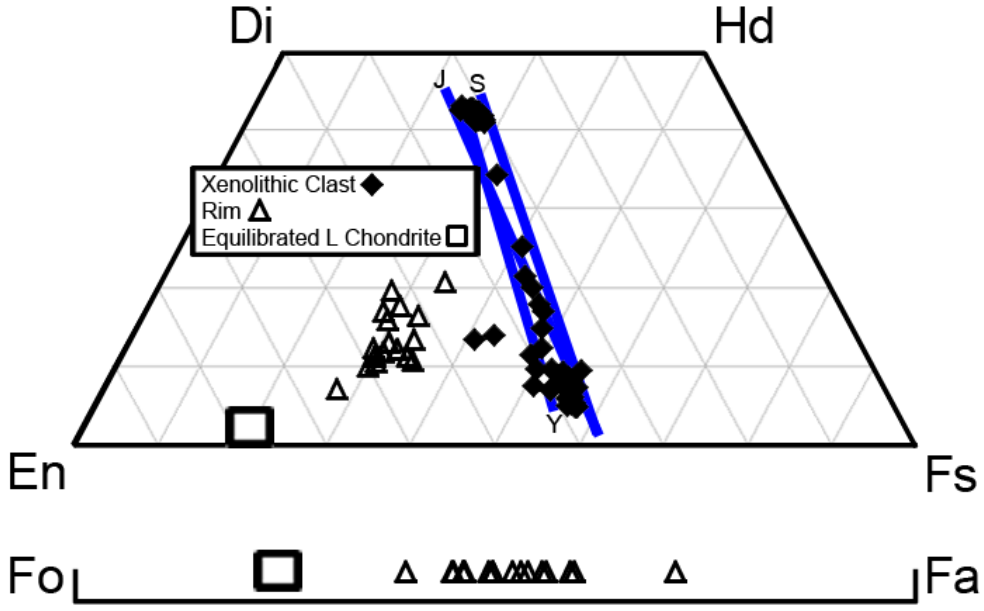

Figure 2.7. Quadrilateral showing pyroxene composition in the xenolithic clast, rim and equilibrated L chondrite material. Mineral short forms are as follows: Diopside (Di), hedenbergite (Hd), enstatite (En), ferrosilite (Fs), forsterite (Fo), fayalite (Fa). Blue lines represent compositional trends for the eucrites Stannern (S), Juvinas (J) and Y-791195 (Y) (Barrat et al. 2007; Warren et al. 1990).

Table 2.1. Composition of primary minerals in xenolithic clast as determined by EPMA (wt. %, ±1σ standard deviation). Italicized values are in element % (not oxide %).

	Pigeonite *n=28*	Augite *n=34*	Anorthite *n=49*	Silica[a] *n=24*	Ilmenite *n=41*	Sulfide[d] *n=13*	
SiO_2	49.63±0.33	50.93±0.44	47.23±1.02	98.70±0.63	0.03±0.09	*0.01±0.02*	*Si*
Na_2O	b.d.	0.05±0.03	1.47±0.28	0.01±0.04	-	-	*Na*
MgO	12.75±0.74	10.55±0.21	0.09±0.08	b.d.	2.21±0.44	*b.d.*	*Mg*
Al_2O_3	0.32±0.22	0.62±0.11	33.87±0.85	0.28±0.38	0.14±0.08	*b.d.*	*Al*
K_2O	-	-	0.17±0.13	0.10±0.07	-	-	*K*
CaO	3.60±1.41	19.68±0.75	17.21±0.59	0.08±0.16	0.06±0.03	-	*Ca*
TiO_2	0.19±0.11	0.33±0.06	b.d.	0.05±0.02	52.73±0.27	*b.d.*	*Ti*
V_2O_3	b.d.	b.d.	-	-	b.d.[b]	*b.d.*	*V*
Cr_2O_3	0.18±0.10	0.25±0.03	-	-	0.45±0.06	*0.01±0.02*	*Cr*
MnO	0.95±0.07	0.46±0.03	b.d.	b.d.	0.72±0.03	*b.d.*	*Mn*
FeO	31.72±2.42	16.28±0.82	0.44±0.20	0.25±0.24	42.71[c]	*63.56±0.28*	*Fe*
Fe_2O_3	-	-	-	-	1.22[c]		
$Fe_{Total\ as\ Fe2+}$					43.81±0.69		
CoO	-	-	-	-	-	*b.d.*	*Co*
NiO	-	-	-	-	-	*b.d.*	*Ni*
ZrO_2	-	-	-	-	0.01±0.03		*Zr*
Nb_2O_5	-	-	-	-	0.05±0.03		*Nb*
	-	-	-	-	-	*36.80±0.31*	*S*
Total	99.34	99.15	100.48	99.47	100.33	100.38	

n signifies the number of points analyzed.

[a]Some of the silica is quartz, while other areas are amorphous or perhaps microcrystalline.

[b]Peak overlap between the Ti $K_ß$ and the V $K_α$ in the WDS measurements does not allow for accurate determination of V by this technique. Comparisons with spectra of standards suggests a V_2O_3 concentration < 0.1 wt.%.

[c]Fe^{2+} and Fe^{3+} determined by minimizing the difference in cation number between the 2+ and 4+ sites.

[d]Sulfide structure was not determined.

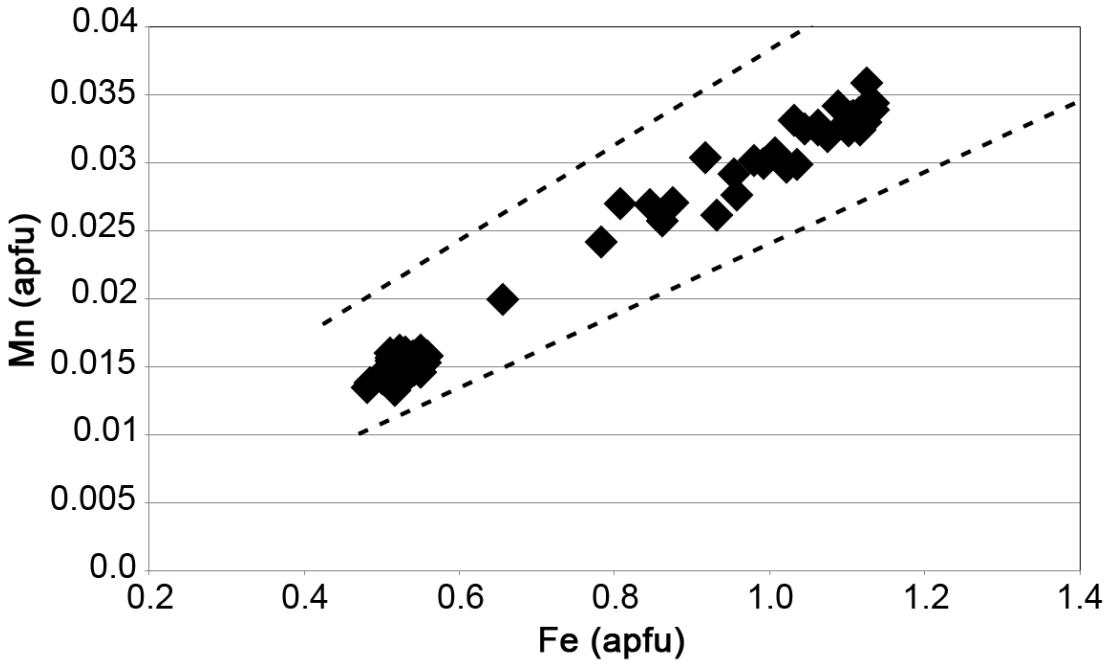

Figure 2.8. Mn versus Fe values for pyroxene in the xenolithic clast (in atoms per formula unit). The dotted lines show the range of basaltic eucrite values (Mayne et al. 2009).

2.4.2.3 Rim

Olivine and pyroxene compositions were measured by quantitative EDS (Appendix 2 - A2.7). Measurements were only taken from grains that did not show extensive zoning in BSE images. These grains were either crystallized in the rim or had undergone thermal metamorphism and brought into (or at least towards) equilibrium with the surrounding melt. Olivine grains showing no direct textural or compositional association with the L chondrite material gave an average composition of $Fa_{51.6 \pm 7.5}$ (Fig. 2.7, Appendix 2 - A2.7). Pyroxene gains crystallized from the melt fall either within the pigeonite field, or have intermediate compositions between augite and pigeonite (Fig. 2.7, Appendix 2 - A2.7) with an average pyroxene composition of $Fs_{31.2 \pm 2.2}Wo_{13.6 \pm 3.7}$.

2.4.3 Oxygen Isotope Characteristics

Oxygen isotope data for the xenolithic clast, rim and chondritic material were acquired (Table 2.2, Fig. 2.9). The chondritic material has oxygen isotope values identical to that

of known L chondrites (Fig. 2.9, Clayton et al. 1991). Analyses of two powder samples from the xenolithic clast are consistent and significantly removed from the L chondrite host rock analyses. The rim material exhibits values intermediate to these two components, falling on a mixing line between these two end-members.

Table 2.2. Oxygen isotope data for xenolithic clast, rim, chondrite clast and matrix.

Sample Description	$\delta^{17}O$	$\delta^{18}O$	$\Delta^{17}O$
Xenolithic Clast	1.63, 1.56	3.55, 3.46	-0.24, -0.26
Rim	2.60	4.31	0.326
L-Chondrite Clast	3.76	5.28	0.982
L-Chondrite Matrix	3.58, 3.71	5.02, 5.01	0.94, 1.08

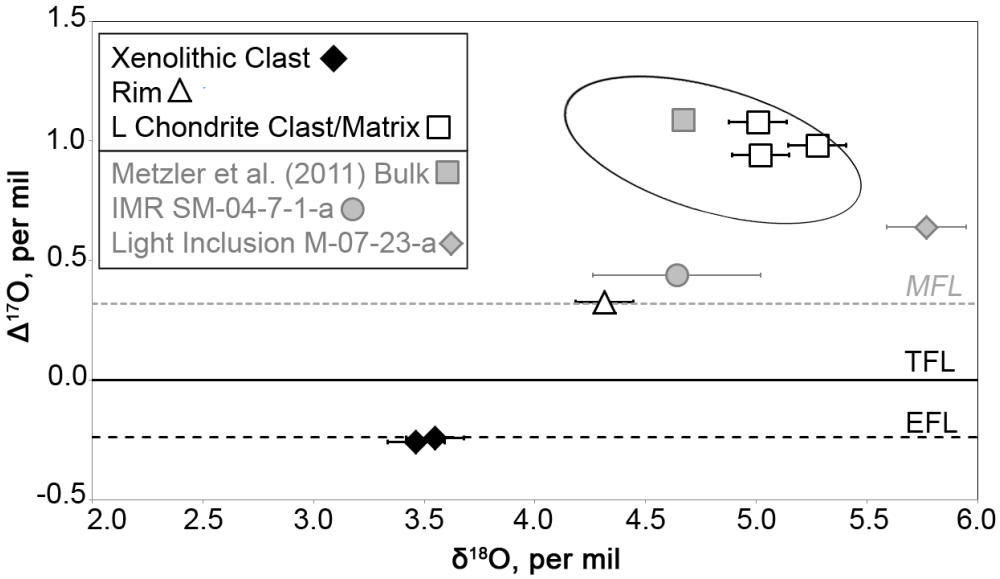

Figure 2.9. Oxygen isotope plot for xenolithic clast, rim and surrounding L-chondrite material. Error bars of two standard deviations are shown for $\delta^{18}O$ values. Two sigma values for $\Delta^{17}O$ are smaller than the plotted points. The terrestrial fractionation line (TFL) is marked along with the eucrite fractionation line (EFL) (Greenwood et al. 2005) and Mars fractionation line (MFL) (Ali et al. 2016). The circled area represents the range of L chondrites (Clayton et al. 1991). Grey data points are from Metzler et al. (2011) and include a bulk sample, an impact melt rock (IMR) clast and a light inclusion.

2.5 Discussion

2.5.1 Chondritic Material

Olivine and pyroxene compositions from equilibrated chondrules and oxygen isotope compositions are consistent with an L chondrite parent body. However, due to the large amount of NWA 869 material and lack of documentation associated with some of the material, it is necessary to confirm a NWA 869 designation prior to publishing information for any given piece (see Metzler et al. 2011). For a detailed confirmation of the NWA 869 designation please see Appendix 2 (A2.9).

2.5.2 Eucrite Classification of the Xenolithic Clast

Pyroxene compositions for the xenolithic clast follow the Mn-Fe trend for basaltic eucrites (Fig. 2.8, Karner et al. 2006; Mayne et al. 2009; Papike et al. 2003) and oxygen isotope values confirm a howardite-eucrite-diogenite (HED) parent body origin (Table 2.2, Fig. 2.9). The major element pyroxene compositions are also comparable to the eucrites Stannern, Juvinas and Y-791195 (Barrat et al. 2007; Warren et al. 1990; Fig. 2.7 this study). Additionally, the composition of anorthite in the clast is within the range of those measured for basaltic eucrites (Mayne et al. 2009). This clast is the first example of eucritic material in an L chondrite breccia.

The abundance of silica and ilmenite in the clast could be seen as anomalous; however, considering the size of the clast, it is reasoned that the material may not be representative of the bulk eucritic rock from which it was sampled. Past studies have found that basaltic eucrites with silica-rich regions are common (e.g., Mayne et al. 2009) and a random sampling of a eucritic lithology could easily include such regions. Examples of eucrites with similarly high modal silica content have been observed (e.g., Caldera and GRA 98098 in Mayne et al. 2009) and a dacite clast from a howardite contains 22.4% silica (Hahn et al. 2017). Stannern group eucrites tend to have high abundances of incompatible elements (e.g., Barrat et al. 2007) and Ti (e.g., Mittlefehldt 2015; Roszjar et al. 2011) and are thought to be the result of main group eucrite compositions being contaminated by partial melting of the HED parent body crust (Barrat et al. 2007). A relation to the

Stannern trend eucrites could also explain the elevated silica and ilmenite (Ti) levels in the clast described here.

2.5.3 Thermal and Shock History While on the Eucrite Parent Body

Eucrite thermal histories can be characterized using a pyroxene homogeneity scale devised by Takeda and Graham (1991). This scale relates the composition and texture of eucrite pyroxene grains to the thermal history of the meteorite. The pyroxene in this clast has been extensively modified by shock and post-shock heating; however, remnant textures and compositions are still visible. Pigeonite with exsolved augite (observable by SEM) is present with no measured inversion to orthopyroxene. This is consistent with a type 4 or 5 eucrite. The variability in both pigeonite composition (Table 2.1, Fig. 2.7) and the extent of augite exsolution along with the irregular occurrence of augite grains, likely reflects remnant variability associated with chemical zonation present in the pyroxene prior to shock and post-shock heating. This suggests a type 4 designation is appropriate. Eucrites in this group experienced thermal metamorphism with temperatures reaching 800-900 °C (Yamaguchi et al. 1996, 2009). Sheared pyroxene grains (Figs. 2.3a and 2.3b) are further evidence of shock. The sheared textures are only seen in the clast itself suggesting the shock, at least in this case, occurred before or during the impact of the eucrite material into the L chondrite parent body. The granular texture seen within remnant pyroxene and plagioclase forms suggests recrystallization from high post-shock temperatures (Fig. 2.4d); however, it is uncertain when this recrystallization occurred.

2.5.4 Xenolithic Achondritic Clasts in L Chondrite Meteorites

The vast majority of igneous clasts in ordinary chondrites are not xenoliths from other parent bodies, but instead are the products of melt processes involving broadly chondritic materials (e.g. Ruzicka et al. 2019). The identification of rare xenolithic clasts from external sources in both regolith breccia meteorites and within unbrecciated chondrites provides a glimpse of processes, such as impact accretion and impact mixing. Examples of xenolithic achondritic clasts in L chondrite breccia include a clast with affinities to the winonaites in the Villalbeto de la Peña L6 chondrite breccia (Bischoff et al. 2013; Dyl et

al. 2012). This clast experienced post accretion modification, including fluid, thermal and further impact alteration (Bischoff et al. 2013). A Cr-rich inclusion has been documented in the Los Martinez L6 chondrite breccia (Brearley et al. 1991), which may be similar to the clast in Villalbeto de la Peña (Bischoff et al. 2013). The Hedjaz L3.7-6 (Fredriksson et al. 1986) chondrite breccia contains a noritic clast which may have been produced from L precursor material that went through multiple heating/melting stages (Misawa et al. 1992).

Some unbrecciated L chondrites also contain xenolithic material. The Barwell L6 meteorite hosts multiple igneous clasts that seem to have a relationship to the H chondrites (Hutchison et al. 1988). The clasts' formation ages suggest they were incorporated into the L chondrite parent body while it was forming and before it experienced the onset of thermal metamorphism (Crowther et al. 2018). Binns (1967) first described cristobalite xenoliths in the Farmington L5 chondrite and a tridymite-bearing clast has been observed in the Bovedy L3 chondrite (Ruzicka et al. 1995). Troctolitic inclusions in the L6 chondrites Yamato-75097 and -793241 have been reported (e.g., Mittlefehldt et al. 1995; Prinz et al. 1984). Igneous textured clasts have also been seen in the Julesberg L3 chondrite; however, their origin may be related to chondrule formation (Ruzicka et al. 1998). A clast associated with melting of an LL-like source has also been found in the L5 chondrite NWA 8645 (Ruzicka et al. 2019). Clasts in Meteorite Hills (MET) 96515, MET 00489 and Queen Alexandra Range 97008 are melt-derived assemblages from an unknown source (Ruzicka et al. 2019).

Many of these potentially xenolithic materials cannot be simply related to known meteorite groups. In many cases there are either no obvious connection to currently studied groups (e.g., Metzler et al. 2011), or the connections are tentative, or complex (e.g., Bischoff et al. 2013). In contrast, the eucrite clast identified in this study is the first such clast found in an L chondrite breccia, providing a window into late mixing between two well-characterized meteorite groups and the lithification of multiple impact components through brecciation and melting (Figs. 2.1 and 2.2). Northwest Africa 869 and the L chondrite parent body, in general, provide a unique opportunity to examine impact processes in the asteroid belt.

The sample size is arguably small, but the materials impacting and being incorporated into the L chondrite parent body do not appear to be equivalent to the materials commonly found in meteorite collections. The differences in composition between these clasts and our meteorite collections could be a consequence of temporal variations in impactor flux. Recently, it has been noted that the sources of meteorites on Earth have changed over time (Heck et al. 2017). Since meteorite collections are only populated by geologically recent impacts, our collections are biased and obviously do not represent the impactor populations and histories of other terrestrial bodies. This difference could also be a result of the L chondrite parent body's location in the solar system. Future work adding to the list of xenolithic materials in L chondrite and other meteorite breccia will allow for an assessment of communication between source populations and chemical reservoirs in the early solar system. Xenolithic materials formed during processes in the early solar system may also be preserved in this breccia, instead of being overprinted by subsequent processes on their original parent body. This could provide access to further materials not represented in the current meteorite record.

2.5.5 Rim Formation Conditions

We can deduce an igneous (melt) origin of rim components on the basis of our textural and chemical observations and glean some information on its thermal history. Intermediate pyroxene compositions (between augite and pigeonite) in the rim reflect an environment of rapid crystallization (Smith and Lindsley 1971). These compositions may be truly homogeneous, or unmixed at the sub-micrometre-scale (see Mellini et al. 1988). Small grains of Mg-rich olivine originating from the chondritic body did not experience melting in the rim (Fig. 2.5e). Instead, these grains show enrichment in iron that is concentric to grain margins, and we interpret these as the result of diffusion. Comparisons with diffusion models (Dohmen and Chakraborty 2007; Dohmen et al. 2007) and experimental work (e.g., Buening and Buseck 1973) suggest that iron diffusion was occurring for a few hours to perhaps tens of hours in order to produce the diffusion profiles observed. The mineral compositions and textures are consistent with rapid crystallization from high temperature, suggesting heating due to impact(s). The question then becomes whether this impact heating was a consequence of the collision of the clast

with the L-chondrite breccia body or whether a later thermal event caused melting of already admixed rim material.

Impact-generated melting during asteroidal accretion is favored or subdued due to a range of factors. Impactor clasts with associated primary impact melt products are a rarity in asteroidal meteorites. This is in part due to the relatively low velocity impacts experienced in the modern main asteroid belt, which currently average ~ 5 km/s (Bottke et al. 1994). This rarity is also the result of the target materials involved. Asteroidal breccias, at least those found in meteorite collections, are lithified and dense in nature. Dense target materials require greater impact velocities for melts to be produced, while unconsolidated and porous targets can melt at much lower impact velocities (e.g. Bland et al. 2014; Hörz and Schaal 1981). The formation of agglutinate-type glasses in lunar soils and general lack of similar impact melt products in meteorite breccia, originating from the asteroid belt, has been a long-observed phenomenon (e.g., Hörz and Schaal 1981).

With regard to impactor survival, hypervelocity impact experiments using Al-spheres and NWA 869 target materials have been carried out by Flynn et al. (2018). The resulting craters formed during these experiments were approximately 12 times the diameter of the impactor. Impact crater size and morphology, like melt formation, are also dependent on the impactor and target material's initial properties. Strong projectiles impacting weak target materials produce a deep tunnel-like crater, close in diameter to the impactor, and allow for the survival of large amounts of impactor material (Baker et al. 1995; Flynn et al. 2015). Impacting velocity also plays a role in the remaining impactor size following the impact. Results of hypervelocity impact experiments using basalt and shale projectiles have shown a decrease in impactor survival with increasing impact velocity (Wickham-Eade et al. 2018).

This knowledge from past impact studies provide a basis for interpreting the impact processes that formed the rim surrounding the eucrite clast in NWA 869. We consider three scenarios that may have formed the rim: 1. The impact occurred at a higher than average impact velocity for an impact in the main asteroid belt, 2. The impact target was unconsolidated or porous material, or 3. A primary impact by the eucrite clast broke up

the rim material and heat from a subsequent, possibly nearby, impact melted the unconsolidated material. All three are considered below in more detail.

The first scenario of increasing the impact velocity is not favored. Although it would produce a rim melt we would expect the extensive evidence of heating and melting in the eucrite clast. Although there is some evidence of melting in the eucrite clast, including inclusions in the silica-rich regions following flow patterns (Fig. 2.5a) and melt mixing of plagioclase and pyroxene (Fig. 2.4), the relative timing of these features' formation is ambiguous. In any case, the level of melting seen in the rim exceeds that observed in the eucrite clast. Fractures observed in the rim often begin near the clast-rim boundary and extend out from the clast, other times they are coincident or nearly coincident with the rim-chondrite breccia boundary (Fig. 2.2). Fractures radiating out from the clast and at the outer rim boundary are the result of cooling and contraction of material as heat was lost; signifying greater heat loss in the rim then surrounding materials. Moreover, we would expect a liquid (magma) rim to be more continuous at the contact with the eucrite as opposed to the discontinuous rim we observe, in places tapering out. In one region, there is no rim component between the eucrite clast and L chondrite. Instead there is a breccia contact with no melt component (Fig. 2.1 and Fig 2.2, top left of clast). This may reflect further impact brecciation postdating the consolidation of the rim. The evident survival of the eucrite clast likewise does not favor an elevated impact velocity.

The second scenario of a porous or less consolidated L chondrite regolith could account for the melting seen in the rim. However, the large amount of well-consolidated NWA 869 material currently in collections requires that the sampling region on the parent body became consolidated at some point in time. An unconsolidated regolith would also allow for a large surviving impactor (the eucrite clast) and smaller diameter region of disruption caused by the impact (the rim).

Finally, an initial impact by the eucritic material could have broken up and mixed the material in the rim region, which was then melted by a subsequent nearby impact. The evidence of pervasive thermal metamorphism seen in the chondritic material in the thin

section supports a secondary heating event. Crystallization of mesostasis is seen in even the most (otherwise) primitive type 3-4 chondrules (Appendix 2 - A2.6).

We propose that the most likely explanation is a combination of aspects of the latter two scenarios. Impact into an unconsolidated regolith would allow for the large surviving eucrite clast and small diameter rim. This type of impact could also produce some melting in the rim. A subsequent impact(s) would be required to consolidate the regolith, producing the NWA 869 material we have in collections today. Subsequent impact processes would have also generated melting in the rim. This scenario aligns well with the textures seen in the melt rim. Melt products near the clast are often fine-grained (Fig. 2.5b). This is likely due to the initial impact generating finer materials closer to the impacting clast. Impact heating near the clast would also be shorter lived, as consolidated materials like the eucrite clast provide a heat sink during the impact heating process (Bland et al. 2014). Further out from the clast the grain size typically coarsens as a result of less initial brecciation and slower cooling (Figs. 2.5c and 2.5d). The interface between the rim and chondritic breccia is variable. For example, some of the surrounding L chondrite shows modification from heating extending out from the rim for tens of micrometres (Figs. 2.6a and 2.6b), while other regions exhibit fine-grained reaction rims, generally in areas where small amounts of unconsolidated material were likely present between larger clasts (Figs. 2.6c and 2.6d). These spatial variations may reflect variability in the initial brecciation process and the reaction of this breccia to further impact heating. There are regions where rim material intrudes into the surrounding L chondrite (Figs. 2.6a and 2.6b) and into the clast (Fig. 2.5a), but in general there are relatively sharp edges between the L chondrite and rim and the eucrite clast and rim. This is consistent with our preferred scenario, since the more unconsolidated material in the rim, generated during the initial impact, would melt and the surrounding denser materials would be less affected. In such a case, no significant gradation of melt products would be expected at these interfaces. Future geochronologic work could help shed more light on the rim's formation.

2.5.6 The Rim as an Example of Chemical Mixing by Impact Accretion

The rim material has oxygen isotope values consistent with mixing of L chondrite host with the eucritic clast (Table 2.2, Fig. 2.9). This composition also falls on the Mars fractionation line. Past work has shown that shergottite-like textures, mineralogies and mineral chemistries can be generated from L chondrite melts (Wu and Hsu 2019). The identification of additional sources of basalt generation and the mixing of chemical reservoirs demands that caution be taken when meteorite source locations are studied, particularly for meteorites composed entirely of breccia and impact melt products. The mixing process seen in this current study includes both melt mixing and physical (brecciation) mixing (Figs. 2.5 and 2.6). As such, this impact-generated mixture provides a unique opportunity to study impact accretion.

Remnant clasts from both the chondritic host and eucrite impactor are found within the rim (Figs. 2.5e, 2.5f and 2.6c). The time-scale of the heating resulting from impact processes was not long enough to completely melt large clasts (e.g., Figs. 2.5f and 2.6c). Some pyroxene grains show remnant L chondrite and eucritic compositions and often provided nucleation points for growth of pyroxene from the melt composition (Figs. 2.5c and 2.5f). Pyroxene which crystallized from the melt is also seen (Figs. 2.5b and 2.5c). Rim pyroxene compositions fall on a mixing line between the average eucrite clast pyroxene composition and equilibrated L chondrite composition (Fig. 2.7). These compositions are sometimes intermediate between the augite and pigeonite fields. Similar intermediate pyroxene compositions have been reported in howardite impact melt clasts (Cohen 2013). The olivine grains found in the rim in the current study are in some cases remnant grains from the L chondrite breccia, showing diffusion profiles from interaction from the rim melt (Fig. 2.5e). Similarly, Fe-rich rims are found around olivine grains in howardite impact melt clasts (Cohen 2013). Olivine in this current study is often also seen with a more homogeneous chemistry signifying extensive thermal metamorphism and/or melting (Figs. 2.5c and 2.7). Olivine compositions in the rim are more Fe-rich than the L chondrite host. This is due to melt contributions from the more Fe-rich eucrite pyroxene, as well as Fe-metal from the L chondrite breccia. Relatively high-Fe olivine

has also been documented in howardite impact melts (Cohen 2013); however, eucrite impact melts are documented with no olivine (NWA 1240, Barrat et al. 2003; NWA 5218, Wittmann et al. 2011). The generation of intermediate pyroxene compositions and relatively Fe-rich olivine are potential markers for impact processes in cases where the melt is not seen in context (e.g., larger scale impact breccias/melts).

There are two cases of clasts in NWA 869 from the work of Metzler et al. (2011) that should be examined within the context of our current study. One clast is referred to as a light inclusion. This inclusion contains zoned olivine and low-Ca-pyroxene, as well as Na-rich feldspar and K-rich feldspar. The clast also contains interstitial quenched Ca-rich plagioclase and Ca-rich pyroxene of varying composition. These compositions and textures are consistent with an impact melt perhaps similar to that seen surrounding the eucritic clast. The light inclusion also has elevated Ca and Al content relative to bulk NWA 869 (Metzler et al. 2011) as would be expected from admixing a pigeonite-augite-anorthite-rich eucritic composition. The oxygen isotope composition, however, does not suggest mixing between an L chondrite and a eucrite composition (Fig. 2.9). Instead this composition points to mixing with material from another, perhaps differentiated, parent body. Metzler et al. (2011) also describes an impact melt rock (IMR) clast with an oxygen isotope composition similar to the rim described surrounding the eucritic clast (Fig. 2.9). This impact melt is composed of zoned olivine grains and partially-devitrified, interstitial material. The impact melt has Ca and Al contents relatively similar to that of bulk NWA 869 material (Metzler et al. 2011) suggesting that mixing with a eucritic component is unlikely.

2.6 Conclusions

Regolith breccias provide a unique opportunity to study asteroid surface processes such as impact accretion. An achondritic impactor clast in NWA 869 has been identified as the first example of eucritic material in an L chondrite breccia. The clast history proceeded in the following manner:

1. Initial crystallization on the eucrite parent body followed by thermal metamorphism with temperatures reaching 800-900 °C.

2. The impact and removal of the clast from the eucrite parent body occurred, perhaps forming the sheared pyroxene grains.

3. Impact into unconsolidated L chondrite regolith mixed the material in the rim region.

4. A subsequent nearby impact helped consolidate the regolith and resulted in melting in the rim. Maximum temperatures reached in the rim were not high enough and were not retained long enough to melt larger clasts, or completely melt the olivine present. However, impact generated melting did produce a broadly basaltic melt with bulk characteristics of some planetary achondrites.

5. Thermal diffusion of iron into olivine proceeded for a few hours to perhaps tens of hours while the rock cooled.

Melt rim pyroxene compositions fall on a mixing line between the average eucrite pyroxene composition and equilibrated L chondrite composition. Some olivine grains in the rim are remnant grains from the L chondrite breccia showing diffusion profiles from interaction with the melt. Olivine compositions in the rim are more Fe-rich than the L chondrite host. The presence of these pyroxene and olivine compositions are potential markers for impact processes in cases where the melt products are not seen in context. The rim's oxygen isotope composition falls on a mixing line between eucrite compositions and L chondrite compositions; however, it also coincidentally falls on the Mars fractionation line. This finding reinforces the importance of integrating the textural and chemical observations of meteorites entirely composed of breccia and impact melt products.

The large amount of NWA 869 material available for study is an exceptional source of a diverse range of meteoritic materials. The textures recorded in these meteorites provide an unparalleled view of impact accretion and near-surface processing.

2.7 References

Ali A., Jabeen, I., Gregory D., Verish R., and Banerjee N. R. 2016. New triple oxygen isotope data of bulk and separated fractions from SNC meteorites: Evidence for mantle homogeneity of Mars. *Meteoritics & Planetary Science* 51(5):981-995.

Baker J. R. 1995. Hypervelocity crater penetration depth and diameter - a linear function of impact velocity? *International journal of impact engineering* 17:25-35.

Barrat J. A., Jambon A., Bohn M., Blichert-Toft J., Sautter V., Göpel C., Gillet P., Boudouma O., and Keller F. 2003. Petrology and geochemistry of the unbrecciated achondrite Northwest Africa 1240 (NWA 1240): an HED parent body impact melt. *Geochimica et Cosmochimica Acta* 67(20):3959-3970.

Barrat J. A., Yamaguchi A., Greenwood R. C., Bohn M., Cotten J., Benoit M., and Franchi I. A. 2007. The Stannern trend eucrites: Contamination of main group eucritic magmas by crustal partial melts. *Geochimica et Cosmochimica Acta* 71(16):4108-4124.

Binns R. A. 1967. Farmington meteorite: cristobalite xenoliths and blackening. *Science* 156(3779):1222-1226.

Bischoff A. and Schultz L. 2004. Abundance and meaning of regolith breccias among meteorites (abstract). *Meteoritics & Planetary Science* 39 (Suppl.):A15.

Bischoff A., Scott E. R. D., Metzler K., and Goodrich C. A. 2006. Nature and origins of meteoritic breccias. In Meteorites and the Early Solar System II, edited by Lauretta D.S., and McSween Jr. H.Y. Tucson: University of Arizona. pp. 679–712.

Bischoff A., Dyl K. A., Horstmann M., Ziegler K., Wimmer K., and Young E. D. 2013. Reclassification of Villalbeto de la Peña-Occurrence of a winonaite-related fragment in a hydrothermally metamorphosed polymict L-chondritic breccia. *Meteoritics & Planetary Science* 48(4):628-640.

Bischoff A., Schleiting M., Wieler R., and Patzek M. 2018. Brecciation among 2280 ordinary chondrites - constraints on the evolution of their parent bodies. *Geochimica et Cosmochimica Acta* 238:516-541.

Bland P. A., Collins G. S., Davison T. M., Abreu N. M., Ciesla F. J., Muxworthy A. R., and Moore J. 2014. Pressure–temperature evolution of primordial solar system solids during impact-induced compaction. *Nature communications* 5: DOI: 10.1038/ncomms6451.

Blum, J., 2018. Dust evolution in protoplanetary discs and the formation of planetesimals. *Space Science Reviews* 214:52.

Bottke Jr W. F., Nolan M. C., Greenberg R., and Kolvoord, R. A. 1994. Velocity distributions among colliding asteroids. *Icarus* 107(2):255-268.

Bottke Jr W.F., Walker R. J., Day J. M., Nesvorny D., and Elkins-Tanton L. 2010. Stochastic late accretion to Earth, the Moon, and Mars. *Science* 330(6010):1527-1530.

Brasser R., Mojzsis S. J., Werner S. C., Matsumura S., and Ida S. 2016. Late veneer and late accretion to the terrestrial planets. *Earth and Planetary Science Letters* 455:85-93.

Brearley A. J. and Jones R. H. 1998. Chondritic meteorites. In Planetary materials, edited by Papike J. J. Reviews in mineralogy, vol. 36. Washington: The Mineralogical Society of America. pp. 3.1–3.398.

Brearley A. J., Casanova I., Miller M. L., and Keil K. 1991. Mineralogy and possible origin of an unusual Cr-rich inclusion in the Los Martinez (L6) chondrite. *Meteoritics* 26(4):287-300.

Buening D. K. and Buseck P. R. (1973). Fe-Mg lattice diffusion in olivine. *Journal of Geophysical Research* 78(29):6852-6862.

Clayton R. N., Mayeda T. K., Goswami J. N., and Olsen E. J. 1991. Oxygen isotope studies of ordinary chondrites. *Geochimica et Cosmochimica Acta* 55(8):2317-2337.

Cohen B. A. 2013. The Vestan cataclysm: Impact - melt clasts in howardites and the bombardment history of 4 Vesta. *Meteoritics & Planetary Science* 48(5):771-785.

Connolly H. C., Zipfel J., Grossman J. N., Folco L., Smith C., Jones R. H., Righter K., Zolensky M., Russell S. S., Benedix G. K., Yamaguchi A., and Cohen B. A. 2006. The Meteoritical Bulletin, No. 90. *Meteoritics & Planetary Science* 41:1383–1418.

Crowther S. A., Filtness M. J., Jones R. H., and Gilmour, J. D. 2018. Old formation ages of igneous clasts on the L chondrite parent body reflect an early generation of planetesimals or chondrule formation. *Earth and Planetary Science Letters* 481:372-386

Day J. M., Floss C., Taylor L. A., Anand M., and Patchen A. D. 2006. Evolved mare basalt magmatism, high Mg/Fe feldspathic crust, chondritic impactors, and the petrogenesis of Antarctic lunar breccia meteorites Meteorite Hills 01210 and Pecora Escarpment 02007. *Geochimica et Cosmochimica Acta* 70(24):5957-5989.

Day J. M., Walker R. J., Qin L., and Rumble III D. 2012. Late accretion as a natural consequence of planetary growth. *Nature Geoscience* 5(9):614-617.

Dohmen R. and Chakraborty S. 2007. Fe-Mg diffusion in olivine II: point defect chemistry, change of diffusion mechanisms and a model for calculation of diffusion coefficients in natural olivine. *Physics and Chemistry of Minerals* 34(6):409-430.

Dohmen R., Becker H. W., and Chakraborty S. 2007. Fe-Mg diffusion in olivine I: experimental determination between 700 and 1,200 C as a function of composition, crystal orientation and oxygen fugacity. *Physics and Chemistry of Minerals* 34(6):389-407.

Dyl K. A., Bischoff A., Ziegler K., Young E. D., Wimmer K., and Bland P. A. 2012. Early Solar System hydrothermal activity in chondritic asteroids on 1–10-year timescales. *Proceedings of the National Academy of Sciences* 109(45):18306-18311.

Flynn G. J., Durda D. D., Patmore E. B., Clayton A. N., Jack S. J., Lipman M. D., and Strait M. M. 2015. Hypervelocity cratering and disruption of porous pumice targets:

Implications for crater production, catastrophic disruption, and momentum transfer on porous asteroids. *Planetary and Space Science* 107:64-76.

Flynn G. J., Durda D. D., Patmore E. B., Jack S. J., Molesky M. J., May B. A., Congram S. N., Strait M. M., and Macke R. J. 2018. Hypervelocity cratering and disruption of the Northwest Africa 869 ordinary chondrite meteorite: Implications for crater production, catastrophic disruption, momentum transfer and dust production on asteroids. *Planetary and Space Science* 164:91-105.

Fredriksson K., Fredriksson B. J., and Kraut F. 1986. The Hedjaz meteorite. *Meteoritics* 21(2):159-168.

Greenwood R. C., Franchi I. A., Jambon A., and Buchanan P. C. 2005. Widespread magma oceans on asteroidal bodies in the early solar system. *Nature* 435(7044):916-918.

Greenwood R. C., Schmitz B., Bridges J. C., Hutchison R., and Franchi, I. A. 2007. Disruption of the L chondrite parent body: New oxygen isotope evidence from Ordovician relict chromite grains. *Earth and Planetary Science Letters* 262(1-2):204-213.

Hahn T. M. Jr., Lunning N. G., McSween Jr H. Y., Bodnar R. J. and Taylor L. A. 2017. Dacite formation on Vesta: Partial melting of the eucritic crust. *Meteoritics & Planetary Science* 52(6):1173-1196.

Heck P. R., Schmitz B., Bottke W. F., Rout S. S., Kita N. T., Cronholm A., Defouilloy C., Dronov A., and Terfelt F., 2017. Rare meteorites common in the Ordovician period. *Nature Astronomy* 1. DOI: 10.1038/s41550-016-0035

Hörz F. and Schaal R. B. 1981. Asteroidal agglutinate formation and implications for asteroidal surfaces. *Icarus* 46(3):337-353.

Hutchison R., Williams C. T., Din V. K., Clayton R. N., Kirschbaum C., Paul R. L., and Lipschutz M. E. 1988. A planetary, H-group pebble in the Barwell, L6, unshocked chondritic meteorite. *Earth and Planetary Science Letters 90*(2):105-118.

Hyde B. C., Tait K. T., Rumble III D., Izawa M. R. M, Thompson M. S., Nicklin I., and Gregory D. A. 2015. Achondritic impactor clasts in Northwest Africa 869 (abstract #1983). 46th Lunar and Planetary Science Conference.

Hyde B. C., Moser D. E., Tait K. T., Barker I. R., and Joy B. R. 2016. Development of quantitative energy dispersive spectrometry with a field emission gun scanning electron microscope for use in meteorite studies (abstract). Electron-Probe Microanalysis 2016. pp.132-133.

Karner J., Papike J. J., and Shearer C. K. 2006. Comparative planetary mineralogy: Pyroxene major-and minor-element chemistry and partitioning of vanadium between pyroxene and melt in planetary basalts. *American Mineralogist* 91(10):1574-1582.

Korochantseva E. V., Trieloff M., Lorenz C. A., Buykin A. I., Ivanova M. A., Schwarz W. H., Hopp J., and Jessberger E. K. 2007. L-chondrite asteroid breakup tied to Ordovician meteorite shower by multiple isochron 40Ar-39 Ar dating. *Meteoritics & Planetary Science, 42*(1):113-130.

Matsuda J., Akane A., and Nishimura C. 2006. Noble gas features of the two desert meteorites Dhofar 008 and Northwest Africa 869 (abstract). *Meteoritics & Planetary Science* 41 (Suppl.):A210.

Mayne R. G., McSween H. Y., McCoy T. J., and Gale A. 2009. Petrology of the unbrecciated eucrites. *Geochimica et Cosmochimica Acta* 73(3):794-819.

McCausland P. J. A., Tait K. T., Nicklin I., and Flemming R. L. 2017. Regolith processing on L chondrite bodies as witnessed by NWA 869 (abstract #1826). 48th Lunar and Planetary Science Conference.

Mellini M., Carbonin S., Dal Negro A., and Piccirillo E.M., 1988. Tholeiitic hypabyssal dykes: how many clinopyroxenes? *Lithos* 22(2):127-134.

Metzler K., Bischoff A., Greenwood R. C., Palme H., Gellissen M., Hopp J., Franchi I. A., and Trieloff M. 2011. The L3–6 chondritic regolith breccia Northwest Africa (NWA)

869: (I) Petrology, chemistry, oxygen isotopes, and Ar-Ar age determinations. *Meteoritics & Planetary Science* 46(5): 652-680.

Misawa K., Watanabe S., Kitamura M., Nakamura N., Yamamoto K., and Masuda A. 1992. A noritic clast from the Hedjaz chondritic breccia: implications for melting events in the early solar system. *Geochemical Journal 26*(6):435-446.

Mittlefehldt D. W., Lindstrom M. M., Wang M. S., and Lipschutz M. E. 1995. Geochemistry and origin of achondritic inclusions in Yamato-75097-793241 and-794046 chondrites. *Antarctic Meteorite Research* 8:251-271.

Mittlefehldt D. W. 2015. Asteroid (4) Vesta: I. The howardite-eucrite-diogenite (HED) clan of meteorites. *Chemie der Erde-Geochemistry* 75(2):155-183.

Osawa T. and Nagao K. 2006. Noble gases in solar gas–rich and solar-gas-free polymict breccias. *Antarctic Meteorite Research* 19:58–78.

Papike J. J., Karner J. M., and Shearer C. K. 2003. Determination of planetary basalt parentage: a simple technique using the electron microprobe. *American Mineralogist* 88: 469–472.

Prinz M., Nehru C. E., Weisberg M. K., Delaney J. S., Yanai K., and Kojima H. 1984. H chondritic clasts in a Yamato L6 chondrite: Implications for metamorphism (abstract). Proceedings, 47th Annual Meeting of the Meteoritical Society. p. 139.

Roszjar J., Metzler K., Bischoff A., Barrat J. A., Geisler T., Greenwood R. C., Franchi I. A., and Klemme S. 2011. Thermal history of Northwest Africa 5073 - A coarse-grained Stannern-trend eucrite containing cm-sized pyroxenes and large zircon grains. *Meteoritics & Planetary Science* 46(11):1754-1773.

Rumble D. III, Farquhar J., Young E. D., and Christensen C. P. 1997. In situ oxygen isotope analysis with an excimer laser using F_2 and Br F_5 reagents and O_2 gas as analyte. *Geochimica et Cosmochimica Acta* 61:4229–4234.

Rumble D. III, Miller M. F., Franchi I. A., and Greenwood R. C. 2007. Oxygen three-isotope fractionation lines in terrestrial silicate minerals: An inter-laboratory comparison of hydrothermal quartz and eclogitic garnet. *Geochimica et Cosmochimica Acta* 71:3592–3600.

Ruzicka A., Kring D. A., Hill D. H., Boynton W. V., Clayton R. N., and Mayeda T. K. 1995. Silica-rich orthopyroxenite in the Bovedy chondrite. *Meteoritics* 30(1):57-70.

Ruzicka A., Snyder G. A., and Taylor L. A. 1998. Mega-chondrules and large, igneous-textured clasts in Julesberg (L3) and other ordinary chondrites: Vapor-fractionation, shock-melting, and chondrule formation. *Geochimica et Cosmochimica Acta* 62(8):1419-1442.

Ruzicka A. M., Greenwood R. C., Armstrong K., Schepker K. L., and Franchi, I.A. 2019. Petrology and oxygen isotopic composition of large igneous inclusions in ordinary chondrites: Early solar system igneous processes and oxygen reservoirs. *Geochimica et Cosmochimica Acta*. 266:497-528.

Schmitz B., Farley K. A., Goderis S., Heck P. R., Bergström S. M., Boschi S., Claeys P., Debaille V., Dronov A., van Ginneken M., and Harper, D. A. 2019. An extraterrestrial trigger for the mid-Ordovician ice age: Dust from the breakup of the L-chondrite parent body. *Science Advances* 5(9):eaax4184.

Schneider C. A., Rasband W. S. and Eliceiri K. W. 2012. NIH Image to ImageJ: 25 years of image analysis. *Nature methods* 9(7):671-675.

Smith D. and Lindsley D. H. 1971. Stable and metastable augite crystallization trends in a single basalt flow. *American Mineralogist* 56:225-233.

Tait K. T. and Day J. M., 2018. Chondritic late accretion to Mars and the nature of shergottite reservoirs. *Earth and Planetary Science Letters* 494:99-108.

Takeda, H. and Graham, A. L. 1991. Degree of equilibration of eucritic pyroxenes and thermal metamorphism of the earliest planetary crust. *Meteoritics* 26(2):129-134.

Thompson, M., Rumble III, D., Tait, K. T., Nicklin, I., and Gregory, D. 2011. Meteorite Northwest Africa (NWA) 869: A study of diverse clasts in the L 4-6 brecciated ordinary chondrite. Proceedings, Geological Association of Canada/Mineralogical Association of Canada annual meeting. pg. 217.

Valley J. W., Kitchen N., Kohn M. J., Niendorf C. R., and Spicuzza M. J. 1995. UWG-2, a garnet standard for oxygen isotope ratios: Strategies for high precision and accuracy with laser heating. *Geochimica et Cosmochimica Acta* 59:5223–5231.

van Drongelen, K. D., Rumble III, D. and Tait, K. T. 2016. Petrology and oxygen isotopic compositions of clasts in HED polymict breccia NWA 5232. *Meteoritics & Planetary Science* 51(6):1184-1200.

Warren P. H., Jerde E. A., Migdisova L. F., and Yaroshevsky A. A. 1990. Pomozdino - an anomalous, high-MgO/FeO, yet REE-rich eucrite (abstract). Proceedings, 20th Lunar and Planetary Science Conference. pp.281-297.

Weidenschilling S. J. 2000. Formation of planetesimals and accretion of the terrestrial planets. *Space Science Reviews* 92:295-310.

Welten K., Leclerc M. D., Ott U., Metzler K., Caffee M. W., Jull A. J. T., and Franke L. 2011. The L3-6 chondritic regolith breccia Northwest Africa (NWA) 869: (II) Noble gases and cosmogenic radionuclides. *Meteoritics &Planetary Science* 46(7):970-988.

Wickham-Eade J. E., Burchell M. J., Price M. C., and Harriss K. H. 2018. Hypervelocity impact fragmentation of basalt and shale projectiles. *Icarus* 311:52-68.

Wittmann A., Hiroi T., Ross D. K., Herrin J. S., Rumble D., and Kring D. A. 2011. Eucrite impact melt NWA 5218 - Evidence for a large crater on Vesta (abstract #1984). 42nd Lunar and Planetary Science Conference.

Wu, Y. and Hsu, W. 2019. Petrogenesis and in situ U-Pb geochronology of a strongly shocked L-melt rock Northwest Africa 11042. *Journal of Geophysical Research: Planets* 123. https://doi.org/10.1029/2018JE005743.

Yamaguchi A., Taylor G. J., and Keil K. 1996. Global crustal metamorphism of the eucrite parent body. *Icarus* 124(1):97-112.

Yamaguchi A., Barrat J. A., Greenwood R. C., Shirai N., Okamoto C., Setoyanagi T., Ebihara M., Franchi I. A., and Bohn M. 2009. Crustal partial melting on Vesta: Evidence from highly metamorphosed eucrites. *Geochimica et Cosmochimica Acta* 73(23):7162-7182.

Chapter 3

Record of rapid, early solar system melting and disk reservoir separation preserved in Northwest Africa 7680 and 6962

3.1 Abstract

Northwest Africa (NWA) 7680 and NWA 6962 preserve a record of early solar system melt environments from the same parent body. The achondrites have olivine compositions of $Fa_{44.8}$ and $Fa_{47.4}$ for NWA 7680 and NWA 6962 respectively. Replicate oxygen isotope analyses of grains and bulk powders from NWA 7680 returned average $\Delta^{17}O$ values of -1.04 and -1.00‰ respectively, which is identical to that reported for NWA 6962. Both meteorites are plagioclase-rich and NWA 7680 is also Fe-metal-rich, suggesting they both formed via short-lived differentiation processes that resulted in the pooling of melt products. Geochemistry shows that both rocks could be formed through fractionation processes on a CR chondrite-like parent body. A secondary Na-Ca-Al-P-rich melt intrusion is observed in both meteorites and melt products include silica-rich, alkali-deficient nepheline. The secondary liquid has re-melted and mixed with primary plagioclase in NWA 6962, whereas it is generally restricted to grain boundaries in NWA 7680, leaving some of the primary plagioclase crystals intact. *In situ* dating of NWA 7680 phosphate minerals (merrillite and fluorapatite) reveals that it has not been heated above 350-550 °C since 4578 ± 17 Myr ago ($^{207}Pb/^{206}Pb$ age ± 2σ, within error of solar system age). Phosphates from the secondary melt in NWA 6962 yield a $^{207}Pb/^{206}Pb$ age of 4556.6 ± 8.2 Myr old (2σ) within 2σ of the NWA 7680 age. The oxygen and chromium isotopic signatures of these meteorites paired with their merrillite and fluorapatite thermochronology together suggest the rapid separation of inner and outer solar system chemical reservoirs within several million years of calcium aluminum-rich inclusion (CAI) formation.

3.2 Introduction

There is now mounting evidence that diverse processes were taking place contemporaneously in the early solar system. Calcium- and aluminum-rich inclusions (CAIs) were formed during a short period at 4567.30 ± 0.16 Myr ago (Connelly et al. 2012). At the same time chondrules had begun to form and continued to form from 4567.32 ± 0.42 to 4564.71 ±0.30 Myr ago (Connelly et al. 2012). During this chondrule formation period, igneous process associated with differentiation had already initiated. Evidence for these early melt environments includes the oldest differentiated meteorite (Steinbach) dated at 4565.47 ± 0.30 Myr old (Connelly et al. 2019), as well as meteorites representing silica-rich basaltic melts: Asuka 881394 at 4564.95 ± 0.53 Myr old (Wimpenny et al. 2019) and NWA 11119 at 4564.8 ± 0.3 Myr old (Srinivasan et al. 2018). This short time interval for planetesimal growth is consistent with the calculated age of the H chondrite parent body which accreted <2 Myr after the formation of CAIs (Pedersen et al. 2019).

This early solar system environment also experienced a segregation of two distinct chemical reservoirs. Isotopic distinctions for these reservoirs are observed in many elements including Cr (e.g., Sanborn et al. 2018; Sanborn et al. in prep.; Warren et al. 2011), Ti (e.g.,Leya et al. 2008; Warren et al. 2011), Mo (e.g., Budde et al. 2016) and Ni (Nanne et al. 2019). The most probable and effective way to separate these two reservoirs was through the rapid formation of Jupiter (Kruijer et al. 2017; Nanne et al. 2019). The results of Kruijer et al. (2017) indicate that Jupiter's core grew to ~20 Earth masses in <1My. With Jupiter in place this separated the solar system's rocky materials into the carbonaceous (outer solar system) materials and non-carbonaceous (inner solar system) materials.

The source of these isotopic differences appears, at least in some cases, to be related to the input of distinct source materials into the two reservoirs. Studies of the carbonaceous chondrite Orgueil show enrichments in ^{54}Cr associated with sub-micrometre Cr-rich grains (likely Cr-spinels). These enrichments are thought to be directly produced in supernovae (Dauphas et al. 2010; Qin et al. 2011). Similarly, the Mo isotopic anomalies

seen in meteorites also require contributions from distinct supernovae processes (Yin et al. 2002). The existence of these reservoirs, alongside geochronological data, provides a powerful tool for reconstructing processes occurring in the early solar system.

Stable isotope studies of some igneous meteorites have linked them to outer solar system carbonaceous chondrite parent bodies (e.g. Sanborn and Yin 2019). These carbonaceous achondrites originate from multiple parent bodies, with one or more parent bodies coming from a CR chondrite-like reservoir. Meteorites from this source region include NWA 6704 and NWA 6693 (Amelin et al. 2019; Hibiya et al. 2019; Warren et al. 2013), NWA 2976 and NWA 011 (Bogdanovski and Lugmair 2004; Sanborn et al. 2013), and NWA 7680 and NWA 6962 (Sanborn et al. 2018; Sanborn et al. in prep.).

This study focuses on the formation environments and ages of the carbonaceous achondrites NWA 7680 and NWA 6962. We present major, minor and trace element compositions of the mineral constituents along with U-Pb ratio phosphate thermochronology and oxygen isotope compositions. These data help place constraints on early melt generation in the outer solar system and the timeline for planet formation.

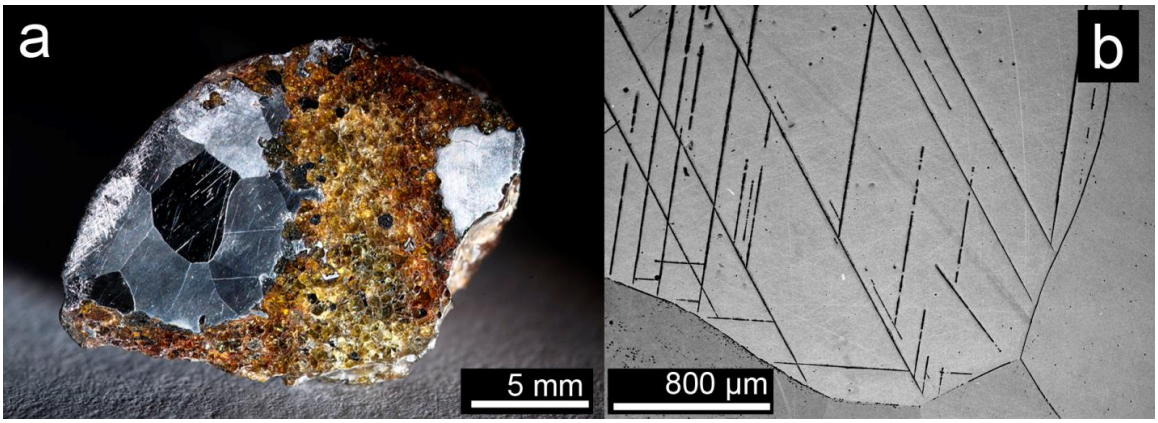

Figure 3.1. a) A polished and etched surface of NWA 7680 revealing polygonal Fe-metal grains and silicate-rich region. b) Backscatter electron image of polygonal metal grains showing Neumann bands.

3.3 Samples and Analytical Methods

3.3.1 Meteorite Samples

The type specimen for NWA 7680 and NWA 6962 were first characterized in 2013 and 2012 respectively (Ruzicka et al. 2015a; Ruzicka et al. 2015b). The samples of NWA 7680 and NWA 6962 used in this study were acquired from the collection of the Royal Ontario Museum (ROM) and are catalogued under the numbers M57074 and M56452 respectively. The entire NWA 7680 meteorite was purchased by David Gregory in Tucson in 2011, as untyped material. The meteorite, in its entirety, was subsequently donated to the ROM. Material from NWA 6962 was subsequently purchased by the ROM for comparative analysis. Two thick sections and one etched slab (Fig. 3.1) of NWA 7680 were used for *in situ* analysis, along with one thick section of NWA 6962. Oxygen isotope analyses used loose grains and bulk powders of NWA 7680.

3.3.2 Backscatter Electron Imaging, Chemical Mapping, Modal Analysis and Cathodoluminescence

Backscatter electron (BSE) imaging, chemical mapping and cathodoluminescence (CL) were carried out using a Hitachi SU6600 Field Emission Scanning Electron Microscope (FE-SEM) at the University of Western Ontario. An Oxford XMax silicon drift detector (80 mm^2) was used for energy dispersive spectrometry (EDS) measurements. Modal analysis used the INCA software package, which utilizes ternary plots to specify phase compositions within element maps. A Gatan Chroma CL detector was used with an accelerating voltage of 10 kV and a working distance of roughly 12.8 mm, which was adjusted for optimal emission/detection. Emissions were binned into 4 channels: red (600–850 nm), green (500–600 nm), blue (400–500 nm), and ultraviolet (300–400 nm) and images were assembled using the Gatan Digital Micrograph software.

3.3.3 Raman Spectroscopy

Raman spectra were acquired using a Horiba LabRAM ARAMIS micro-Raman spectrometer at the Royal Ontario Museum. A 532 nm, 50 mW laser was used, but was filtered to 1.64 mW to prevent sample damage. A 1200 groove/mm grating and 100 µm slit were used during collection. A Si reference material was used for calibration. Two

spectra were collected for 50 s at each point and the results were averaged. The RRUFF Raman database and CrystalSleuth (Lafuente et al. 2016) were used for rapid identification, followed by literature comparisons.

3.3.4 Electron Probe Microanalysis

Electron probe microanalysis (EPMA) using wavelength dispersive spectrometry (WDS) was conducted at Queen's University on a JEOL JXA-8230 equipped with five wavelength dispersive spectrometers. All analyses used a 15 kV accelerating voltage. A beam current of 10 nA was used for merrillite analyses, 20 nA beam was used for silicate, fluorapatite and chromite analyses and 30 nA was used for metal and sulfides. Standards used for microprobe analyses are given in the supplementary material (Appendix 3 - A3.1). A spot size of 7 µm and 14 µm were used for fluorapatite and a Na-rich silicate respectively. Analysis of the Durango apatite standard showed no obvious change in F Kα X-ray count rate over a period of 10 minutes with the set-up used for fluorapatite in these samples. Time dependant analyses were carried out for fluorapatite (F) as well as the Na-rich silicate (Na) using the Probe for EPMA software package to process the data. Chromite Fe(II) to Fe(III) calculations used an iterative procedure in which Fe(III) was calculated by charge balance and then matrix corrections were recalculated. This procedure was repeated until the resulting changes were below the uncertainty levels for measured Fe.

3.3.5 Trace Element and U-Pb Isotope Ratio Analyses

Laser ablation inductively coupled plasma mass spectrometry (LA-ICP-MS) data were collected as a time series using two systems. Trace elements were measured on an Agilent 7500cs (quadrupole) ICP-MS system with a New-Wave UP213 (213 nm) solid-state Nd:YAG laser. Olivine, pyroxene and plagioclase were analyzed with spot sizes of 30-100 µm, a laser repetition rate of 10 Hz and fluence of 3.6-5.0 J cm^{-2}. The ablation cell was flushed with He gas flow of 1 L/min and Ar was introduced before reaching the torch. Analytical runs consisted of 15 s of background and 25 s of ablation. Background and sample intervals were selected using SILLS software (Guillong et al., 2008). Each LA-ICP-MS analysis was normalized to CaO as measured by EPMA. Replicate LA-ICP-

MS analyses of the NIST 612 standard were run after 3-7 sample analyses and yielded a precision of better than ±9.2% (2σ relative standard deviation) for all reported measurements.

Additional trace element characterization and U-Pb isotope ratio analyses were carried out using an Analytic Jena Plasma Quant MS Elite ICP-MS with an ASI RESOlution SE 193 nm excimer laser. Phosphate, plagioclase and pyroxene were analyzed with spot sizes of 25-50 µm, a laser repetition rate of 4 Hz and a fluence of 4-4.5 J cm^{-2} to obtain trace element concentrations. Uranium-lead isotopic ratio measurements on phosphates were carried out with spot sizes of 20-30 µm, a laser repetition rate of 2-4 Hz and fluence of 2.5-4 J cm^{-2}. To correct for instrumental mass bias and within-run drift, analyses were normalized to the 473.5 ± 0.7 Myr old Madagascar fluorapatite (Thomson et al., 2012), which was measured each 2-3 sample analyses. The primary Madagascar analyses were corrected for variable common lead correction using a ^{207}Pb correction (Chew et al. 2014). Durango apatite and McClure apatite were measured as secondary reference materials to monitor accuracy and precision, yielding ages of 31.9 ± 6.8 Myr old and 503 ± 26 Myr old respectively, which are within 2σ of reference values (McDowell et al. 2005; Thomson et al., 2012).

3.3.6 Oxygen Isotope Analyses

Acid-washed bulk powders and cleaned grain separates were used for triple oxygen isotope analysis at the University of Western Ontario. The grains used were predominantly olivine; however, chromite inclusions were common and unavoidable. Embayment of associated plagioclase was also a likely minor constituent in the samples. The laser line and methodology used in this study are similar to that used in Ali et al. (2016) and Ali et al. (2018). The reader is directed to these studies for a more thorough description of methodology; however, a brief description is provided here. The laser line used is equipped with a 25 W 10.6 µm CO_2 laser (Merchantek, Bozeman, MT, USA; Model MIR10-25) and a custom-designed sample holder (Ali et al. 2016; Ali et al. 2018). The laser line was prepared the night before the analytical session. One to two milligrams of dried sample was placed in the sample wells and the sample holder was placed in the reaction chamber. The samples were preheated to 110 °C overnight under vacuum. After

cooling the sample chamber, prefluorination with BrF_5 was carried out for at least 3 h. The laser heating was carried out in a stepwise fashion starting with a defocused wide beam and increasing focus and laser power over time. After each laser reaction, the liberated O_2 gas was separated and purified using cryogenic methods and a KCl trap. Finally, the O_2 gas was adsorbed using 5 Å molecular sieve at liquid nitrogen temperature (-196 °C). To further purify this oxygen from any NF_3 impurities, the molecular sieve trap was heated using an ethanol-liquid N_2 bath to -100 °C and pure oxygen gas released was then collected in a separate tube by readsorption onto 5 Å molecular sieve using liquid nitrogen. This O_2 gas was then analyzed using a Delta V Plus mass spectrometer in dual inlet mode with Isodat3.0 software. External precision (1SE) for an analytical batch was determined by analyzing UWG-2 (Valley et al. 1995). Eight individual runs of UWG-2 analyzed on a single day provided an external precision of ±0.04‰ $\delta^{17}O$ and ±0.08‰ in $\delta^{18}O$.

3.4 Results

3.4.1 Petrography

NWA 7680 is metal-rich (57.3 area %) with a silicate portion composed of roughly mm-scale olivine grains (35.6 %) bordered predominantly by feldspar (6.0 %) (Fig. 3.2). Upon etching, the metallic potion of the meteorite exhibits polygonal crystals with well-defined edges. Linear bands are visible within individual metal crystals and never cross multiple grains (Fig. 3.1). Clinopyroxene (<0.1 %) is present as a minor phase and is often found along grain boundaries associated with sulfide (0.5 %) and a Na-rich silicate (<0.1 %). The Na-rich silicate is a minor component. Raman spectra of the phase are consistent with a nepheline-tridymite-like mineral (Fig. 3.3). The grouping of peaks between 950 and 1050 cm^{-1} seen in both NWA 7680 and NWA 6962 is diagnostic for nepheline suggesting this is the most likely identity; however, the dominant peak at 400-415 cm^{-1} always contains a shoulder similar to the peak splitting seen in tridymite (Fig. 3.3). Chromite (0.5 %) is also found throughout the section along with minor merrillite and fluorapatite (0.1 % phosphate) (Fig. 3.4). NWA 6962 has olivine (70 %) similar in size to NWA 7680; however, in this case the grains are bordered by a mixture of feldspar (19.9 %), clinopyroxene (4.2 %) and merrillite (3.6 % phosphate) (Fig. 3.2 and Fig. 3.4).

The clinopyroxene is more ubiquitous in NWA 6962 and exhibits complex zonation. Chromite (1.7 %), sulfide (0.3 %), metal (0.2 %), minor fluorapatite and a similar Na-rich silicate (Fig 3.2d) are also found in the section.

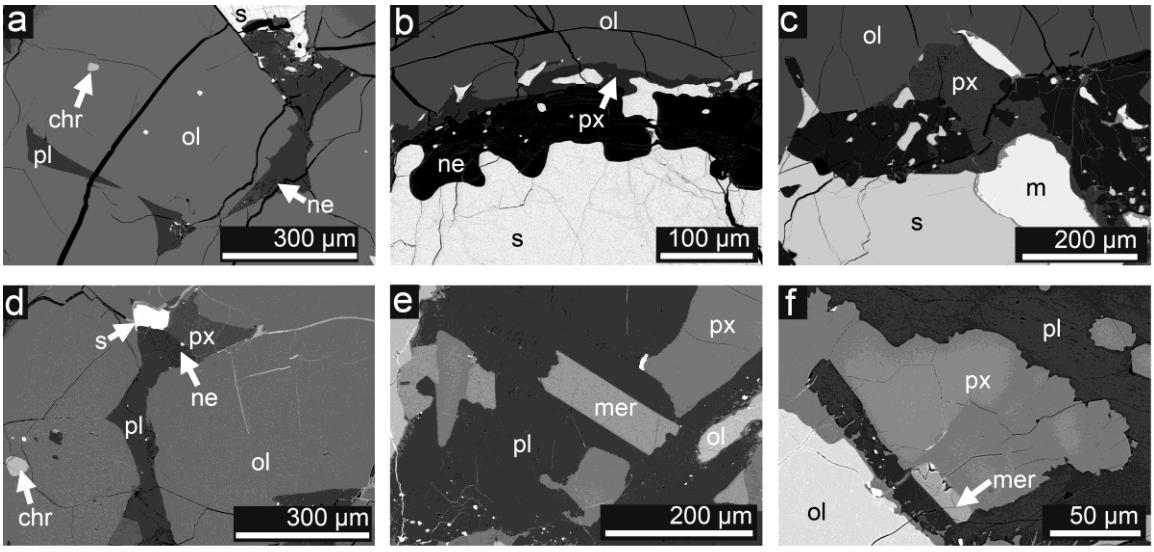

Figure 3.2. a-c) BSE images of common textures and mineral associations seen in the silicate-rich portion of NWA 7680. d-f) Textures and mineral associations from NWA 6962. Mineral short forms are as follows: Olivine (ol), plagioclase (pl), chromite (chr), nepheline (ne), sulfide (s), Fe-metal (m), pyroxene (px), merrillite (mer).

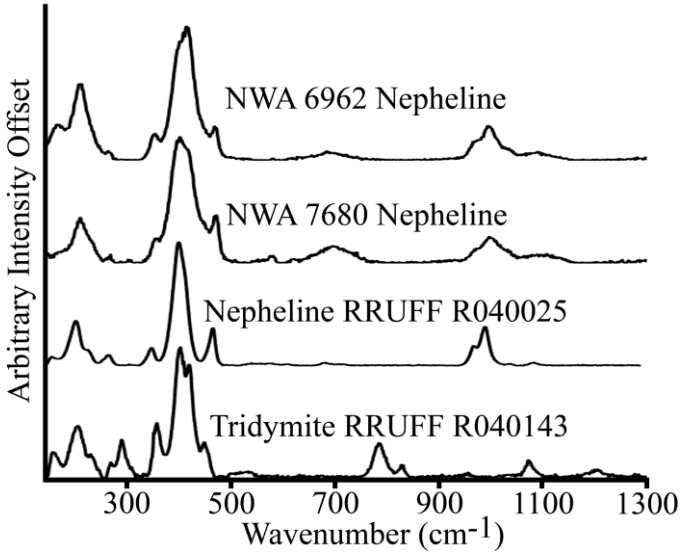

Figure 3.3. Raman spectra of the Na-rich silicate, nepheline (RRUFF) and tridymite (RRUFF).

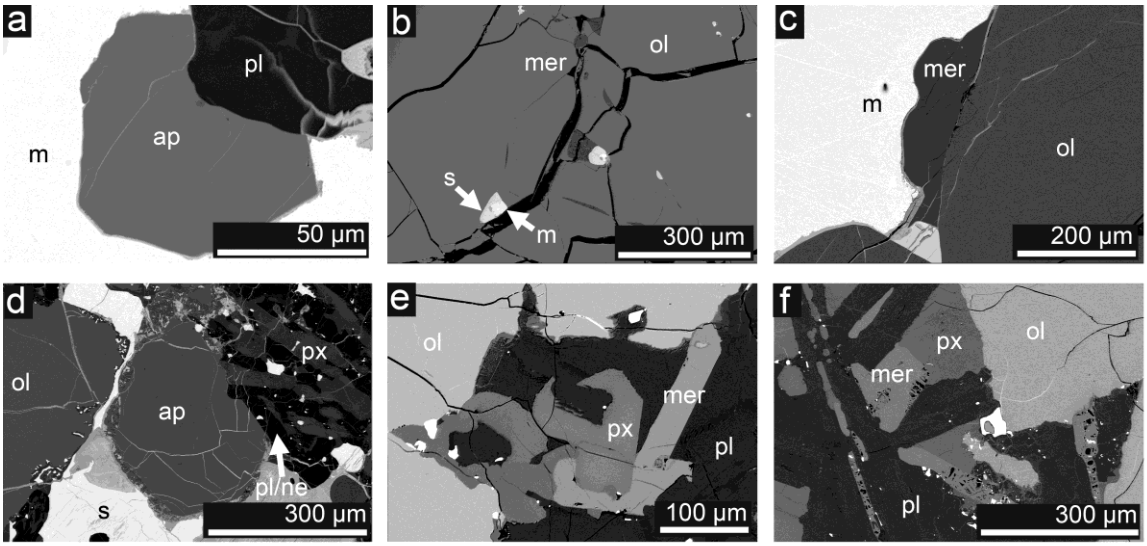

Figure 3.4. a-c) BSE images of phosphate minerals and associations seen in NWA 7680. d-f) Phosphate minerals and associations from NWA 6962. Mineral short forms are as follows: Fluorapatite (ap), merrillite (mer), olivine (ol), plagioclase (pl), nepheline (ne), sulfide (s), Fe-metal (m), pyroxene (px).

3.4.2 Mineral Compositions

All average mineral compositions can be found in Tables 3.1 and 3.2, with the exception of the extremely variable feldspar composition. Individual point compositions for the feldspars are available in supplementary material (Appendix 3 - A3.2). NWA 7680 contains Fe-metal grains multiple millimetres across with a median Ni content of 5.99 wt.%. Small regions with high Ni content are found with concentrations as high as 57.38 wt.%. The olivine is homogeneous ($Fa_{44.8 \pm 0.2}$, Fig. 3.5, Table 3.1) with notable Ca content (Fig. 3.6), while the feldspar shows a variable composition ($An_{2.1\text{-}51.1}Or_{1.0\text{-}83.7}$, Fig. 3.7, Appendix 3 - A3.2). The K-rich feldspar is rare and generally found along grain boundaries. Clinopyroxene is present as a minor phase. Most grains have minimal zonation; however, some have zones of varying composition ($Fs_{11.0\text{-}22.8}Wo_{46.6\text{-}48.6}$, Fig. 3.5). Clinopyroxene is often found along grain boundaries and associated with sulfide and Na-rich silicate. The chemistry of the Na-rich silicate, along with its Raman spectrum, identifies the phase as silica-rich, alkali-deficient nepheline (Dollase and Thomas 1978). Chromite has an average Fe_2O_3 content of 1.66 wt.%. The Ti content is quite variable (Table 3.1). Generally, the centre of large grains has a TiO_2 content of less than 3 wt.%, whereas grain edges and chromite inclusions have higher concentrations, reaching as high as 5.32 wt.%. The Fe-sulfides have pyrrhotite-group compositions and a minor Ni-rich-sulfide is also present. The Cl content in the fluorapatite is below detection limits and element totals suggest that hydroxyl group (OH) is less than 1 wt.%, if it is present. The merrillite has a notable quantity of FeO (average = 1.41 wt.%).

NWA 6962 also contains homogeneous olivine ($Fa_{47.2\pm0.3}$, Fig. 3.5 and Fig. 3.6). However, in this case the grains are mainly associated with a mixture of feldspar ($An_{4.1\text{-}33.9}Or_{0.2\text{-}3.3}$, Fig. 3.7), clinopyroxene ($Fs_{11.9\text{-}23.4}Wo_{42.3\text{-}48.7}$, Fig. 3.5) and merrillite (Table 3.2). Chromite has an average Fe_2O_3 content of 1.76 wt.%. The Ti content is similar to that of NWA 7680 in some respects with large grain centres generally having a TiO_2 content of less than 3 wt.%; however, grain edges and chromite inclusions have even higher concentrations, reaching as high as 11.94 wt.%. Rare anhedral grains of titanian chromite are also observed (TiO_2 = 14.68 – 18.74 wt.%). The sulfides have pyrrhotite-group compositions. Metal in NWA 6962 has a notably lower Ni content (median value

of 1.39 wt.%) than that of NWA 7680. The merrillite is again Fe-rich (FeO average = 1.02 wt.%). In some areas the merrillite has developed a sponge-like texture (Fig. 3.4f) and analyses return low totals. The minor fluorapatite contains measurable Cl (sub wt.%) and appears to be anhydrous. The Na-rich silicate in NWA 6962 is also silica-rich, alkali-deficient nepheline (Fig. 3.3).

Table 3.1. Average (±1σ) mineral compositions (wt.%) for NWA 7680. Italicized values are in element % (not oxide %).

NWA 7680	Olivine	Clinopyroxene	Nepheline	Merrillite	Fluorapatite	Chromite	Metal	Sulfide	
	n=72	*n=42*	*n=17*	*n=26*	*n=10*	*n=35*	*n=246*	*n=52*	
SiO_2	34.96±0.17	53.20±0.59	49.30±1.12	0.11±0.03	0.21±0.06	0.04±0.02	*b.d.*	*b.d.*	*Si*
P_2O_5	-	-	-	45.99±0.45	41.52±0.19	-	*b.d.*	*b.d.*	*P*
Na_2O	b.d.	0.71±0.15	16.17±0.17	2.76±0.09	0.29±0.03	-	-	-	*Na*
MgO	26.48±0.16	13.33±0.99	0.07±0.01	3.04±0.10	0.02±0.01	3.46±0.84	*b.d.*	*b.d.*	*Mg*
Al_2O_3	b.d.	0.91±0.19	30.71±0.59	b.d.	b.d.	12.67±3.29	*b.d.*	*b.d.*	*Al*
K_2O	b.d.	b.d.	2.95±0.45	0.09±0.03	b.d.	-	-	-	*K*
CaO	0.47±0.05	22.67±0.45	0.36±0.07	46.50±0.32	54.05±0.19	-	-	-	*Ca*
TiO_2	b.d.	0.30±0.20	b.d.	-	-	3.09±1.29	*b.d.*	*b.d.*	*Ti*
V_2O_3	b.d.	b.d.	-	-	-	0.74±0.05	*b.d.*	*b.d.*	*V*
Cr_2O_3	0.02±0.03	0.91±0.32	-	-	-	46.27±1.25	*b.d.*	*b.d.*	*Cr*
MnO	0.52±0.02	0.11±0.02	b.d.	0.03±0.02	b.d.	0.39±0.03	*b.d.*	*b.d.*	*Mn*
FeO	38.26±0.24	8.04±1.36	0.39±0.13	1.41±0.27	0.79±0.23	30.94±1.81	*90.22±8.07*	*63.29±0.33*	*Fe*
Fe_2O_3	-	-	-	-	-	1.66±0.41			
CoO	b.d.	b.d.	-	-	-	0.03±0.03	*0.50±0.17*	*b.d.*	*Co*
NiO	b.d.	b.d.	-	-	-	*b.d.*	*8.98±7.92*	*b.d.*	*Ni*
	-	-	-	-	-	-	-	*36.46±0.20*	*S*
	-	-	b.d.	-	3.61±0.10	-	-	-	*F*
	-	-	-	-	b.d.	-	-	-	*Cl*
					-1.52				*O = F*
									O = Cl
Total	100.71	100.18	99.95	99.93	98.97	99.29	99.7	99.75	

Table 3.2. Average (±1σ) mineral compositions (wt.%) for NWA 6962. Italicized values are in element % (not oxide %).

NWA 6962	Olivine	Clinopyroxene	Nepheline	Merrillite	Fluorapatite	Chromite	Metal	Sulfide	
	n=45	*n=75*	*n=26*	*n=22*	*n=22*	*n=37*	*n=17*	*n=29*	
SiO_2	35.04±0.20	52.07±1.05	48.58±1.32	0.13±0.03	0.20±0.09	0.05±0.02	b.d.	*0.02±0.02*	*Si*
P_2O_5	-	-	-	46.40±0.51	41.76±0.28	-	b.d.	b.d.	*P*
Na_2O	b.d.	1.01±1.27	17.16±0.28	2.85±0.05	0.08±0.03	-	-	-	*Na*
MgO	24.69±0.20	12.38±1.29	0.15±0.07	3.16±0.08	0.03±0.01	3.74±0.85	b.d.	*b.d.*	*Mg*
Al_2O_3	b.d.	1.81±2.25	31.16±0.86	b.d.	b.d.	14.38±4.04	b.d.	*b.d.*	*Al*
K_2O	b.d.	b.d.	2.95±0.33	0.04±0.01	b.d.	-	-	-	*K*
CaO	0.43±0.06	21.35±1.67	0.05±0.04	46.77±0.26	55.04±0.34	-	-	-	*Ca*
TiO_2	b.d.	0.84±0.31	b.d.	-	-	3.51±2.59	b.d.	*b.d.*	*Ti*
V_2O_3	b.d.	b.d.	-	-	-	0.70±0.04	b.d.	*b.d.*	*V*
Cr_2O_3	0.02±0.03	0.80±0.26	-	-	-	43.70±1.20	b.d.	*b.d.*	*Cr*
MnO	0.54±0.02	0.19±0.05	b.d.	0.02±0.02	b.d.	0.37±0.04	b.d.	*b.d.*	*Mn*
FeO	39.67±0.28	9.67±2.10	0.51±0.15	1.02±0.18	0.31±0.20	31.27±2.88	98.76±1.70	*63.63±0.27*	*Fe*
Fe_2O_3	-	-	-	-	-	1.78±0.34			
CoO	b.d.	b.d.	-	-	-	*b.d.*	*0.23±0.10*	*b.d.*	*Co*
NiO	b.d.	b.d.	-	-	-	*b.d.*	*2.31±1.72*	*b.d.*	*Ni*
	-	-		-	-	-	-	*36.56±0.17*	*S*
	-	-	*b.d.*	-	3.99±0.28	-	-	-	*F*
	-	-	-	-	0.40±0.20	-	-	-	*Cl*
					-1.68				*O = F*
					-0.09				*O = Cl*
Total	100.39	100.12	100.56	100.39	100.04	99.5	101.3	100.21	

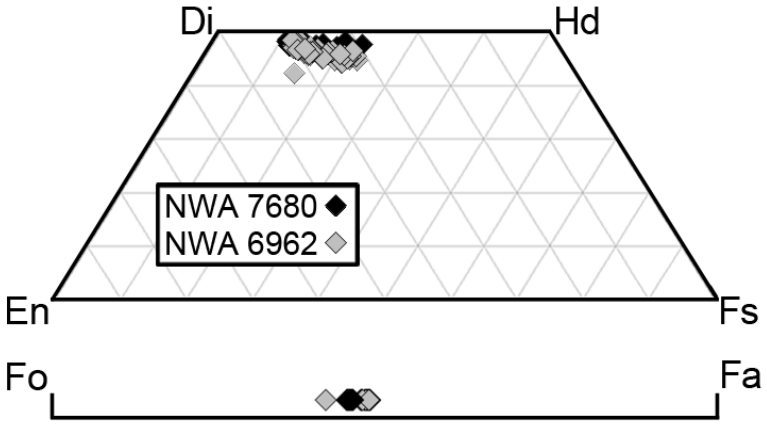

Figure 3.5. Clinopyroxene (top) and olivine (bottom) major element compositions for NWA 7680 and NWA 6962. Mineral short forms are as follows: Diopside (Di), hedenbergite (Hd), enstatite (En), ferrosilite (Fs), forsterite (Fo), fayalite (Fa).

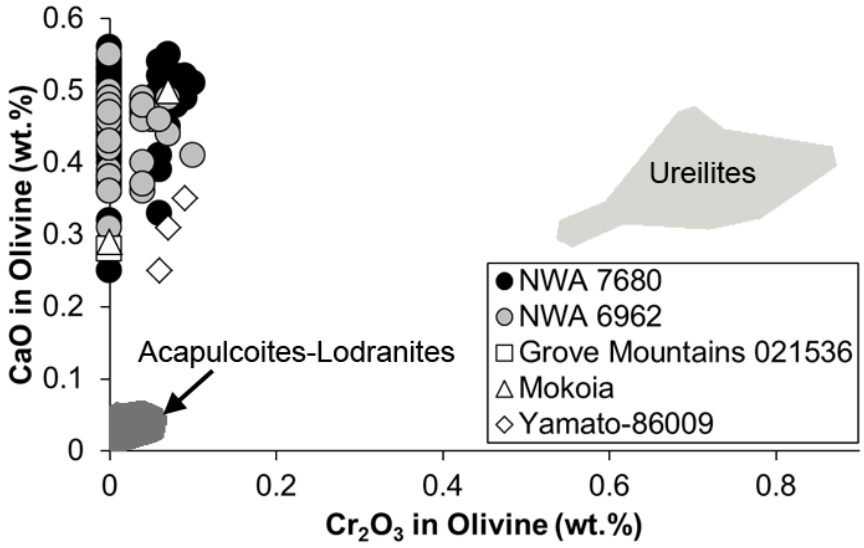

Figure 3.6. CaO and Cr_2O_3 content of olivine in NWA 7680 and NWA 6962 for comparison with acapulcoites-lodranites and ureilites (Goodrich and Righter 2000 and references therein), a Grove Mountains 021536 clast (Zhang et al. 2010) and clasts in Mokoia and Yamato-86009 (Jogo et al. 2013).

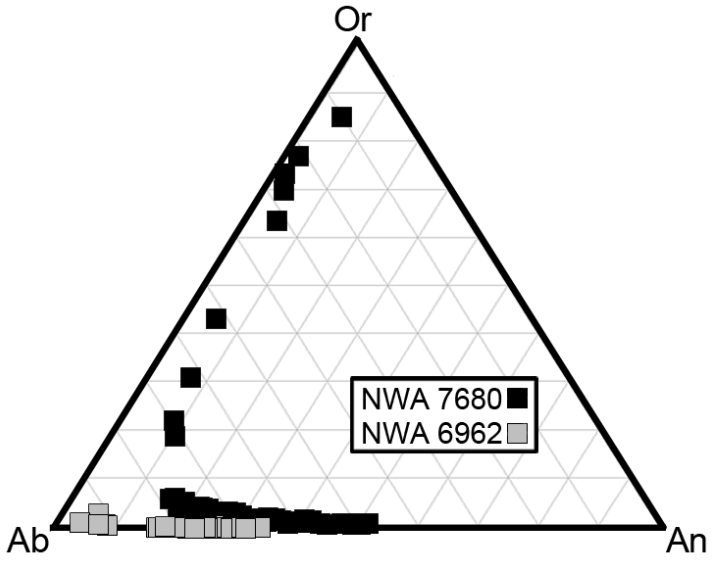

Figure 3.7. Feldspar major element compositions for NWA 7680 and NWA 6962.

3.4.3 Rare Earth Element Compositions

Trace element compositions were measured for phosphates, plagioclase, olivine and pyroxene in both NWA 7680 and NWA 6962 (Fig. 3.8, Appendix 3 - A3.3). The phosphates have a trend that slopes downward toward heavy rare earth element (HREE) masses (Fig. 3.8a). The phosphates also have a negative Eu anomaly. Both merrillite and fluorapatite have similar rare earth element (REE) patterns for both samples; however, merrillite generally has higher REE concentrations than fluorapatite. Plagioclase also appears to have a trend that slopes downward towards HREE (Fig. 3.8a); however, some elements were below detection limits for the examined grains. The plagioclase in both samples has a positive Eu anomaly. Olivine in both NWA 7680 (Fig. 3.8b) and NWA 6962 (Fig. 3.8c) have a slope that increases to HREE. Pyroxene in NWA 7680 (Fig. 3.8b) has a relatively flat REE pattern, while most NWA 6962 grains have REE profiles that slope upward towards HREE and have negative Eu anomalies (Fig. 3.8c).

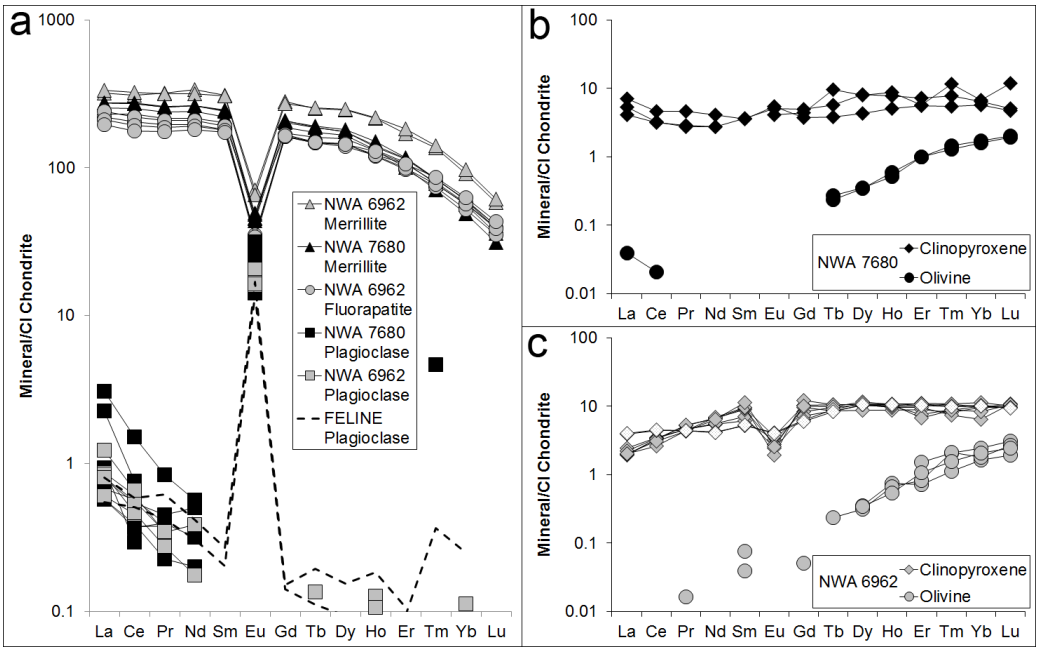

Figure 3.8. Rare earth element compositions for a) Phosphates and plagioclase, b) NWA 7680 pyroxene and olivine, and c) NWA 6962 pyroxene and olivine. Note in c) the patterns that are not uniform grey are pyroxene grains formed as replacement of olivine (See Figure 3.2d). CI chondrite normalization values from McDonough and Sun (1995).

3.4.4 Oxygen Isotope Characteristics

Oxygen isotope data for NWA 7680 were acquired (Fig. 3.9). Olivine grain separates (minor chromite and plagioclase) gave average values of $\delta^{17}O = 2.39$; $\delta^{18}O = 6.58$; $\Delta^{17}O = -1.04‰$. and acid-washed bulk powders gave average values of $\delta^{17}O = 3.07$; $\delta^{18}O = 7.80$; $\Delta^{17}O = -1.00‰$.

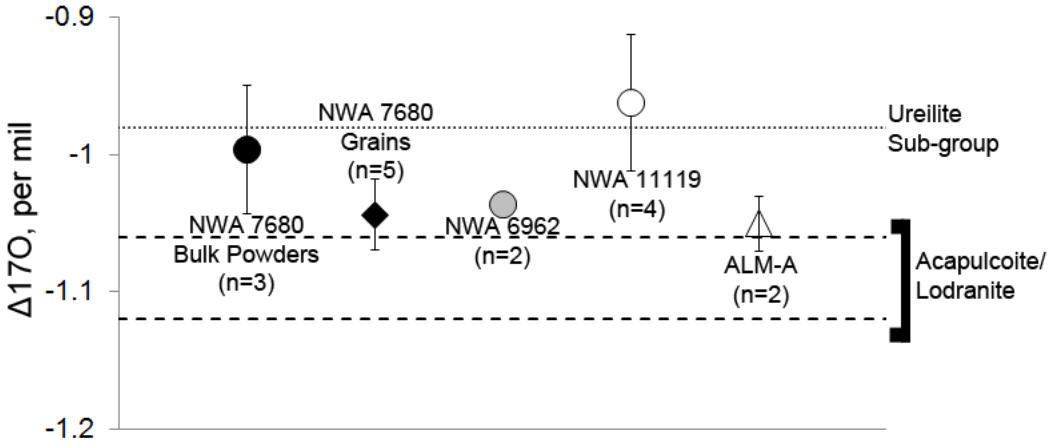

Figure 3.9. Average oxygen isotope values for NWA 7680 bulk powders and grains. Compositions for NWA 6962 (Irving et al. 2013), NWA 11119 (Srinivasan et al. 2018), ALMA-A (Bischoff et al. 2014), ureilites (Rumble et al. 2010) and acapulcoites/lodranites (Greenwood et al. 2012) are shown for comparison. Error bars represent 2 SE and *n* denotes the number of analyses.

3.4.5 U-Pb and ^{207}Pb-^{206}Pb ages

Measurements of U-Pb ratios were taken from eleven spots in NWA 7680. Ten of the spots were from merrillite grains (four different grains) and one spot was from fluorapatite. Seven spots were measured in NWA 6962. Four of the spots were merrillite grains (4 different grains) and three spots were from fluorapatite (1 grain). The data (Table 3.3) have been plotted on Tera-Wasserburg plots for examination (Fig. 3.10). One spot from NWA 7680 produced a $^{207}Pb/^{206}Pb$ age and uncertainty that place it as chronologically older than CAIs (Connelly et al. 2012). Texturally there is no reason to suggest the grain is presolar. With this point removed, the weighted mean $^{207}Pb/^{206}Pb$ age for NWA 7680 is 4578 ± 17 Myr old (2σ). All of the data from NWA 6962 are

concordant or near concordant and the resulting weighted mean $^{207}Pb/^{206}Pb$ age is 4556.6 ± 8.2 Myr old (2σ).

Table 3.3. *In situ* spot analyses of U-Pb from phosphates in NWA 7680 and 6962.

NWA 7680	$^{238}U/^{206}Pb$	2σ	$^{207}Pb/^{206}Pb$	2σ
Section 3 Merrillite 1a	0.896	0.047	0.614	0.022
Section 3 Merrillite 1b	0.914	0.048	0.651	0.025
Section 3 Merrillite 1c	0.937	0.050	0.630	0.023
Section 3 Merrillite 1d	0.907	0.047	0.636	0.024
Section 3 Merrillite 1e	0.922	0.047	0.624	0.021
Section 3 Merrillite 1f	0.931	0.053	0.620	0.022
Section 3 Merrillite 2	0.888	0.049	0.648	0.025
Section 3 Merrillite 3	0.933	0.056	0.661	0.030
Section 3 Merrillite 3b	0.815	0.055	0.630	0.032
Section 1 Merrillite 8	1.096	0.038	0.625	0.016
Section 1 Fluorapatite 3	0.862	0.097	0.645	0.071
Merrillite average (n=5) U(ppm) = 0.40±0.11, Th(ppm) = 5.14±0.71				
NWA 6962	$^{238}U/^{206}Pb$	2σ	$^{207}Pb/^{206}Pb$	2σ
Merrillite 3	0.974	0.037	0.627	0.012
Merrillite 5	0.924	0.036	0.623	0.012
Merrillite 6	0.957	0.036	0.627	0.012
Merrillite 23	0.953	0.036	0.619	0.010
Fluorapatite 1	1.001	0.034	0.619	0.009
Fluorapatite 1b	1.009	0.034	0.620	0.007
Fluorapatite 1c	0.984	0.034	0.617	0.008
Merrillite average (n=2) U(ppm) = 1.84±0.24, Th(ppm) = 9.59±1.76, Fluorapatite (n=4) U(ppm) = 4.35±1.03, Th(ppm)=8.96±0.80				

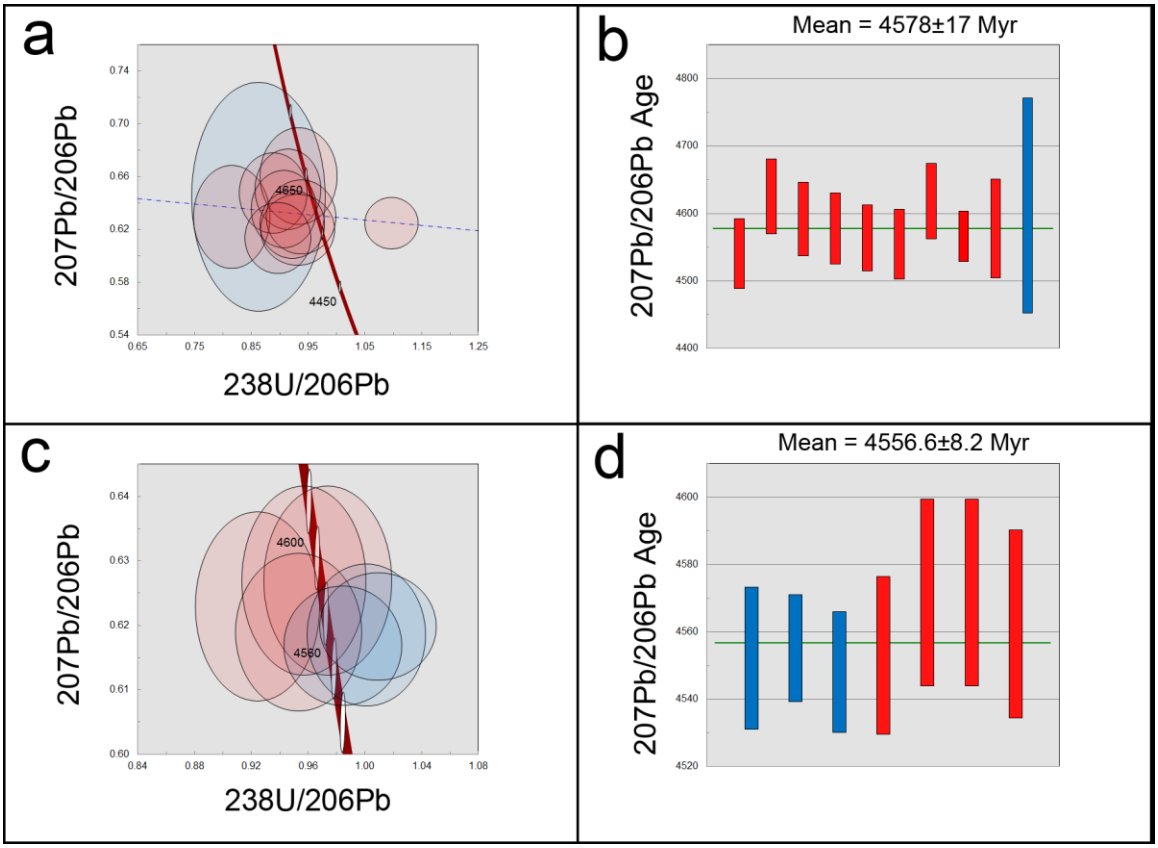

Figure 3.10. Tera-Wasserburg plots of phosphate data from a) NWA 7680 and c) NWA 6962. Corresponding data used for weighted mean ^{207}Pb-^{206}Pb age shown in b) NWA 7680 and d) NWA 6962. Red data is from merrillite and blue data is from fluorapatite. All uncertainties are 2σ.

3.5 Discussion

3.5.1 Parent Body

The mineralogical and geochemical similarities suggest that NWA 7680 and NWA 6962 are from the same parent body. Major and minor element composition in NWA 7680 and NWA 6962 olivine and pyroxene (Fig. 3.5 and Fig. 3.6) along with oxygen isotope compositions (Fig. 3.9) suggest no direct relationship with established achondrite groups. Oxygen isotope values are similar to that of ureilites and acapulcoites/lodranites (Fig. 3.9); however, NWA 7680 and NWA 6962 are more FeO-rich than either of these groups. Minor element compositions in olivine (Fig. 3.6) also do not suggest a direct relation to either the ureilites or acapulcoites/lodranites. Instead, the minor element

compositions overlap with clasts from CM (Zhang et al. 2010) and CV (Jogo et al. 2013) chondrites. These clasts are olivine-rich, most contain plagioclase and pyroxene and some contain nepheline and/or merrillite as well as chromite, Fe-Ni-metal and sulfides including pyrrhotite and pentlandite (Jogo et al. 2013; Zhang et al. 2010). However, the olivine grains in these clasts are smaller and have lower FeO content (Fa_{34-39}) than those in NWA 7680 and NWA 6962. All of these clasts have oxygen isotope compositions that place them near the carbonaceous chondrite anhydrous mineral (CCAM) line. These clasts may have originated from the interior of the CV parent body (Jogo et al. 2013; Zhang et al. 2010). Another potentially related material is the feldspar-nepheline (FELINE) clast found in the Parnallee LL 3.6 chondrite (Bridges et al. 1995). This clast is nepheline-rich (12 modal %) and has an oxygen isotope composition that also falls near the CCAM line (Bridges et al. 1995). The REE compositions from the FELINE feldspar match that from NWA 7680 and NWA 6962 (Fig. 3.8).

The clinopyroxene REE compositions of NWA 7680 and NWA 6962 are dependent on their formation mechanism. Pyroxene that nucleates along grain olivine boundaries or replaces olivine (Fig. 3.2d) have flatter more primitive REE patterns. The pyroxene grains in NWA 7680 are all formed in this manner (Fig. 3.8b). One pyroxene region measured in NWA 6962 exhibited the same flat pattern; however, the majority of grains in NWA 6962 formed in association with plagioclase, in a later stage melt (Fig. 3.8c). The pyroxene patterns for NWA 6962 are somewhat similar to those of acapulcoites-lodranites; however, the NWA 6962 grains exhibit smaller Eu anomalies (Fig. 3.8c; Floss 2000; Guan and Crozaz 2000, 2001). The NWA 6962 compositions actually overlap with compositions from augite in carbonaceous chondrites (e.g. Jacquet et al. 2012). These compositions suggest a primitive parent body for NWA 7680 and NWA 6962. Concentrations of REE are above those expected for ureilite clinopyroxene and olivine (Fig. 3.8b and Fig. 3.8c, Guan and Crozaz 2000, 2001).

These observations along with Cr isotopic compositions have confirmed a carbonaceous (outer solar system) origin for NWA 7680 and NWA 6962 and suggest a CR-type chondrite-like reservoir (Sanborn et al. 2018; Sanborn et al. in prep.). Using a modal recombination to mimic bulk compositions, it is apparent that, geochemically, both rocks

can be formed through fractionation processes on a CR chondrite-like parent body (Fig. 3.11). Other carbonaceous achondrites have more complex histories (Fig. 3.11 and Hibiya et al. 2019). This simple fractionation trend and the identification of similar clasts in carbonaceous chondrites suggest that melts similar to NWA 7680 and NWA 6962 may be common amongst carbonaceous chondrite parent bodies.

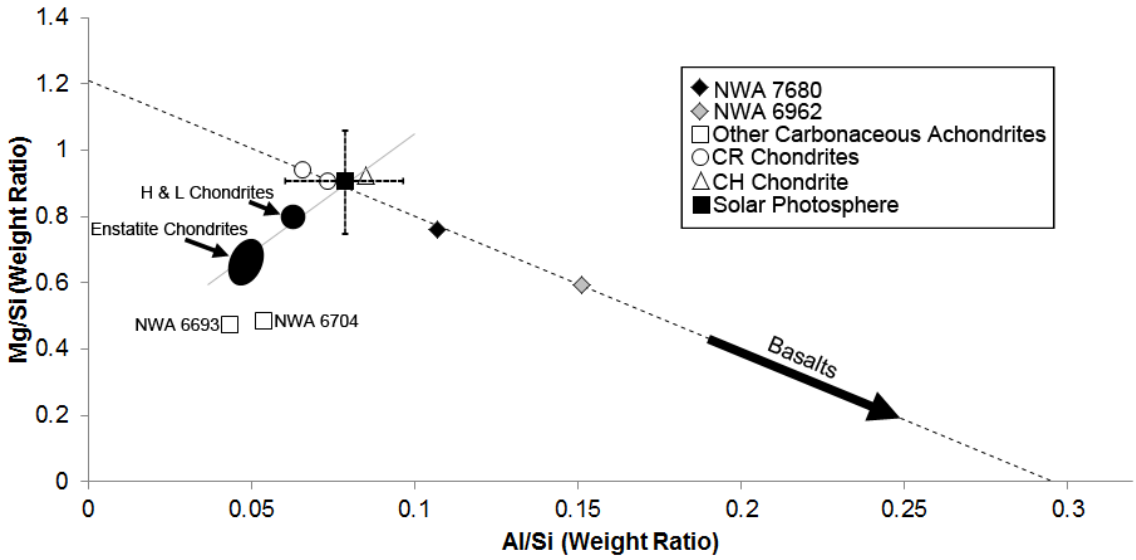

Figure 3.11. Plot of modal recombination compositions for NWA 7680 and NWA 6962. A trend line is drawn through CR chondrite data, NWA 7680 and NWA 6962. An arrow indicates the direction where fractionation would lead to a roughly basaltic melt composition. CH chondrite and CR chondrite data taken from Ivanova and Petaev (2015) and Weisberg et al. (1993) and references therein. The cosmochemical trend line is modified from Jagoutz et al. (1979) and Righter et al. (2006).

3.5.2 Formation Environment

As mentioned, both NWA 7680 and NWA 6862 can be formed through fractionation processes on a CR chondrite-like parent body (Fig. 3.11). Both meteorites are plagioclase-rich, suggesting a feldspathic melt pooled in their formation area. NWA 7680 is also Fe-metal-rich, suggesting Fe-rich melts were also being produced on the parent body. In a larger terrestrial body, feldspathic and Fe-rich melts would separate through gravity-driven differentiation. It is clear that such processes were short-lived on the NWA

7680 and NWA 6962 parent body, resulting in the pooling of melt products. Following an initial crystallization, a secondary melt intruded the region. The Na-Ca-Al-P-rich melt had the most extensive effect on NWA 6962, in which the secondary melt re-melted and mixed with primary plagioclase (Fig. 3.2d-f). The secondary melt was less invasive in NWA 7680, often appearing along grain boundaries and leaving some of the primary plagioclase crystals intact (Fig. 3.12). This secondary melt injection actually removed and redistributed primary grains (Fig 3.12a inset). A modal recombination was carried out to emulate a whole rock REE pattern and the produced REE plots reflect the meteorites' formation environments (Fig. 3.13). NWA 7680 is largely sub-chondritic, due to its high Fe-metal content. It also has a positive Eu anomaly as a result of its super-chondritic plagioclase content. NWA 6962 has a pattern that reflects the abundant phosphate in the sample.

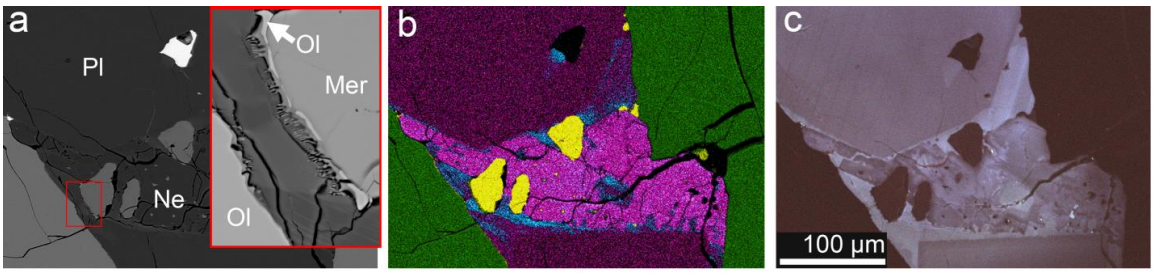

Figure 3.12. a) BSE image of NWA 7680 showing secondary melt intrusion between two large plagioclase crystals and two large olivine crystals. Inset image shows close-up of merrillite grain that has been broken off of surrounding olivine during the melt intrusion. b) Chemical map of the same region highlighting Mg (green), Na (purple), P (yellow) and K (blue). c) RGB-UV CL image showing primary structure in the large plagioclase grains, new growth along edges and mottled melt intrusion.

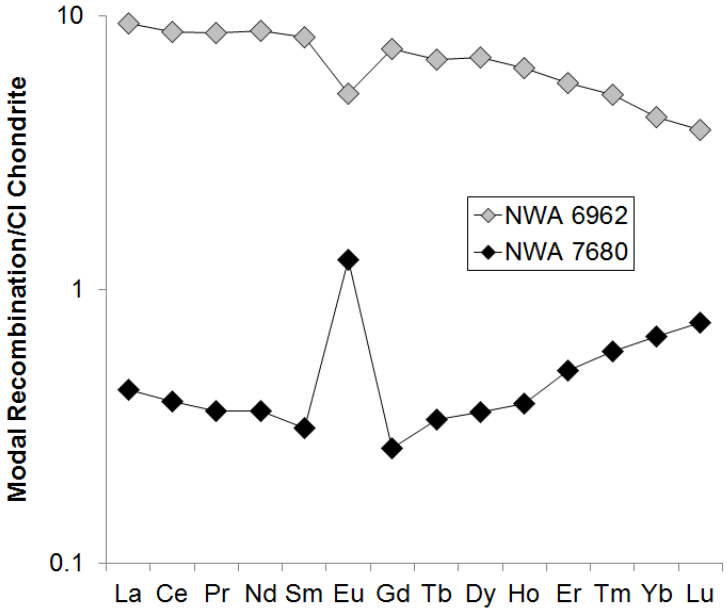

Figure 3.13. Rare earth element patterns calculated from modal recombinations of constituent minerals (whole rock equivalent). CI chondrite normalization values are taken from McDonough and Sun (1995).

3.5.3 Nepheline, Zirconium-Phases and the Secondary Melt Intrusion

Both NWA 7680 and NWA 6962 contain silica-rich, alkali-deficient nepheline. Raman analysis (Fig. 3.3) shows similarities between nepheline and tridymite. This is consistent with the similarities in structure with nepheline simply being "stuffed tridymite" (Buerger 1954). The chemistry of the phase confirms that it is silica-rich, alkali-deficient nepheline similar, in chemistry, to terrestrial examples (e.g., Dollase and Thomas 1978). Nepheline has been observed in a number of carbonaceous chondrites and is thought to form through aqueous activity and metasomatic processes (e.g., Matsumoto et al. 2014; Matsumoto et al. 2017; Tomeoka and Itoh 2004). However, CR2 carbonaceous chondrite CAIs are devoid of nepheline (Makide et al. 2009) suggesting they did not experience the metasomatic processes experienced by CAIs in CV chondrites (Krot et al. 1998). Carbonaceous chondrite nepheline is similar in composition to that of NWA 7680 and NWA 6962; however, the Si-enrichment in the carbonaceous achondrites generally exceeds that of reported chondritic nepheline. Micrometre-scale zirconium-phases are

also found in the sections, usually associated with the secondary melt intrusion. The most common phase is baddeleyite, but zirconolite is also seen.

3.5.4 Iron-Metal

Etching of the largest metal-rich area in a slab of NWA 7680 revealed polygonal domains, each a few millimetres across (Fig. 3.1). Neumann bands were observed within the polygonal domains (Fig. 3.1). These bands form during high pressure events, such as impacts, but temperatures must remain below 600 °C and probably below 300 °C (Uhlig 1955) for them to remain intact. Metal from the polygonal domains as well as some of the metal associated with silicates have Co/Ni values similar to, but slightly removed from, that of primitive CI chondrite ratio (Fig. 3.14). Metal from NWA 6962 has a similar Co/Ni value. Nickel-rich blebs found within the polygonal domains of NWA 7680 have low Co concentrations relative to primitive values. Some of the metal associated with silicates in NWA 7680 also exhibit non-primitive Co/Ni values; both high Co and low Co compositions are observed.

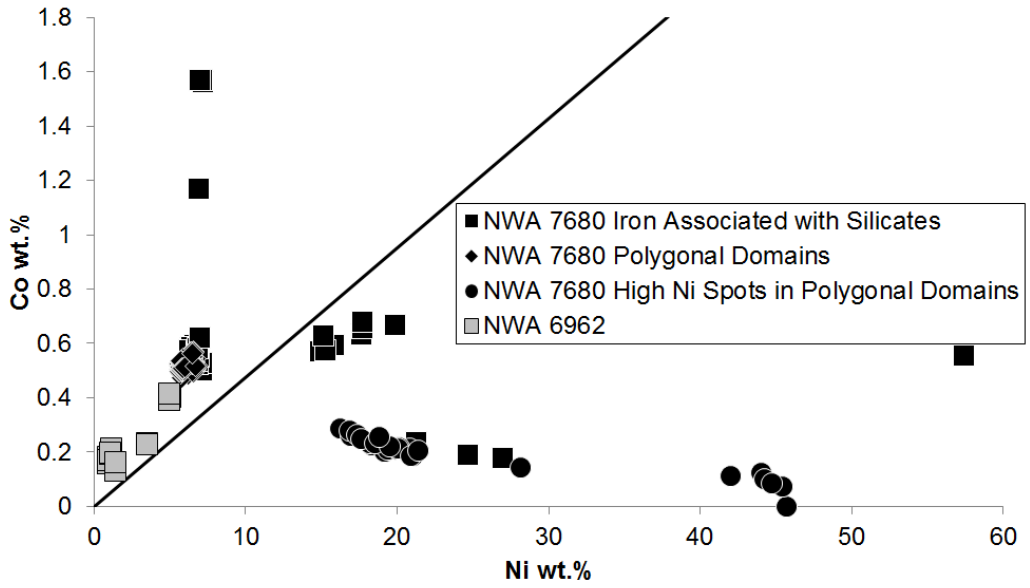

Figure 3.14. Co and Ni concentrations for metal components in NWA 7680 and NWA 6962. The solid line represents the primitive solar ratio (e.g., Davidson et al. 2014).

The metal Co/Ni composition of CR chondrites is generally primitive, although some scatter is evident (Connolly et al. 2001; Jacquet et al. 2013; Krot et al. 2002). This primitive composition is the result of limited or no thermal metamorphism being experienced by the majority of these meteorites. Limited short-term thermal metamorphism is evident in two studied CR chondrites (Briani et al. 2013), but these appear to be outliers.

Since NWA 6962 experienced the largest degree of melting from the secondary melt injection, it is possible that its Fe-metal composition reflects a melting and re-homogenization of the local primitive Fe-metal sources to produce a primitive signature. This is probably also largely true for the polygonal metal domain in NWA 7680. The nickel-rich blebs in the polygonal domain as well as some of the other Fe-metal grains in NWA 7680 deviate from the primitive CI chondrite ratio due to thermal metamorphism. Low levels of thermal metamorphism in ordinary, CO and CV chondrites (Kimura et al. 2008; Davidson et al. 2014) result in non-primitive Co/Ni values very similar to the trends seen in (Fig. 3.14).

Phosphates in some chondrites are associated with metal, suggesting P-rich metal was the initial source of phosphorous (e.g., Perron et al. 1992; Ward et al. 2017). This is consistent with numerous phosphate grains being associated with metal in NWA 7680 (Fig. 3.4a and Fig. 3.4c) and in some cases in NWA 6962. However, the merrillite in NWA 6962 appears to be from a more evolved melt.

3.5.5 Timing, Phosphate Closure Temperature and Constraining Disk Reservoir Separation

The U-Pb closure temperature for apatite is 350 – 550 °C depending on grain size and cooling rate (Cherniak et al. 1991; Harrison et al. 2002). Apatite and merrillite from NWA 6962 have identical formation ages (within uncertainty), suggesting they have experienced similar thermal pathways since formation. Some of the merrillite in NWA 6962 has a sponge-like texture (Fig. 3.4f) possible due to terrestrial weathering and these grains were not used for U-Pb ratio isotopic analyses. Oxygen isotope compositions for NWA 7680 and NWA 6962 overlap those of the acapulcoites and lodranites (Fig. 3.9 and

Greenwood et al. 2012) and fall within the field of ureilite compositions. Past research has suggested that there are subsets within the ureilites based on oxygen isotope compositions, with the largest subset having a $\Delta^{17}O$ of -0.98‰ (Ash et al. 2000; Franchi 2008; Rumble et al. 2010). The ureilite field has since been shown to be a continuum (e.g., Greenwood et al. 2017). However, the large number of ureilites at -0.98‰ $\Delta^{17}O$ could be the result of one of the source materials that have come together to form the ureilite parent body.

Additionally, meteorites such as NWA 11119 (Srinivasan et al. 2018) and ALM-A (Almahata Sitta) (Bischoff et al. 2014) also fall in the same region of oxygen isotope space (Fig. 3.9). Sanborn et al. (2018), Sanborn et al. (in prep.) and references therein have shown that these meteorites originate from the inner solar system, whereas NWA 7680 and NWA 6962 originate from the outer solar system. One possible explanation for this is the spreading of a single large oxygen isotope reservoir. Following this, Jupiter must have been in place prior to the establishment of the observed Cr-isotope trend (Sanborn et al. 2018; Sanborn et al. in prep.). Additionally, the Cr isotope trend must have been established before the formation of NWA 7680 and NWA 6962. Since NWA 7680 and NWA 6962 have not been heated above 350–550 °C since crystallizing, it is certain that the observed Cr isotope compositions were not introduced by a later high temperature event. With this sequence of events in mind and the thermochronology data from our current study, we suggest that: 1. The spreading of the ~ -1‰ $\Delta^{17}O$ oxygen isotope reservoir and 2. Disk reservoir separation and likely the establishment of Jupiter must have occurred prior to the phosphate date measured in NWA 7680. This requires that Jupiter be in place within several million years of CAI formation. This is consistent with past work suggesting a very quick Jupiter formation. Kruijer et al. (2017) recently used Mo and W isotope measurements of iron meteorites to observe that the meteorites derive from two distinct reservoirs. They suggest that the separation of these reservoirs was the result of Jupiter's formation, reaching ∼20 Earth masses in less than 1 million years.

3.6 Conclusions

Early solar system melt environments have been preserved in NWA 7680 and NWA 6962. The meteorites have mineralogical and geochemical similarities that confirm they are from the same parent body. The meteorites have plagioclase contents above that of chondritic meteorites and NWA 7680 is also Fe-metal-rich suggesting they both formed through short-lived differentiation processes that resulted in the pooling of melt products. The meteorites were formed through fractionation processes on a CR chondrite-like parent body. Evidence of a secondary Na-Ca-Al-P-rich melt intrusion is observed in both meteorites. The secondary melt products include silica-rich, alkali-deficient nepheline. *In situ* dating of merrillite and fluorapatite reveals that NWA 7680 has remained cool (below 350-550 °C) for 4578 ± 17 Myr. Phosphates in NWA 6962 also formed early (4556.6 ± 8.2 Myr ago) and remained cool. The oxygen and chromium isotopic compositions of these meteorites along with thermochronology data places constraints on reservoir separation in the early solar system, which has to have occurred within several million years of CAI formation.

3.7 References

Ali A., Jabeen I., Gregory D., Verish R. and Banerjee N. R. 2016. New triple oxygen isotope data of bulk and separated fractions from SNC meteorites: Evidence for mantle homogeneity of Mars. *Meteoritics & Planetary Science* 51(5):981-995.

Ali A., Jabeen I., Banerjee N. R., Osinski G. R., Nicklin I., Gregory D. and Herrmann P. 2018. The oxygen isotope compositions of olivine in main group (MG) pallasites: New measurements by adopting an improved laser fluorination approach. *Meteoritics & Planetary Science* 53(6):1223-1237.

Amelin Y., Koefoed P., Iizuka T., Fernandes V. A., Huyskens M. H., Yin Q. Z. and Irving A. J. 2019. U-Pb, Rb-Sr and Ar-Ar systematics of the ungrouped achondrites Northwest Africa 6704 and Northwest Africa 6693. *Geochimica et Cosmochimica Acta* 245:628-642.

Ash R. D., MacPherson G. J. and Rumble III D. 2000. Oxygen isotopes, ureilite genesis, and the geology of asteroids (abstract #5288). 63rd Annual Meeting of the Meteoritical Society.

Bischoff A., Horstmann M., Barrat J. A., Chaussidon M., Pack A., Herwartz D., Ward D., Vollmer C. and Decker S. 2014. Trachyandesitic volcanism in the early solar system. *Proceedings of the National Academy of Sciences* 111(35):12689-12692.

Bogdanovski O. and Lugmair G. W. 2004. Manganese-chromium isotope systematics of basaltic achondrite Northwest Africa 011 (abstract #1715). 35th Lunar and Planetary Science Conference.

Bridges J. C., Hutchison R., Franchi I. A., Alexander C. M. and Pillinger C. T. 1995. A feldspar-nepheline achondrite clast in Parnalle. *Antarctic Meteorite Research* 8:195-203.

Budde G., Burkhardt C., Brennecka G. A., Fischer-Gödde M., Kruijer T. S. and Kleine T. 2016. Molybdenum isotopic evidence for the origin of chondrules and a distinct genetic heritage of carbonaceous and non-carbonaceous meteorites. *Earth and Planetary Science Letters* 454:293-303.

Buerger M. J. 1954. The stuffed derivatives of the silica structures. *American Mineralogist* 39(7-8):600-614.

Cherniak D. J., Lanford W. A. and Ryerson F. J. 1991. Lead diffusion in apatite and zircon using ion implantation and Rutherford Backscattering techniques. *Geochimica et Cosmochimica Acta* 55(6):1663-1673.

Chew D. M., Petrus J. A. and Kamber B. S. 2014. U–Pb LA–ICPMS dating using accessory mineral standards with variable common Pb. *Chemical Geology* 363:185-199.

Connelly J. N., Bizzarro M., Krot A. N., Nordlund Å., Wielandt D. and Ivanova M. A. 2012. The absolute chronology and thermal processing of solids in the solar protoplanetary disk. *Science* 338:651-655.

Connelly J. N., Schiller M. and Bizzarro M. 2019. Pb isotope evidence for rapid accretion and differentiation of planetary embryos. *Earth and Planetary Science Letters* 525:115722, doi.org/10.1016/j.epsl.2019.115722

Connolly Jr H. C., Huss G. R., and Wasserburg G. J. 2001. On the formation of Fe-Ni metal in Renazzo-like carbonaceous chondrites. *Geochimica et Cosmochimica Acta* 65(24):4567-4588.

Dauphas N., Remusat L., Chen J. H., Roskosz M., Papanastassiou D. A., Stodolna J., Guan Y., Ma C. and Eiler J. M. 2010. Neutron-rich chromium isotope anomalies in supernova nanoparticles. *The Astrophysical Journal*, 720:1577-1591.

Davidson J., Schrader D. L., Alexander C. M. O. D., Lauretta D. S., Busemann H., Franchi I. A., Greenwood R. C., Connolly Jr H. C., Domanik K. J. and Verchovsky A. 2014. Petrography, stable isotope compositions, microRaman spectroscopy, and presolar components of Roberts Massif 04133: A reduced CV 3 carbonaceous chondrite. *Meteoritics & Planetary Science* 49(12):2133-2151.

Dollase W. A. and Thomas W. M. 1978. The crystal chemistry of silica-rich, alkali-deficient nepheline. *Contributions to Mineralogy and Petrology* 66(3):311-318.

Floss C. 2000. Complexities on the acapulcoite-lodranite parent body: Evidence from trace element distributions in silicate minerals. *Meteoritics & Planetary Science* 35(5):1073-1085.

Franchi I. A. 2008. Oxygen isotopes in asteroidal materials. *Reviews in Mineralogy and Geochemistry*, *68*(1), edited by MacPherson G. J., Mittlefehldt D. W., Jones J. H. and Simon S. B. Virginia: Mineralogical Society of America. pp.345-397.

Goodrich C. A. and Righter K. 2000. Petrology of unique achondrite Queen Alexandra Range 93148: A piece of the pallasite (howardite-eucrite-diogenite?) parent body? *Meteoritics & Planetary Science* 35(3):521-535.

Greenwood R. C., Franchi I. A., Gibson J. M. and Benedix G. K. 2012. Oxygen isotope variation in primitive achondrites: The influence of primordial, asteroidal and terrestrial processes. *Geochimica et Cosmochimica Acta* 94:146-163.

Greenwood R. C., Burbine T. H., Miller M. F. and Franchi I. A. 2017. Melting and differentiation of early-formed asteroids: The perspective from high precision oxygen isotope studies. *Chemie der Erde* **77**(1):1-43.

Grossman J. N. and Brearley A. J. 2005. The onset of metamorphism in ordinary and carbonaceous chondrites. *Meteoritics & Planetary Science* 40(1):87-122.

Guan Y. and Crozaz G. 2000. Light rare earth element enrichments in ureilites: a detailed ion microprobe study. *Meteoritics & Planetary Science* 35(1):131-144.

Guan Y. and Crozaz G. 2001. Microdistributions and petrogenetic implications of rare earth elements in polymict ureilites. *Meteoritics & Planetary Science* 36(8):1039-1056.

Guillong M., Meier D. L., Allan M. M., Heinrich C. A. and Yardley B. W. 2008. Appendix A6: SILLS: A MATLAB-based program for the reduction of laser ablation ICP-MS data of homogeneous materials and inclusions. *Mineralogical Association of Canada Short Course, 40*, edited by Sylvester, P. Vancouver: Mineralogical Association of Canada. pp.328-333.

Harrison T. M., Catlos E. J. and Montel J. M. 2002. U-Th-Pb dating of phosphate minerals. *Reviews in Mineralogy and Geochemistry* 48(1), edited by Kohn M. J., Rakovan J., Hughes J. M. Virginia: Mineralogical Society of America. pp.524-558.

Hibiya Y., Archer G. J., Tanaka R., Sanborn M. E., Sato Y., Iizuka T., Ozawa K., Walker R. J., Yamaguchi A., Yin Q. Z. and Nakamura T. 2019. The origin of the unique achondrite Northwest Africa 6704: Constraints from petrology, chemistry and Re–Os, O and Ti isotope systematics. *Geochimica et Cosmochimica Acta* 245:597-627.

Irving A. J., Kuehner S. M. and Ziegler, K. 2013. Petrology and oxygen isotopic composition of brachinite-like achondrites Northwest Africa 7388 and Northwest Africa

7605, and evidence for late-stage methane-triggered reduction (abstract #2192). 44th Lunar and Planetary Science Conference.

Ivanova M. A. and Petaev M. I. 2015. Characteristics and origin of the components of the carbonaceous chondrite NWA 470. *Petrology* 23(2):150-167.

Jacquet E., Alard O. and Gounelle M. 2012. Chondrule trace element geochemistry at the mineral scale. *Meteoritics & Planetary Science* 47(11):1695-1714.

Jacquet E., Paulhiac-Pison M., Alard O., Kearsley A. T. and Gounelle M. 2013. Trace element geochemistry of CR chondrite metal. *Meteoritics & Planetary Science* 48(10):1981-1999.

Jagoutz E., Palme H., Baddenhausen H., Blum K., Cendales M., Dreibus G., Spettel B., Lorenz V. and Wänke H. 1979. The abundances of major, minor and trace elements in the earth's mantle as derived from primitive ultramafic nodules (abstract). 10th Lunar and Planetary Science Conference 2031-2050.

Jogo K., Nagashima, K., Hutcheon I. D., Krot A. N. and Nakamura T. 2013. Heavily metamorphosed clasts from the CV chondrite breccias Mokoia and Yamato-86009. *Meteoritics & Planetary Science* 47(12):2251-2268.

Kimura M., Grossman J. N. and Weisberg M. K. 2008. Fe-Ni metal in primitive chondrites: Indicators of classification and metamorphic conditions for ordinary and CO chondrites. *Meteoritics & Planetary Science* 43(7):1161-1177.

Krot A. N., Petaev M. I., Scott E. R., Choi B. G., Zolensky M. E. and Keil K. 1998. Progressive alteration in CV3 chondrites: More evidence for asteroidal alteration. *Meteoritics & Planetary Science* 33(5):1065-1085.

Krot A. N., Meibom A., Weisberg M. K. and Keil K. 2002. The CR chondrite clan: Implications for early solar system processes. *Meteoritics & Planetary Science* 37(11):1451-1490.

Kruijer T. S., Burkhardt C., Budde G. and Kleine T. 2017. Age of Jupiter inferred from the distinct genetics and formation times of meteorites. *Proceedings of the National Academy of Sciences* 114(26):6712-6716.

Lafuente B., Downs R. T., Yang H. and Stone N. 2016. The power of databases: The RRUFF project. In Highlights in Mineralogical Crystallography, edited by Armbruster T. and Danisi R. M. Berlin: Walter de Gruyter. pp. 1-29.

Leya I., Schönbächler M., Wiechert U., Krähenbühl U. and Halliday A.N. 2008. Titanium isotopes and the radial heterogeneity of the solar system. *Earth and Planetary Science Letters* 266:233-244.

Makide K., Nagashima K., Krot A. N., Huss G. R., Hutcheon I. D. and Bischoff A. 2009. Oxygen-and magnesium-isotope compositions of calcium–aluminum-rich inclusions from CR2 carbonaceous chondrites. *Geochimica et Cosmochimica Acta* 73(17):5018-5050.

Matsumoto M., Tomeoka K., Seto Y., Miyake A. and Sugita M. 2014. Nepheline and sodalite in the matrix of the Ningqiang carbonaceous chondrite: Implications for formation through parent-body processes. *Geochimica et Cosmochimica Acta* 126:441-454.

Matsumoto M., Tomeoka K. and Seto Y. 2017. Nepheline and sodalite in chondrules of the Ningqiang carbonaceous chondrite: Implications for a genetic relationship with those in the matrix. *Geochimica et Cosmochimica Acta* 208:220-233.

McDonough W. F. and Sun S.-S. 1995. The composition of the Earth. *Chemical Geology* 120:223–253.

McDowell F. W., McIntosh W. C. and Farley K. A. 2005. A precise ^{40}Ar–^{39}Ar reference age for the Durango apatite (U–Th)/He and fission-track dating standard. *Chemical Geology* 214(3-4):249-263.

Nanne J. A., Nimmo F., Cuzzi J. N. and Kleine T. 2019. Origin of the non-carbonaceous-carbonaceous meteorite dichotomy. *Earth and Planetary Science Letters* 511:44-54.

Pedersen S. G., Schiller M., Connelly J. N. and Bizzarro M. 2019. Testing accretion mechanisms of the H chondrite parent body utilizing nucleosynthetic anomalies. *Meteoritics & Planetary Science* 54(6):1215-1227.

Perron C., Bourot-Denise M., Marti K., Kim J. S. and Crozaz G. 1992. The metal-phosphate connection in chondrites. *Meteoritics* 27(3):275.

Qin L., Nittler L. R., Alexander C. O. D., Wang J., Stadermann F. J. and Carlson R. W. 2011. Extreme ^{54}Cr-rich nano-oxides in the CI chondrite Orgueil - Implication for a late supernova injection into the solar system. *Geochimica et Cosmochimica Acta* 75:629-644.

Righter K., Drake M. J. and Scott E. 2006. Compositional relationships between meteorites and terrestrial planets. In Meteorites and the early solar system II, edited by Lauretta D. S. and McSween H. Y. Arizona: University of Arizona Press. pp. 803-828.

Rumble D., Zolensky M. E., Friedrich J. M., Jenniskens P. and Shaddad M. H. 2010. The oxygen isotope composition of Almahata Sitta. *Meteoritics & Planetary Science* 45(10-11):1765-1770.

Ruzicka A., Grossman J., Bouvier A., Herd C. D. K. and Agee C. B. 2015a. The meteoritical bulletin, No. 102. *Meteoritics & Planetary Science* 50:1662.

Ruzicka A., Grossman J., Bouvier A., Herd C. D. K. and Agee C. B. 2015b. The Meteoritical Bulletin, No 101. *Meteoritics & Planetary Science* 50:1661.

Sanborn M. E. and Yin Q.-Z. 2019. Magmatism in the outer solar system: What we know now from isotope forensics of carbonaceous achondrites (abstract #1498). 50th Lunar and Planetary Science Conference.

Sanborn M. E., Yamakawa A., Yin Q. Z., Irving A. J. and Amelin Y. 2013. Chromium isotopic studies of ungrouped achondrites NWA 7325, NWA 2976, and NWA 6704 (abstract #5220). 76th Annual Meeting of the Meteoritical Society.

Sanborn M. E., Yin Q. Z., Hyde B. C., Tait K. T. and Moser D. E. 2018. Early differentiation in the carbonaceous chondrite forming region of the solar nebula: New insight from the achondrites Northwest Africa 7680/6962 (abstract #2296). 49th Lunar and Planetary Science Conference.

Sanborn M. E., Yin Q.-Z., Hyde B. C., Tait K.T. and Moser D. E. in prep. Northwest Africa 7680 and 6962: Insight into timing of early differentiation in the outer solar system. To be submitted to *Meteoritics & Planetary Science.*

Srinivasan P., Dunlap D. R., Agee C. B., Wadhwa M., Coleff D., Ziegler K., Zeigler R. and McCubbin F. M. 2018. Silica-rich volcanism in the early solar system dated at 4.565 Ga. *Nature Communications* 9, 3036, doi:10.1038/s41467-018-05501-0

Tomeoka K. and Itoh D. 2004. Sodium-metasomatism in chondrules in CO3 chondrites: Relationship to parent body thermal metamorphism. *Meteoritics & Planetary Science* 39(8):1359-1373.

Thomson S. N., Gehrels G. E., Ruiz J. and Buchwaldt R. 2012. Routine low-damage apatite U-Pb dating using laser ablation–multicollector–ICPMS. *Geochemistry, Geophysics, Geosystems, 13*(2):Q03017.

Uhlig H.H. 1955. Contribution of metallurgy to the origin of meteorites Part II–the significance of Neumann bands in meteorites. *Geochimica et Cosmochimica Acta* 7(1-2):34-42.

Valley J. W., Kitchen N., Kohn M. J., Niendorf C. R. and Spicuzza M. J. 1995. UWG-2, a garnet standard for oxygen isotope ratios: strategies for high precision and accuracy with laser heating. *Geochimica et Cosmochimica Acta* 59(24):5223-5231.

Ward D., Bischoff A., Roszjar J., Berndt J. and Whitehouse M. J. 2017. Trace element inventory of meteoritic Ca-phosphates. *American Mineralogist* 102(9):1856-1880.

Warren P. H. 2011. Stable-isotopic anomalies and the accretionary assemblage of the Earth and Mars: A subordinate role for carbonaceous chondrites. *Earth and Planetary Science Letters* 311: 93-100.

Warren P. H., Rubin A. E., Isa J., Brittenham S., Ahn I. and Choi B. G. 2013. Northwest Africa 6693: A new type of FeO-rich, low-$\Delta^{17}O$, poikilitic cumulate achondrite. *Geochimica et Cosmochimica Acta* 107:135-154.

Weisberg M. K., Prinz M., Clayton R. N. and Mayeda T. K. 1993. The CR (Renazzo-type) carbonaceous chondrite group and its implications. *Geochimica et Cosmochimica Acta* 57(7):1567-1586.

Wimpenny J., Sanborn M. E., Koefoed P., Cooke I. R., Stirling C., Amelin Y. and Yin Q.-Z. 2019. Reassessing the origin and chronology of the unique achondrite Asuka 881394: Implications for distribution of ^{26}Al in the early Solar System. *Geochimica et Cosmochimica Acta* 244:478–501.

Yin Q., Jacobsen S. B. and Yamashita K. 2002. Diverse supernova sources of pre-solar material inferred from molybdenum isotopes in meteorites. *Nature* 415:881-883.

Zhang A., Guan Y., Hsu, W., Liu Y. and Taylor L.A. 2010. Origin of a metamorphosed lithic clast in CM chondrite Grove Mountains 021536. *Meteoritics & Planetary Science* 45(2):238-245.

Chapter 4

Northwest Africa 11950 and 11951: A textural analysis of diamond formation in the ureilite parent body

4.1 Abstract

Determining the paragenesis of diamond in the carbon-rich domains of ureilites is necessary to evaluate whether the assemblage can be used for inferring paleodepth and, ultimately, size of the parent body. Northwest Africa (NWA) 11950 and 11951 are diamond-bearing ureilites with similar mineralogy, mineral compositions and oxygen isotope compositions. The olivine in NWA 11950 has core compositions of $Fa_{21.1\pm0.2}$ and pyroxene core compositions of $Fs_{17.9\pm0.1}Wo_{7.5\pm0.1}$. Similarly, NWA 11951 has olivine core composition of $Fa_{19.6\pm0.2}$ and pyroxene core compositions of $Fs_{17.1\pm0.1}Wo_{5.4\pm0.1}$. The oxygen isotope analyses for NWA 11950 ($\Delta^{17}O$ = -0.94, -0.96‰) and NWA 11951 ($\Delta^{17}O$ = -0.80, -0.75‰) place them both at the heavy $\delta^{18}O$ end of the known ureilite compositional range. The carbon-rich areas of the two meteorites consist of mixtures of diamond and graphite, which are more abundant in NWA 11950. The textural relationships of the two phases have been revealed through spatially-correlated large-scale Raman and cathodoluminescence mapping and Raman point analyses to generate a novel view of mineralogy and mineral associations of carbon phases in ureilites. In NWA 11950, the central parts of the carbon-rich regions generally consist of graphite and the edges next to silicate grains are often composed of diamond. In NWA 11951, the carbon-rich regions are dominated by diamond. The location of diamond along carbon-silicate grain boundaries supports formation by inhomogeneous and short-lived pressure environments active along maximum gradients in shock impedance, as opposed to static metamorphic growth within in a planet-sized parent body.

4.2 Introduction

Ureilites are a unique type of achondrite due to their isotopic and compositional heterogeneity. This group of meteorites originate from a single initial parent body, but contain heterogeneous oxygen isotope compositions (e.g., Rumble et al. 2010) remaining

from their source materials. The mineralogy, texture and in some cases geochemistry appear to be from an evolved parent body, with studies suggesting they represent partial-melt residues from the mantle of their parent body (e.g., Scott et al. 1993; Warren et al. 2006). The ureilite parent body has even generated trachyandesite composition lavas forming crustal rocks, indicating a highly evolved parent body (Bischoff et al. 2014). This peculiar set of heterogeneous, yet evolved characteristics is likely due to a late accretion of the parent body, resulting in lower concentrations of ^{26}Al, less radiogenic heating and consequently a lower degree of melting and homogenization compared to an early formed parent body of comparable size (Budde et al., 2015).

Ureilites also contain a uniquely large amount of native carbon (e.g., Grady et al. 1985; Smith et al. 2001) in one case measuring 34 modal % (Day et al. 2017). The carbon-rich regions of ureilites can contain graphite, diamond, amorphous carbon and lonsdaleite (e.g., Le Guillou et al. 2010; Nakamuta and Toh 2013). The origin of the carbon and its timing of entry into the system are still in debate; however, a poor correlation between carbon abundance and olivine core compositions in ureilites suggests that the carbon was introduced following primary silicate formation (Day et al. 2017; Warren and Huber 2006). The formation mechanism for diamond in ureilites is also a heavily debated topic with formation mechanisms ranging from shock from impacts (e.g., Lorenz et al. 2019), formation at depth in a potentially Mars-size planetesimal (e.g., Nabiei et al., 2018) and chemical vapor deposition (e.g., Nagashima et al. 2012).

The examination of diamonds from terrestrial impact craters could shed light on diamond formation mechanisms in extraterrestrial environments. Diamonds found at the Ries Crater have revealed that shock-induced diamond formation occurred where the difference in shock impedance between minerals was highest (El Goresy et al. 2001). This is consistent with simulations that confirm that the presence of highly impedant surrounding materials aid in the formation of diamond from graphite by generating a progressive increase in pressure through a shock accumulation process (Pineau et al. 2015).

Studies of large-scale textural relationships between diamond and surrounding phases in ureilites are often limited by the length-scale of the analytical techniques being used. In studies most similar to this one (e.g. Lorenz et al. 2019) high quality analyses of single microdiamonds by photoluminescence and Raman spectroscopy are reported as indicating an origin through shock processes acting on a variety of carbonaceous starting materials. Here we present larger-scale context for the diamond-bearing regions of the ureilites NWA 11950 and 11951. This is accomplished through Raman and cathodoluminescence (CL) mapping of carbon phases to test for diamond distributions and associations predicted by longer-term static vs. short-term dynamic processes on the ureilite parent body.

4.3 Samples and Analytical Methods

4.3.1 NWA 11950 and 11951 Materials Used in this Study

Materials from NWA 11950 and 11951 were acquired from the Royal Ontario Museum's meteorite collection (museum accession numbers M53446 and M58189 respectively). For analysis, a thin section and two polished mounts were used for each sample. All materials were first cut from the main masses using a Well Diamond Wire Saw (model 6234) with a 0.42 mm diameter wire. The saw uses wires from two sources: Well Diamond Wire Saws, Inc. and Tianjin Mande Industry & Trade Co., Ltd. Thin sections were produced by a commercial lab, while the polished mounts were generated in-house. A large polished mount of each sample was produced through polishing first with silicon carbide to remove saw cut marks, followed by 6 µm diamond film (Buehler), 1 µm diamond paste and 0.5 µm diamond paste (Beta Diamond Products). Polishing was done using oil (Beta Diamond Products) for lubrication. The samples were placed in isopropyl alcohol for sonication following each polishing step. A diamond polish was used to produce the flattest surface possible for large-scale observations. As a check for possible diamond contamination, smaller polished mounts were made of each meteorite, utilizing alumina powder (Buehler) in place of diamond products.

4.3.2 Backscatter Electron Imaging, Chemical Mapping, and Cathodoluminescence

Backscatter electron (BSE) imaging and chemical mapping (Figs. 4.1 and 4.2) were carried out using a Hitachi SU6600 Field Emission Scanning Electron Microscope (FE-SEM) at the University of Western Ontario. An Oxford XMax silicon drift detector (80 mm^2) was used for energy dispersive X-ray spectrometry (EDS) measurements (INCA software). A Gatan Chroma CL detector was used with an accelerating voltage of 10 kV and a working distance of roughly 12.8 mm, which was adjusted for optimal emission/detection. Emissions were binned into 3 channels: red (600–850 nm), green (500–600 nm), and blue (400–500 nm) and images were assembled using the Gatan Digital Micrograph software.

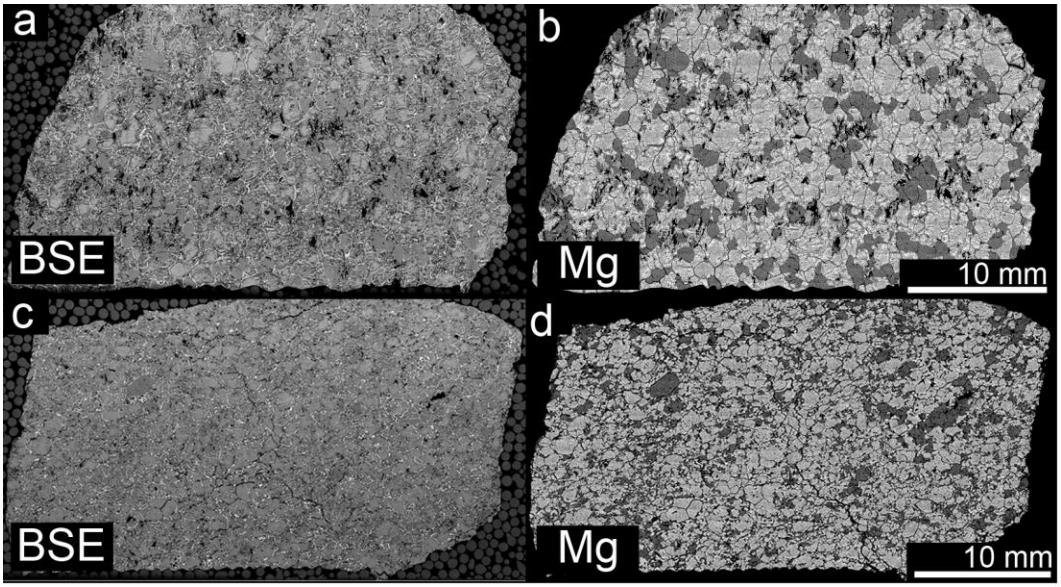

Figure 4.1. Section of NWA 11950 in a) BSE imaging and b) Mg compositional map. Section of NWA 11951 in c) BSE imaging and d) Mg compositional map. In the BSE images, white areas are metal and lesser sulfides, the grey areas are silicates and the black areas are carbon (and cracks). Note that the samples are surrounded by epoxy and glass beads. In the Mg compositional maps the silicates can be differentiated, with the olivine appearing brighter than the pyroxene. These images are from carbon-coated thin sections, whereas later Raman analyses of carbon phases were carried out on uncoated sections. Note: Faint horizontal lineations seen are artefacts from the mosaicking process.

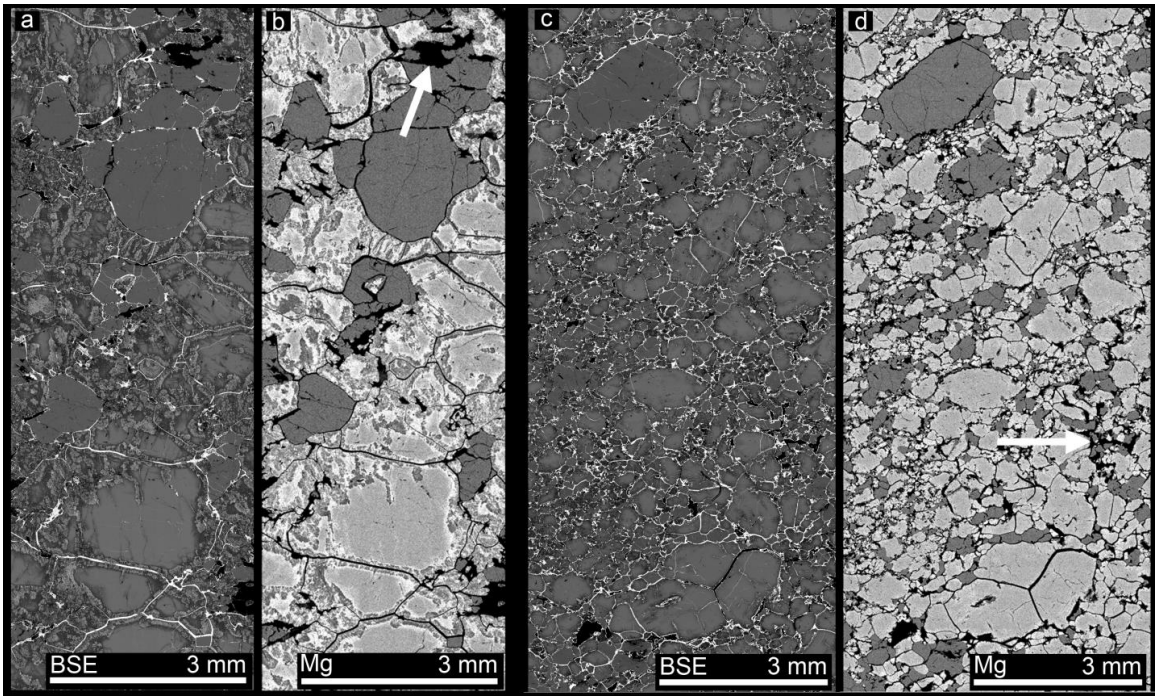

Figure 4.2. Backscatter electron and Mg compositional maps of NWA 11950 and NWA 11951. a) a BSE mosaic and b) a Mg compositional map showing typical textures in NWA 11950. The more homogeneous grains with less Mg are pyroxene, whereas the grains showing extensive Mg-enrichment at boundaries are olivine. Bright regions in BSE around silicates are generally Fe-metal (or oxidized Fe-metal). Larger black areas are carbon-rich regions. A representative carbon-rich area is indicated with a white arrow. c) a BSE mosaic and d) a Mg compositional map showing typical textures in NWA 11951. Mineral identifications are the same as those for NWA 11950; however, the Mg-rich rims are less obvious in this case. There is an obvious bimodality in grain size for both olivine and pyroxene in NWA 11951. A cluster of carbon-rich areas is indicated with a white arrow.

4.3.3 Quantitative Energy Dispersive Spectrometry and Wavelength Dispersive Spectrometry

Quantitative standards-based energy dispersive spectrometry (EDS) analyses were performed on olivine and pyroxene using the FE-SEM previously discussed. A conductive Si standard (commercial wafer) was used to verify and adjust peak positions and adjust for changes in beam current. Beam current was found to only vary by a

relative standard deviation of 0.7 % over two days. Beam current was monitored during runs and adjusted when required. Quantification of Mg and Si was carried out by EDS, while minor elements and Fe were measured using WDS. For EDS analysis, a natural forsterite standard was used. For WDS measurements natural fayalite (Fe), natural diopside (Ca), synthetic Cr_2O_3 (Cr) and synthetic Mn_2SiO_4 (Mn) were used. During processing a pulse pile-up correction was applied to the EDS data; however, the resulting compositions were identical (within uncertainty) to those of "uncorrected" data, so the correction was not used in final calculations. A previously studied ureilite (NWA 7630) was used as a natural reference and yielded an olivine composition of $Fa_{20.7\pm0.2}$ with a Cr_2O_3 content of 0.71 ± 0.02 wt. % and a CaO content of 0.32 ± 0.01 wt. % indistinguishable from measurements of Barrat et al. (2015).

4.3.4 Oxygen Isotope Analyses

Triple-oxygen isotope analyses of two subsamples from each meteorite were carried out by laser fluorination techniques at the University of New Mexico. The samples were pre-treated by a weak HCl acid-wash followed by a rinse in distilled water to remove terrestrial weathering products. Samples were then pre-fluorinated with BrF_5 in vacuum. Laser-assisted fluorination was carried out with a 50 W far-infrared CO_2 laser in a BrF_5 atmosphere. The set-up and methodology followed that of Sharp (1990). Oxygen compositions were measured using a dual inlet isotope ratio mass spectrometer (Thermo Finnigan MAT 253/253 Plus). The isotope ratios were calibrated against San Carlos olivine. The value used for the slope of the terrestrial fractionation line (TFL) in this study is 0.528.

4.3.5 Raman Spot Analyses and Mapping

Raman analyses were carried out on carbon phases using a Horiba LabRAM ARAMIS micro-Raman spectrometer. The carbon phases were initially identified by reflected light, appearing darker than the surrounding silicates and Fe-metal. These identifications were followed up by test points with the micro-Raman, prior to final spot analyses and mapping. For spot analyses, a 532 nm laser was used with the power filtered down to 1.64 mW to prevent sample damage. A 1800 groove/mm grating, 100 µm slit and 50x

long working distance objective were used during collection. A Kr light source was used for calibration and a 100 µm confocal hole was used to reduce the contribution of out of focus light from surrounding materials reaching the detector. Spectra were collected 20 times at each spot for 10 s and the results were averaged. Peak fitting for spot analyses used the Fityk program (Wojdyr 2010). A pseudo-Voigt peak shape was used for fitting and peak centre, full width at half maximum (FWHM) and shape parameters were manually adjusted to minimize the fit residuals (Appendix 4 - A4.1). The measured peak parameters consist of the sample's peak profile plus the profile of the instrument used. A mathematical correction was used to remove the contributions of the instrument (Nasdala et al. 2016; Váczi 2014). This is the only way to compare data obtained from different instruments. Measurements from diamond preparation products gave a peak position of 1332.8 ± 0.2 cm^{-1} (1σ), providing a measure of wavenumber accuracy. Raman mapping used the same set-up except with a 1200 groove/mm grating, 400 µm confocal hole and a laser power of 1.63 mW. A Si wafer was used to calibrate prior to mapping. Maps were collected in increments of 2 µm by 2 µm. Two spectra were collected for 1.5 s at each point in the map and the results were averaged. An autofocus feature along with the long working distance objective provided the ability to map large areas (see Hyde et al. 2014).

4.4 Results

4.4.1 General Petrography

The mineralogy of NWA 11950 is predominantly olivine and pyroxene with grain size generally ranging from 0.5 to 3 mm (Figs. 4.1 and 4.2). The meteorite has a granoblastic texture with triple junctions being common. Olivine grains have reduced rims, showing Mg-enrichment alongside Fe-metal (Fig. 4.3). Minor reduction is also seen along pyroxene grain boundaries. All of the olivine grains contain Ca, Cr-rich inclusions likely composed of multiple phases (Fig. 4.3). The silicate grain boundaries are sometimes poorly defined and are often surrounded by metal. Carbon-rich regions are also present throughout the meteorite and are found along silicate grain boundaries and often associated with metal (Fig. 4.1).

NWA 11951 is also predominantly olivine and pyroxene. Grains in the meteorite can be as large as 3 mm, but regions of small grains (10s to 100s of micrometres) are also common (Figs. 4.1 and 4.2). The meteorite has a visibly bimodal grain size distribution. Olivine grains have reduced rims also showing Mg-enrichment alongside metallic Fe. The smallest grains often show pervasive reduction. Minor reduction is also seen along pyroxene grain boundaries and metal is abundant along the silicate grain boundaries. The meteorite has carbon-rich regions and difficulty during the cutting process gave the early impression that the meteorite is diamond-rich. The carbon-rich regions are found along silicate grain boundaries and often associated with metal (Fig. 4.1). Minor phases include chromite (10s of micrometres) and a Si-rich phase(s) found in veins and along grain boundaries.

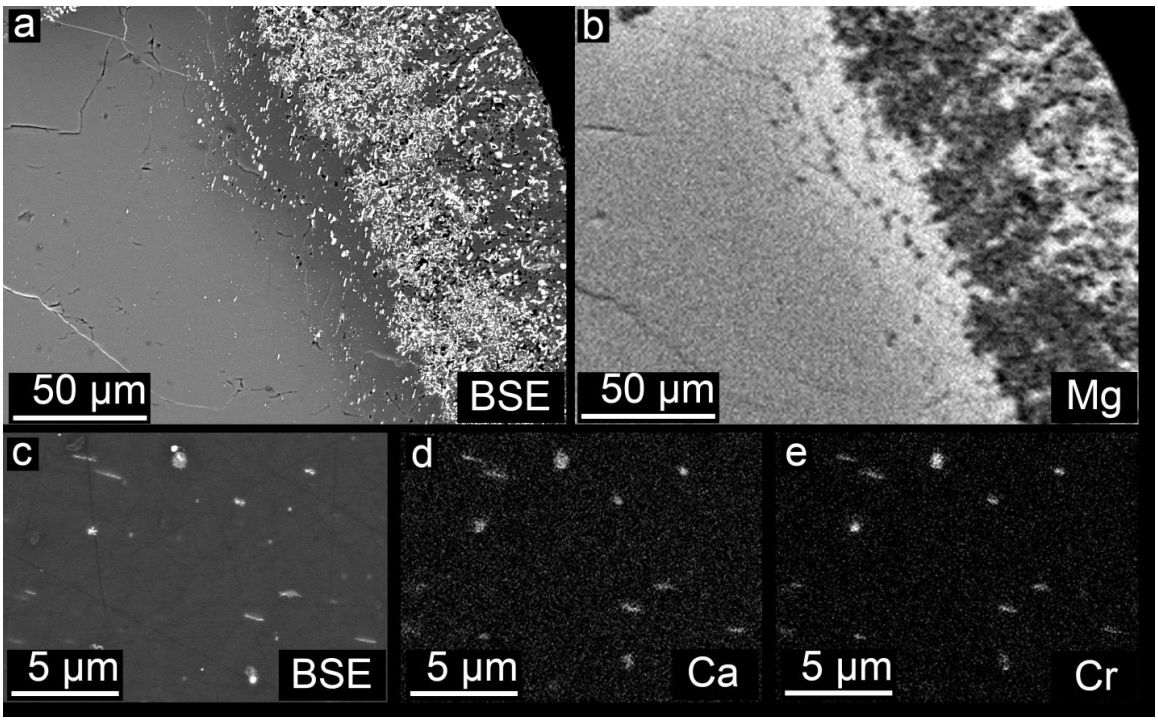

Figure 4.3. a) Backscatter electron map and b) Mg map showing a typical olivine reduction rim in NWA 11950. Note that the silicate portion of the rim shows Mg-enrichment alongside Fe-metal. c) Backscatter electron map, d) Ca map and e) Cr map showing dense (bright in BSE) Ca, Cr-rich inclusions in olivine from NWA 11950.

4.4.2 Mineral Compositions and Geochemistry

NWA 11950 has olivine core compositions of $Fa_{21.1 \pm 0.2}$ with a Cr_2O_3 content of 0.58 ± 0.04 wt. % and a CaO content of 0.28 ± 0.03 wt. % (Table 4.1, Fig. 4.4). Pyroxene cores in this meteorite have compositions of $Fs_{17.9 \pm 0.1}Wo_{7.5 \pm 0.1}$ (Table 4.1). Oxygen isotope analyses of two acid-washed subsamples by laser fluorination gave compositions of $\delta^{17}O$ = 3.91, 3.73, $\delta^{18}O$ = 9.18, 8.89 and $\Delta^{17}O$ = -0.94, -0.96‰ (Fig. 4.5).

The olivine in NWA 11951 has a core composition of $Fa_{19.6 \pm 0.2}$ with a Cr_2O_3 content of 0.72 ± 0.02 wt. % and a CaO content of 0.30 ± 0.01 wt. % (Table 4.1, Fig. 4.4). Pyroxene cores have a composition of $Fs_{17.1 \pm 0.1}Wo_{5.4 \pm 0.1}$ in the meteorite (Table 4.1). Oxygen isotopes analyses for two samples of NWA 11951 gave compositions of $\delta^{17}O$ = 3.86, 3.83, $\delta^{18}O$ = 8.83, 8.67 and $\Delta^{17}O$ = -0.80, -0.75‰ (Fig. 4.5).

Table 4.1. Average (±1σ) mineral core compositions (wt. %) for NWA 11950 and 11951.

	Olivine		Pyroxene	
	NWA 11950 (n=15)	NWA 11951 (n=14)	NWA 11950 (n=15)	NWA 11951 (n=17)
SiO_2	38.82 ± 0.10	38.94 ± 0.13	55.00 ± 0.15	55.34 ± 0.15
TiO_2	-	-	0.06 ± 0.01	0.06 ± 0.01
Al_2O_3	-	-	0.64 ± 0.04	0.48 ± 0.01
Cr_2O_3	0.58 ± 0.03	0.72 ± 0.02	1.10 ± 0.04	1.16 ± 0.04
CaO	0.28 ± 0.02	0.30 ± 0.01	3.79 ± 0.06	2.73 ± 0.03
MnO	0.42 ± 0.03	0.42 ± 0.03	0.42 ± 0.02	0.43 ± 0.02
FeO	19.18 ± 0.27	17.83 ± 0.16	11.51 ± 0.10	11.10 ± 0.10
MgO	40.26 ± 0.13	41.03 ± 0.12	26.96 ± 0.10	28.16 ± 0.08
Total	99.54	99.24	99.48	99.46

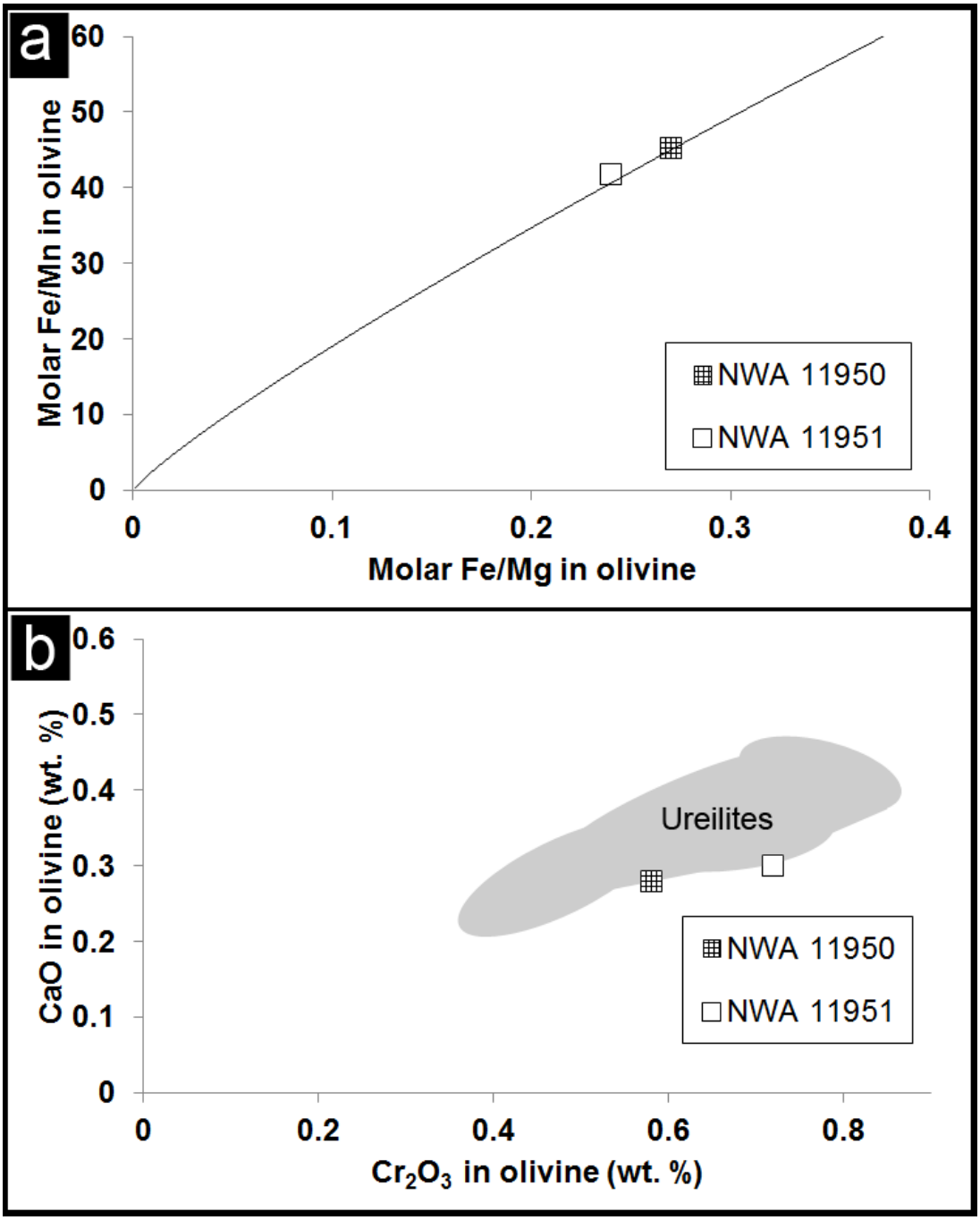

Figure 4.4. a) Plot of Fe/Mn and Fe/Mg ratios for olivine cores in NWA 11950 and NWA 11951. The solid line given is the relationship determined by Goodrich et al. (2006) for olivine and low Ca-pyroxene ureilites. b) CaO and Cr_2O_3 concentrations for olivine cores found in NWA 11950 and NWA 11951. The grey region is the range of ureilite compositions given in Goodrich et al. (2011) and references therein.

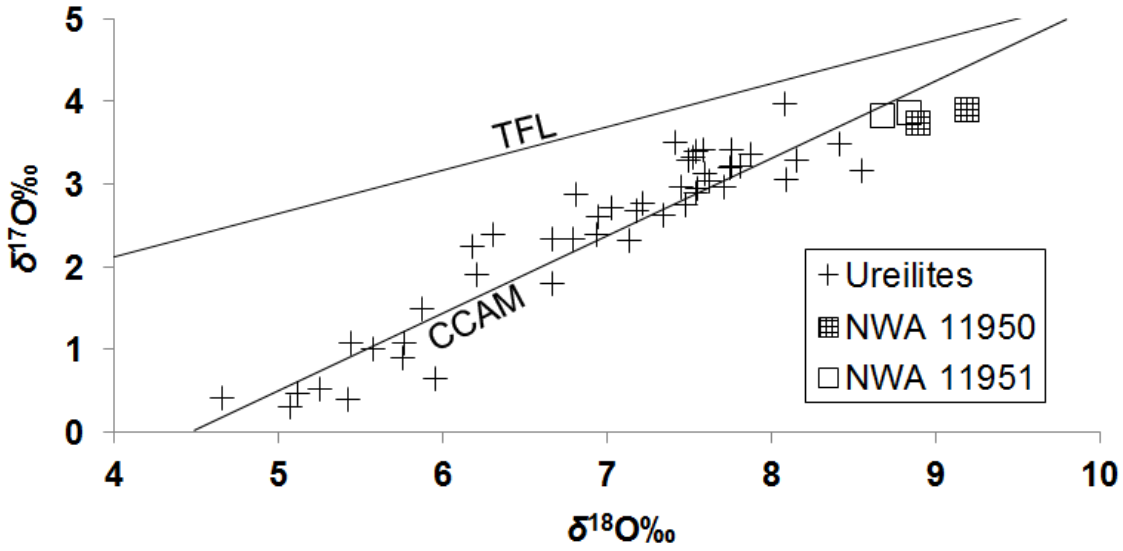

Figure 4.5. Oxygen isotope compositions for NWA 11950 and NWA 11951 compared to known ureilite compositions from Clayton and Mayeda (1996). The terrestrial fractionation line (TFL) and carbonaceous chondrite anhydrous mineral (CCAM) line from Clayton and Mayeda (1999) are given for reference.

4.4.3 Carbon Phases

Carbon-rich regions in NWA 11950 and NWA 11951 that represent the variability in size and surrounding mineralogy were chosen for Raman analysis. Spot analyses and mapping confirm that both diamond and graphite are present in both meteorites. The diamond spectra contain one main peak at ~1332 cm^{-1} (e.g. Ross et al. 2011). The spectra containing diamond often have a high fluorescence background and also contain a broad peak partially overlapping the diamond peak and continuing to higher wavenumbers (Fig. 4.6d). A similar broad peak is seen in high fluorescence diamond spectra in Ross et al. (2011) and these spectra in general are thought to be influenced by defect structures in the diamond lattice. Lorenz et al. (2019) also found a similar feature and attributed it to photoluminescence resulting from nitrogen atoms and vacancies in the diamond structure. The broad peak also falls within the range of the amorphous carbon peak assignment provided in Himics et al. (2016). Whichever the case may be, the diamond peak parameters are not affected in any systematic way by the overlapping broad peak. Graphite spectra match that of many previous studies (e.g., Ferroir et al. 2010;

Nagashima et al. 2012) and show the diagnostic D and G bands at ~1350 and ~1580 cm^{-1} respectively. For textural characterization, an integrated method of observing Raman spot analyses, Raman maps combined with CL imaging was used for visualization (Fig. 4.6). Diamond-rich regions found in the Raman maps match well with CL active regions providing an unparalleled view of large-scale carbon phase textures in ureilites.

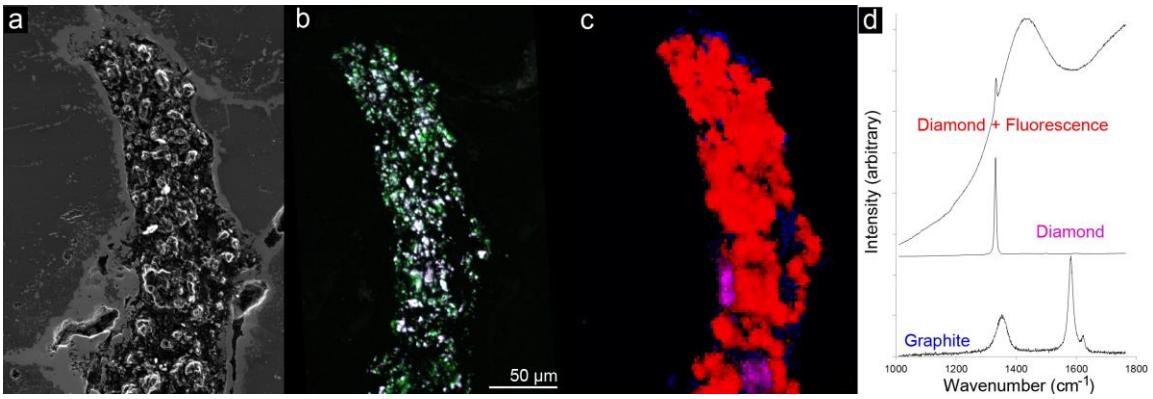

Figure 4.6. a) A secondary electron (SE) image showing a carbon-rich region in NWA 11951. b) Cathodoluminescence (RGB) image showing active regions that correspond to diamonds in Raman maps (c). The diamond maps are constructed by colour coding spectra from each point in the map. Example spot analyses are shown in (d) with their corresponding colours: diamond + fluorescence (red), diamond (purple) and graphite (blue).

Raman peak positions for diamonds in NWA 11950 range from 1329.1 to 1332.7 cm^{-1} and for NWA 11951 they range from 1329.7 to 1332.5 cm^{-1} (Fig. 4.7). Full width at half maximum values for diamonds in NWA 11950 range from 6.2 to 12.8 cm^{-1} and for NWA 11951 they range from 7.5 to 10.8 cm^{-1} (Fig. 4.6). Ureilite diamond parameter values are easily separated from those of the diamond preparation products (diamond wire and diamond film) used, except for one point from the diamond polishing film. This point was from a used (but cleaned) portion of diamond film and we surmise that this point represents contamination from a ureilite source. Diamonds from unused diamond film always remained distinct from the ureilite diamonds. One analysis from the diamond wire produced a spectrum with an anomalously low peak position. The cause of this is unclear, and the point is presently treated as an outlier. Spectra from the diamond polishing paste

used for some sections show very weak and broad peaks that are easily distinguishable from the ureilite diamonds (Appendix 4 - A4.2). Diamonds from ureilite samples polished with and without diamond polishing compounds both have peak parameters that separate them from the diamond preparation products (Fig. 4.7).

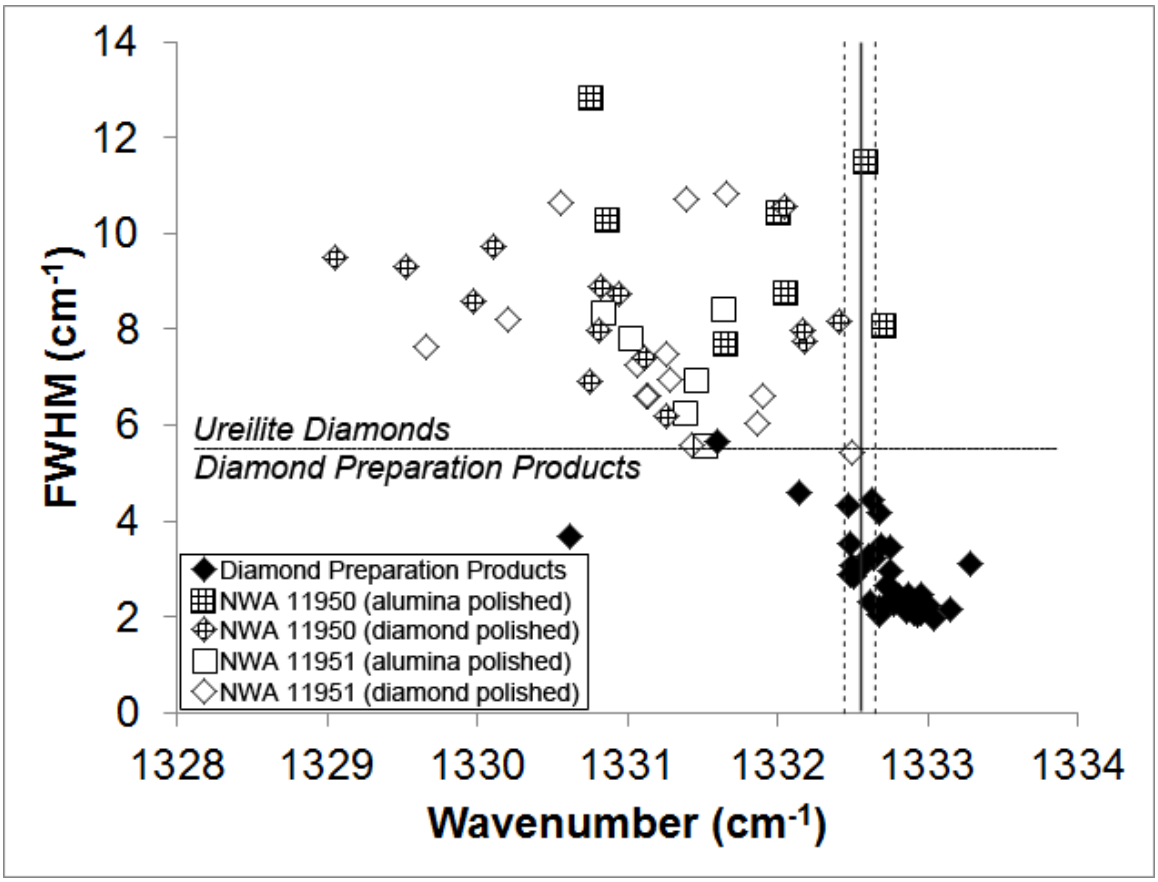

Figure 4.7. Plot of peak positions and FWHM for Raman spot analyses of diamonds in NWA 11950 and NWA 11951. The spot analyses were acquired from three different carbon domains in each meteorite. Analyses from sections polished with diamond and alumina are both plotted. Data are also plotted for diamond preparation products, including diamonds from the diamond wire saw and diamond film. The solid vertical line is the value for terrestrial kimberlite diamonds given in Ross et al. (2011) and the dotted lines are the associated uncertainties.

Both Raman maps and CL images show that the carbon-rich regions in NWA 11950 and 11951 have diamond and graphite closely associated. These carbon-rich regions are

found adjacent to silicate phases. The broader-scale distribution of these associations can be seen in Figure 4.1 with higher magnification of the carbon-rich regions seen in Figures 4.6 and 4.8. The carbon-rich regions in NWA 11950 contain more graphite. In general, the diamond in this meteorite is found along the edges on the carbon-rich regions and adjacent to silicates (Fig. 4.8 and Appendix 4 - A4.3). The carbon-rich areas examined in NWA 11951 are diamond-rich with areas of diamond often associated with small amounts of graphite (Figs. 4.6, 4.8 and Appendix 4 - A4.3). Qualitatively, the CL colours for the ureilite diamonds in this study are different from those of the diamond preparation products and alumina polishing powder. The red-green-blue values for these images can also be plotted to give a clearer view of the differences between diamond sources (Appendix 4 - A4.4 and A4.5). In general, the diamond preparation products have a wider range in colour. This may be due to the commercial diamonds having multiple sources.

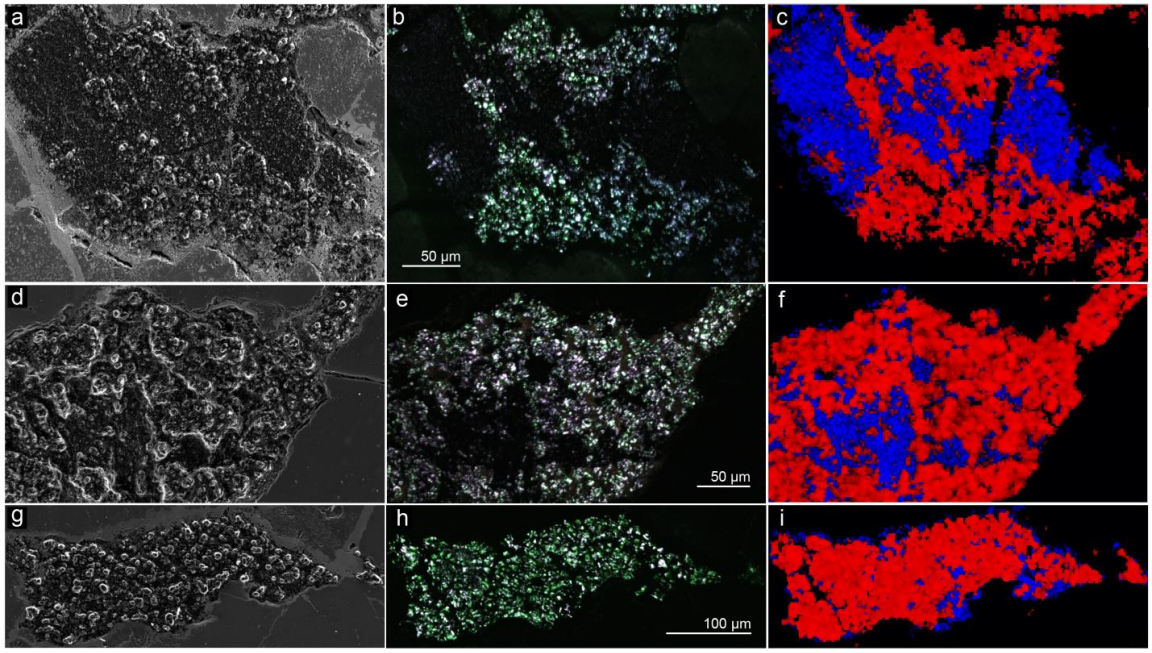

Figure 4.8. Secondary electron images (a, d), CL images (b, e) and Raman maps (c, f) of carbon-rich regions in NWA 11950. g) Secondary electron image, h) CL image and i) Raman map of a carbon-rich region in NWA 11951. Note: the Raman maps include diamond + fluorescence (red), diamond (purple) and graphite (blue).

4.5 Discussion

4.5.1 NWA 11950 and 11951 Compared to Previously Studied Ureilites

Carbon-rich regions are pervasive in ureilites (e.g., Grady et al. 1985; Smith et al. 2001) as are the regions seen in NWA 11950 and 11951. The major element compositions of olivine and pyroxene are consistent with forsterite and pigeonite, which are common for ureilites. Reduction rims are seen in the silicates from both NWA 11950 and 11951 (Figs. 4.2 and 4.3), are ubiquitous in ureilites, and are thought to have formed during the disruption of the ureilite parent body (e.g. Herrin et al. 2010). The Ca, Cr-rich inclusions seen in olivine from NWA 11950 (Fig. 4.3) are similar to inclusions seen in other ureilites. Olivine in the ureilites LAP 03587 and CMS 04048 contain numerous inclusions that tend to be elongated and aligned and generally <1 μm in length (Goodrich et al. 2013; Goodrich et al. 2014). The inclusions consist of mainly two phases and are likely symplectic (exsolution) intergrowths of chromite and Ca-rich pyroxene. These are thought to form during cooling and contraction, with Cr being excluded from the olivine structure and pyroxene taking up the less compatible divalent elements like Ca (Goodrich et al. 2013; Goodrich et al. 2014). This description is consistent with the inclusions in NWA 11950, which also show alignment in some cases and appear to consist of at least two phases.

Minor element (Mn, Ca and Cr) compositions of olivine from NWA 11950 and 11951 are likewise consistent with a ureilite parent body origin (Fig. 4.4). Oxygen isotope compositions for NWA 11950 and 11951 place them at the high $\delta^{18}O$ end of the known ureilite compositional range (Fig. 4.5). The compositions of these meteorites place them outside the range of most ureilites; however, the compositions are still in the region of the CCAM line like all other ureilites. This along with the textural, mineralogical and compositional data discussed above provides ample evidence for a ureilite parent body origin for NWA 11950 and 11951.

4.5.2 Raman Peak Parameters as Evidence for High Pressure Events

The Raman peak parameters of ureilite diamonds can place constraints on their formation environments and reveal any subsequent high-pressure events that have taken place post formation (e.g., Ross et al. 2011). Diamonds from terrestrial kimberlites have a Raman peak position of 1332.55 ± 0.1 cm^{-1} (Ross et al. 2011). These samples should have low residual stress in their structure and represent a point of comparison for ureilite diamonds. This value is consistent with the peak position determined in this current study for diamond polishing products (1332.8 ± 0.2 cm^{-1}) (Fig. 4.7). Peak positions that deviate from this position may indicate residual stresses caused by high pressure events or trace elements in the diamond structure. Positive shifts (above 1332.55 cm^{-1}) in peak position represent a residual compressive stress, while negative shifts represent residual tensile stress (Himics et al. 2016). A linear relationship has been found between these Raman peak shifts and static pressures (Fujii and Ohfuji 2015; Sharma et al. 1985). Ureilite diamonds show a broad range of peak positions and FWHM values (e.g. Ross et al. 2011) and we observe a broad range for NWA 11950 and 11951 as well. Not all of the peaks seen here are shifted, but the majority of peaks that are shifted have a negative shift in peak position (Fig. 4.7), representing residual tensile stress in the diamond structure. Similar negative shifts were observed by Ross et al. (2011) for ureilites, including those from the Almahata Sitta fall. Negative shifts, along with increases in FWHM (as seen in Fig. 4.7), can be attributed to shock formation environments (Nagashima et al. 2012; Miyamoto et al. 1993). Negative shifts can also be attributed to grain size in cases where diamond grains are on the order of a few nanometres. In such cases, the surface area to volume ratio is high enough that grain boundary effects dominate the spectra resulting in a negative shift (~1330 cm^{-1}) (Birrell et al. 2005). In the case of NWA 11950 and 11951, there is no obvious correlation between grain size and peak position. During the study of diamonds from the Ries Crater it was determined that diamond grains contained subgrain boundaries (El Goresy et al. 2001). Observation of this phenomenon at the nano-scale could be carried out on NWA 11950 and 11951 to further rule out grain size effects.

High pressure environments can also create the carbon phase known as lonsdaleite. It has recently been suggested that lonsdaleite is not a discrete structure, but is instead faulted and twinned cubic diamond (Németh et al. 2014). However, researchers have still located possible diagnostic peaks for the material. Smith and Godard (2009) suggest that lonsdaleite has a wide, weak and asymmetrical band centred at 1324 ± 4 cm^{-1} and possible a weaker wide band centred around 1225 cm^{-1}. Another study has suggested that the most intense peak occurs at 1292–1303 cm^{-1} with a less intense peak occurring at 1219–1244 cm^{-1} (Goryainov et al. 2014). The spectra observed for NWA 11950 and 11951 show no strong evidence for the presence of lonsdaleite.

4.5.3 Ruling out Diamond Contamination and Spectral Modification

The possibility of diamond contamination during the preparation of samples for study is an ever-present concern. Diamonds recently studied from the Earth's oldest zircons from the Jack Hills conglomerate are now thought to be contaminates (Dobrzhinetskaya et al. 2014). Nasdala et al. (2016) have shown that some diamond preparation products have spectra with broad diamond peaks and downshifted peak locations. Others have lesser, but positive band broadening at normal (ambient pressure) band positions. This is seen to some extent in the data presented in this current study. There is arguably a trend towards broader peaks and downshifted peak positions in some of the diamond preparation products (Fig. 4.7); however, this shift is not as significant as those seen in Nasdala et al. (2016) and our ureilite data are clearly separated from the diamond preparation products used here. This current study also confirmed that carbon-rich regions in the ureilites showed the same textural relationships in cases when they were polished with diamond and in cases where they were polished with alumina. When diamond preparation products are used these types of checks are essential, as it may not always be possible to tell the difference between these products and the samples in question (Nasdala et al. 2016).

Heating during Raman analyses can cause negative peak shifts in the diamond spectra (Gusakov et al. 2017) and these effects are grain size dependent (Zhao et al. 1998). In this current study, a low laser power was used to minimize the chances of peak shifts resulting from overheating the sample. The laser power used here is similar to that used

in other studies (e.g., Le Guillou et al. 2010; Nagashima et al. 2012) and in some cases lower (e.g., Hezel et al. 2008; Miyahara et al. 2015). Laser power tests were also run on the diamond preparation products to test for any spectral changes due to laser heating and no changes were found for the laser power used in this study (Appendix 4 - A4.6). Additionally, our data showed that many of the ureilite diamond grains actually have no shift at all. This confirms that they were unaffected by laser heating and it is unlikely that other grains measured in the same samples under the same conditions would show laser heating effects. This suggests that the peak shifting in the samples was caused by a heterogeneous process and not the result of direct heating by the laser.

4.5.4 Assessing Diamond Formation by Shock Metamorphism

In NWA 11950, the carbon-rich regions generally contain a central region rich in graphite. The edges of these regions are dominated by diamond next to the surrounding silicate grains (Fig. 4.8, Appendix 4 - A4.3). Examination of diamonds from the Ries Crater have revealed that shock-induced diamond formation occurred only in undeformed graphite at graphite-garnet, graphite-sillimanite, or graphite-rutile interfaces, where the difference in shock impedance was highest (El Goresy et al. 2001). This is consistent with simulations that show the presence of highly impedant surrounding materials favor the transition from graphite to diamond by generating a progressive increase in pressure through a shock accumulation process (Pineau et al. 2015). Based on texture, diamonds in NWA 11950 appear to have formed in the same manner. The highest pressures experienced in the carbon-rich regions of NWA 11950 were experienced along carbon-silicate grain boundaries, which is consistent with shockwaves passing from lower shock impedance materials (carbon) to higher shock impedance materials (silicates).

In NWA 11951, the carbon-rich regions are dominated by diamond, but also contain graphite. The association of these carbon phases, in both meteorites, suggests that the carbon-rich regions experienced inhomogeneous and dynamic pressure environments. This is again similar to diamond formation at the Ries Crater where textural relationships between graphite and diamond allow for a clear determination of the solid-state formation of diamond from graphite (El Goresy et al. 2001). The work of Le Guillou et al. (2010) on the ureilite NWA 4742 showed that there is a genetic relationship between diamond,

distorted graphite and disordered carbon that can be explained by shock formation of diamond from preexisting carbon phases. A study of the ureilite UAE 001 noted that compressed graphite around the diamonds, the existence of polycrystalline secondary graphite, and the large amounts of graphite accompanying the diamonds present are most easily explained by diamond formation during a shock event (Hezel et al. 2008).

A study of four ureilites (Lorenz et al. 2019) reported that the diamond grain size, morphology, textural relationships and photoluminescence spectral properties vary widely even within a single ureilite. They suggest the simplest explanation for this is that the diamonds were formed by shock metamorphism of diverse carbonaceous materials of differing structure, crystallinity and nitrogen content. The widely variable Raman peak shifting seen in this current study (Fig. 4.7) could be reasoned similarly; however, the variability could also be the result of a shock-induced process that generates heterogeneous conditions on a localized scale.

X-ray diffraction studies of diamond-bearing ureilites have shown the presence of compressed graphite, which is evidence of high-pressure conversion of graphite to diamond (Nakamuta and Aoki 2000). The coexistence of both high-pressure (diamond) and low-pressure (graphite) suggests the phase transition did not reach a state of equilibrium, supporting a short duration high-pressure event (Nakamuta and Aoki 2000). The work of Nakamuta and Toh (2013) on the Goalpara ureilite found that lonsdaleite and diamond form directly from graphite through boat-type buckling and chair-type puckering of hexagonal carbon planes, which suggests a shock origin of diamond in ureilites.

The work of Nakamuta et al. (2016) suggests that diamonds formed during shock events with metallic Fe as a catalyst. This could be a viable mechanism for many ureilites, as metal and carbon-rich regions are generally both located between silicate grains. This, however, does not seem to be the case for NWA 11950, which in one instance at least, exhibits metal veining right next to graphite (Fig. 4.8a) and diamonds forming in regions where metal is not present in the section (Fig. 4.8a-f, Appendix 4 - A4.3).

Limited CL work has been carried out to assess the connection between diamonds in ureilites and shock processes. However, the presence of diamond has been linked to shock stage for some ureilites (Bischoff et al. 1999) and similarities have been seen between CL spectra from ureilite diamonds and impact crater diamonds (Grund and Bischoff 1999). The combined CL and Raman mapping of NWA 11950 and 11951 adds needed contextual background for drawing links between CL identified diamonds and shock processes in ureilites.

4.5.5 Planetary (Static) and Chemical Vapor Deposition versus Shock Formation of Diamonds

Nabiei et al. (2018) suggest the composition and morphology of the inclusions in diamonds from the Almahata Sitta ureilite can be explained by the formation pressures in a Mercury- to Mars-sized planetesimal. While intriguing, this conclusion assumes a phase heritage for the inclusions, which requires further exploration. Locating these inclusions in additional ureilites will also be required before applying these conclusions to the ureilite parent body as a whole. Recent work on the same sample utilized by Nabiei et al. (2018) has concluded a shock origin for the diamonds present in the sample (Goodrich et al. 2020). The carbon-rich areas in which diamonds occur in the sample are in the shape of graphite laths. This is unlikely to occur during long-term static pressures and instead suggests a rapid (shock) production, which allows the graphite crystal form to remain (Goodrich et al. 2020). Larger-scale diamonds found in Almahata Sitta have also prompted suggestions that these diamonds may have formed in the deep interior of a large parent body. Fine-scale heterogeneous distribution of impurities (zonation) seen in these diamonds suggests slow growth (Miyahara et al. 2015). Single diamond grains seen in NWA 11950 and 11951 are generally < 10 μm in diameter (Fig. 4.6, Fig. 4.8, Appendix 4 - A4.3). Grains even smaller than this size range are difficult to form even in static high-pressure experiments (e.g., Sumiya et al. 2004), which has been used as an argument against shock formation of diamond in ureilites. However, it has been proposed that diamonds as large as ~1 cm could be formed by impacts (DeCarli et al. 2002). Seemingly large diamond grains (up to 200 μm) have been found at Ries Crater;

however, it was determined that these grains contained subgrain boundaries (El Goresy et al. 2001). This could be the case for NWA 11950 and 11951 as well.

Past Raman work on ureilite diamonds has shown peak shifts to higher wavenumbers and larger FWHM values. The shift of the diamond peaks to higher wavenumbers is generally thought to only be observed in chemical vapor deposition (CVD) diamonds (Nagashima et al. 2012). However, ultrahigh-pressure (UHP) metamorphic diamonds have also shown an upshift in peak position. The UHP studies suggest that the cause is not related to residual stress. Instead it may be related to structural defects and/or trace elements (Korsakov et al. 2015; Yang et al. 2003). Thus, positive peak shifts do not necessarily equate with CVD formation. In the case of NWA 11950 and 11951 the peak shifts, when they are present, are generally negative. The noble gas composition of some ureilite diamonds has also been attributed to CVD formation (Matsuda et al. 1991; Matsuda et al. 1995); however, work by Le Guillou et al. (2010) has shown that at least some ureilite diamond is formed from graphite. This led to a complex model of diamonds in ureilites that relies on multiple diamond formation mechanisms (Le Guillou et al. 2010).

Ureilites containing “shock generated diamonds” also tend to contain silicates with relatively few dislocations. Weber et al. (2003) suggested that the parent body must have been locally hot during the impact event(s), or that it heated up post-impact in order to minimize visible shock features in the silicates. The silicates in NWA 11950 and 11951 have a shock stage of U-S2 suggesting shock pressures of < 5GPa (Stoëffler et al. 2018). These pressures are still high enough to enter the diamond stability field (Bundy 1989) and higher pressures produced along carbon-silicate boundaries would increase the probability of forming diamond. It would actually be difficult to retain the graphite-diamond textures seen in NWA 11950 (Fig. 4.8, Appendix 4 - A4.3) at higher pressures, as the central graphite would be converted to diamond as well.

4.6 Conclusions

The meteorites NWA 11950 and 11951 are diamond-bearing ureilites. The mineralogical, textural and compositional properties of these meteorites suggest they are comparable to previously studied ureilites; however, oxygen isotope compositions place them both at

the heavy $\delta^{18}O$ end of the known ureilite compositional range. Larger-scale textural analysis and spectroscopic mapping reveals that both meteorites contain domains comprised of diamond and graphite. The carbon-rich regions in NWA 11950 consist of central graphite-rich regions. The edges of these regions contain diamond when adjacent to silicate grains. In NWA 11951, the carbon-rich regions are largely diamond. The association of these carbon phases suggests a formation environment that experienced spatially variable pressure conditions. The highest pressures were experienced along carbon-silicate grain boundaries, which is consistent with shockwaves passing from lower shock impedance materials (carbon) to higher shock impedance materials (silicates). This textural evidence for a shock metamorphic origin for the diamonds in NWA 11950 and 11951 adds to the growing list of studies linking ureilite diamonds to impact processes without the need for static pressurization within early planetesimals.

4.7 References

Barrat J. A., Rouxel O., Wang K., Moynier F., Yamaguchi A., Bischoff A. and Langlade J. 2015. Early stages of core segregation recorded by Fe isotopes in an asteroidal mantle. *Earth and Planetary Science Letters* 419:93-100.

Birrell J., Gerbi J. E., Auciello O., Gibson J. M., Johnson J. and Carlisle J. A. 2005. Interpretation of the Raman spectra of ultrananocrystalline diamond. *Diamond and Related Materials* 14(1):86-92.

Bischoff A., Goodrich C. A. and Grund T. 1999. Shock-induced origin of diamonds in ureilites (abstract #1100). 30th Lunar and Planetary Science Conference.

Bischoff A., Horstmann M., Barrat J. A., Chaussidon M., Pack, A., Herwartz D., Ward D., Vollmer C. and Decker S. 2014. Trachyandesitic volcanism in the early Solar System. *Proceedings of the National Academy of Sciences* 111(35):12689-12692.

Budde G., Kruijer T. S., Fischer-Gödde M., Irving A. J. and Kleine T. 2015. Planetesimal differentiation revealed by the Hf–W systematics of ureilites. *Earth and Planetary Science Letters* 430:316-325.

Bundy F. P. 1989. Pressure-temperature phase diagram of elemental carbon. *Physica A: Statistical Mechanics and its Applications* 156(1):169-178.

Clayton R. N. and Mayeda T. K. 1996. Oxygen isotope studies of achondrites. *Geochimica et Cosmochimica Acta* 60(11):1999-2017.

Clayton R. N. and Mayeda T. K. 1999. Oxygen isotope studies of carbonaceous chondrites. *Geochimica et Cosmochimica Acta* 63(13-14):2089-2104.

Day J. M., Corder C. A., Cartigny P., Steele A., Assayag N., Rumble III D. and Taylor L. A. 2017. A carbon-rich region in Miller Range 091004 and implications for ureilite petrogenesis. *Geochimica et Cosmochimica Acta* 198:379-395.

DeCarli P. S., Bowden E., Jones A. P. and Price G. D. 2002. Laboratory impact experiments versus natural impact events. *In Catastrophic Events and Mass Extinctions: Impacts and Beyond*, edited by Koeberl C. and MacLeod K. G. Boulder: Geological Society of America. pp. 595-605.

Dobrzhinetskaya L., Wirth R. and Green H. 2014. Diamonds in Earth's oldest zircons from Jack Hills conglomerate, Australia, are contamination. *Earth and Planetary Science Letters* 387:212-218.

El Goresy A., Gillet P., Chen M., Künstler F., Graup G. and Stähle V. 2001. In situ discovery of shock-induced graphite-diamond phase transition in gneisses from the Ries Crater, Germany. *American Mineralogist* 86(5-6):611-621.

Ferroir T., Dubrovinsky L., El Goresy A., Simionovici A., Nakamura T. and Gillet P. 2010. Carbon polymorphism in shocked meteorites: Evidence for new natural ultrahard phases. *Earth and Planetary Science Letters* 290(1-2):150-154.

Fujii T. and Ohfuji H. 2015. Pressure estimation using the 'diamond Raman scale' at low pressures in diamond anvil cell experiments using a highly confocal Raman system. *Measurement Science and Technology* 26(2) doi:10.1088/0957-0233/26/2/025501

Goodrich C. A., Wlotzka F., Ross D. K. and Bartoschewitz R. 2006. Northwest Africa 1500: Plagioclase-bearing monomict ureilite or ungrouped achondrite? *Meteoritics & Planetary Science* 41(6):925-952.

Goodrich C. A., Kita N. T., Spicuzza M. J., Valley J. W., Zipfel J., Mikouchi T. and Miyamoto M. 2011. The Northwest Africa 1500 meteorite: Not a ureilite, maybe a brachinite. *Meteoritics & Planetary Science* 45(12):1906-1928.

Goodrich C. A., Sutton S. R., Wirick S. and Jercinovic M. J. 2013. Chromium valences in ureilite olivine and implications for ureilite petrogenesis. *Geochimica et Cosmochimica Acta* 122:280-305.

Goodrich C. A., Harlow G. E., Van Orman J. A., Sutton S. R., Jercinovic M. J. and Mikouchi T. 2014. Petrology of chromite in ureilites: deconvolution of primary oxidation states and secondary reduction processes. *Geochimica et Cosmochimica Acta* 135:126-169.

Goodrich C. A., Kita N. T., Sutton S. R., Wirick S. and Gross J. 2017. The Miller Range 090340 and 090206 meteorites: Identification of new brachinite-like achondrites with implications for the diversity and petrogenesis of the brachinite clan. *Meteoritics & planetary science* 52(5):949-978.

Goodrich C. A., Nestola F., Jakubek R., Erickson T., Fries M., Fioretti A. M., D. K. Ross D. K. and Brenker F. E. 2020. The origin of diamonds in ureilites (abstract #1411). 51st Lunar and Planetary Science Conference.

Goryainov S. V., Likhacheva A. Y., Rashchenko S. V., Shubin A. S., Afanas'ev V. P. and Pokhilenko N. P. 2014. Raman identification of lonsdaleite in Popigai impactites. *Journal of Raman Spectroscopy* 45(4):305-313.

Grady M. M., Wright I. P., Swart P. K. and Pillinger C. T. 1985. The carbon and nitrogen isotopic composition of ureilites: implications for their genesis. *Geochimica et Cosmochimica Acta* 49(4):903-915.

Grund T. and Bischoff A. 1999. Cathodoluminescence properties of diamonds in ureilites: Further evidence for a shock-induced origin (abstract). *Meteoritics and Planetary Science Supplement* 34:A48.

Gusakov G. A., Samtsov M. P. and Voropay E. S. 2017. The effect of the laser-radiation power on the characteristics of the Raman line for diamond single crystals. *Journal of Applied Spectroscopy* 84(4):573-580.

Herrin J. S., Zolensky M. E., Ito M., Le L., Mittlefehldt D. W., Jenniskens P., Ross A. J. and Shaddad M. H. 2010. Thermal and fragmentation history of ureilitic asteroids: Insights from the Almahata Sitta fall. *Meteoritics & Planetary Science* 45(10-11):1789-1803.

Hezel D. C., Dubrovinsky L., Nasdala L., Cauzid J., Simionovici A., Gellissen M. and Schönbeck T. 2008. In situ micro-Raman and X-ray diffraction study of diamonds and petrology of the new ureilite UAE 001 from the United Arab Emirates. *Meteoritics & Planetary Science* 43(7):1127-1136.

Himics L., Tóth S., Veres M. and Koós M. 2016. Spectral properties of the zero-phonon line from ensemble of silicon–vacancy center in nanodiamond. *Optical and Quantum Electronics* 48(8):394.

Hyde B. C., Day J. M., Tait K. T., Ash R. D., Holdsworth D. W. and Moser D. E. 2014. Characterization of weathering and heterogeneous mineral phase distribution in brachinite Northwest Africa 4872. *Meteoritics & Planetary Science* 49(7):1141-1156.

Korsakov A. V., Toporski J., Dieing T., Yang J. and Zelenovskiy P. S. 2015. Internal diamond morphology: Raman imaging of metamorphic diamonds. *Journal of Raman Spectroscopy* 46(10):880-888.

Le Guillou C., Rouzaud J. N., Remusat L., Jambon A. and Bourot-Denise M. 2010. Structures, origin and evolution of various carbon phases in the ureilite Northwest Africa 4742 compared with laboratory-shocked graphite. *Geochimica et Cosmochimica Acta* 74(14):4167-4185.

Lorenz C. A., Shiryaev A. A., Vlasov I. I. and Borisovsky S. E. 2019. Metamorphism of four desert ureilites and luminescence spectroscopy of defects in ureilitic diamonds. *Meteoritics & Planetary Science* 54(6):1197-1214.

Matsuda J. I., Fukunaga K. and Ito K. 1991. Noble gas studies in vapor-growth diamonds: Comparison with shock-produced diamonds and the origin of diamonds in ureilites. *Geochimica et Cosmochimica Acta* 55(7):2011-2023.

Matsuda J.I., Kusumi A., Yajima H. and Syono Y. 1995. Noble gas studies in diamonds synthesized by shock loading in the laboratory and their implications on the origin of diamonds in ureilites. *Geochimica et cosmochimica acta* 59(23):4939-4949.

Miyahara M., Ohtani E., El Goresy A., Lin Y., Feng L., Zhang J. C., Gillet P., Nagase T., Muto J. and Nishijima M. 2015. Unique large diamonds in a ureilite from Almahata Sitta 2008 TC3 asteroid. *Geochimica et Cosmochimica Acta*, 163:14-26.

Miyamoto M., Takase T. and Mitsuda Y. 1993. Raman spectra of various diamonds. *Mineralogical Journal* 16(5):246-257.

Nabiei F., Badro J., Dennenwaldt T., Oveisi E., Cantoni M., Hébert C., El Goresy A., Barrat J. A. and Gillet P. 2018. A large planetary body inferred from diamond inclusions in a ureilite meteorite. *Nature communications* 9(1):1327.

Nagashima K., Nara M. and Matsuda J. I. 2012. Raman spectroscopic study of diamond and graphite in ureilites and the origin of diamonds. *Meteoritics & Planetary Science* 47(11):1728-1737.

Nakamuta Y. and Aoki Y. 2000. Mineralogical evidence for the origin of diamond in ureilites. *Meteoritics & Planetary Science* 35(3):487-493.

Nakamuta Y. and Toh S. 2013. Transformation of graphite to lonsdaleite and diamond in the Goalpara ureilite directly observed by TEM. *American Mineralogist* 98(4):574-581.

Nakamuta Y., Kitajima F. and Shimada, K. 2016. In situ observation, X–ray diffraction and Raman analyses of carbon minerals in ureilites: Origin and formation mechanisms of diamond in ureilites. *Journal of Mineralogical and Petrological Sciences* 111:252-269.

Nasdala L., Steger S. and Reissner C. 2016. Raman study of diamond-based abrasives, and possible artefacts in detecting UHP microdiamond. *Lithos* 265:317-327.

Németh P., Garvie L. A., Aoki T., Dubrovinskaia N., Dubrovinsky L. and Buseck P. R. 2014. Lonsdaleite is faulted and twinned cubic diamond and does not exist as a discrete material. *Nature communications* 5 doi:10.1038/ncomms6447.

Pineau N., Soulard L., Colombet L., Carrard T., Pellé A., Gillet P. and Clérouin J. 2015. Molecular dynamics simulations of shock compressed heterogeneous materials. II. The graphite/diamond transition case for astrophysics applications. *Journal of Applied Physics* 117(11) doi: 10.1063/1.4914481

Ross A. J., Steele, A., Fries M. D., Kater L., Downes H., Jones A. P., Smith C. L., Jenniskens, P. M., Zolensky M. E. and Shaddad M. H. 2011. MicroRaman spectroscopy of diamond and graphite in Almahata Sitta and comparison with other ureilites. *Meteoritics & Planetary Science* 46(3):364-378.

Rumble D. III, Zolensky M. E., Friedrich J. M., Jenniskens P. and Shaddad M. H. 2010. The oxygen isotope composition of Almahata Sitta. *Meteoritics & Planetary Science* 45(10-11):1765-1770.

Scott E. R., Taylor G. J. and Keil, K. 1993. Origin of ureilite meteorites and implications for planetary accretion. *Geophysical Research Letters* 20(6):415-418.

Sharma S. K., Mao H. K., Bell P. M., and Xu J. A. 1985. Measurement of stress in diamond anvils with micro-Raman spectroscopy. *Journal of Raman Spectroscopy* 16:350-352.

Sharp Z. D. 1990. A laser-based microanalytical method for the *in situ* determination of oxygen isotope ratios of silicates and oxides. *Geochimica Cosmochimica Acta* 54:1353-1357.

Smith C., Franchi I., Wright I., Grady M. and Pillinger C. 2001. New data on carbon isotopic compositions of some ureilites (abstract #1878). 32nd Lunar and Planetary Science Conference.

Smith D. C. and Godard G. 2009. UV and VIS Raman spectra of natural lonsdaleites: Towards a recognised standard. *Spectrochimica Acta Part A: Molecular and Biomolecular Spectroscopy* 73:428-435.

Sumiya H., Irifune T., Kurio A., Sakamoto S. and Inoue T. 2004. Microstructure features of polycrystalline diamond synthesized directly from graphite under static high pressure. *Journal of Materials Science* 39(2):445-450.

Stoëffler D., Hamann C. and Metzler K. 2018. Shock metamorphism of planetary silicate rocks and sediments: Proposal for an updated classification system. *Meteoritics & Planetary Science* 53(1):5-49.

Váczi T. 2014. A new, simple approximation for the deconvolution of instrumental broadening in spectroscopic band profiles. *Applied spectroscopy* 68(11):1274-1278.

Warren P. H. and Huber H. 2006. Ureilite petrogenesis: A limited role for smelting during anatexis and catastrophic disruption. *Meteoritics & Planetary Science* 41(5):835-849.

Warren P. H., Ulff-Møller F., Huber, H. and Kallemeyn G. W. 2006. Siderophile geochemistry of ureilites: a record of early stages of planetesimal core formation. *Geochimica et Cosmochimica Acta* 70(8):2104-2126.

Weber I., Bischoff A. and Weber D. 2003. TEM investigations on the monomict ureilites Jalanash and Hammadah al Hamra 064. *Meteoritics & Planetary Science* 38(1):145-156.

Wojdyr M. 2010. Fityk: a general-purpose peak fitting program. *Journal of Applied Crystallography* 43(5-1):1126-1128.

Yang J., Xu Z., Dobrzhinetskaya L. F., Green H. W., Pei X., Shi R., Wu C., Wooden J. L., Zhang J., Wan Y. and Li H. 2003. Discovery of metamorphic diamonds in central China: an indication of a > 4000-km-long zone of deep subduction resulting from multiple continental collisions. *Terra Nova* 15(6):370-379.

Zhao X. Z., Cherian K. A., Roy R. and White W. B. 1998. Downshift of Raman peak in diamond powders. *Journal of materials research* 13(7):1974-1976.

Chapter 5

Conclusions

The three substantive chapters of this thesis describe the meteoritic evidence for three types of early solar system processes observed in the rock record of asteroidal bodies. Collectively they present new knowledge regarding; regolith assembly, time constraints on early differentiation processes, and the nature of shock processes over-printing evidence of early melt environments. They include several important contributions such as a first documentation of an evolved eucrite impinging on a more primitive chondrite, and the discovery of remarkably old thermochronology ages from phosphate in asteroids. The information gained through this thesis has deepened our knowledge of early formative and modification processes on asteroids and developed a methodology for unlocking the rich meteoritic record of mechanisms at play prior to and during the formation of planets, moons and asteroids. Below are the primary conclusions of this work and suggestions for future work.

5.1 Primary Conclusions

5.1.1 Accretionary Impact Melting (Chapter 2)

Careful electron beam and isotopic analysis of an achondritic impactor clast in the meteorite NWA 869 resulted in the first recognition of eucritic material in an L chondrite breccia. This impact mixed the material in a rim around most of the clast and which experienced secondary heating and melting indicative of additional impact(s). The resulting basaltic melt exhibits bulk characteristics of some planetary achondrites and the rim's oxygen isotope composition falls on a mixing line between eucrite compositions and L chondrite compositions. It also coincidentally falls on the Mars fractionation line for oxygen isotopes. These findings underpin the importance of integrating the textural and chemical observations of meteorites entirely composed of breccia and impact melt products to preclude misinterpretation of provenance. Melt rim pyroxene compositions also fall on a mixing line between the average eucrite pyroxene composition and equilibrated L chondrite composition. Olivine compositions in the rim are more Fe-rich

than the L chondrite host. These pyroxene and olivine compositions are potential markers of such secondary impact melting processes in some complex, brecciated meteorites where meteorite melt products are not seen in context. Whereas larger impacts are thought to produce differentiation products (Fig. 5.1; Weiss and Elkins-Tanton 2013), the clast-rim in NWA 869 provides a level of context unavailable from these larger melt bodies and offers a window into the geochemical mixing occurring during these events albeit at a smaller scale. The juxtaposition of a differentiated clast (eucrite) in more primitive material indicates parallel differentiation paths operating at different rates during disk consolidation.

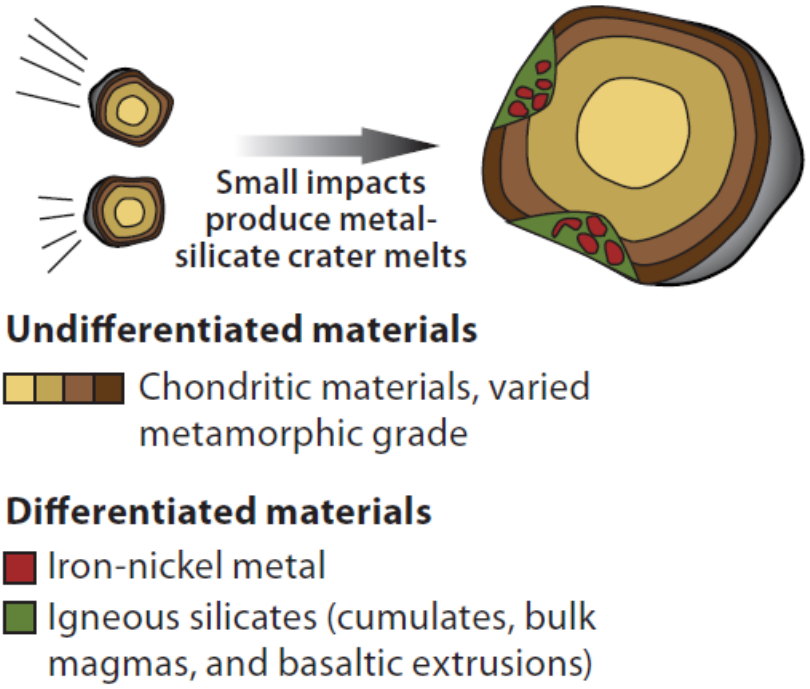

Figure 5.1. Production of differentiated materials through impacts (modified from Weiss and Elkins-Tanton 2013).

5.1.2 Thermal History of a Primitive Asteroid (Chapter 3)

Chapter 3 documents the first evidence of two stages of early asteroidal melting in the meteorites NWA 7680 and NWA 6962 and a first quantification of their thermal history through phosphate LA-ICP-MS geochronology. The meteorites are shown to be from the same parent body through observations of mineralogical and geochemical similarities.

Both meteorites have plagioclase abundances above that of chondritic meteorites and NWA 7680 is also Fe-metal-rich, suggesting they both formed through short-lived differentiation processes that resulted in the pooling of melt products. This occurred on a primitive CR chondrite-like parent body. Evidence of a secondary melt intrusion is observed in both meteorites. *In situ* dating of merrillite and fluorapatite reveals that NWA 7680 has remained below 350-550 °C for 4578 ± 17 Myr. Phosphates in NWA 6962 give similar ages to NWA 7680, falling within 2σ of the reported age (4556.6 ± 8.2 Myr old). The stable isotope compositions of these meteorites along with thermochronology data place constraints on reservoir separation in the early solar system, which has to have occurred within the first several million years after CAI formation. This study provides definitive evidence for early formed planetesimals and early differentiation. These differentiation processes could have occurred on a planetesimal with a differentiated interior, and a primitive (CR chondrite-like) exterior. A similar scenario has been proposed for the CV-CK chondrite parent body (Fig. 5.2; Elkins-Tanton et al. 2011). These parent bodies grew large enough to heat and differentiate on their interiors, but remained cool enough towards their exteriors to retain primitive textures. Another option is that NWA 7680 and NWA 6962 were formed from large-scale impact melting (Fig. 5.1); however, geochemical constraints and textural knowledge require that the impacting bodies in question had similar primitive compositions. The impact-melt would also have to remain molten long enough to produce the relatively coarse-grained textures seen. Additionally, a secondary impact would likely be required to produce the secondary melt intrusion. The conclusion is that very early processes, unmodified for most of the history of the solar system, are preserved in these classes of meteorites, opening the door to their further use in discriminating among competing disk evolution models.

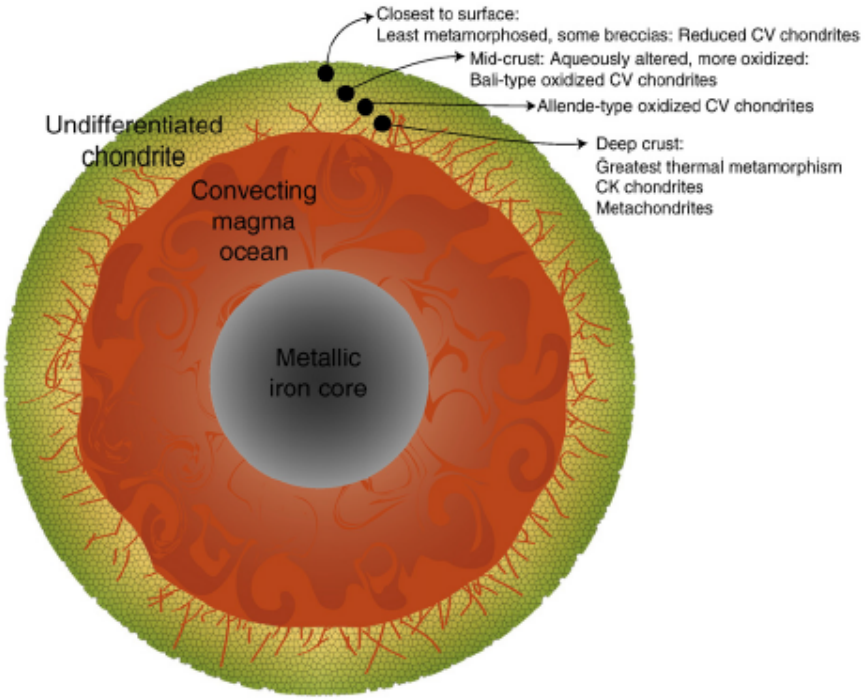

Figure 5.2. A cross-section of a proposed chondritic parent body with a differentiated central region and primitive crust with increasing metamorphic textures at depth (Elkins-Tanton et al. 2011).

5.1.3 Diamond Formation on a Partially Differentiated Parent Body (Chapter 4)

The ureilites NWA 11950 and 11951 are both diamond-bearing, yet the significance of the processes that created such diamonds ranges widely in the current literature between cm-scale shock wave-mineral interactions to Mars-size planetesimal interiors. It is shown that the ureilite mineralogical, textural and compositional properties are similar to those of previously studied ureilites; however, their oxygen isotope compositions place them both at the heavy $\delta^{18}O$ end of the known ureilite compositional range. Large-scale textural analysis and spectroscopic mapping of carbon domains revealed the distribution of diamond and graphite. The carbon-rich regions in NWA 11950 consist of central graphite-rich areas. The edges of these regions often contain diamond when adjacent to silicate grains. In NWA 11951, the carbon-rich regions are largely diamond. The intimate association of these carbon phases points to a formation environment that experienced

spatially variable pressure conditions. The highest pressures were experienced along carbon-silicate grain boundaries, which is consistent with shock waves passing from lower shock impedance materials (carbon) to higher shock impedance materials (silicates). The shock formation of diamonds in ureilites complicates the examination of early differentiation processes, as some studies suggest the requirement of a large planetesimal to form the diamonds through static pressures at depth (e.g., Nabiei et al. 2018). Detailed examination of the diamonds present in ureilites is required before placing pressure constraints on the early melting and differentiation processes recorded in ureilites.

5.2 Future Work

Several opportunities for additional discovery have been identified in the areas of geochronology and textural analysis. Further geochronology work on the eucrite clast in NWA 869 could reveal the absolute timing of the impact processes involved in the accretion of this material to the L chondrite parent body. The eucrite clast is particularly rich in the mineral zircon. Since this is a common geochronology micromineral, the study of the mineral's structure and its age can reveal a great deal about the clast's history. Examination of the microstructure of the zircons in the clast has already been carried out (Appendix 5) in preparation for future *in situ* U-Pb isotope ratio dating work. This would build on two studies that I coauthored during my Ph.D. One analyzed the microstructure and ages of the mineral baddeleyite in martian meteorites (Darling et al. 2016) and the other systematically looked at zircon textures in a variety of meteorites (Roszjar et al. 2017). Likewise, phosphate thermochronology on many different types of meteorites would test the extent of low-temperature processes at play in the early solar system. Low temperature thermochronometers are particularly useful for dating impact events in the solar system, since these events can provide a low-level heat source to large areas of the solar system through secondary impact heating (e.g. Yin et al. 2014). A systematic look at thermochronology records in a variety of meteorites may allow us to piece together impact histories for many regions of the solar system.

Large-scale mapping of carbon phases in a large number of ureilites would allow for a better view of impact processes in ureilites as a whole. There could in fact be multiple

formation mechanisms for diamond formation in ureilites. Through the observations of NWA 11950 and 11951 in this thesis, evidence can be shown for an impact origin of diamonds. However, this cannot be generalized to all ureilites without further study. Linking these large-scale textures to geochemical data could further inform our ideas of diamond formation mechanisms on the ureilite parent body. Linking these textures to smaller scale observations would also provide additional context for the diamond formation environments. In particular, cross-sections of diamonds could be examined using techniques already utilized in this thesis (e.g. Raman mapping and CL). These cross-sections could be produced using focused ion beam techniques or ion polishing techniques currently being explored by Desmond Moser. These cross-sections could also be examined with EBSD to look for changes in structure at the scale of 100's of nm.

5.3 References

Darling J. R., Moser D. E., Barker I. R., Tait K. T., Chamberlain K. R., Schmitt A. K. and Hyde B. C. 2016. Variable microstructural response of baddeleyite to shock metamorphism in young basaltic shergottite NWA 5298 and improved U–Pb dating of Solar System events. *Earth and Planetary Science Letters* 444:1-12.

Elkins-Tanton L. T., Weiss B. P. and Zuber M. T. 2011. Chondrites as samples of differentiated planetesimals. *Earth and Planetary Science Letters* 305(1-2):1-10.

Nabiei F., Badro J., Dennenwaldt T., Oveisi E., Cantoni M., Hébert C., El Goresy A., Barrat J. A. and Gillet P. 2018. A large planetary body inferred from diamond inclusions in a ureilite meteorite. *Nature communications* 9(1):1327.

Roszjar J., Moser D. E., Hyde B. C., Chanmuang C., and Tait K. 2017. Comparing chemical microstructures of some early solar system zircon from differentiated asteroids, Mars and Earth. *In Microstructural Geochronology: Planetary Records Down to Atom Scale*, edited by Moser D.E., Corfu F., Darling J.R., Reddy S.M., and Tait, K. Washington: American Geophysical Union. pp. 113-135.

Weiss B. P. and Elkins-Tanton L. T. 2013. Differentiated planetesimals and the parent bodies of chondrites. *Annual Review of Earth and Planetary Sciences* 41:529-560.

Yin Q. Z., Zhou Q., Li Q. L., Li X. H., Liu Y., Tang G. Q., Krot A. N. and Jenniskens P. 2014. Records of the Moon-forming impact and the 470 Ma disruption of the L chondrite parent body in the asteroid belt from U-Pb apatite ages of Novato (L6). *Meteoritics & Planetary Science*, *49*(8):1426-1439.

Appendix 1

Development of quantitative energy dispersive spectrometry with a field emission gun scanning electron microscope for use in meteorite studies

The Hitachi SU6600 Field Emission Gun Scanning Electron Microscope (FE-SEM) housed in the Zircon and Accessory Phase Laboratory is being developed for non-destructive *in situ* characterization of meteorites and their geochronology phases. Electron backscatter diffraction (EBSD) and cathodoluminescence (CL) protocols have already been established to examine mineral orientation and chemical microstructure, respectively (Moser et al. 2013). Here we present initial results of quantitative standards-based analyses of olivine via energy dispersive spectrometry (EDS), with the goal of assessing precision and accuracy of EDS point and mapping analyses to determine if evaluation of olivine equilibration is possible with this instrument. According to the Meteorite Nomenclature Committee, equilibrated meteorite olivine has measured fayalite numbers (Fa=Fe/Fe+Mg, in AFU) with standard deviations (σ) below 1.6, hence precision below this value is required.

The mineral standards used include forsterite (Mogok, Myanmar), fayalite (Rockport, Massachusetts) and olivine from the Springwater pallasite meteorite (Table A1.1). All minerals are from the collection of the Royal Ontario Museum (ROM). The forsterite and fayalite have been developed as standards for use in electron probe microanalysis (EPMA) wavelength dispersive spectrometry (WDS) at Queen's University, and Springwater olivine is included in the list of Smithsonian Microbeam Standards (Jarosewich 2002).

Beam stability was tested using a Faraday cup, positioned in the column, with two different aperture set-ups. The first arrangement consisted of a 50 µm anode aperture and 100 µm objective aperture, while the second comprised a 30 µm anode aperture and 50 µm objective aperture. The second set-up provided better stability, and this appears to be independent of beam current (Fig. A1.2). Beam stability was also measured with a Faraday cup on the sample stage prior to analyses ($\sigma < 0.007$ nA). The beam conditions

used at this optimal aperture setting were 15 kV accelerating voltage and 0.272 nA beam current. An Oxford XMax silicon drift detector (80 mm^2) was used for EDS measurements (INCA software). A conductive Si standard (commercial wafer) was used to verify and adjust peak positions and monitor beam current. Carbon coat thicknesses of the two standard mounts in use were 17.2 nm and 27.8 nm, as determined by GMRfilm software (Waldo 1988). Standards and unknowns were always coated with the same thickness. Standardization points and points treated as "unknowns" from the standards were analyzed in point mode (500,000x magnification - submicrometre) for 180 s and 150 s respectively (>200,000 total counts on unknowns). Dead time was kept at ~10% for the olivine to minimize coincidence peaks (Newbury and Ritchie 2013). For quantitative mapping, a resolution of 256 x 192 pixels was used, and 4 frames were acquired with a dwell time of 120 ms per pixel. All values from mapped spots were normalized and used in calculations.

The point analyses provided major and some minor element compositions, and the 2σ ranges from the FE-SEM EDS and EPMA WDS data always overlapped (Table A1.1). All oxygen values were determined by stoichiometry and totals were between 99.42 and 100.82 wt.%. The use of Springwater olivine as the Fe standard for fayalite analyses did require a large extrapolation. However, Fe was also determined with a magnetite standard resulting in an identical Fe composition (within 2σ range). Fortunately, for future unknown samples, all three olivine standards will be available for use. Quantitative mapping of Springwater olivine provided major element compositions; however, σ values were much larger (Table A1.1) than point analyses due to lower dwell times at each spot and the inclusion of points containing associated phases, edge effects, cracks and other imperfections.

This instrument provides quantitative EDS capabilities alongside other analytical modes (e.g. CL and EBSD). The EDS analysis times and precision are similar to EPMA WDS; however, WDS analyses are needed to measure concentrations below EDS detection limits and are preferred when EDS peaks overlap. For point analyses, the equilibrated Springwater olivine has a Fa 2σ value of 0.3, meaning equilibration of olivine in meteorites can be examined with this instrument. Lower count times could be used for

faster determinations of equilibration, but precision would need to be monitored. Mapping data are useful for determining average composition and phase associations. Future work will expand the EDS practices to other phases and WDS capabilities will be developed for this instrument.

Table A1.1. EPMA WDS or bulk, EDS point and mapping compositions. "BRJ EPMA" – EPMA WDS standard compositions determined by author. "N.Q." - present, but not quantified. Standards used were 1forsterite (Mg, Si), 2fayalite (Fe), 3Springwater (Fe, Mg, Si) and not discussed here 4spessartine (Mn).

	Mg	Si	Ca	Cr	Mn	Fe	Zn	O	Total	[Data Source],Museum #
Wt.% ±1σ										***Standards used***
Forsterite (N=40)	34.49±0.13	19.97±0.06	0.03±0.01	-	0.01±0.01	0.07±0.01	-	45.49±0.12	100.06	[BRJ EPMA], ROM M56929
EDS Points (N=10)	**34.83±0.14**	**19.81±0.12**	-	-	-	-	-	**45.48±0.22**	**100.12**	*3*
Fayalite (N=43)	0.01±0.004	13.81±0.04	0.03±0.01	-	1.87±0.03	52.29±0.22	0.91±0.03	31.50±0.09	100.42	[BRJ EPMA], ROM E2197
EDS Points (N=10)	-	**13.64±0.06**	-	-	**1.90±0.04**	**52.23±0.17**	**N.Q.**	**31.28±0.10**	**99.05**	*3, 4*
Springwater Olivine (Bulk)	26.28	18.21	-	0.01	0.23	12.92	-	41.82	99.47	[Jarosewich 2002],
EDS Points (N=9)	**26.20±0.07**	**18.41±0.07**	-	-	**0.26±0.04**	**13.17±0.11**	-	**42.07±0.11**	**100.12**	ROM M56009
EDS Map	**26.34±1.22**	**18.62±1.35**	-	-	-	**12.98±2.32**	-	**42.19±0.90**	**100.13**	1, 2, 4

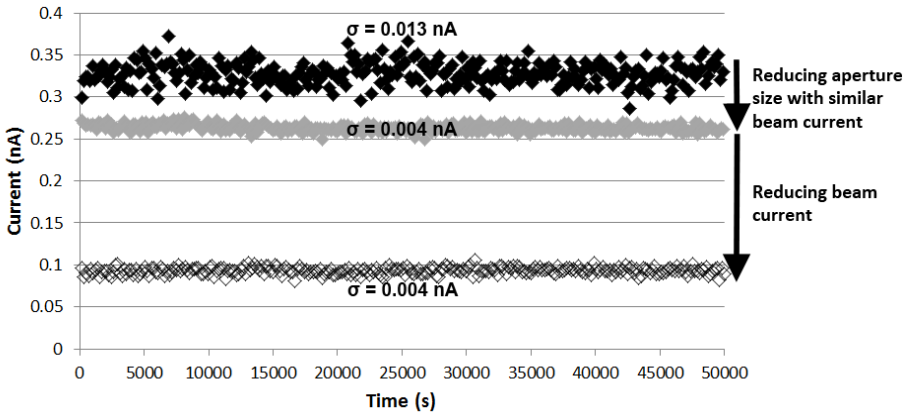

Figure A1.2. Electron beam stability. Beam current data are averaged over the analysis time used for points.

References

Jarosewich E. 2002. Smithsonian microbeam standards. *Journal of Research of the National Institute of Standards and Technology* 107(6):681.

Moser D. E., Chamberlain K. R., Tait K. T., Schmitt A. K., Darling J. R., Barker I. R. and Hyde B. C. 2013. Solving the Martian meteorite age conundrum using micro-baddeleyite and launch-generated zircon. *Nature* 499: 454-457.

Newbury D. E. and Ritchie N. W. 2013. Is scanning electron microscopy/energy dispersive X-ray spectrometry (SEM/EDS) quantitative? *Scanning* 35(3):141-168.

Waldo R. A. 1988. in Microbeam Analysis, edited by Newbury D. San Francisco: San Francisco Press). pp. 310-314.

Appendix 2

Chapter 2 – Supplementary Material

Table A2.1. EPMA Standards (left) used for analysis of sample (top) compositions. Elements standardized from each standard are given in the table.

Standards\Sample	Pigeonite	Augite	Anorthite	Silica[a]	Ilmenite	Sulfide[b]
Albite	Na	Na	Na	Na		Al
Anorthite	Al	Al	Si, Al, Ca	Al, Ca		
Chromite					Cr, Al, Mg	
Forsterite			Mg	Mg		
Ilmenite					Ti, Fe	
Orthoclase			K	K		
Quartz				Si		
Rhodonite	Mn	Mn	Mn	Mn		Mn
Rutile	Ti	Ti	Ti	Ti		Ti
Zircon					Zr	
Co Metal						Co
Ni Metal						Ni
V Metal						V
Synthetic CoNb2O6					Nb	
Synthetic Cr2O3	Cr	Cr				Cr
Synthetic Diopside	Si, Mg, Ca	Si, Mg, Ca			Si, Ca	Si, Mg
Synthetic Fayalite	Fe	Fe	Fe	Fe		
synthetic hausmannite					Mn	
Synthetic Pyrrhotite						S, Fe
Synthetic V2O3	V	V			V	

[a]Some of the silica is quartz, while other areas are amorphous or perhaps microcrystalline.

[b]Sulfide structure was not determined.

Table A2.2. Quantitative EDS/WDS Standards (left) used for analysis of sample (top) compositions. Elements standardized from each standard are given in the table. The lower half of the table presents analysis conditions for the two set-ups used.

Standards\Sample	Olivine	Pyroxene*
Forsterite	Mg, Si	Mg
Fayalite	Fe	Fe
Diopside		Si, Ca
	Quantitative EDS	Quantitative EDS/WDS(Fe)
Accelerating Voltage (kV)	15	15
Beam Current (nA)	0.28	15.19
Analysis Time (s)		
Standard	180	90(EDS),100(WDS)
Sample	150	70(EDS),80(WDS)
Standard Background (WDS) (s)		25
Sample Background (WDS) (s)		20

* Compositions are often intermediate between pigeonite and augite.

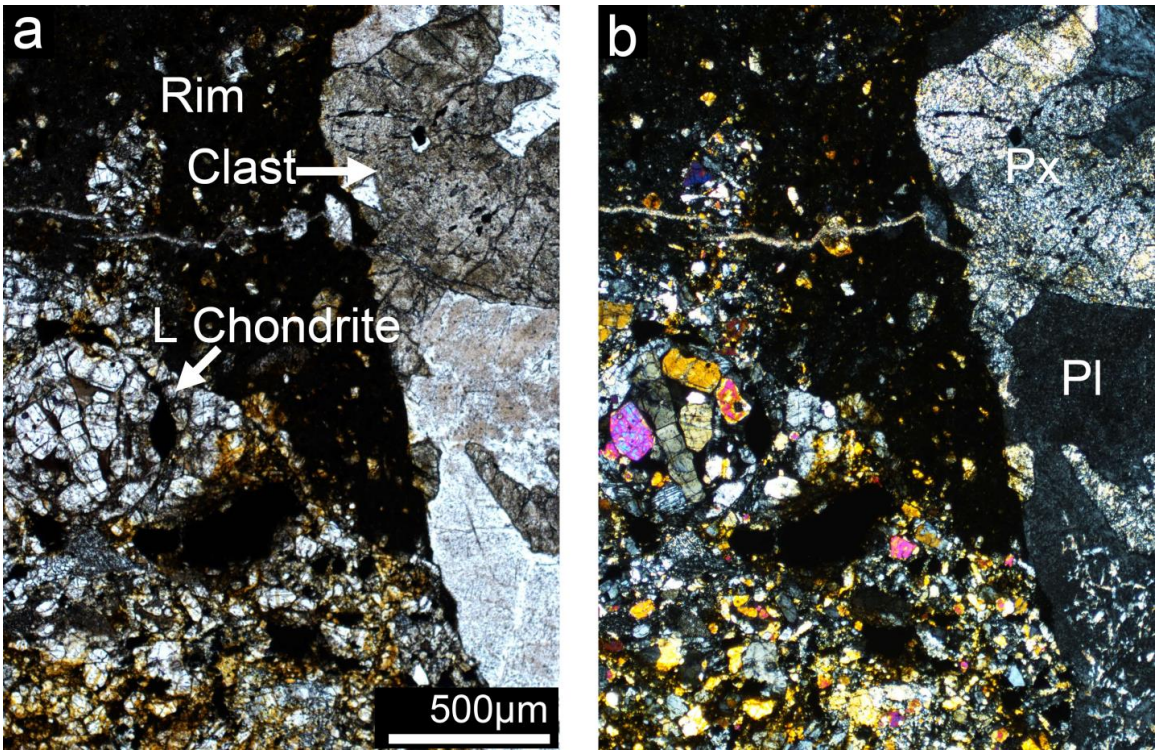

Figure A2.3. a) Plane-polarized light and b) crossed-polarized light images of the three lithologies present in the thin section.

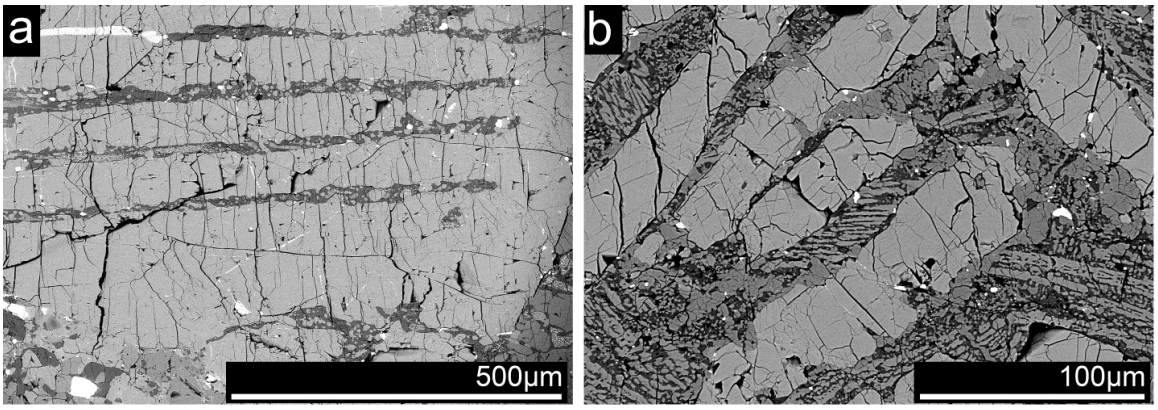

Figure A2.4. Backscatter electron images of equilibrated chondrules showing primitive textures and evidence of later thermal metamorphism such as: a) barred olivines and b) crystalized mesostasis of pyroxene and plagioclase.

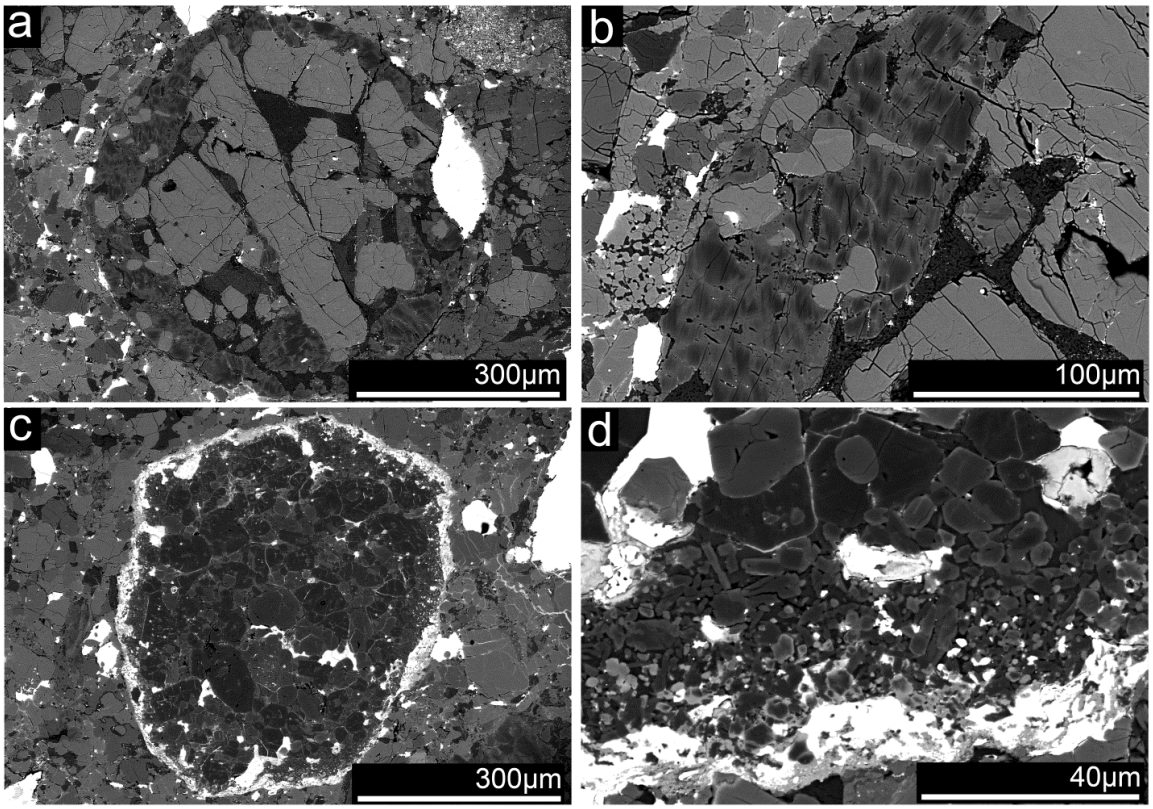

Figure A2.5. Backscatter electron images of a) Unequilibrated pyroxene in chondrule showing zoned pyroxene (b). c) An armored chondrule with an igneous rim (d).

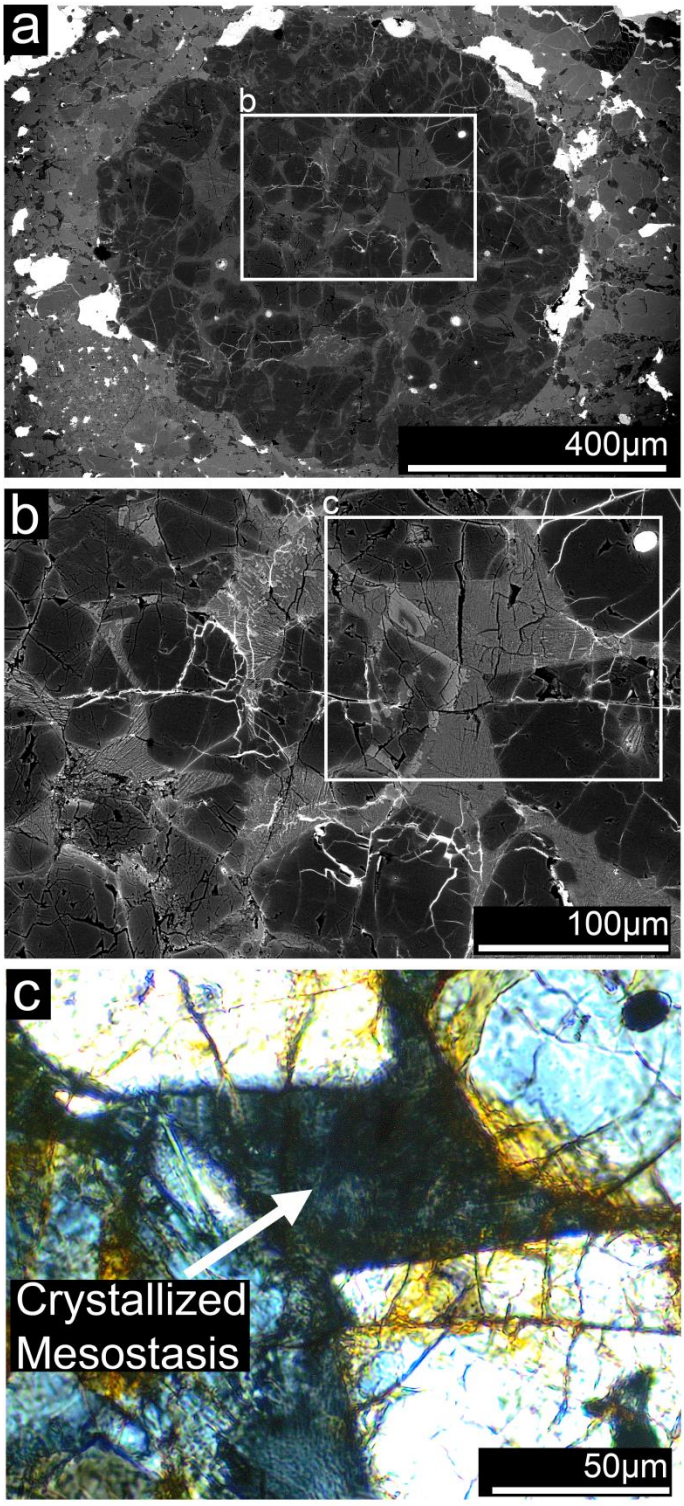

Figure A2.6. Backscatter electron images of a) and b) show a dark (in BSE) magnesium-rich chondrule with abundant veins of iron and crystallized mesostasis regions (c).

Table A2.7. Composition of olivine and pyroxene from the unequilibrated chondrules and the melt rim as determined by quantitative EDS.

	Olivine Fa (mol%)			Low-Ca Pyroxene Fs (mol%)		
Lithology	Average ±1σ	Min-Max	n	Average ±1σ	Min-Max	n
Unequilibrated Olivine Chondrules						
Armored chondrule with igneous rim	10.2±2.4	6.5-14.4	10	3.9±0.8	3.3-5.8	10
Fe-poor chondrule	2.4±2.9	0.5-9.5	10	1.0±0.7	0.7-3.1	11
Unequilibrated Pyroxene Chondrules						
Chondrule adjacent rim	24.2±0.3	23.7-24.6	8	12.0±5.3	3.6-18.8	16
Chondrule away from rim	21.0±0.7	20.2-22.1	10	9.0±3.7	4.5-16.2	17

	Olivine Fa (mol%)			Low-Ca Pyroxene Fs, Wo (mol%)		
	Average ±1σ	Min-Max	n	Average ±1σ	Min-Max	n
Rim Composition	51.6±7.5	39.4-71.5	17	31.2±2.2, 13.6±3.7	28.0-34.9, 7.3-20.9	17

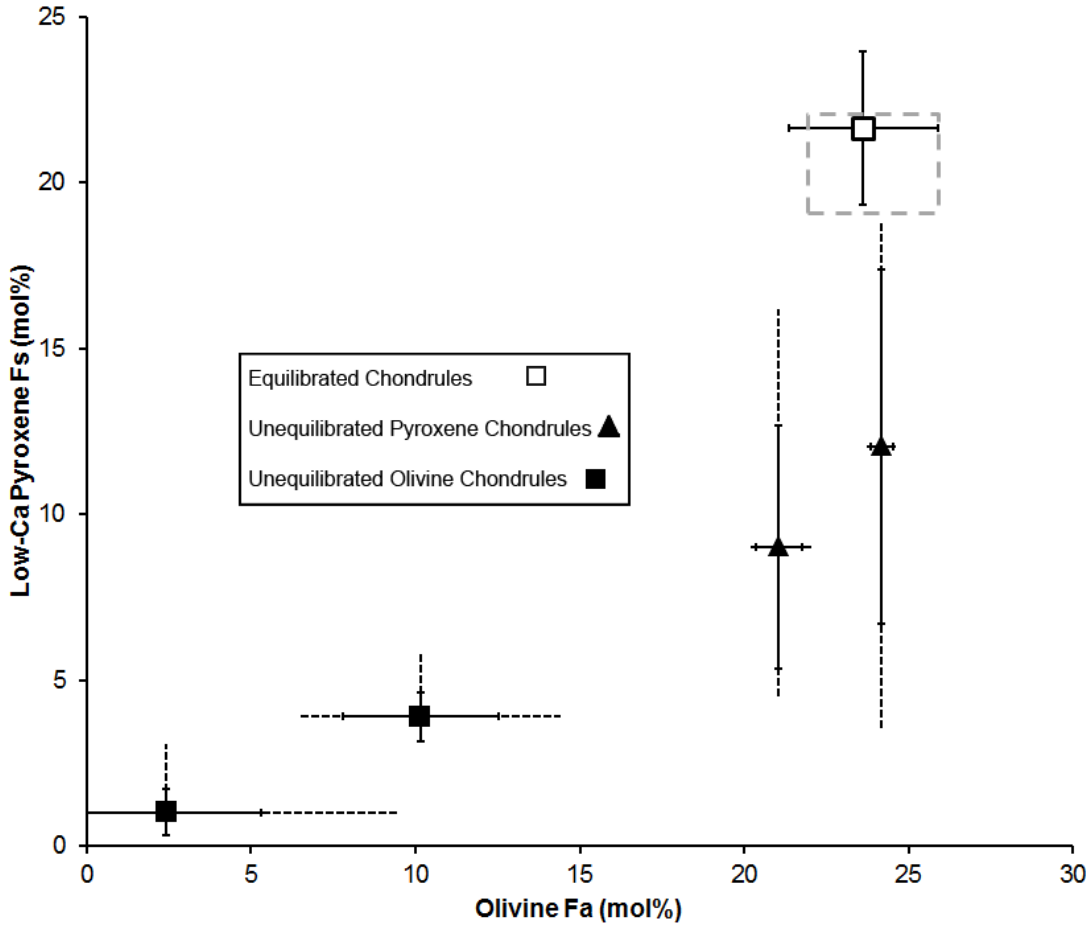

Figure A2.8. Fayalite (Fa) and ferrosilite (Fs) values for olivine and low-Ca pyroxene for chondrules in NWA 869. Solid lines denote the standard deviation and dotted lines show the full range of values for the unequilibrated materials. The region for equilibrated L-chondrites (Brearley and Jones 1998) is outlined in grey.

A2.9 The NWA 869 Designation

As mentioned previously, the stone used in this study was purchased alongside the type specimen. Also, olivine and pyroxene compositions and oxygen isotope compositions are consistent with and L chondrite (Appendix 2 - A2.7 and A2.8, Fig. 2.9). Unequilibrated chondrules were found including chondrules containing compositionally zoned pyroxene, an armored chondrule with an igneous rim and an Mg-rich chondrule (Appendix 2 - A2.5 and A2.6). These unequilibrated chondrules have more Mg-rich pyroxene compositions then the surrounding equilibrated material. In cases where olivine is also unequilibrated,

the Mg-content is also higher (Appendix 2 - A2.7 and A2.8). Unequilibrated materials with Mg-rich compositions have been seen in past work on NWA 869 (Metzler et al. 2011). The inclusion of a xenolithic clast and preserved melt/breccia rim suggest the impacted material (see Rim Formation section) was near surface and suffered very little brecciation following the impact. This is consistent with NWA 869 being termed a regolith breccia in past studies (e.g., Welten et al. 2011). In summary, the current study material should be designated as NWA 869 for the following reasons:

1. Determined to be an L chondrite breccia through multiple techniques;

2. Contains both equilibrated and unequilibrated chondrules as seen in past work on NWA 869;

3. Contains pristine impactor material and melt/breccia suggestive of a regolith origin.

Future work on potential NWA 869 material could use a simplified plan of study to confirm the materials designation. Confirmation of the material as an L chondrite breccia is an obvious first step. Locating unequilibrated chondrules could be done visually by looking for textures described here (Appendix 2 - A2.5 and A2.6). Armored chondrules, igneous rims and zoned pyroxene are all easily identified primitive textures. Information regarding the materials provenance should also be included especially in cases where material can be related to previously studied material and/or the type material (e.g., identical collection and/or dealer). Linking potential NWA 869 meteorites to noble gas and cosmogenic radionuclide measurements, when possible, can provide additional details of the samples regolith origins (Welten et al. 2011).

The L chondrite breccia material in this specific stone showed textures related to shock and post-shock heating. The extent of brecciation resulted in formation of “chondrule-clasts” and post-shock heating has crystallized mesostasis (e.g., Appendix 2 - A2.6c). This breakdown and crystallization are further signatures left by the impact processes involved in regolith formation.

References

Brearley A. J. and Jones R. H. 1998. Chondritic meteorites. In Planetary materials, edited by Papike J. J. Reviews in mineralogy, vol. 36. Washington: The Mineralogical Society of America. pp. 3.1–3.398.

Metzler K., Bischoff A., Greenwood R. C., Palme H., Gellissen M., Hopp J., Franchi I. A., and Trieloff M. 2011. The L3–6 chondritic regolith breccia Northwest Africa (NWA) 869: (I) Petrology, chemistry, oxygen isotopes, and Ar-Ar age determinations. *Meteoritics & Planetary Science* 46(5): 652-680.

Welten K., Leclerc M. D., Ott U., Metzler K., Caffee M. W., Jull A. J. T., and Franke L. 2011. The L3-6 chondritic regolith breccia Northwest Africa (NWA) 869: (II) Noble gases and cosmogenic radionuclides. *Meteoritics &Planetary Science* 46(7):970-988.

Appendix 3

Chapter 3 – Supplementary Material

Table A3.1. EPMA Standards (left) used for analysis of sample (top) compositions. Elements standardized from each standard are given in the table.

Standards\Sample	Olivine	Clinopyroxene	Feldspar	Nepheline	Fluorapatite	Chromite	Metal	Sulfide
Olivine	Si, Mg	Mg			Si, Mg			
Albite	Al, Na	Al, Na	Si, Na	Si, Na	Na		Al, Na	Al, Na
Rutile	Ti	Ti	Ti	Ti		Ti		
Chromite	Cr	Cr						
Rhodonite	Mn	Mn	Mn	Mn	Mn			
Diopside	Ca	Si, Ca	Mg	Mg		Si		
Orthoclase	K	K	K	K	Al, K			
Bytownite			Al, Ca					
Anorthite				Al, Ca				
Tugtupite				Cl	Cl			
Hematite					Fe			
Apatite					Ca, P, F			
Gahnite						Zn		
Co Metal	Co	Co				Co	Co	Co
Pure Si							Si	Si
Ni Metal							Ni	Ni
Cr Metal							Cr	Cr
Fe Metal							Fe	Fe
Ti Metal							Ti	Ti
Mn Metal							Mn	Mn
Synthetic V_2O_3	V	V						
Synthetic V_2O_5						V		
Synthetic Fayalite	Fe	Fe	Fe	Fe				
Synthetic Liebenbergite	Ni	Ni						
Synthetic Spinel						Al, Mg		
Synthetic Cr_2O_3						Cr		
Synthetic Magnetite						Fe		
Synthetic Hausmannite						Mn		
Synthetic Ni-Olivine						Ni		
Synthetic Pyrrhotite							S	S
Synthetic Forsterite							Mg	Mg
Synthetic $Ca_2P_2O_7$							P	P

Table A3.2. Composition of feldspar in order of increasing An-content.

NWA 7680						NWA 6962					
K_2O	**CaO**	**Na_2O**	**Or**	**An**	**Ab**	**K_2O**	**CaO**	**Na_2O**	**Or**	**An**	**Ab**
12.48	0.43	2.92	72.23	2.09	25.68	0.29	0.9	11.37	1.58	4.12	94.29
13.12	0.51	2.47	75.83	2.48	21.70	0.63	1.43	11.25	3.33	6.34	90.33
12.04	0.77	3.16	68.84	3.70	27.46	0.22	1.57	10.86	1.22	7.31	91.47
14.14	1.11	1.19	83.76	5.52	10.71	0.2	1.65	11.36	1.06	7.35	91.59
10.92	1.17	3.62	62.74	5.65	31.61	0.22	1.82	10.82	1.21	8.40	90.39
7.53	1.19	5.96	42.81	5.68	51.50	0.17	1.93	10.82	0.93	8.89	90.18
5.47	1.59	7.2	30.82	7.52	61.66	0.09	3.71	9.83	0.50	17.17	82.33
3.95	1.94	8.09	22.10	9.12	68.79	0.09	3.8	9.92	0.49	17.38	82.13
3.36	2.29	8.16	19.00	10.88	70.13	0.11	3.84	9.83	0.60	17.65	81.75
1.15	3.54	9.18	6.36	16.45	77.19	0.1	4.04	9.8	0.54	18.45	81.00
1.16	3.64	8.96	6.50	17.14	76.35	0.14	4.03	9.74	0.76	18.47	80.77
0.99	4.05	8.77	5.59	19.20	75.22	0.12	4.44	9.56	0.65	20.29	79.06
0.59	4.13	9.21	3.27	19.21	77.52	0.09	4.6	9.46	0.49	21.08	78.43
0.47	4.61	8.89	2.63	21.69	75.68	0.07	4.84	9.3	0.38	22.25	77.37
0.86	4.72	8.7	4.77	21.97	73.27	0.08	4.87	9.29	0.44	22.36	77.20
0.74	4.69	8.6	4.17	22.19	73.64	0.07	4.92	9.11	0.39	22.90	76.72
0.57	4.69	8.69	3.22	22.23	74.55	0.1	5.18	9.37	0.54	23.28	76.19
0.81	4.78	8.51	4.56	22.61	72.83	0.11	5.13	9.24	0.60	23.34	76.07
0.57	4.91	8.88	3.13	22.67	74.20	0.1	5.13	9.23	0.54	23.37	76.09
0.73	4.78	8.45	4.15	22.83	73.02	0.05	5.2	9.32	0.27	23.50	76.23
0.62	4.82	8.47	3.53	23.08	73.39	0.09	5.11	9.12	0.49	23.53	75.98
0.52	4.9	8.59	2.94	23.26	73.80	0.04	5.15	9.19	0.22	23.59	76.19
0.79	5.09	8.61	4.35	23.55	72.10	0.04	5.19	9.22	0.22	23.67	76.11
0.58	5.14	8.81	3.17	23.61	73.22	0.07	5.5	9.57	0.36	24.02	75.62
0.53	5.73	8.36	2.94	26.66	70.40	0.06	5.43	9.13	0.32	24.66	75.02
0.66	5.73	8.07	3.72	27.13	69.15	0.11	5.44	8.91	0.60	25.08	74.32
0.54	5.89	8.28	2.99	27.37	69.64	0.08	5.36	8.77	0.45	25.13	74.42
0.60	5.97	7.87	3.41	28.53	68.06	0.09	5.53	8.95	0.49	25.33	74.18
0.50	6.28	7.87	2.82	29.74	67.44	0.06	5.56	8.95	0.33	25.47	74.20
0.43	7.13	7.56	2.40	33.44	64.16	0.07	5.68	9.11	0.37	25.53	74.10
0.31	7.2	7.41	1.76	34.32	63.92	0.1	5.53	8.67	0.56	25.92	73.53
0.42	7.11	7.24	2.41	34.33	63.26	0.07	5.76	9.05	0.38	25.92	73.70
0.41	7.57	7.31	2.29	35.56	62.14	0.06	6.03	8.93	0.32	27.09	72.59
0.35	7.71	7.17	1.97	36.54	61.49	0.04	5.92	8.67	0.22	27.34	72.44
0.24	7.99	7.04	1.36	38.02	60.62	0.06	5.97	8.72	0.33	27.36	72.31
0.30	8.23	6.74	1.72	39.60	58.68	0.07	5.93	8.45	0.39	27.83	71.77
0.28	8.38	6.69	1.60	40.25	58.15	0.17	6.51	9.05	0.88	28.19	70.93

0.35	8.33	6.56	2.02	40.40	57.58	0.05	6.25	8.75	0.27	28.22	71.51
0.32	8.71	6.55	1.82	41.59	56.59	0.06	6.08	8.5	0.33	28.24	71.43
0.30	8.83	6.65	1.68	41.61	56.71	0.09	6.42	8.68	0.48	28.87	70.64
0.29	8.72	6.57	1.65	41.61	56.74	0.08	6.51	8.63	0.43	29.29	70.28
0.23	8.99	6.34	1.32	43.35	55.33	0.14	6.61	8.68	0.74	29.40	69.86
0.19	9.4	6.33	1.07	44.59	54.34	0.05	6.42	8.38	0.28	29.66	70.06
0.23	9.64	5.92	1.33	46.74	51.94	0.1	6.63	8.59	0.53	29.74	69.73
0.23	10.22	5.81	1.30	48.65	50.05	0.08	6.69	8.67	0.42	29.77	69.81
0.23	10.24	5.82	1.30	48.66	50.04	0.06	6.75	8.71	0.32	29.89	69.79
0.21	10.27	5.85	1.18	48.66	50.16	0.05	6.55	8.36	0.27	30.13	69.59
0.20	10.58	5.73	1.12	49.94	48.94	0.08	7.02	8.55	0.42	31.08	68.50
0.21	10.36	5.52	1.21	50.29	48.49	0.12	6.86	8.19	0.65	31.43	67.91
0.22	10.44	5.37	1.28	51.13	47.59	0.08	7.1	8.48	0.42	31.50	68.08
						0.06	6.85	8.15	0.33	31.61	68.06
						0.08	6.97	8.23	0.43	31.74	67.82
						0.1	7.33	7.94	0.55	33.60	65.86
						0.1	7.34	7.84	0.55	33.91	65.54

Table A3.3. Average CI chondrite normalized rare earth element compositions for minerals in NWA 7680 and 6962.

NWA 7680	olivine	plagioclase	phosphate	pyroxene
La		1.268	260.987	5.524
Ce		0.602	260.261	3.702
Pr		0.446	245.237	3.434
Nd		0.395	248.403	3.202
Sm			230.392	3.623
Eu		20.424	46.377	4.865
Gd			194.784	4.334
Tb	0.253		180.039	6.386
Dy	0.345		171.130	6.739
Ho	0.550		138.513	7.179
Er	0.995		111.050	6.137
Tm	1.364		80.146	8.236
Yb	1.669		57.193	6.250
Lu	1.982		37.423	7.254

NWA 6962	olivine	plagioclase	phosphate	pyroxene
La		0.870	253.558	2.562
Ce		0.549	237.281	3.504
Pr		0.322	233.387	4.635
Nd		0.280	238.249	5.730
Sm	0.057		223.108	7.869
Eu		17.298	45.382	3.087
Gd			201.742	8.758
Tb			182.747	9.338
Dy	0.339		177.818	10.477
Ho	0.653	0.116	154.078	10.026
Er	1.035		126.875	9.336
Tm	1.712		98.887	9.344
Yb	1.978		69.534	9.454
Lu	2.523		45.976	10.066

Appendix 4

Chapter 4 – Supplementary Material

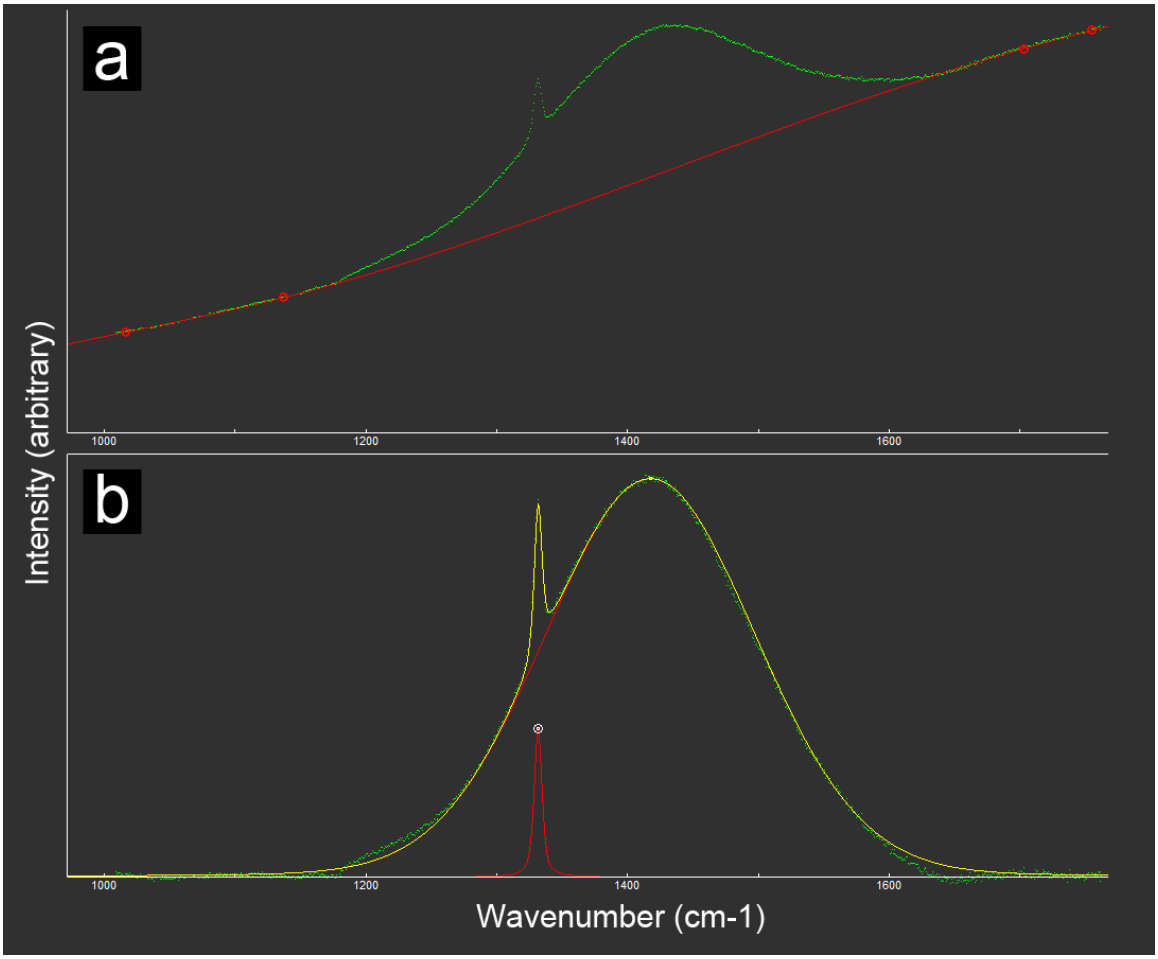

Figure A4.1. Peak fitting for spot analyses using the Fityk program (Wojdyr 2010). a) Background fluorescence is first removed (red line). b) pseudo-Voigt peak shapes are then used for fitting (red). Peak centres, full width at half maximums (FWHM) and shape parameters were manually adjusted to give the best fit (yellow).

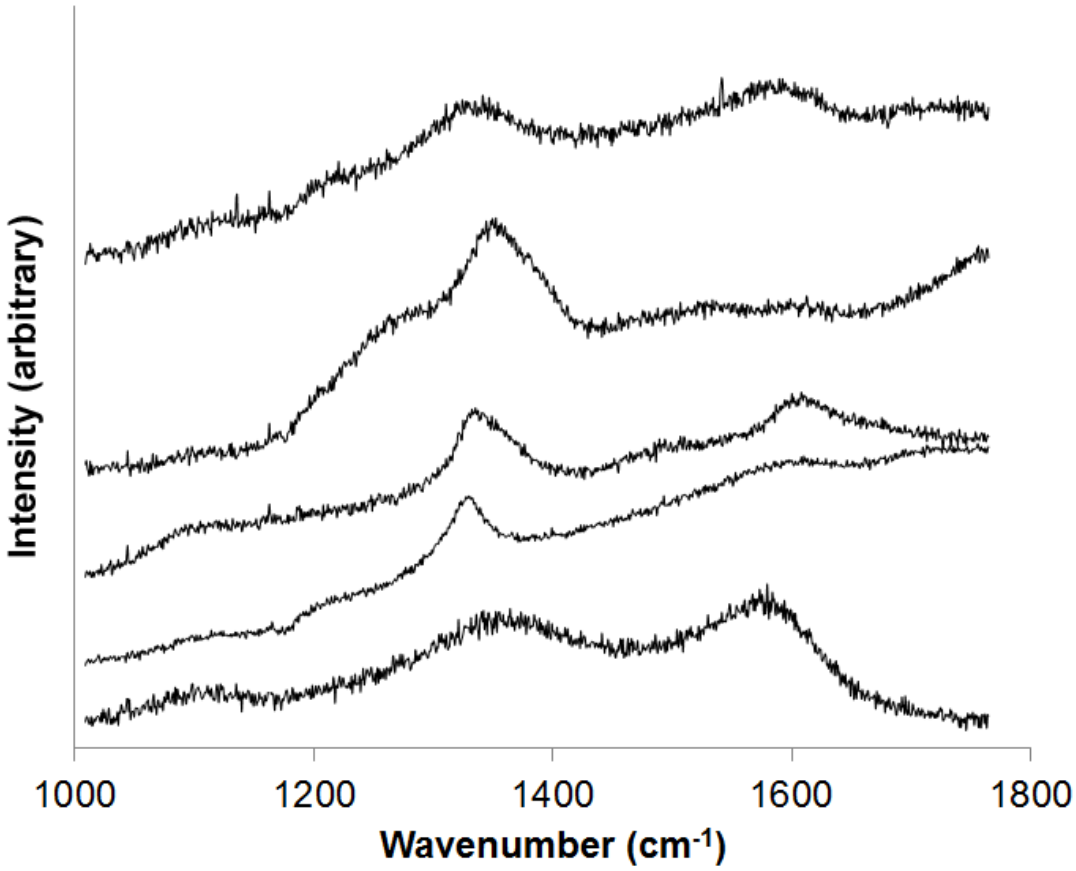

Figure A4.2. Example Raman spectra from the 1 µm and 0.5 µm polishing paste used to polish some of the ureilite sections.

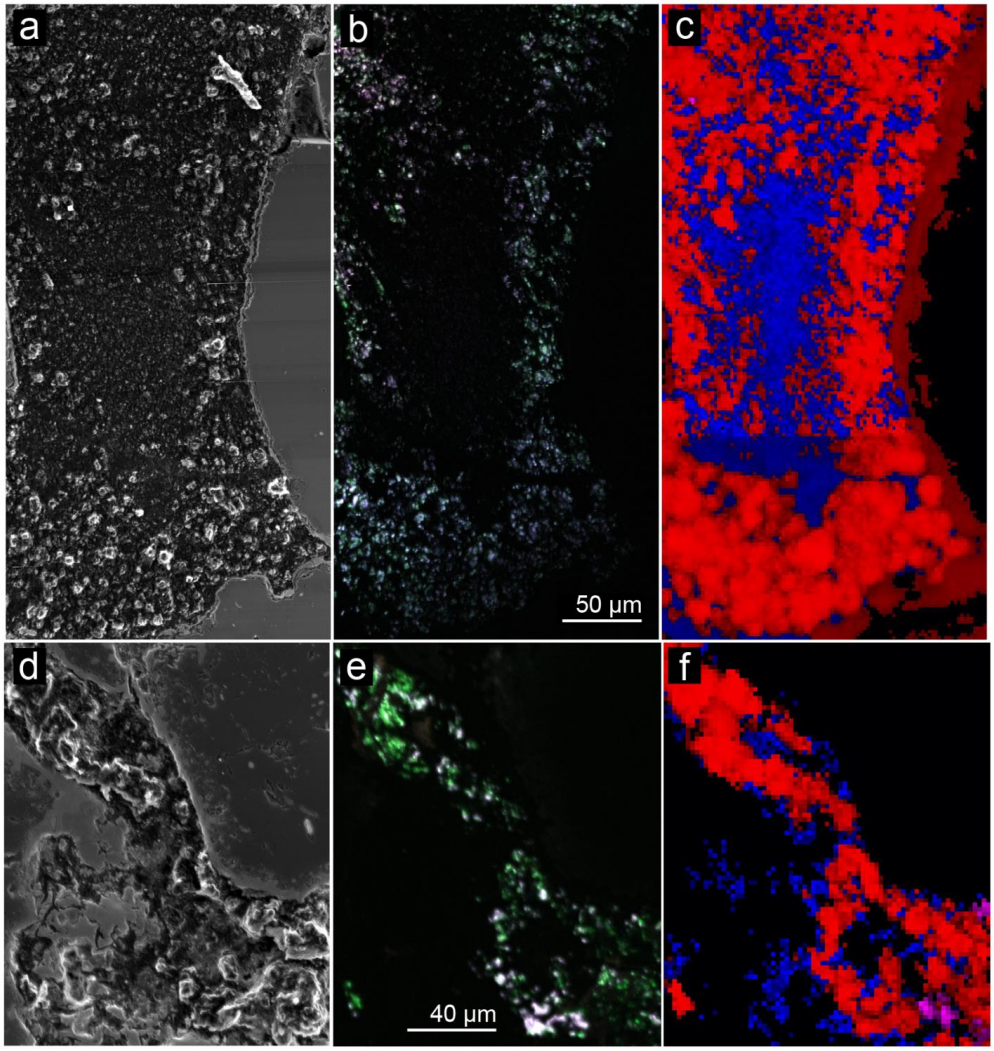

Figure A4.3. Additional images of carbon-rich areas. A region of NWA 11950 is shown through a) a Secondary electron image, b) CL image and c) Raman map. Please note that due to an under estimation of the autofocus distance required, there are some image artifacts in the Raman map. The lower third of the map is out of focus resulting in the muted colours in the map. Additionally, the edge of the carbon-rich region (dark red) is misidentified as having a diamond component. Nevertheless, the diamond-graphite textural relationships are texturally comparable to those seen in other maps. A region of NWA 11951 is shown through d) a Secondary electron image, e) CL image and f) Raman map. Note that this section was diamond-rich and polished using alumina, resulting in a large amount of topography. However, the region is texturally comparable to diamond-polished samples of the same meteorite.

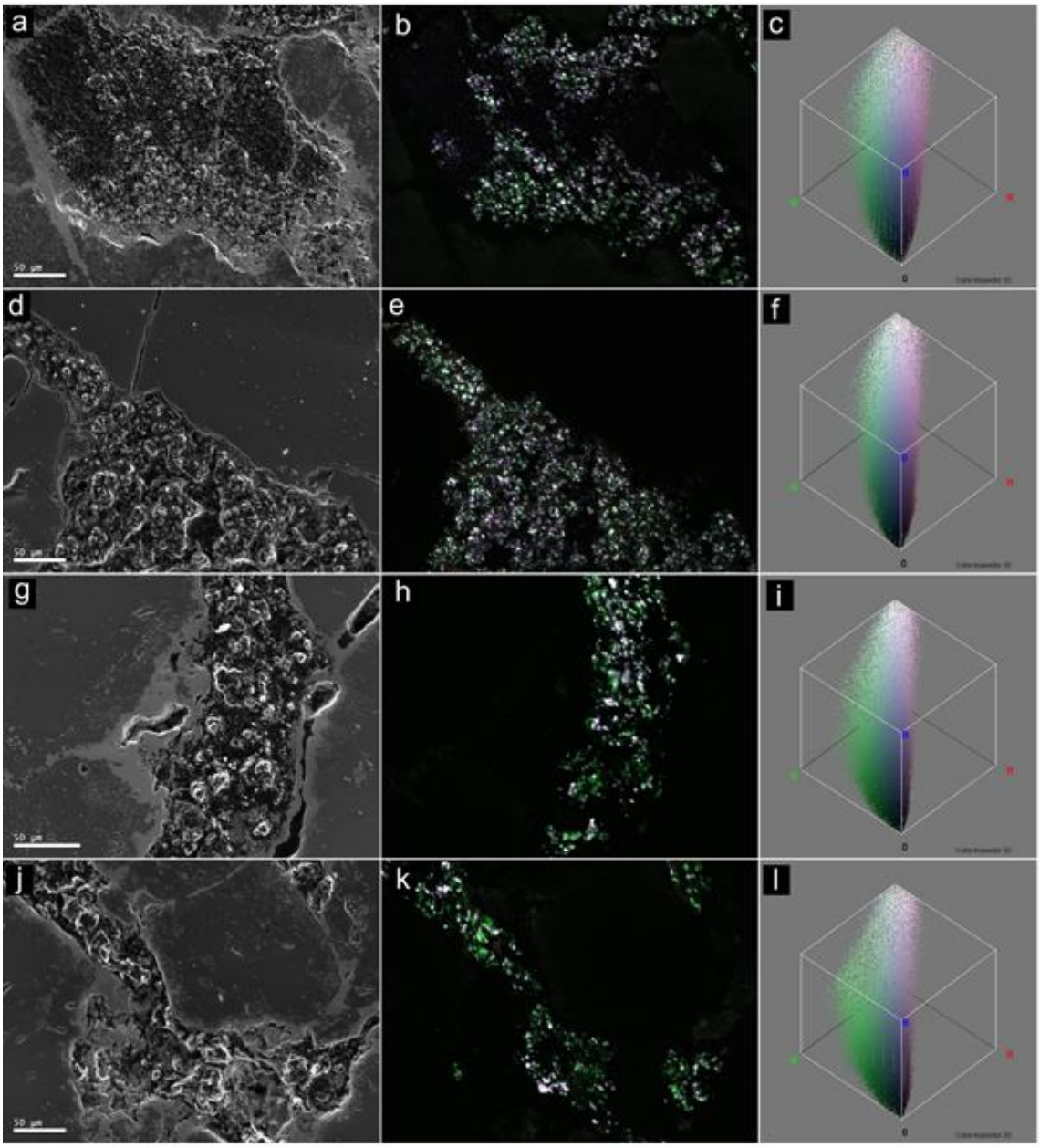

Figure A4.4. From left to right SE images, CL images and RGB plots of the CL data are shown for carbon-rich regions in the two meteorites. a)-f) for NWA 11950 and g)-l) for NWA 11951. For the RGB plots, the three colours are plotted along three axes. The "0" value is shown and intensities for each colour plot away from this "0" point. The Colour Inspector 3D plugin for Image J was used for plotting (Kai Uwe Barthel, Internationale Medieninformatik, Berlin, Germany).

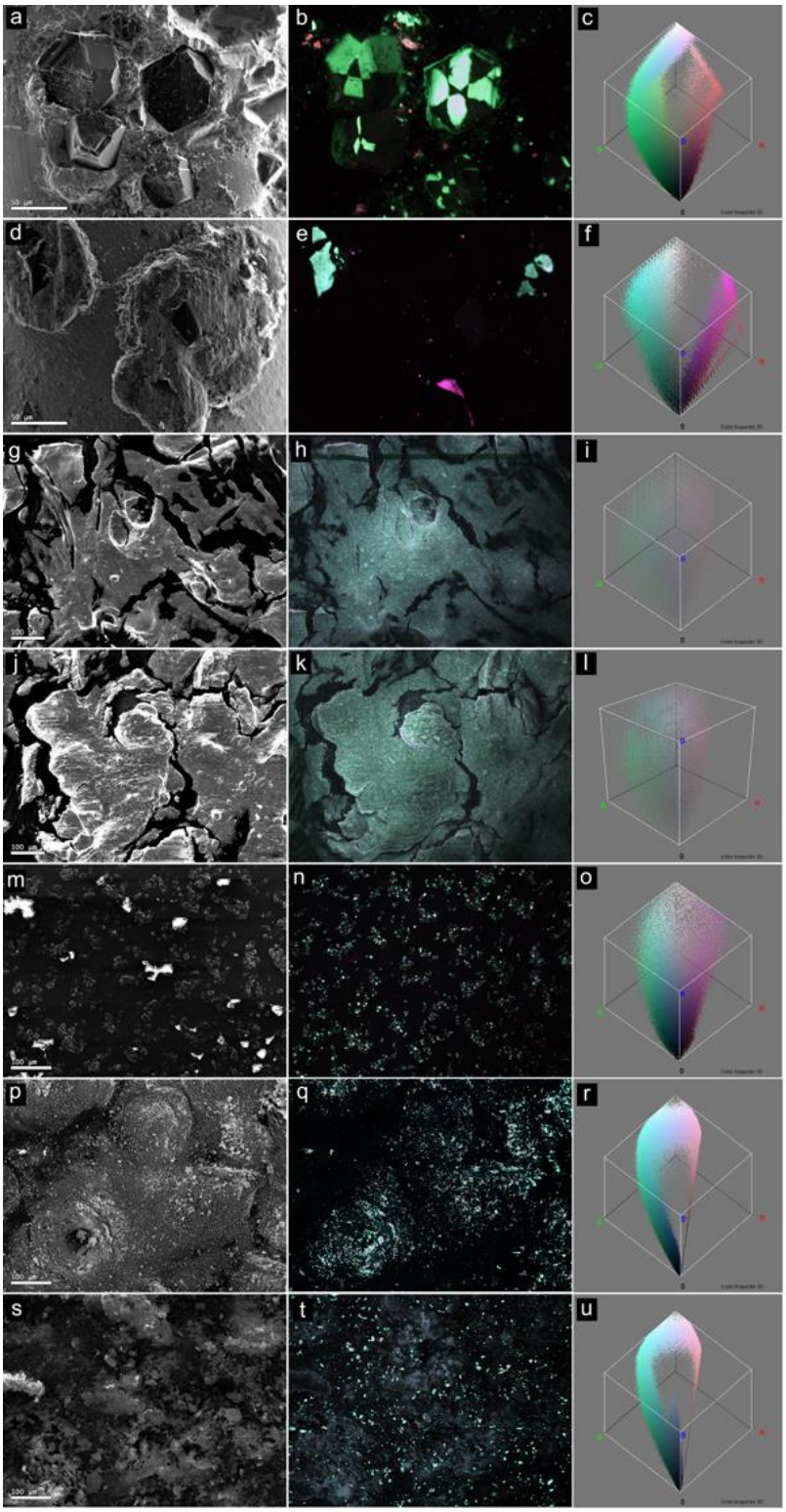

Figure A4.5. From left to right SE images, CL images and RGB plots of the CL data are shown for the diamond preparation products and alumina polishing powder. a-c) for one diamond wire source, d)-f) for a second diamond wire source, g)-i) for the 0.5 µm diamond paste, j)-l) for the 1 µm diamond paste, m-o) for the diamond film, p-r) for 1 µm alumina powder and s-u) for 0.3 µm alumina powder.. For the RGB plots, the three colours are plotted along three axes. The “0” value is shown and intensities for each colour plot away from this “0” point.

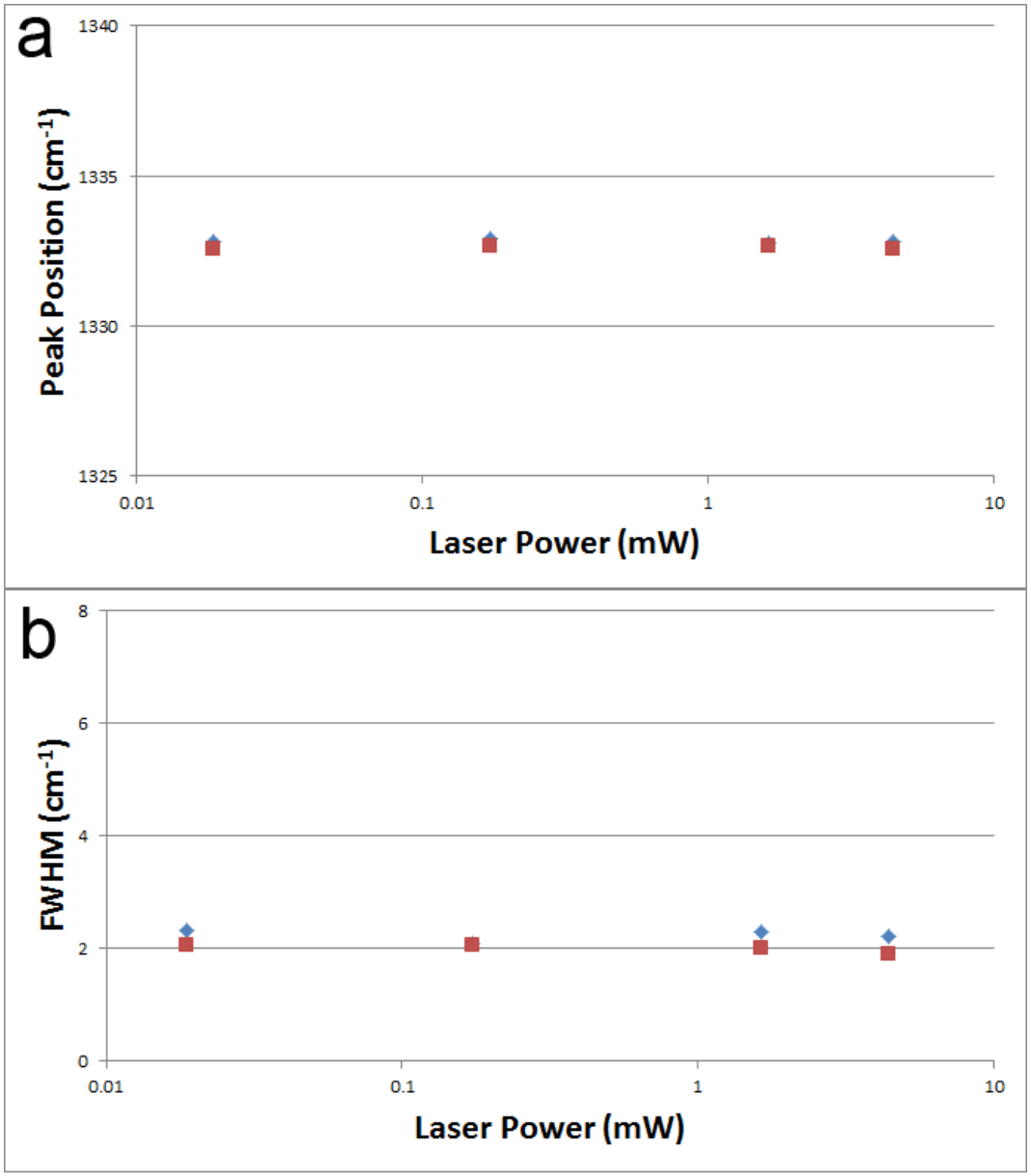

Figure A4.6. a) Measured peak positions for two diamonds from the diamond preparation products. The peak positions stay the same (within stated uncertainty) with increasing laser power. b) Measured FWHM for the same diamonds.

Reference

Wojdyr M. 2010. Fityk: a general-purpose peak fitting program. *Journal of Applied Crystallography* 43(5-1):1126-1128.

Appendix 5

Zircon morphology, chemical zoning and orientation microstructure in the NWA 869 eucrite clast and rim

Northwest Africa 869 is a chondritic regolith breccia meteorite with reported impact accretion of material from the eucrite parent body (Chapter 2). The impactor component is zircon-rich (Fig. A5.1) offering a unique opportunity to characterize the preservation/modification of zircon grains found in impactor materials from primordial crusts. The goal is to discriminate between primary and metamorphic zircon formation in preparation for dating small-scale impact processes.

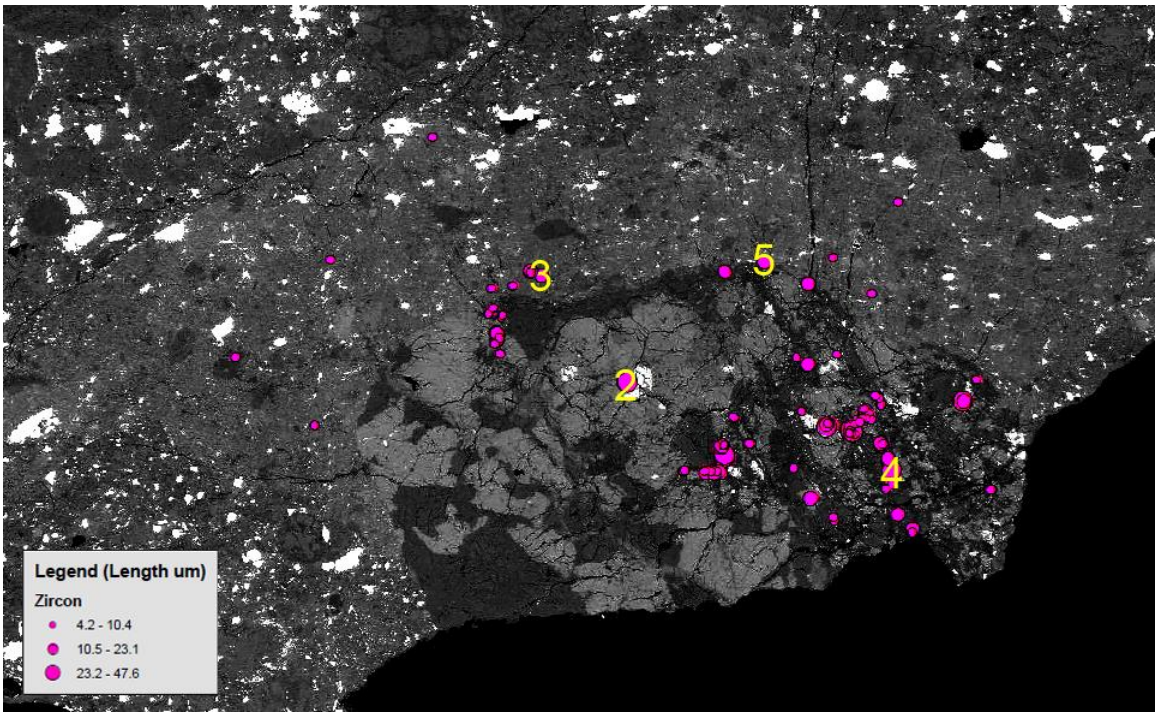

Figure A5.1. Backscattered electron image with zircon grains mapped. The size of the grains is shown in the legend. Zircon grains from subsequent figures have been numbered. Note: Figures are A5.#, # values shown above.

The zircon morphology, chemical zoning and orientation microstructure in and around the impactor were analyzed using a Hitachi SU6600 Field Emission Scanning Electron Microscope (FE-SEM). This study utilized cathodoluminescence (CL), backscatter

electron (BSE) imaging and electron backscatter diffraction (EBSD) mapping. For the CL set-up used, please refer to Chapter 3 and for the EBSD set-up, please refer to Chapter 4. Preliminary Raman work used a Horiba LabRAM ARAMIS micro-Raman spectrometer. For the Raman set-up used, please refer to Chapter 3.

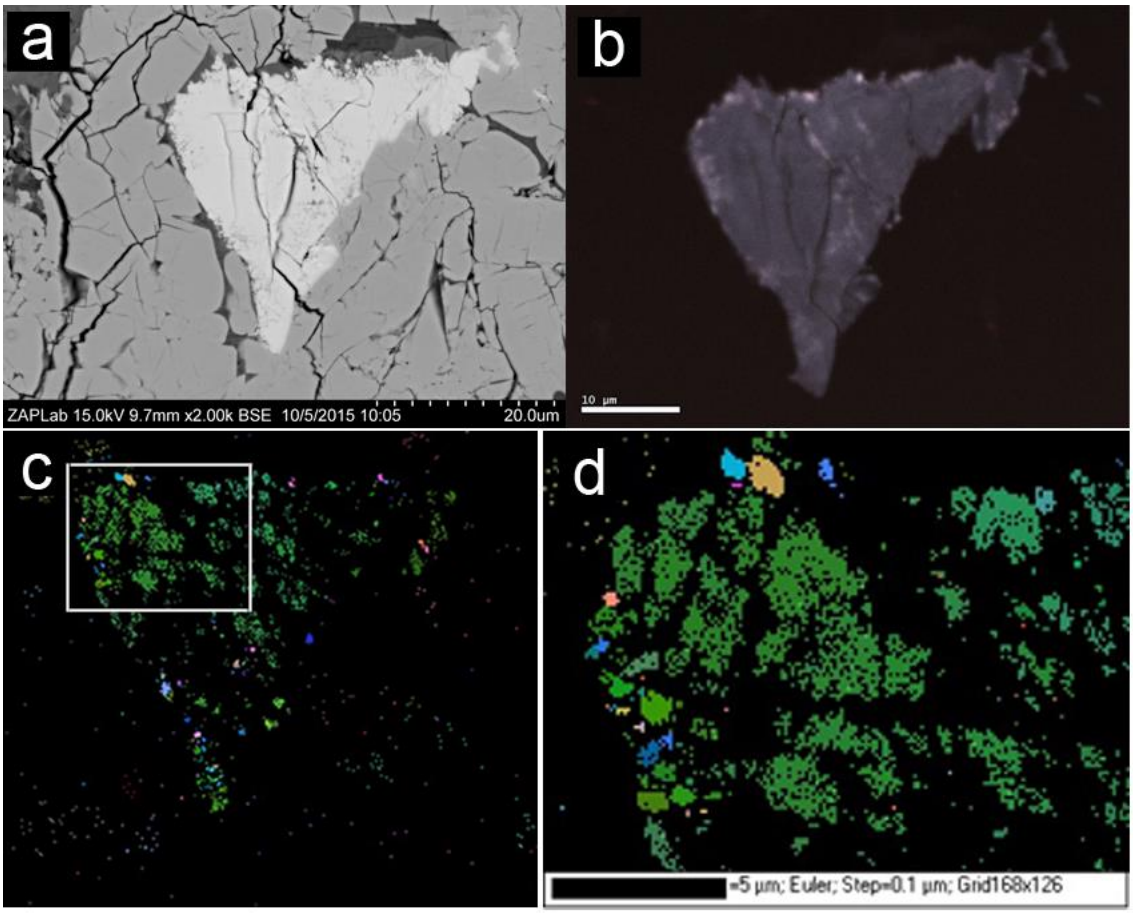

Figure A5.2. A zircon grain within ilmenite. a) BSE image of the grain, b) CL image of the grain, c) Euler angle map showing that there is variability in orientation of granules along the edge of the grain. Some areas of the grain show no diffraction (black), d) a higher resolution Euler angle map of the area highlighted in c).

Zircon grains within, and associated with, ilmenite are fractured and consist of crystalline domains exhibiting crystal plastic deformation as well as areas that appear to have been amorphized by shock (Fig. A5.2). Some of these grains have randomly oriented granules around their edges suggesting local impact heating/recrystallization (Fig. A5.2). A zircon in the breccia/melt rim partially shielded by ilmenite has even retained apparent igneous

zonation (Fig. A5.3). As seen in some eucrites (Roszjar et al. 2017), zircon in or near SiO_2-rich zones occur as aggregates of rounded concentrically CL-zoned regions suggesting a pre-impact, metamorphic origin (Fig. A5.4). Zircon grains show the most significant impact modification near the edge of the impactor. In this region whole grains are replaced by granular (submicrometre) zircon (Fig. A5.5). The granular zircons do not diffract suggesting they are amorphous, poorly crystalline, or crystalline at a length scale not resolvable by conventional EBSD (<50 nm). Preliminary, Raman analysis is consistent with this observation. Raman patterns from crystalline zircon show sharp peaks, whereas the granular zircons show weak peaks overlapped with amorphous humps and/or fluorescence (Fig. A5.6). This suggests the zircon is either poorly crystalline, or that a mixture of crystalline and amorphous material is present. High pressure zircon polymorphs and the high temperature breakdown of zircon to baddeleyite + SiO_2 have not been observed. The data provided in this study allow us to distinguish pre-impact zircon textures from shocked zircon textures. Coupled U-Pb dating and mineral chemistry will enable us to obtain a more accurate petrogenetic reconstruction of the accretionary process.

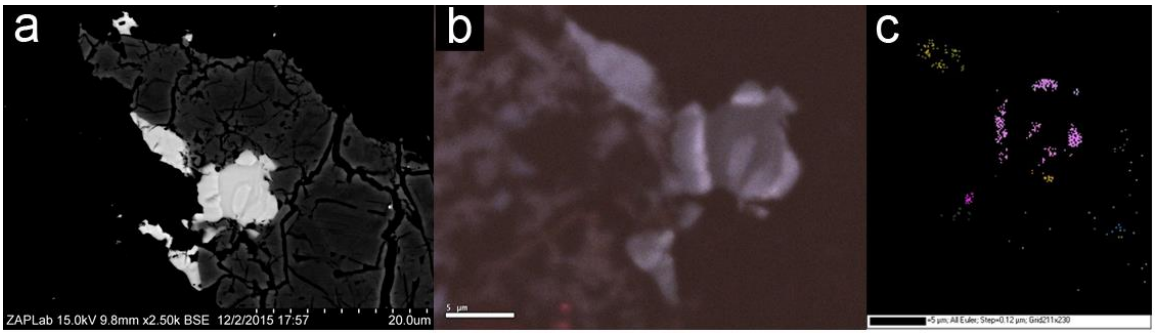

Figure A5.3. A zircon in the rim partially shielded by ilmenite. a) BSE image, b) CL image showing zonation, c) Euler angle map showing crystalline zones in the same orientation suggesting an igneous origin.

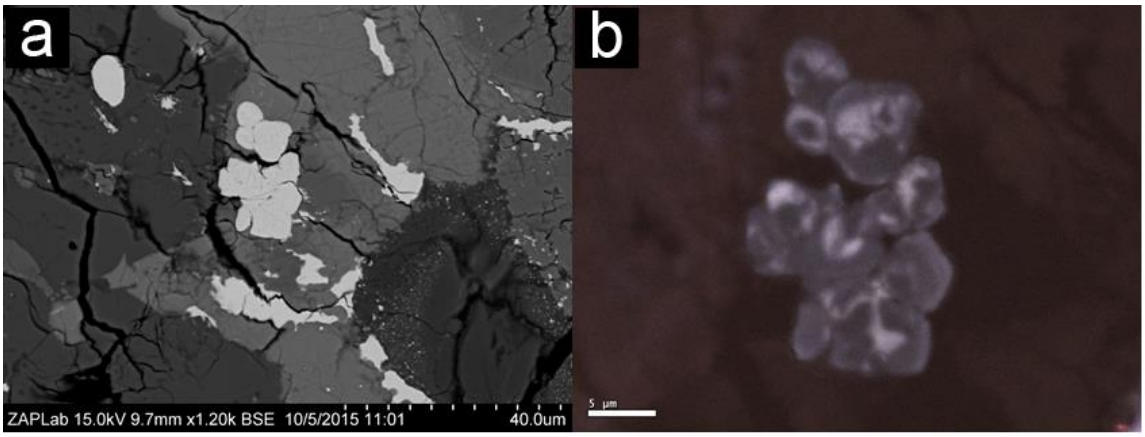

Figure A5.4. Zircon in SiO_2-rich region. a) BSE image, b) CL image showing aggregates of rounded concentrically CL-zoned regions.

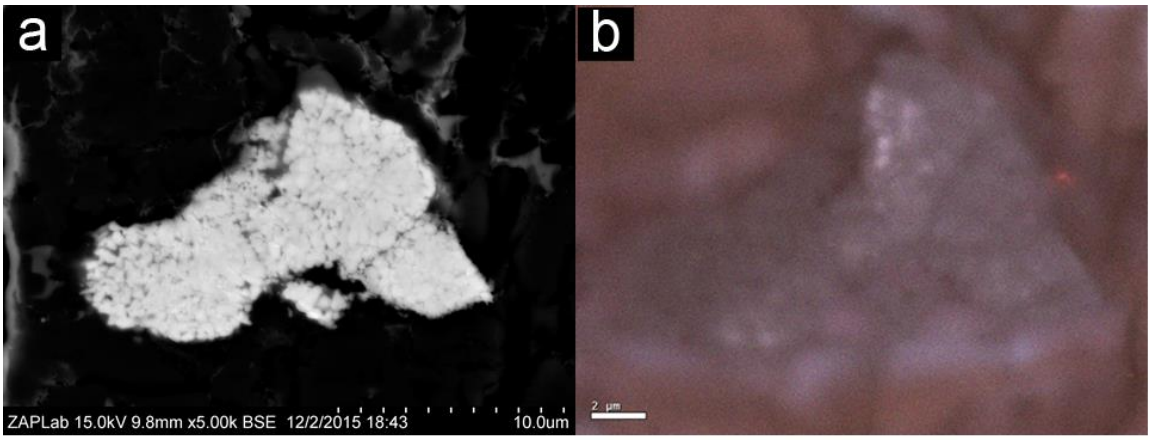

Figure A5.5. Zircon grain near the edge of the impactor. a) BSE image showing that the grain has been replaced by granular (submicrometre) zircon, b) CL image showing variability in intensity amongst the granules.

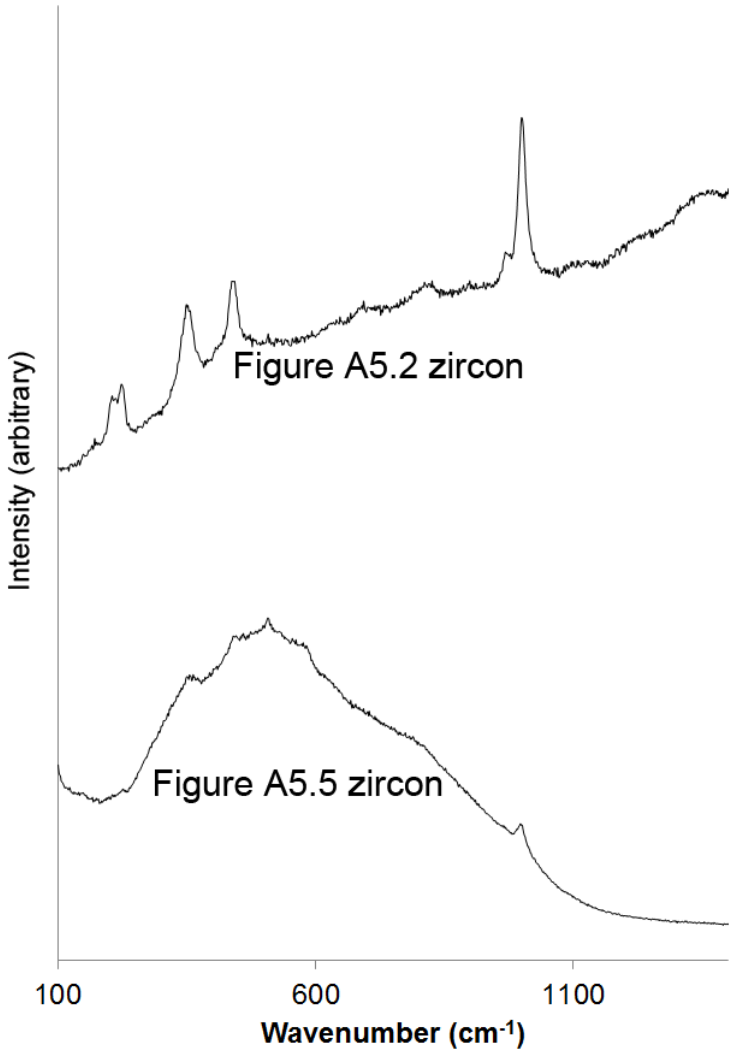

Figure A5.6. Raman pattern from crystalline zircon (top) showing sharp peaks and Raman pattern from granular zircon showing weak peaks overlapped with amorphous humps and/or fluorescence.

Reference

Roszjar J., Moser D. E., Hyde B. C., Chanmuang C., and Tait K. 2017. Comparing chemical microstructures of some early solar system zircon from differentiated asteroids, Mars and Earth. *In Microstructural Geochronology: Planetary Records Down to Atom Scale*, edited by Moser D.E., Corfu F., Darling J.R., Reddy S.M., and Tait, K. Washington: American Geophysical Union. pp. 113-135.

Curriculum Vitae

Brendt C. Hyde

Education

Ph.D. Candidate, at Western University (expected January 2020)

M.Sc. Geology, at the University of Western Ontario. (June 2009)

Honours B.Sc. Planetary Science, at the University of Western Ontario. (April 2006)

Academic Awards and Achievements

- Ontario Graduate Scholarship (OGS) (2018-2019)
- Western Doctoral Excellence Research Award (2016-2018)
- Postgraduate Scholarship Ph.D. level (PGS D) from the Natural Sciences and Engineering Research Council (NSERC) (2015-2018)
- Mineralogical Association of Canada Travel/Research Grant (2016)
- OGS (2015-2016, declined)
- OGS (2008-2009, declined)
- Canada Graduate Scholarship M.Sc. level (CGS M) from NSERC (2007-2008)
- Canadian Space Agency Supplement to CGS M from NSERC (2007-2008)
- Mineralogical Association of Canada Travel/Research Grant (2007)
- OGS (2006-2007)
- Undergraduate Student Research Award (USRA) from NSERC (2003, 2004, 2006)
- Robert and Ruth Lumsden Scholarship in Earth Science (2005)
- Robert and Ruth Lumsden Scholarship in Science (2002)
- The Western Scholarship of Excellence (2001)

Recent Work and Research Experience

Ph.D. Candidate, Dr. Desmond Moser and Dr. Kimberly Tait, the University of Western Ontario and the Royal Ontario Museum (ROM) (September 2015 – Present)

- The main objective of my Ph.D. is to describe the early melt processes initiating on asteroidal bodies, as represented in meteorites, and to obtain a detailed chronology of low temperature processes occurring on these bodies.
- Research materials involve numerous meteorite samples ranging from regolith breccia to materials formed in partial melt environments during asteroid differentiation.

- Instrumentation used includes field emission scanning electron microscopy (FE-SEM) equipment. In particular, backscatter electron (BSE) imaging, quantitative energy dispersive and wavelength dispersive spectrometry (EDS and WDS), cathodoluminescence (CL) and electron backscatter diffraction (EBSD).
- Further instrumentation used includes Raman spectroscopy and laser ablation inductively coupled plasma mass spectrometry (LA-ICP-MS). Use of the LA-ICP-MS included measurements of U-Pb from phosphate minerals.

Research Technician, Dr. Kimberly Tait, the Royal Ontario Museum (ROM)

(February 2010 - August 2015)

- Carried out research on minerals and meteorites
- Supervised the mineralogy laboratories containing X-ray diffraction (XRD), Raman microscopy and SEM equipment.
- Supervised and trained undergraduate and graduate students on the laboratory equipment
- Carried out duties as the Radiation Safety Officer (RSO) including training from the Radiation Safety Institute of Canada - RSO-1 course (2012) and X-ray Safety Officer (XSO) course (2012)
- Received ROM Health and Safety Award (2012)
- Received ROM Department of Natural History Travel Grant (2012, 2013, 2014)
- Presented research to visitors, donors, mineral club members and academics
- Generated information for displays and special events

Research Assistant, Dr. Brian Hart, Surface Science Western, the University of Western Ontario, (March 2009 – February 2010)

- Carried out experiments using a laboratory scale ball mill and flotation equipment
- Prepared grain mounts
- Carried out SEM analyses on natural ores and materials from laboratory experiments
- Carried out analyses on time of flight secondary ion mass spectrometry (ToF-SIMS)
- Took optical images and performed grain counts on samples

Student Researcher/ M.Sc. Student, Dr. Penny King, the University of Western Ontario, (May 2006 – May 2009)

- Carried out fieldwork at salt lakes in British Columbia. Measured pH, conductivity, dissolved oxygen, water temperature, water depth and GPS coordinates of lakes and measured air temperature and relative humidity. Collected mineral and rock samples for analysis
- Created microenvironments to control relative humidity to create hydrated sulfate minerals and keep them stable
- Synthesized iron sulfates in the laboratory using acidic solutions
- Characterized laboratory and field samples using combinations of XRD, infrared

Fourier transform spectroscopy, electron microprobe, SEM, inductively coupled plasma optical emission spectroscopy (ICP-OES), ion chromatography (IC) and mass spectrometry methods

Honours Thesis Student, Dr. Philip J. Stooke, the University of Western Ontario, (September 2005 – April 2006)

- Utilized spectral data from the Clementine lunar mission
- Processed lunar images using Adobe Photoshop to created mosaics and geologic maps

Teaching

Teaching Assistant, Western University, Earth Science 3312b: Genesis of Meteorites and Planetary Materials. Instructor: Roberta Flemming (January-April 2018)

- Helped prepare meteorite labs for third year students
- Supervised student use of micro-X-ray Diffractometer
- Marked laboratory work, assignments and final projects
- Helped create course content
- Guest lectured

Guest Lecturer, the University of Toronto, ESS 382: Meteorites and Space. Instructor: Kimberly Tait (February 2017)

- Created course content for a lesson on primitive achondrite meteorites
- Instructed a class on this topic
- Assisted students with a laboratory project on ordinary chondrites

Teaching Assistant, Western University, Earth Sciences 2240g: Catastrophic Events in Earth History. Instructor: Elizabeth Webb (January - April 2017), Sean Shieh (January - April 2016)

- Helped students develop writing and critical thinking skills and marked scientific essays (2016, 2017)

Teaching Assistant, Western University, Earth Sciences 200a: Tectonics and Lithology. Instructor: Dazhi Jiang (September - December 2007) and David Lescinsky (September - December 2006)

- Prepared rock and mineral labs for second year geology students
- Assisted students in lab work and graded labs and exams

Acquired Skills and Training

- Qualified to use many analytical instruments including: **SEM, XRD, Raman spectrometer**
- Qualified to **supervise students in class and laboratory** settings
- Qualified to **instruct university classes**
- Experience with **radiation and X-ray safety**
- Able to work with **unstable/time-sensitive materials**
- Able to **analyze visual images and large digital datasets**
- Experienced in the **writing of scientific papers** and conference abstracts
- Familiar with **Microsoft Office, Adobe Photoshop, Image J, SEM, XRD and Raman Spectroscopy software**
- Able to care out **fieldwork** duties including onsite measurements and sample collection
- Extensive problem solving and presentation skills
- Able to follow instructions and work independently

Publications

Citation Statistics (Google Scholar)

Citations	262
h-index	8
i10-index	8

Theses

Hyde, B.C. (2009) Bulk analysis, micro-analysis, IR spectroscopy and alpha particle X-ray spectroscopy of Fe-H-Sulfates. M.Sc. the University of Western Ontario.

Hyde, B.C. (2006) Sampling sites in the South Pole-Aitken Basin of the Moon. Honours B.Sc. the University of Western Ontario.

Chapters in Refereed Books

Roszjar J., Moser D.E., **Hyde B.C.**, Chanmuang C., and Tait K. (2017) Comparing Chemical Microstructures of Some Early Solar System Zircon from Differentiated Asteroids, Mars and Earth. In *Microstructural Geochronology: Planetary Records Down*

to Atom Scale, edited by Moser D.E., Corfu F., Darling J.R., Reddy S.M., and Tait, K. Washington: American Geophysical Union. pp. 113-135.

Articles in Refereed Journals

Hyde, B.C., Tait, K.T., Moser, D.E., Rumble, D., Thompson, M.S. (2020) Accretionary mixing of a eucrite impactor and the regolith of the L chondrite parent body. *Meteoritics & Planetary Science*, 55:20-35

Kizovski, T.V., Izawa, M.R.M., Tait, K.T., Moser, D.E., Day, J.M.D., **Hyde, B. C.**, White, L.F., Kovarik, L., Taylor, S.D., Perea, D.E., Barker, I.R., Joy, B. (In review) Petrogenesis, alteration, and shock history of intermediate shergottite Northwest Africa 7042: Evidence for hydrous magmatism on Mars? *Geochimica et Cosmochimica Acta*.

Darling, J.R., Moser, D.E., Barker, I.R., Tait, K.T., Chamberlain, K.R., Schmitt, A.K. and **Hyde, B.C.** (2016). Variable microstructural response of baddeleyite to shock metamorphism in young basaltic shergottite NWA 5298 and improved U–Pb dating of Solar System events. *Earth and Planetary Science Letters*, *444*:1-12.

Shaw, A., Daly, M.G., Cloutis, E., Basic, G., Hamilton, D., Tait, K., **Hyde, B.**, Lymer, E. and Balachandran, K. (2016). Reflectance properties of grey-scale Spectralon® as a function of viewing angle, wavelength, and polarization. *International Journal of Remote Sensing*, *37*(11):2510-2523.

Hyde, B.C., Day, J.M.D., Tait, K.T., Ash, R D., Holdsworth, D.W., and Moser, D.E. (2014) Characterization of weathering and heterogeneous mineral phase distribution in brachinite Northwest Africa 4872. *Meteoritics & Planetary Science*, 49:1141–1156.

Moser, D.E., Chamberlain, K.R., Tait, K.T., Schmitt, A.K., Darling, J.R., Barker, I.R., and **Hyde, B.C.** (2013) Solving the Martian meteorite age conundrum using micro-baddeleyite and launch-generated zircon. *Nature*, 499:454-457.

Zhou, B., Michaelis, V., Pan, Y., Yao, Y., Tait, K.T., **Hyde, B.C.**, Wren, J., Sherriff, B., and Kroeker, S. (2012) Crystal structure refinements of borate dimorphs inderite and

kurnakovite using 11B and 25Mg nuclear magnetic resonance and DFT calculations. *American Mineralogist*, 97:1858-1865.

Hyde, B.C., King, P.L., Dyar, M.D., Spilde, M.N., and Ali, A.-M.S. (2011) Methods to analyze metastable and microparticulate hydrated and hydrous iron sulfate minerals. *American Mineralogist*, 96:1856-1869.

Foster, I.S., King, P.L., **Hyde, B.C.**, and Southam, G. (2010) Characterization of halophiles in natural $MgSO_4$ salts and laboratory enrichment samples: Astrobiological implications for Mars. *Planetary and Space Science*, 58:599-615.

Lane, M.D., Bishop, J.L., Dyar, M.D., King, P.L., Parente, M., and **Hyde, B.C.** (2008) Mineralogy of the Paso Robles soils on Mars. *American Mineralogist*, 93:728-739.

Conference Abstracts

Yokoyama, S.T., Tait, K.T., Di Cecco, V.E. and **Hyde, B.C.** (2019) Determination of Petrologic Subtypes of CV3 Chondrites by Raman Spectroscopy. *82nd Annual Meeting of the Meteoritical Society*. Abstract 6450.

Sanborn, M.E., Yin, Q.Z., **Hyde, B.C.**, Tait, K.T. and Moser, D.E. (2018) Early Differentiation in the Carbonaceous Chondrite Forming Region of the Solar Nebula: New Insight from the Achondrites Northwest Africa 7680/6962. *49th Lunar and Planetary Science Conference*. Abstract 2296.

Hyde, B.C., Moser, D.E, Tait, K.T., Darling, J.R. and Moreira, H. (2017) In Search of a Group for the Ungrouped Achondrites NWA 7680 and NWA 6962. *48th Lunar and Planetary Science Conference*. Abstract 2168.

Hyde, B.C., Moser, D.E, Tait, K.T., Darling, J.R., Moreira, H., Barker, I.R., Nicklin, I. and Gregory, D. (2017) Pieces of the Planet Building Puzzle: Characterization of Early Solar System Melt Environments Recorded in the Ureilite, Lodranite-Acapolcoite and Metachondrite Meteorite Groups. *Advances in Earth Science Research Conference*. Abstract.

Roszjar, J., Moser, D.E., **Hyde, B.C.**, Chanmuang, C., and Tait, K.T. (2017) A Comparison of Microstructures Among Some of the Earliest-Formed Zircons. *80th Annual Meeting of the Meteoritical Society*. Abstract 6217.

Moser, D.E., Barker, I., Arcuri, G., Hey, J., **Hyde, B.**, Jones, G., Morissette, L. and Rolleman, J. (2017) The Zircon and Accessory Phase Laboratory (ZAPLab); A Canadian advance in nano- to atom-scale geochronology applied to resource and planetary evolution. *GAC-MAC 2017*. Abstract.

Hyde, B.C., Moser, D.E., Tait, K.T., Barker, I.R. and Joy, B.R. (2016) Development of Quantitative Energy Dispersive Spectrometry with a Field Emission Gun Scanning Electron Microscope for Use in Meteorite Studies. *Electron Probe Microanalysis Topical Conference (EPMA 2016)*, Abstract.

Roszjar, J., Moser, D.E., **Hyde, B.C.**, Chanmuang, C., Tait, K.T. and Nasdala, L. (2016) Comparison of Chemical Zoning of Eucrite and Martian Micro-Zircon. *79th Annual Meeting of the Meteoritical Society*, Abstract 6184.

Hyde, B.C., Tait, K.T., Rumble, D., Izawa, M.R.M, Thompson, M.S., Nicklin, I., Gregory, D. A. (2015) Achondritic Impactor Clasts in Northwest Africa 869. *46th Lunar and Planetary Science Conference*, Abstract 1983.

Izawa M.R.M., Tait, K.T., Moser D.E., Barker, I.R. and **Hyde, B.C.** (2015) Mineralogy, Petrology and Geochronology of Intermediate Shergottite NWA 7042. *46th Lunar and Planetary Science Conference*, Abstract 2523.

Ali, A., Banerjee, N.R., Jabeen, I., Tait, K.T., **Hyde, B.C.**, Nicklin, I., and Herrmann, P. (2014) An Oxygen Isotope Perspective on the Parent Body for Eagle Station Pallasites. *Meteoritics and Planetary Science Supplement*, 77: Abstract 5376.

Ali, A., Jabeen, I., Banerjee, N.R., Osinski, G.R., Tait, K.T., **Hyde, B.C.**, Nicklin, I., Ganderton, T., and Gregory, D. (2014) Oxygen isotope variations in main group pallasites and HEDs. *45th Lunar and Planetary Science Conference*, Abstract 2390.

Hyde, B.C., Tait, K.T., Nicklin, I., Gregory, D.A., Ali, A., Jabeen, I., Banerjee, N.R. (2013) Northwest Africa 7680: An ungrouped achondrite with affinities to primitive achondrite groups. *Meteoritics and Planetary Science Supplement*, 76: Abstract 5207.

Hyde, B.C., Tait, K.T., Nicklin, I., Day, J.M.D., Ash, R.D., and Moser, D.E. (2013) Use of micro-CT and precision cutting to assess meteorite heterogeneity: An example using brachinite NWA 4872. *Meteoritics and Planetary Science Supplement*, 76: Abstract 5301.

Ali, A., Jabeen, I., Banerjee, N.R., Osisnski, G., Tait, K.T., **Hyde, B.C.**, and Nicklin, I. (2013) Precise triple oxygen isotope analysis of Eagle Station and Itzawisis meteorites. *Meteoritics and Planetary Science Supplement*, 76: Abstract 5293.

Fowler-Gerace, N.A., Tait, K.T., Moser, D.E., **Hyde, B.C.**, and Barker, I. (2013) Mineralogical investigation of the phosphorus-rich Springwater pallasite. *Meteoritics and Planetary Science Supplement*, 76: Abstract 5276.

Ali, A., Jabeen, I., Banerjee, N.R., Tait, K.T., **Hyde, B.C.**, Nicklin, I., and Gregory, D. (2013) Potential for Bimodality in Main Group Pallasites: An Oxygen Isotope Perspective. *Meteoritics and Planetary Science Supplement*, 76: Abstract 5243.

Hyde, B.C. and Tait, K.T. (2012) The colors of suolunite from the Lac D'amiante mine, Quebec. 38th Rochester Mineralogical Symposium. *Rocks & Minerals*, 87(5):445-446.

Moser, D.E., Chamberlain, K.R., Tait, K.T., Schmitt, A.K., Barker, I.R., and **Hyde, B.C.**, and Darling, J.R., (2012) Microstructure and U–Pb dates of Martian baddeleyite rimmed by zircon indicate a 'young'igneous and metamorphic history for shergottite NWA 5298. *43rd Lunar and Planetary Science Conference*, Abstract 2173.

Hyde, B.C., King, P.L., Dyar, M.D., Spilde, M.N., Ali, A.-M.S., Atudorei, N.V. (2010) Hydrated and hydrous iron sulfate synthesis and analysis on the bulk and micro-scales. *2010 GSA Denver Annual Meeting*, Abstract 262-4.

King, P.L., Gellert, R., Campbell, J.L., **Hyde, B.C.**, Schofield, C.D.M., Perrett, G., Brown-Bury, W., Spilde, M.S., Boyd, N., Ollila, A., Lanza, N., Aran, T., McCutcheon,

W., and Newsom, H. (2010) Extended calibrations for the APXS for the Mars Science Laboratory mission. *41st Lunar and Planetary Science Conference*, Abstract 2539.

Hyde, B.C., Hart, B.R. and Dimov, S.S. (2009) ToF-SIMS Analysis of Pyrite Surface Oxidation on Samples Ground with Mild Steel and Stainless Steel Grinding Media. *17th International Conference on Secondary Ion Mass Spectrometry*.

Hyde, B.C., and King, P.L. (2009) Determining the water content on the martian surface using reflectance infrared spectroscopy of Fe-H-sulfates. Eos Trans. *AGU*, 90/(22), Abstract MA22A-05.

Foster, I.S., King, P.L., **Hyde, B.C.**, and Southam, G.S. (2009). Characterization of bacterial enrichments and natural MgSO4 salts containing halophilic Archaea and bacteria using reflectance IR, protein assays, and confocal microscopy: Implications for identifying biomarkers on Mars and the Jovian satellites. Eos Trans. *AGU*, 90/(22), Abstract MA22A-01.

King, P.L., Gellert, R., Schofield, C.D.M., **Hyde, B.C.**, Campbell, J.L., Perrett, G., Brown-Bury, W., Boyd, N., Ollila, A., Spilde, M.S., and Newsom, H. (2009) The APXS for the Mars Science Laboratory Mission – Extended Calibrations. Eos Trans. *AGU*, 90/(22), Abstract MA22A-02.

Lane, M.D., Bishop, J.L., Dyar, M.D., King, P.L., and **Hyde, B.C.** (2009) Iron Sulfate and Sulfide Spectroscopy at Thermal Infrared Wavelengths. *Workshop on Modeling Martian Hydrous Environments*. LPI Contribution No. 1482:34-35.

Hyde, B.C., King, P.L., Spilde, M.N., and Ali, A.-M. S. (2008) Characterization of Fe-sulfate minerals: Preparation for Mars sample return. *Ground Truth from Mars: Science Payoff from a Sample Return Mission*. LPI Contribution No. 1401:35-36

King, P.L., Lane, M.D., **Hyde, B.C.,** Dyar, M.D., and Bishop, J.L. (2008) Fe-sulfates on Mars: Considerations for martian environmental conditions, Mars sample return and hazards. *Ground Truth from Mars: Science Payoff from a Sample Return Mission*. LPI Contribution No. 1401:46-47.

Lane, M.D., Bishop, J.L., Dyar, M.D., King, P.L., and **Hyde, B.C.** (2008) Iron Sulfate and Sulfide Spectroscopy at Thermal Infrared Wavelengths for Application to Mars. *AGU,* Abstract P43B-1398.

Hyde, B.C., Foster, I., King, P.L., Southam G., and Nushaj, D. (2007) Limits of detection for life on Mars: An example using IR spectroscopy of sulfate salts and halophiles from lakes in British Columbia, Canada. *38th Lunar and Planetary Science Conference*, Abstract 2278.

Lane, M.D., Bishop, J.L., Dyar, M.D., Parente, M., King, P.L., and **Hyde, B.C.** (2007) Identifying the phosphate and ferric sulfate minerals in the Paso Robles soils (Gusev Crater, Mars) using an integrated spectral approach. *38th Lunar and Planetary Science Conference*, Abstract 2176.

Lane, M.D., Bishop, J.L., Dyar, M.D., Parente, M., King, P.L., and **Hyde, B.C.** (2007) The ferric sulfate and ferric phosphate minerals in the light-toned Paso Robles rover track soils: A multi-instrument analysis. *7th International Conference on Mars Conference*. LPI Contribution No. 1353:3331.

Non-refereed contributions

Hyde B.C. (2014) The "nature" of minerals. *Magazine of the Royal Ontario Museum*, 46(3):15.